12-6-2017 2:00 PM

Intraoperative Photoacoustic Imaging of Breast Cancer

Ivan Kosik, *The University of Western Ontario*

Supervisor: Jeffrey Carson, *The University of Western Ontario*

A thesis submitted in partial fulfillment of the requirements for the Doctor of Philosophy degree in Medical Biophysics

Abstract

Breast cancer is one of the most common cancers to affect women, presenting a lifetime risk of 1 in 8. Treatment of stage 1 and 2 cancers usually involves breast conserving surgery (BCS). The goal of BCS is to remove the entire tumour with a surrounding envelope of healthy tissue, referred to as a negative margin. Unfortunately, up to 50% of surgeries fail to remove the whole tumour. To minimize the risk of cancer recurrence, a second surgery, must therefore be performed. Currently, there is no widely accepted intraoperative tool to significantly mitigate this problem. Employed systems are usually based on imaging, such as x-ray or ultrasonography. Unfortunately, sensitivity and specificity deficits, especially related to breast density, reduce the effectiveness of these methods. Photoacoustic tomography (PAT) is a relatively new imaging modality which uses safe near-infrared laser illumination to generate 3-D images of soft tissues to a depth of up to several cm. We used a custom designed and built intraoperative PAT system, called iPAT, to perform a 100 patient study on freshly excised breast lumpectomy specimens within the surgical setting. The system enabled the evaluation of tumour extent, shape, morphology and position within lumpectomy specimens measuring up to 11 cm in diameter. Scan results were used to compare iPAT-derived tumour size to the gold-standard pathologic examination, and when available, to x-ray, ultrasonography and DCE-MRI. Imaging results were also used to classify specimen margins as close or wide, and positive predictive values (PPV), negative predictive values (NPV), sensitivity and specificity were then calculated to estimate the effectiveness of the iPAT system at predicting lumpectomy margin status. With a close margin prevalence of 35%, the PPV, NPV, sensitivity and specificity of iPAT were found to be 71%, 83%, 69%, and 84%, respectively. Information provided by the iPAT system identified 9 out of the 12 positive specimens, potentially reducing the positive margin rate by 75%. Contrary to expected photoacoustic contrast mechanisms, iPAT images of hemoglobin distribution correlated poorly with US and X-ray tumour imaging, while hypo-intense regions in lipid-weighted iPAT images were in excellent agreement.

Keywords: Breast cancer, Photoacoustic imaging, Breast conserving surgery, Intraoperative imaging, Surgical guidance, Tumour volume, Tumour diameter, Lumpectomy margins

Co-Authorship

The contribution by other authors to the work in Chapters 2, 3, and 4 is described here. Also the contribution to the work in Appendices 1 and 2 is included.

Chapter 2: Ivan Kosik, Muriel Brackstone, Anat Kornecki, Astrid Chamson-Reig, Philip Wong, Morteza Haydari Araghi, and Jeffrey J.L. Carson. "Intraoperative photoacoustic tomography (iPAT) of breast cancer: a novel imaging instrument and preliminary results",

In preparation for submission to Journal of Biomedical Optics.

Dr. Brackstone provided access to freshly excised lumpectomy specimens and contributed to discussion from surgical perspective. Dr. Kornecki provided interpretation of conventional imaging results from a radiologist perspective. Dr. Chamson-Reig facilitated project management and helped out with technical intraoperative tasks. Mr. Wong developed software for image co-registration and reconstruction in Matlab. Mr. Araghi provided software development in Labview. Dr. Carson provided general project supervision, aided with software and hardware expertise and manuscript editing. I designed and constructed the portable iPAT system, performed the experiments, performed intraoperative imaging, analyzed the data and wrote the manuscript.

Chapter 3: Ivan Kosik, Muriel Brackstone, Anat Kornecki, Astrid Chamson-Reig, Philip Wong, Morteza Haydari Araghi, and Jeffrey J.L. Carson. "Comparison of breast tumor size by intraoperative photoacoustic tomography, magnetic resonance imaging and pathology",

In preparation for submission to Annals of Surgery.

Dr. Brackstone provided access to freshly excised lumpectomy specimens and contributed to discussion from surgical perspective. Dr. Kornecki provided interpretation of conventional imaging results from a radiologist perspective. Dr. Chamson-Reig facilitated project management and helped out with technical intraoperative tasks. Mr. Wong developed software for image co-registration and reconstruction in Matlab. Mr. Araghi provided software development in Labview. Dr. Carson provided general project supervision, aided with software and hardware expertise and manuscript editing. I designed and constructed the portable iPAT system, performed the experiments, performed intraoperative imaging, analyzed the data and wrote the manuscript.

Chapter 4: Ivan Kosik, Muriel Brackstone, Anat Kornecki, Astrid Chamson-Reig, Philip Wong, Morteza Haydari Araghi, and Jeffrey J.L. Carson. "Intraoperative photoacoustic imaging of breast cancer: a new perspective on malignancy visualization and surgical guidance",

In preparation for submission to Nature Medicine.

Dr. Brackstone provided access to freshly excised lumpectomy specimens and contributed to discussion from surgical perspective. Dr. Kornecki provided interpretation of conventional imaging results from a radiologist perspective. Dr. Chamson-Reig facilitated project management and helped out with technical intraoperative tasks. Mr. Wong developed software for image co-registration and reconstruction in Matlab. Mr. Araghi provided software development in Labview. Dr. Carson provided general project supervision, aided with software and hardware expertise and manuscript editing. I designed and constructed the portable iPAT system, performed the experiments, performed intraoperative imaging, analyzed the data and wrote the manuscript.

Appendix 1. Ivan Kosik, Jeffrey JL Carson, "Reat-time Multispectral Imaging of Blood Phantoms" SPIE Annual Meeting Symposium on Biomedical Optics, 2013.

Dr. Carson provided general project supervision, aided with software and hardware expertise and manuscript editing. I designed and constructed the multispectral photoacoustic system, performed the experiments, analyzed the data and wrote the manuscript.

Appendix 2. Ivan Kosik, Jeffrey JL Carson. "Combined 3D photoacoustic and 2D fluorescence imaging of indocyanine green contrast agent flow." SPIE Annual Meeting Symposium on Biomedical Optics, 2013.

Dr. Carson provided general project supervision, aided with software and hardware expertise and manuscript editing. I designed and constructed the multispectral photoacoustic system, performed the experiments, analyzed the data and wrote the manuscript.

Acknowledgements

The work completed over the course of my PhD studies would not have been possible without the support, encouragement and dedication of numerous people.

First of all, many thanks are owed to my supervisor, Jeff. While you were an amazing supervisor and a friend, you were really much more than that. The atmosphere that you established in the lab, and generally during all activities, nurtured the creativity and free thinking that great research so strongly depends on. Our regular brain-storming sessions, especially in the first years of my PhD, opened my mind up to a new way of looking at old problems and significantly contributed to many of the vitally needed breakthroughs.

Astrid, as the project coordinator/manager, you somehow always managed to guide me to the dim light at the end of that long dark chaotic tunnel. As a friend, for all the long days, early mornings and late nights, especially surgery days, thank you.

Part of the challenge of this project was the need for a broad range of highly specialized skill sets, including technical as well as clinical. To Muriel, for your surgical expertise and patience while we worked out the bugs in the system, thank you. To Anat, for your time and guidance in image interpretation from a radiologist's perspective, many thanks. To Phil, your perseverance in working out a suitable image reconstruction approach is much appreciated.

The financial needs of this project were great and I would like to thank the many faces behind support provided by the Western Graduate Scholarship (WGRS), the Translational Breast Cancer Research Unit (TBCRU), the Canadian Institutes of Health Research (CIHR) and the Ontario Graduate Scholarship (OGS).

I would also like to thank my family and friends. To Starka, Mamka, Tony, sisters and brother, for a seemingly inexhaustible display of pride for every one of my successes, no matter how small. You made me believe in myself.

And finally, to my beautiful wife Melissa. I know you didn't sign up for raising two amazing boys while I tackled a PhD. Thank you for supporting me on this uncertain journey while gracefully putting up with my stress-induced fits. I dedicate this work to your dad, Sam, for instilling in you his calm, cool demeanor and enduring strength of character.

Table of Contents

List of Figures

List of Tables

List of Appendices

List of Abbreviations

2D	two dimensional
3D	three dimensional
BCS	Breast conserving surgery
BIRADS	Breast imaging and reporting data system
cm	Centimeter
CT	Computed tomography
DAQ	Data acquisition
DCE	Dynamic Contrast Enhanced
DCIS	Ductal carcinoma in situ
DRS	Diffuse reflectance spectroscopy
FOV	Field of view
FWHM	Full width at half-maximum
Hz	Hertz
IDC	Invasive ductal carcinoma
IL	Intralipid™
ILC	Invasive lobular carcinoma
kHz	Kilohertz
LCIS	Lobular carcinoma in situ
LOIS	Light optoacoustic imaging system
MHz	Megahertz
mJ	Millijoule
mm	Millimeter
MRI	Magnetic resonance imaging
ms	Millisecond
Nd:YAG	Neodymium-doped yttrium aluminum garnet
NIRS	Near infrared spectroscopy
ns	Nanosecond
OCT	Optical coherence tomography
OPO	Optical parametric oscillator
PA	Photoacoustic
PAI	Photoacoustic imaging
PAM	Photoacoustic microscopy

PAT	Photoacoustic tomography
PC	Personal computer
PET	Positron emission tomography
RECIST	Response Evaluation Criteria in Solid Tumors
RF	Radio frequency
RTB	Residual tumour burden
s	Second
SNR	Signal-to-noise ratio
SVD	Singular value decomposition
US	Ultrasound
μm	Micrometer
μs	Microsecond

Chapter 1: Introduction

1.1 Background

1.1.1 Cancer overview

Cancer is an umbrella term used to describe a class of diseases that arise due to abnormal cell division and growth. While this may appear to be a relatively simple concept, the specific ways by which a normal cell alters its behavior to become a cancer, or malignant cell, seem insurmountably complex. Nevertheless, in their highly influential work, "The Hallmarks of Cancer", cancer researchers Hanahan and Weinberg identify six crucial characteristics that differentiate cancer cells from their normal counterparts[1]. Briefly, they summarize the "hallmarks" of cancer cells as (1) possessing a self-sufficiency in growth signals, (2) insensitivity to anti-growth signals, (3) evasion of apoptosis, or cell death, (4) limitless replicative potential, (5) sustained angiogenesis, or vascular recruitment, and (6) tissue invasion and metastasis. It is the sixth identifying characteristic, namely the cancer cell's potential to spread, or metastasize to other parts of the body that is of most concern to doctors and patients alike. The most common locations where cancer spreads are the liver, lung, bone and brain. Indeed, the majority of cancer fatalities are not caused by the primary tumour. Instead it is the uninterrupted progression of the disease to the metastatic stage that results in a terminal diagnosis, and this is of paramount concern for most cancers, including breast cancer.

1.1.2 The breast and breast cancer

About 1 in 8 women in the developed world are expected to develop breast cancer during their lifetime[2]. For women, this means that breast cancer is the most common cancer and the second leading cause of cancer mortality.

The main function of the female breast is to host the milk producing gland, known as the mammary gland. As such, its composition can be reduced to several key constituents. The most relevant components of the female breast are outlined in Figure 1.1. Depending on the individual, and to a lesser degree, age, subcutaneous fat is found throughout the breast to varying degrees, giving it its characteristic shape as well as firmness, or density. Specifically, breast density is determined by the proportion of fat to the more dense fibrous and glandular tissue, sometimes called fibro-glandular tissue. Fibrous tissue includes suspensory ligaments and generally structural stroma, while glandular tissue comprises the mammary gland. The mammary gland begins at the nipple, from which ductal tissue begins branching out and ultimately terminates at the lobules. The lobules are organized into a number of much larger lobes, with stroma filling the space between.

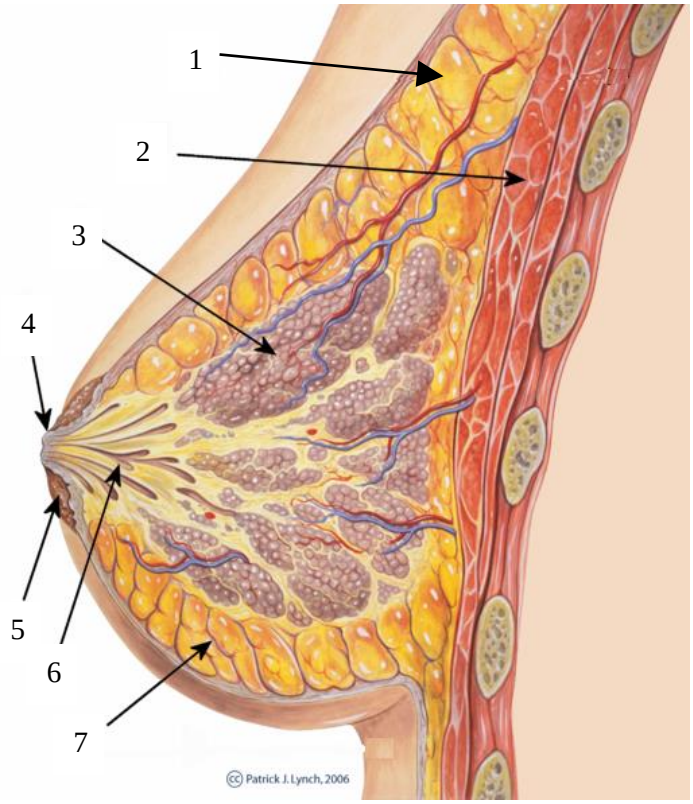

Figure 1.1. Female breast anatomy. (1) Subcutaneous fat, (2) pectoralis muscle, (3) lobules organized into larger lobes, (4) nipple, (5) areola, (6) branching ducts, (7) suspensory ligaments. (Adapted from [3])

Today, it is well known that dense breasts, which contain a higher proportion of fibrous and glandular tissue, increase the risk-factor for developing breast cancer and reduce the effectiveness of currently employed diagnostic methods[4]. To combat this problem, the American College of Radiology (ACR), a leading authority on standardization of cancer assessment and reporting methods, established a lexicon for the categorization of breast density based on the proportion of fatty and fibro-glandular tissue found throughout the breast[5]. Table 1.1 lists the standardized categories as well as the expected accuracy of current diagnostic methods.

Table 1.1. ACR classification of breast tissue and associated diagnostic accuracy. [adapted from [5]]

ACR	Description	Diagnostic accuracy
1	Mostly fatty	Very high
2	Fibro-glandular	High
3	Heterogeneously dense	Limited
4	Dense	Limited

Breast cancer sub-types are numerous, but most can be grouped based on their site of origin and level of infiltration. Breast cancer that begins in the ducts and invades the surrounding fatty or fibro-glandular tissue, is referred to as invasive ductal carcinoma (IDC). IDC is by far the most commonly diagnosed breast cancer, representing about 80% of invasive cancer diagnoses. If the cancer does not invade the surrounding tissue but instead remains confined within the ducts, it is called ductal carcinoma in-situ (DCIS). As a common precursor to invasive ductal cancer, DCIS is often found along with it. Similarly, when the cancer starts within the lobules, invasive lobular carcinoma (ILC), and lobular carcinoma in-situ (LCIS) refer to invasive and non-invasive types of the disease, respectively. Lobular cancers represent about 10% of invasive cancer diagnoses. Other sub-types of breast cancer can occur, but are rare.

1.1.3 Breast cancer screening, diagnosis and staging

Carcinoma of the breast presents with many variations in both the microscopic and macroscopic regime. Our desire to understand, detect, and treat the condition, has led to the development of an equally complex arsenal of diagnostic and surgical procedures, imaging methods, and therapies. In spite of the steadily rising incidence rate of breast cancer, these developments have led to a dramatic improvement in survival and quality of life for patients dealing with the disease today, as compared to a few decades ago. This improvement is largely due to the early detection of cancers via regional screening programs[6,7].

Thanks to the availability of medical imaging technology, routine breast cancer screening programs are now a relatively standard practice in the developed world[7]. Most women over the age of 50, or younger at-risk individuals, are encouraged to undertake annual mammograms. The Breast Imaging and Reporting Data System (BIRADS), introduced by the ACR, is commonly used to standardize results of imaging studies[8,9]. These results are categorized in range from negative or benign (BIRADS 1 and 2), to proven malignancy (BIRADS 6). Ultimately, microscopic tissue samples are extracted from the suspect area of the affected breast, usually by needle core biopsy, and histological tissue analysis determines the basis for a BIRADS 6 diagnosis.

In cases that lead to a BIRADS 6 classification, cancer staging is typically performed to determine the extent, or progression, of the disease[10]. Staging refers to the size of the primary malignant lesion as well as the extent to which the cancer has spread beyond its original location. The most common staging convention assesses the disease on a scale of 0 to 4 where stages 1 to 4 are indicated using roman numerals I to IV [11]. The disease assessment depends on various factors such as lesion diameter, sentinel lymph node involvement, and distant metastasis. Often cancer staging is used to group the disease progression into either early stage, locally advanced, or metastatic breast cancer.

Early stage breast cancer refers to lesions that are less than 5 cm in diameter with no more than 3 lymph nodes involved. This includes stage I and most stage II diagnoses. On the other hand, locally advanced

breast cancer includes lesions that are more than 5 cm in diameter. Furthermore, locally advanced disease implies that cancer has spread to more than 3 lymph nodes, or was found in other nearby tissues, such as muscle and skin. Locally advanced breast cancer includes some stage II and all stage III diagnoses, as well as inflammatory breast cancer. Finally, metastatic, or advanced breast cancer, consists of disease that has spread to other organs in the body. It is referred to as stage IV breast cancer[11]. Fortunately, in the developed and developing world today, most diagnoses of breast cancer occur at relatively early stages, usually stage I or II [2].

1.1.4 Breast conserving surgery and lesion localization techniques

Typically treatment of stage I and II diagnoses of breast cancer includes Breast Conserving Surgery (BCS), sometimes referred to as lumpectomy. The goal of the procedure is to excise all malignant tissue from the breast surrounded by a continuous envelope of normal tissue. A successful procedure results in a negative margin and is depicted in Figure 1.2(a).[12] Currently, the necessary width of a lumpectomy margin to minimize cancer recurrence is a topic of debate. Opinions range from less than 2 mm to more than 10 mm depending on age, cancer type and therapies employed. [12–14] Nevertheless, in clinical practice the procedure often fails, resulting in a positive margin being reported by pathology at a later time. This occurs in up to 60% of cases and is shown in Figure 1.2(b). [15,16] To minimize the risk of cancer recurrence such a finding usually leads to need for a second surgery. This situation has a negative impact on hospital resources and patients, by delaying adjuvant therapy, elevating stress levels and degrading cosmetic outcome. Reducing BCS re-excision rates would translate to a substantial improvement in breast cancer care from both a monetary and personal perspective.

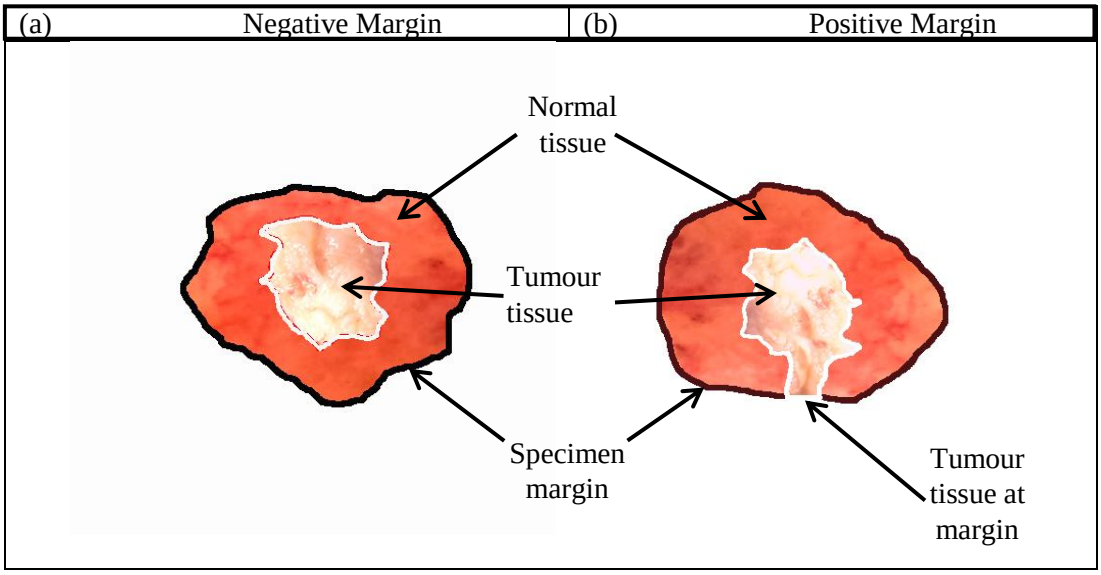

Figure 1.2. Possible outcomes of breast conserving surgery. (a) The tumour tissue is enclosed in a continuous envelope of normal tissue, indicating a lumpectomy specimen with negative margin. (b) Specimen with positive margin. The margin is clearly invaded by tumour tissue.

Traditionally, preoperative lesion localization is performed to guide the surgeon and aid in successful surgical outcomes. Various approaches have been implemented with differing rates of success. One of the earliest and widely used techniques, known as wire-guided localization (WGL), involves the insertion of one, or more, fine hooked wires into the lesion of interest. To ensure that the hooked-end of the wire is placed inside the lesion, the insertion is performed under medical imaging guidance. During BCS the surgeon uses the localization wire as a guide towards malignant tissue, thereby improving the chances of success[17].

A more frequently successful localization technique, called radio-guided localization, uses a radiotracer that is injected into the lesion under imaging guidance[18]. However, the use of injectable radiotracers complicates the protocol, and consequently, the use of radio-guided localization has not seen widespread implementation. On the other hand, a similar procedure, called radioactive seed localization, is enjoying more widespread use as it delivers the precision and convenience of radio-guidance without the need for tracer injection. Instead, in radioactive seed localization, a small radioactive Iodine-125 seed is inserted into the lesion under imaging guidance[12]. Nevertheless, with either tracer or seed localization, the

operating surgeon enjoys the convenience of a gamma proximity probe to locate the source of radioactivity, and with it, the lesion.

1.2 Clinical breast cancer imaging and surgical guidance

There are many possible candidate techniques for the assessment of disease extent or tumor size. Currently, the accepted gold standard is postsurgical histopathological examination. Unfortunately, for obvious reasons, the examination results are not available to guide pre-surgical decisions.

Physical breast examination via palpation remains useful due to its relative simplicity, enabling patients to perform routine self-exams and offering the possibility of catching a tumor early, especially if located peripherally. Unfortunately, palpation has been shown to be unreliable, particularly in dense breasts, as well as dependent on examiner experience and nature of tumor. In clinical trials, physical examination has been shown to be one of the least accurate techniques in correlation with histopathological examination[19].

1.2.1 Diagnostic and preoperative in vivo imaging

Current clinical practice in the treatment of breast cancer usually involves a number of medical imaging technologies that are used to carry out, or aid in, a variety procedures. As mentioned earlier, preoperative lesion localization techniques, such as wire-guided or radio-guided localization, depend on image guidance to ensure accurate placement. However, application of medical imaging technology toward treatment of breast cancer is much broader. From breast cancer screening, diagnosis and staging, to treatment monitoring and biopsy guidance, medical imaging plays a vital role throughout the treatment process. Here, the most frequently used imaging methods are described.

As a generally accepted breast cancer screening tool and due to its relatively good balance between cost, complexity, sensitivity and specificity, X-ray mammography is perhaps the most widely used breast

imaging technique[7,19]. On the other hand, studies have demonstrated a significant sensitivity and specificity reduction in younger patients, and independently in denser breasts, particularly when monitoring response to neoadjuvant therapy[20]. Furthermore, in cases with spiculated lesions, the 2-D nature of mammographic images can make the true 3-D size of tumors difficult to estimate.

Ultrasonography (US) has demonstrated better sensitivity than mammography but suffers from lesion size underestimation and, due to its operator dependence, is not a reproducible procedure with good repeatability statistics[10,19,21]. Notably, some studies have demonstrated a significant improvement in sensitivity when a combination of US and mammography was used, and generally, overall improvement in disease extent assessment when multiple modalities were employed. From a practical perspective, the expense and complexity of using multiple imaging modalities to assess single cases points toward an unmet need in this area.

Dynamic contrast enhanced magnetic resonance imaging (DCE-MRI) has established itself as the best single imaging modality in the detection and evaluation of breast cancer. It's effectiveness for estimating in vivo tumor burden has been validated in numerous studies and shown to be superior to both mammography and ultrasound[10,21,22]. The success of DCE-MRI, particularly in differentiating various soft tissues, is largely attributed to its inherent molecular source of contrast. Compared to mammography and sonography, both of which derive contrast based on tissue physical density, DCE-MRI offers sensitivity and specificity towards specific molecules, such as H_2O, and lipids. Consequently, the technique is capable of differentiating fatty tissues from muscle, glandular and connective tissues. Furthermore, by use of time-resolved intravenous contrast perfusion tracking DCE-MRI can estimate tissue specific parameters, such as tissue permeability, which is instrumental in differentiating malignant lesions from other tissue types. On the downside, specificity deficits lead to a sub-optimal false positive rate particularly in breasts exhibiting high background parenchymal enhancement. Large studies have shown that frequent use of DCE-MRI leads to unnecessary repeat surgical procedures and mastectomies due to overestimates of tumour size and detection of numerous non-specific lesions.[23] Consequently, this

feature has prevented DCE-MRI from being recommended for general population screening and second-look ultrasound is often used to cross check suspicious MRI findings. Finally, these shortcomings combined with the high cost and complexity of DCE-MRI mean that its use will likely be limited to mammographically/sonographically occult lesions and cases where mammography and US produce ambiguous findings[24].

18FDG-PET imaging, an excellent whole body distant metastasis detector, has been proposed and occasionally used to also assess tumor stage and monitor therapy efficacy. However, the procedural complexity as well as use of radiotracers combined with limited sensitivity for small (<2-3 cm) tumors and a rather high false positive rate, reduces the utility of PET as an efficient tumor extent assessment tool[25].

1.2.2 Intraoperative ex-vivo specimen imaging

Beyond patient imaging, medical imaging continues to aid in breast cancer treatment in the surgical arena. Below, we describe two of the most common intraoperative lumpectomy specimen imaging methods, aimed at ensuring negative margins during BCS.

Specimen transmission X-ray imaging, sometimes called radiography, involves scanning of surgical specimens using a specialized X-ray tissue scanner. To perform the scan a freshly excised lumpectomy specimen is placed in the scanner under a known orientation with respect to the surgical cavity. Therefore, if the scan results show indications of a close or positive margin, the surgeon can perform a re-excision in the correct area, potentially sparing the patient a repeat surgery. Specimen radiography is a convenient specimen examination method with the capability to visualize surgical aids like tissue clips, I-125 seeds, and localization wires with high contrast and resolution (Figure 1.3). Unfortunately it offers poor contrast in soft tissues, especially in denser breasts, resulting in poor correlation with histological measurements. [26]

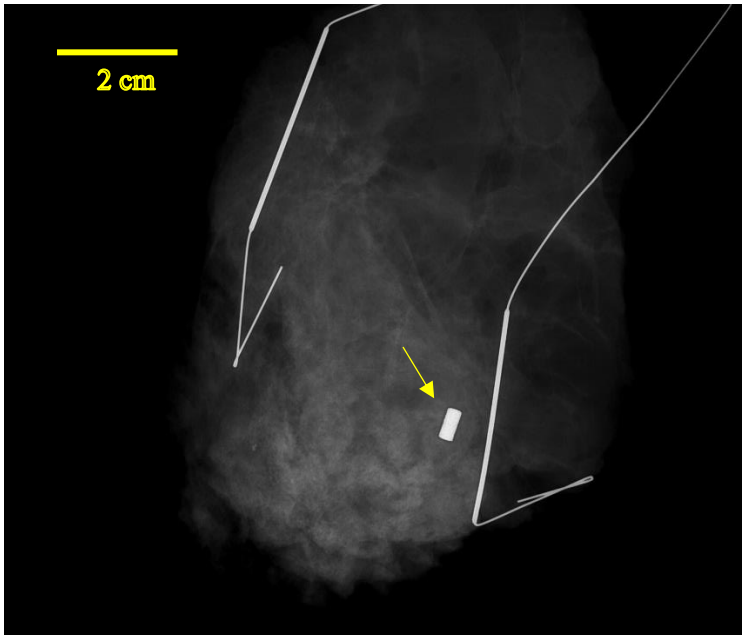

Figure 1.3. Example of an intraoperative lumpectomy specimen transmission X-ray image, or radiograph. The image clearly shows the localization wires as well as the tissue marker (arrow) inside the specimen. The use of two wires implies a bracketing technique which is often used to excise poorly circumscribed, or non-mass lesions, characteristic of DCIS.

Intraoperative specimen ultrasound examination is a non-destructive method with reported high specificity. During the procedure, the surgeon first attaches at least two surgical orientation sutures to the superior and lateral specimen margins, thereby establishing a fixed point of reference with respect to the surgical cavity. Following excision, the specimen is scanned using a hand-held ultrasound probe, producing measurements of the margins. If tumour tissue appears too close to the edge, further tissue may be excised from the relevant margin by use of the orientation sutures. Ultrasound specimen examination is an effective margin assessment method, however, it is not applicable to ultrasound-occult lesions, and remains unable to overcome sensitivity problems in denser breasts, especially with high grade tumours exhibiting intraductal component.[27,28]

1.2.3 Intraoperative lumpectomy specimen examination

Intraoperative specimen imaging has demonstrated the potential for improved success rates in BCS, however, current methods suffer from limited applicability or sensitivity. Clearly, an alternative intraoperative specimen margin assessment method could be of great benefit if it is able to quickly detect and visually guide the operating surgeon towards a broad range of lesion types with high sensitivity and specificity. There are several techniques that have been implemented. Here we describe some of the most prominent.

Frozen sectioning allows for visual inspection of the margin but requires special expertise, is time consuming, and can be difficult to interpret due to artefacts caused by the freezing process.[29]

Intraoperative contact cytology reduces the processing time but is limited to surface examination and suffers from variable sensitivity related to pathologist skill level.[30]

Of note is a recently FDA approved device called the MARGINProbe, which uses radio frequency spectroscopy to interrogate a 7 mm diameter area of interest to a depth of up to 1 mm. The device features a hand-held probe that makes measurements by contacting tissue for about 1.5 seconds. On the downside, limited sensitivity (65%), specificity (50%), field of view and penetration, imply that complete margin assessment is neither practical nor possible leading to a possibility of missed malignant tissue within the margin.[31]

1.2.4 Postoperative lumpectomy specimen histopathological examination

Histological examination of excised tissue specimens represents the gold standard in tissue analysis, and ultimately, disease diagnosis[29]. Typically, freshly excised and suture oriented lumpectomy specimens are fixed in a formalin solution for at least 24 hours, or more for large specimens. After fixation, the specimen margins are identified using the sutures and each of the six margins surfaces are inked using a

different colour. Following inking, the specimens are serially sectioned and a gross examination of the slices is performed. At this stage, grossly visible tumour is measured on each slice and the maximum dimension is recorded. Measurement of the shortest distance between the inked surface and tumour grossly establishes the width of each of the six resection margins. This information is then used to decide on sections that may need a more detailed microscopic examination.

Following gross sectioning and examination, selected slices are prepared for microscopic examination by embedment in paraffin and staining with hematoxylin-eosin, or H&E stain. This procedure allows different cellular components, such as nuclei, to be readily identifiable based on specific stain colours. Examination under an optical microscope then reveals a host of information including the microscopic status of the resection margins, as well as the appearance of the tumour cells. In brief, using the Nottingham histologic grading score, tumours are assigned a grade from 1 to 3, depending on how different, or differentiated, the cells appear compared to normal cells[32]. Grade 1 tumours tend to contain cells that appear only somewhat different, and are characterized by slow growth, or low aggressiveness. On the other hand, grade 3 tumour cells are typically well differentiated from normal cells and associated with rapid growth, or high aggressiveness. This information is then used to further guide the course of treatment.

1.3 Emerging breast cancer imaging techniques and surgical guidance

The methods and technologies that are applied in current clinical treatment of breast cancer have made a dramatic impact on prognosis. Nevertheless, the advancement and availability of specialized devices such as lasers and light emitting diodes (LEDs), as well as acoustic, electromagnetic and optical sensors, have catalyzed the development of highly promising alternatives. For example, recent studies using optical techniques, such as Raman spectroscopy, auto-fluorescence spectroscopy, optical coherence tomography and diffuse reflectance spectroscopy, have demonstrated superior soft tissue contrast resulting in margin

assessment sensitivity as high as 100% and specificity near 92%[33–37]. The desirable performance of optical methods for assessing soft tissue can be partially explained by the strong wavelength-dependent interaction that occurs between photons and tissue. This property can be appreciated by examination of Figure 1.4, which shows the absorption spectra of relevant compounds found throughout the human breast. It is this spectral specificity that gives rise to the ability of multispectral optical methods to differentiate various tissues, including diseased tissues.

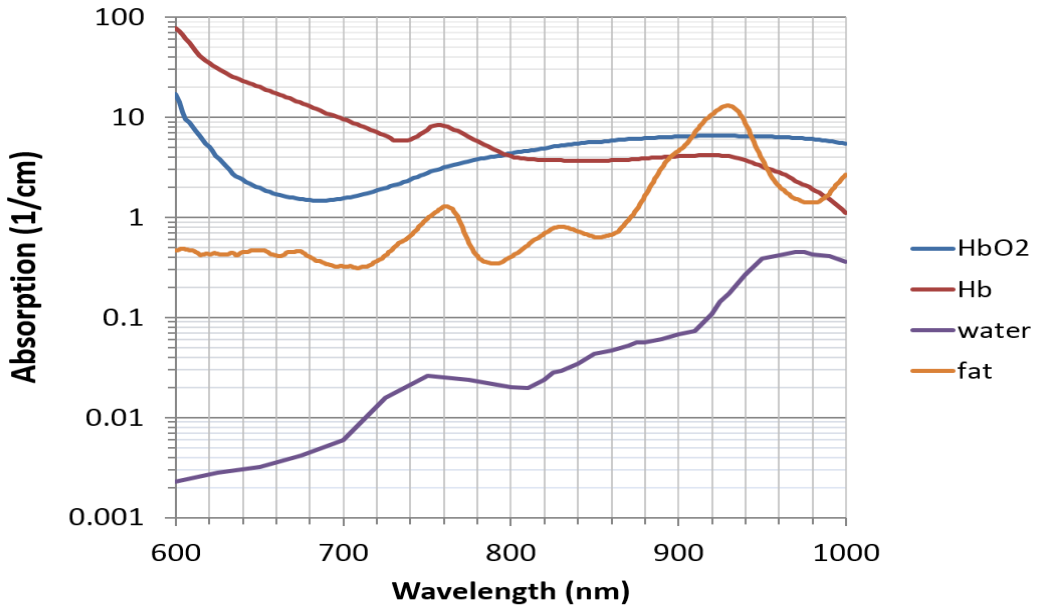

Figure 1.4. Optical absorption NIR spectra of relevant compounds found in human breasts, including oxygenated hemoglobin (HbO_2), de-oxygenated hemoglobin (Hb), water, and fat. The figure was adapted from sources available at [http://omlc.ogi.edu/spectra] and cross checked to data in [38].

Rather than relying on absorption of photons, other optical methods derive their specificity by measuring the rate at which photons scatter in tissue. Since malignant tissues are known to be highly cellularized they are effectively more turbid than normal tissues, and consequently exhibit more optical scattering. These features, combined with the deep penetration of NIR light in tissue, equip optical imaging methods with unique advantages compared to non-optical alternatives. Here we describe methods that have been applied towards patient and specimen imaging as well as specimen examination.

1.3.1 Optical in vivo breast cancer imaging

Diffuse optical methods that have been investigated for whole breast imaging can be divided into two categories. Optical reflectance mammography refers to techniques where the transmitter of optical signals is placed on the same side of the breast as the receiver[39,40]. On the other hand, in optical transmission mammography, the receiver and transmitter are on opposite sides of the breast[41]. Consequently, the optical signals, or photons, are required to either reflect from or transmit through, the tissue. The transmitter typically consists of a light source such as an arc lamp, laser or an LED, while the receiver is usually a CCD camera or a type of photodiode. By measuring the amount of transmitted or reflected photons, these methods can estimate the type and degree of interaction between various wavelengths of light and the tissue under scrutiny. In particular, the optical absorption coefficient and the reduced scattering coefficient can be derived. The derived coefficient values can then be compared to known values for various molecules and hence tissue types, such as fat, fibro-glandular tissue, or tumour tissue.

Optical mammography studies on patients with confirmed malignancies have demonstrated significantly altered tissue properties in and around the lesion area with total hemoglobin concentration sometimes as much as double that of normal surrounding tissue. In particular, one study of 26 patients with breast cancer found that cancerous lesions were found to contain reduced lipid content (-8%) as well as increased water (+7%) and hemoglobin content (+2.4 μM)[41]. Furthermore, reduced scattering coefficient measurements have shown increased scattering in tumour areas thought to result from the expected increases in cellularity associated with malignancy. The main limitation preventing clinical adoption of optical mammography techniques is low resolution and its inverse relationship with imaging depth. The resolution, on the order of cm, implies that optical mammography methods are most useful when used in conjunction with high resolution methods such as X-ray mammography and sonography. In that context,

optical mammography can be thought of as a supplementary procedure aimed to increase the specificity of current clinical techniques.

1.3.2 Optical ex-vivo breast cancer imaging

Diffuse optical imaging demonstrated the potential for improved specificity in whole breast imaging, however the poor resolution of the technique eliminated it as a stand-alone replacement of current clinical modalities. Fortunately, the evaluation of surgical resection margins in excised specimens relies much more heavily on specimen surface properties, and this represents a unique opportunity for high resolution optical imaging methods.

Diffuse reflectance spectroscopy (DRS), as the analogue of diffuse optical mammography, operates under similar principles (see above), but is aimed at surface and shallow sub-surface tissue examination[35,42]. While the use of NIR light in diffuse optical mammography allows the recovery of photons from deep tissue at low resolution, DRS typically employs shorter-wavelength visible light. The shorter wavelength light enables higher resolution at the cost of penetration depth, which is typically less than 2 mm. One DRS investigation of 55 resection margins in 48 patients undergoing BCS yielded an accuracy in identifying positive and negative margins of 75% [34].

Due to similarities in instrumentation employed by DRS and auto-fluorescence spectroscopy, the two techniques are frequently implemented in one device[35,36]. Auto-fluorescence imaging begins with illumination, or excitation, of tissue, usually using an ultraviolet wavelength of light. However, auto-fluorescence imaging does not rely on the immediately reflected photons. Instead, some photons are absorbed by molecules in the tissue, causing the molecules to reach a higher energy, or, excited state. Following excitation, molecules drop through a cascade of lower and lower excited states, eventually reaching back to the ground state. The energy difference between the ground state and the next excited state is typically released as a photon of specific energy, or characteristic wavelength. It is these photons

that are collected and used to form an image. The intensity of fluorescence can be related to the concentration of specific compounds or fluorophores, some of which have been linked to cancerous tissue. In differentiating cancerous from benign tissue types, one study of 56 malignant and benign breast lesions, employing a combination of DRS and auto-fluorescence, produced a sensitivity of 70.0% and specificity of 91.7% [36].

Thanks in part to its near-histologic level resolution, optical coherence tomography (OCT) represents one of the most promising newcomers in the arena of lumpectomy margin evaluation. During OCT imaging a suitably short-coherence light beam is split into two beams. One beam is then allowed to interact with tissue before being recombined inside an interferometer with the non-interacting beam. The level of interference that occurs between the two recombined beams can be used to estimate the amount of scattering that photons underwent in the tissue under examination. Since scattering is known to be elevated in malignant lesions, and reduced in fatty tissue, OCT is able to indirectly differentiate various tissue types. In practice, OCT is capable of non-destructively examining breast tissue specimens to a depth of 1 mm – 2 mm with micrometer-level resolution. Unfortunately, long image acquisition times imply that OCT may not be ideal for time-sensitive intraoperative examination. Furthermore, by mimicking the scattering properties of tumour areas, cautery artefacts as well as bloody surfaces can confound OCT. Nevertheless, one investigation of breast lumpectomy specimens yielded a sensitivity of 100% and specificity of 82% [37].

Raman spectroscopy and imaging offers molecular specificity along with very high resolution, making it a potential contender for soft tissue specimen examination. Raman spectroscopy takes advantage of inelastic scattering of photons as they interact with molecules in tissue. When photons travel through turbid media most experience elastic scattering, however, a small fraction interacts in-elastically thereby undergoing an energy transfer. Since only specific energy states are permitted, the change in energy of the photons can be used to infer the nature of the molecular environment where the interaction occurred. Finally, by filtering out unwanted elastically scattered photons, a Raman spectra of the tissue volume

under investigation can be obtained. On the downside, the need for each microscopic volume to be sampled separately results in excessive scan times, on the order of many hours. This feature has prevented Raman spectroscopy to be applicable in the intraoperative setting. However, by use of auto-fluorescence imaging, recent advances in the field have devised methods to optimize the sampling strategy, producing dramatically improved scan times. A recent study employing this technique for differentiation of ductal carcinoma from normal tissue in fresh samples was able to achieve a sensitivity of 95.6% and a specificity of 96.2% [33]. The reported image acquisition rate was near 15 minutes for a 5 mm x 5 mm area. While this rate is still too slow for clinical application on typically-sized lumpectomy specimens, future advances in data acquisition technology may bring Raman spectroscopy into an acceptable range.

1.3.3 New approaches to intraoperative lumpectomy specimen examination

Beyond imaging, alternative intraoperative methods have been devised and tested for the examination of specimens. ClearSight™ is a novel intraoperative MRI system that was recently implemented for the study of tissue samples. Based on the same principles as conventional MRI, the device is essentially a sophisticated MR spectrometer capable of estimating the apparent diffusion coefficient in tissue. Each measurement takes between 1 and 2 seconds to complete, and interrogates a 4 mm diameter area to a depth of about 1 mm. In MRI, the apparent diffusion coefficient is a measure of the diffusion, or mobility, of water. Since malignant tissue is known to be highly cellularized, water molecules are presented with a higher density of cell membranes, compared to normal tissue. As a result, the apparent diffusion of water is slower in tumours, and this is reflected in the measurements of the apparent diffusion coefficient. The prototype ClearSight™ system was used to assess 77 surgeon-selected specimens, each measuring 6 mm in diameter and 2 mm to 5 mm in depth. The resulting sensitivity was 91% and specificity was near 93% [43]. While these numbers are impressive, it remains to be seen if the large

sampling volume (analogous to low resolution), limited penetration, and unknown practicability, have an adverse effect on true clinical results.

Intelligent knife, or iKnife, is an intraoperative tissue analysis method based on rapid evaporative ionization mass spectrometry (REIMS). The technique consists of an aerosol, or smoke, collection system coupled to standard electrosurgical tools. During surgery, the fumes that are emitted via cautery are captured and analyzed using REIMS. Real-time lipidomic profiling is performed, yielding results classifying tissue as cancerous or normal. The system was used during 81 resections, including 2 for breast cancer, and was able to correctly match histological diagnosis in all 81 cases[44]. Furthermore, the generated lipidomic profiles were distinguishable between various histological tumour sub-types, implying high specificity in diagnosis. iKnife seems to be a highly promising approach, however, since the method does not concretely confirm the presence of the target tumour within the excised specimen, or estimate the width of the resection margin, there are questions as to the widespread translatability of the technology.

1.4 Photoacoustic imaging

The imaging methods and intraoperative specimen examination techniques described above highlight some very promising indications. For example, tissue contrast derived from optical imaging appears to possess the potential to differentiate cancerous lesions with superior sensitivity and specificity, compared to conventional methods. Furthermore, altered tissue chromophore concentrations, particularly lipids, appear to be a strong indicator of disease, as highlighted by the effectiveness of lipidomic profiling in identifying malignancy[44]. Unfortunately, the desirable diagnostic properties of these methods are offset by either their limited penetration depth or insufficient resolution. The limited sensing depth eliminates these methods in practical applications concerned with detection of tumours or measurements of specimen margin width. On the other hand, low resolution implies that these methods alone may not provide sufficient spatial information to facilitate the conservative nature of BCS. A margin evaluation

method encompassing the specificity and sensitivity of optical imaging but with deep tissue penetration (i.e. > 10 mm) and sufficient resolution, would therefore offer substantial advantages over currently employed techniques.

Photoacoustic imaging (PAI) has recently been used to demonstrate highly desirable capabilities in the arena of *ex vivo* and *in vivo* soft tissue visualization. The success of this technique is in large part due to its ability to sway contrast towards specific tissue chromophores, such as oxyhemoglobin, deoxyhemoglobin, lipid or calcium oxalate and hydroxyapatite (i.e. microcalcifications).[45–47] Furthermore, PAI overcomes limited depth penetration by ultrasonically encoding deep tissue optical contrast, and therefore, similarly to diagnostic ultrasound, is able to achieve several centimeters of penetration and near millimeter, or sub-millimeter, resolution.[48–50] Table 1.2 compares lumpectomy assessment performance measures determined by one PAI investigation to measures derived from other methods.

Table 1.2 Relative strengths and weaknesses of competing intraoperative lumpectomy margin evaluation methods

Method	Penetration depth (mm)	Processing time	Sampling or resolution (mm)	Sensitivity (%)	Specificity (%)
Sonography[26]	50	5 min	< 1	48	99
Radiography[27]	> 50	2 min	< 0.1	61	64
Frozen Section[29]	Full depth	27-53 min	< 0.1	83	95
Contact cytology[30]	Surface	13 min	< 0.1	72	97
MARGINProbe[31]	1	5 min*	7	65	50
ClearSight™ (MRI)[43]	1	12 min*	4	91	93
iKnife (REIMS)[44]	Surface	Real-time	Not applicable	98	97
Auto-fluorescence/DRS[36]	2	100 min*	0.25	70	92
OCT[37]	2	98 min*	0.035	100	82
Raman/Auto-fluorescence[33]	2	79 hrs*	0.01	96	96
Photoacoustics[62]	> 3	17 min*	0.125	100	75

* For a surface area representative of a 5 cm diameter lumpectomy specimen

Here we introduce photoacoustic imaging, sometimes called optoacoustic imaging, and motivate its use towards breast cancer imaging in both the diagnostic and intraoperative setting.

1.4.1 Principles of photoacoustic imaging

Photoacoustic imaging is a hybrid imaging technique based on the photoacoustic (PA) effect. The photoacoustic effect was discovered over a 130 years ago by Alexander Graham Bell during experiments with sunlight[51]. Bell noticed a distinct sound produced by sudden exposure of materials to sunlight. While the underlying principles are the same, today, photoacoustic imaging typically employs lasers or high power LEDs for illumination and ultrasonic detectors, or transducers, for signal detection.

In general, PAI involves illumination of a turbid imaging target by either a pulsed or modulated light source. Upon illumination, photons are diffusely scattered and absorbed in the target. Volumes inside the target with relatively high absorption coefficients preferentially absorb the light energy and undergo slight but rapid heating, followed by near instantaneous thermo-elastic expansion. The expansion generates a spatially varying three dimensional pressure distribution which is proportional to the locally absorbed energy. Shortly after the illumination is reduced, the pressure is dissipated as an acoustic transient wave in the ultrasound frequency range. To generate images, acoustic transducers of appropriate frequency range, or bandwidth, surround the imaging target and detect the dissipating transient waves. By utilizing an image reconstruction method such as back-projection, the detected signals can be used to solve for the original pressure, and hence absorber, distribution[52].

Photoacoustic wave theory:

(Note: Information provided in the remainder of this section is based on "Biomedical Optics: Principles and Imaging", L.V. Wang and H.I. Wu, 2007)

To gain further understanding of how properties of the PA signal-carrying wave depend on the illumination and resultant pressure distribution, it is instructive to consider a fully symmetrical and homogeneous absorber, such as the dark gray sphere of radius R in Figure 1.5a. It is straight forward to show that in order to generate acoustic waves with a waveform and amplitude that is a good representation of the locally absorbed light energy, two conditions must be met. First, the heat generated

during the illumination phase must not have sufficient time, referred to as thermal relaxation time τ_{th}, to diffuse out of the region of interest before the illumination is reduced. This is referred to as thermal confinement and the thermal relaxation time is given by

$$\tau_{\text{th}} = \frac{d_c^2}{4D_T} \tag{1.1}$$

where d_c is the size (mm), or characteristic dimension, of the region of interest, and D_T is the thermal diffusivity of the material of interest. Therefore, for the sphere of radius R, and a thermal diffusivity similar to soft tissue of $D_T \sim 0.1$ mm^2/s, the thermal relaxation time is $\tau_{th} = R^2/0.4$ s.[56] This means that for an accurate thermal response profile of a 1 mm sphere, the illumination time must not exceed 1/0.4 = 2.5 s. This can be easily achieved using conventional illumination sources; however, the other condition, namely stress confinement, is more stringent. Stress confinement implies that the thermo-elastically induced pressure wave does not have sufficient time, called stress relaxation time τ_s, to travel out of the region of interest before the illumination is reduced. The stress relaxation time is given by

$$\tau_{\text{s}} = \frac{d_c}{v_s} \tag{1.2}$$

where v_s is the speed of sound in the material of interest, typically around 1.5 mm/μs for soft tissue. Again, considering the soft tissue sphere with radius R = 1 mm implies that to satisfy stress confinement the illumination time must not exceed $\tau_s = 1/1.5$ μs, or about 0.7 μs. This can typically be achieved using pulsed lasers and LEDs, as well as some arc lamp sources.

According to fluid mechanics, the fractional volume change dV/V of a region of interest expressed as a function of local change in pressure at constant temperature Δp and local change in temperature at constant pressure ΔT, can be approximated by

$$\frac{dV}{V} = \beta \Delta T - \kappa \Delta p \tag{1.3}$$

where β is the thermal coefficient of volume expansion and κ is the isothermal compressibility. However, if a very short illumination time τ_i is implemented then the thermal and stress confinement requirements, described by Equations 1.1 and 1.2, will be significantly exceeded (i.e. $\tau_i << \tau_{th}$ and $\tau_i << \tau_s$). This suggests that the fractional volume change during illumination is negligible, or $dV/V \sim 0$. Therefore, Equation 1.3 can be written as

$$\Delta p = \frac{\beta \Delta T}{\kappa} \tag{1.4}$$

Equation 1.4 quantifies the local pressure reached as a function of the temperature rise during the illumination pulse. If we further assume that all absorbed light energy was converted into heat, then the temperature rise ΔT can be expressed as a function of the locally absorbed light through

$$\Delta T = \frac{\mu_a F}{\rho C_v} \tag{1.5}$$

where μ_a is the local optical absorption coefficient, F is the local optical fluence, ρ is the local physical density and C_v is the specific heat capacity at constant volume. Using Equation 1.5 the initial local pressure reached can be expressed as a function of the local fluence and absorption coefficient,

$$\Delta p = \frac{\beta \mu_a F}{\kappa \rho C_v} = \Gamma \mu_a F \tag{1.6}$$

where $\Gamma = \beta / \kappa \rho C_v$ is the dimensionless Grueneisen parameter which parametrizes the material's inherent photoacoustic energy-conversion efficiency, and is estimated to be around $\Gamma \sim 0.24$ for soft tissues.[56] The studies undertaken in this work involved soft breast tissues, known to have an optical absorption coefficient near $\mu_a \sim 0.06$ cm^{-1}. As a result, given the utilized fluence of $F \sim 4$ mJ/cm^2, the expected pressure generated near the surface was ~ 58 Pa.[41]

Equation 1.6 implies that knowledge of the local fluence F coupled with pressure measurements Δp, can be used to estimate the local absorption coefficient μ_a. As discussed above, the value of μ_a is of

significant importance in the characterization of various tissue types. Indeed Figure 1.4 clearly demonstrates the potential differentiation of tissue constituents based solely on absorption coefficient values.

Nevertheless, Equation 1.6 tells us nothing about how the initial local pressure within some sample can be related to the time-resolved acoustic pressure measurements, which arrive and are collected later in time.

In order to relate the non-local pressure wave measurements to the local initial pressure distribution, the general wave equation describing propagation of pressure waves under thermal confinement is used

$$\left(\nabla^2 - \frac{1}{v_s^2} \frac{\partial^2}{\partial t^2} \right) p(\mathbf{r}, t) = -\frac{\beta}{C_p} \frac{\partial H}{\partial t} \qquad 1.7$$

where H is the heating function which depends on the temperature, and via Equation 1.5, the optical fluence, and is given by

$$H(\mathbf{r},t) = \rho C_v \frac{\partial T(\mathbf{r},t)}{\partial t} \qquad 1.8$$

The right side of Equation 1.7 describes the initial pressure as a function of position and time, and it is clear that in order to generate a wave (i.e. $\partial H/\partial t \neq 0$) the heating function must not be constant. Once again, this necessary condition is satisfied as long as the optical energy is converted into heat under thermal confinement.

Equation 1.7 is an inhomogeneous differential equation and the solution, typically provided by invoking Green's function for a δ impulse source, is given by

$$p(\mathbf{r},t) = \frac{1}{4\pi v_s^2} \frac{\partial}{\partial t} \left[\frac{1}{t v_s} \int d\mathbf{r}' \, p_0(\mathbf{r}') \, \delta\left(t - \frac{|\mathbf{r}-\mathbf{r}'|}{v_s} \right) \right] \qquad 1.9$$

Equation 1.9 gives the pressure p at location $\mathbf{r}$ and time t, given an initial pressure p_0 at location $\mathbf{r}'$ and time $t' = t - \frac{|\mathbf{r}-\mathbf{r}'|}{v_s}$. Thus, by using numerous pressure measurements after illumination of an imaging

target, in conjunction with reconstruction algorithms such as back-projection, Equation 1.9 can be used to recover the original pressure and hence absorber distribution. The equation essentially models the propagation of acoustic pressure waves and so can provide an estimate of the expected pressure distribution measured at one location given an initial pressure distribution at a different location.

For example, consider again the dark-gray uniform sphere of radius R, shown in Figure 1.5a. Below the sphere is a plot of the time dependent pressure signal that is representative of homogeneous illumination by the light source L, followed by measurements by the acoustic transducer T. In accordance with the photoacoustic effect and Equation 1.9, the sphere produces an N-shaped signal whose temporal width τ is proportional to R, and whose amplitude is proportional to the optical density, or absorption coefficient, represented by the dark shade of gray. It therefore follows that a sphere of radius 2R and half the optical density, represented by the light shade of gray in Figure 1.5b, will produce a signal with twice the temporal width 2τ and half the amplitude. This example serves to illustrate two critical properties of the photoacoustic effect:

(1) The absorber dimension along the line of acoustic wave detection is proportional to the period, and therefore inversely proportional to the frequency, of the emitted transient wave.

(2) The absorber's optical absorption coefficient is proportional to the amplitude of the emitted wave.

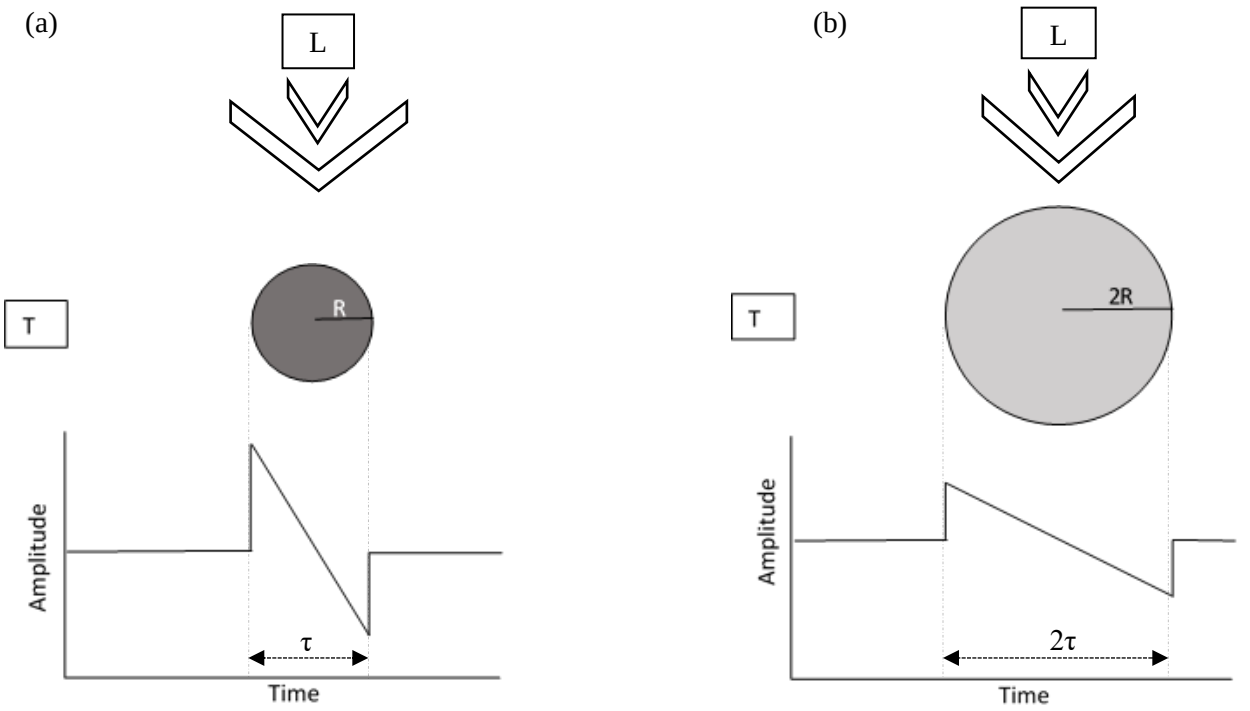

Figure 1.5. Representative examples illustrating the expected time-dependent PA waveforms for varying sizes and optical densities of absorbers. Figure (a) shows a dark-shade sphere of radius R along with the expected signal measured at T after homogeneous illumination by L. Figure (b) shows a light-shade sphere of radius 2R. The expected results demonstrate that object size is inversely proportional to PA signal frequency, while object optical density is directly proportional to PA signal amplitude.

While these properties seem relatively simple, they have profound consequences on PAI system design and performance. For example, property (1) implies that complex imaging targets may emit acoustic transients of very wide range of frequencies, while property (2) suggests that such targets may simultaneously emit a wide range of amplitudes. Consequently, designing an effective PAI system requires careful consideration of the intended imaging targets, ensuring that the utilized detector electronics have sufficient dynamic range in both the amplitude and frequency domains. Insufficient range will likely result in images showing a distorted or inaccurate absorber distribution, or may result in images with missing absorbers.

1.4.2 Optimizing photoacoustic imaging system design

The previous section outlined basic principles of PAI, illustrating potential considerations necessary in designing an effective imaging system. For example, since real acoustic transducers have an intrinsically finite frequency bandwidth, selecting a specific model will allow the detection of signals originating from an equally specific range of absorber sizes. Absorbers in the mm and sub-millimeter range will typically generate acoustic signals in the MHz frequency range. On the other hand, detecting signals from absorbers in the cm range, typical of stage 1 and 2 breast tumours, requires transducers sensitive in the 100 kHz range[53]. Hence very careful attention must be given when deciding on transducer bandwidth.

Another major consideration in designing a PAI system is the illumination scheme. Traditionally, pulsed lasers are employed due to their high-power output enabling high signal-to-noise-ratios (SNR) and consequently extending the attainable imaging depth in soft tissues to several cm[50]. On the downside, lasers tend to be expensive and technically challenging to maintain within optimal operating condition. However, recent advances in LED technology are beginning to open new opportunities featuring virtually maintenance free operation. Nevertheless, a critical aspect of the illumination strategy is ability to select the appropriate wavelength for specific imaging tasks. Similarly to transducer selection, use of an inappropriate illumination wavelength can produce results with low SNR, or at worst, completely fail to generate signals from the intended imaging target. This can be appreciated in Figure 4, which shows the NIR optical absorption spectrum of relevant tissue chromophores. Inspection of the spectrum reveals the effectiveness of specific wavelengths in generating signals from specific tissues. For example, if targeting of lipids is desired, a wavelength of around 930 nm is optimal. Alternatively, the high absorption of hemoglobin at a wavelength of 600 nm would be effective at detecting vasculature, but would likely fail at visualizing lipids.

Many variations of PAI technology have been realized, usually tailored towards a specific imaging task. For example, by using high frequency focused-transducer scanning systems, along with focused

illumination, PA microscopy, or PAM, produces images exhibiting microvascular trees with the ability to resolve single red blood cells[54]. While PAM is a great research tool, the often hours-long image acquisition time and sub-millimeter imaging depth, result in limited clinical potential, particularly towards breast cancer intraoperative and diagnostic imaging. Therefore, the focus of the remainder of this discussion will not be on PAM, and instead placed on another major PAI variation, namely photoacoustic tomography, or PAT.

In PAT imaging, staring or scanning unfocused transducer arrays, coupled with diffuse optical illumination, can generate PA images in seconds to minutes at clinically relevant depths of several cm and near-millimeter resolution. Consequently, PAT comprises the ideal contender for diagnostic breast imaging and intraoperative examination of tissue specimens during BCS. In the following sections the most prominent investigations to date into the application of PAT towards breast cancer imaging will be discussed.

1.4.3 In vivo photoacoustic breast imaging

Currently there are four groups that have performed PAT of the breast, two of which focused specifically on detection and visualization of breast cancer. Oraevski et al. was first to design and test a PAT instrument dedicated to breast cancer detection[55]. However, the novel PAT system employed a fixed wavelength of 1064 nm and only 12 transducers in a linear configuration, resulting in limited scanning efficiency and low resolution. Furthermore, the investigation was carried out using ex-vivo mastectomy specimens, raising questions about in-vivo applicability. Nevertheless, the high-contrast detected between normal and tumour breast tissues (near 300%) was encouraging, leading the group to develop a new generation scanner, dubbed laser optoacoustic imaging system (LOIS)[56]. Among improvements over the earlier version was the redesigned transducer array, featuring arc-shaped geometry and 64 ultra-wideband Polyvinylidene fluoride (PVDF) transducers. Combined with a high-power Alexandrite laser producing 750 mJ pulses at the more hemoglobin-relevant fixed wavelength of 757 nm, LOIS exhibited

exquisite sensitivity capable of detecting tumour mimicking phantoms at sub-millimeter resolution throughout a semicircular slice 70 mm in radius. Even more excitingly, during clinical testing of the LOIS imager on 20 patients with US-detected IDC, the system successfully visualized 18 (90%) of the lesions. In spite of this success, the 2D nature of the LOIS imager as well as fixed-wavelength, prevented multispectral specificity and volumetric visualization capability, from being realized.

Another group, based at the University of Twente in the Netherlands, developed a PAT based breast imaging system referred to as the Twente photoacoustic mammoscope, or PAM[57]. The system featured a densely packed array of 590 transducer elements as well as a laser delivering 30 mJ/cm^2 fixed-wavelength 1064 nm pulses at a repetition frequency of 10 Hz. The wide-band polymer based (PVDF) transducer elements were distributed on a planar phase-array in a circular fashion. The array and measurement area consisted of 40 mm x 40 mm and required a scan time of 25 minutes to sample all transducers using 100 averages per measurement.

While the LOIS system employed an orthogonal illumination scheme, the Twente-PAM featured transmission-mode illumination. Similar to conventional mammography, this strategy permitted slight breast compression to be applied between the planar array and a transparent compression paddle, enabling deeper light penetration and improving the SNR. Additionally, the transmission illumination strategy ensured that weak, deeply-sourced PA signals, were detected prior to the strong signals from the illuminated surface, avoiding interference from back-reflected US clutter, further improving the effective SNR. In comparison, the simultaneous detection of deeply-sourced and surface-sourced PA signals by the LOIS system caused extensive illumination artefacts requiring sophisticated signal and image processing, which ultimately reduced the attainable resolution.

The Twente-PAM system was used to scan 13 patients with 12 breast cancers and one cyst. Unfortunately, various technical difficulties were blamed for 7 scan failures, and only 2 cases were presented in published work. Nevertheless, the results were sufficient for continuation of the project and the group recently reported on a study of 30 patients with 33 malignancies using an upgraded version of

the scanner[58]. The upgrades included a significantly increased measurement area (85 mm x 90 mm) as well as reduced scan time (10 min), yielding visualization of 32 of the 33 (97%) malignancies. Notably, to establish the effect of breast density on contrast in PAT images of breast lesions, the study included a two stage version of the ACR breast density lexicon and concluded that PAT performance appeared independent of breast density. On the downside, the authors noted the presence of other high intensity areas throughout the reconstructed imaging volumes, which reduced the specificity of the results. While the Twente-PAM produced high-contrast 3D images of chromophore distribution, it utilized a sub-optimal illumination wavelength of 1064 nm, failing to take advantage of multispectral specificity associated with other optical methods.

By employing transducer arrays with wide 130% fractional bandwidth and relatively low 1 MHz center frequency, the Oraevsky and Twente groups recognized the value in implementing an imaging system capable of sensing the optical properties of bulk breast tissue. Since breast tumours are known to contain altered chromophore concentrations compared to normal tissue, and are typically on the order of cm in size at the time of diagnosis, this design decision likely played a major role in the successful visualization of breast lesions. In contrast, by employing narrow-bandwidth and relatively high-frequency transducers, Kruger et al. developed a dedicated PAT imaging system for angiography of the breast[59]. The system employed a hemispherical transducer array with 128 individual elements arranged in a unique helical pattern, enabling a relatively wide 64 mm x 64 mm field of view (FOV). The elements had a 5 MHz center frequency with a fractional bandwidth of 70%. Intriguingly, imaging of healthy breasts of two volunteers revealed visualization of vasculature at sub-millimeter resolution to a depth of 40 mm using 800 nm, relatively low energy, 1 mJ/cm^2 laser pulses. Furthermore, the image acquisition time was only 24 seconds, highlighting the clinical potential of the technique. These results motivated the group to later redesign their detector array using 512 transducers at a lower 2 MHz center frequency[60]. These developments, along with an adjustable scan pattern, enabled a clinically relevant FOV of up to 24 cm, encompassing some 90% of breast sizes encountered in practice. Testing of the upgraded system on four

healthy volunteers demonstrated visualization of breast vasculature down to an impressive depth of up to 53 mm including the chest wall.

More recently, a group in Munich, Germany, led by D. Razansky, applied their previously-developed real-time multispectral hand-held PAT scanner to breast imaging[61]. However, after testing on two healthy volunteers, the high center frequency of 4 MHz and relatively narrow acoustic aperture resulted in only 2 centimeters of penetration depth and was limited to visualization of vasculature. Nevertheless, the multispectral nature of the device permitted differentiation of arterial and venous blood vessels, with the potential of functional imaging of blood oxygenation in the breast. Finally, by demonstrating similar contrast in dense and fatty breast tissue, the investigation also demonstrated the independence of imaging performance on breast density.

1.4.4 Ex vivo photoacoustic imaging of breast cancer

At this point it is clear that the marriage of optical specificity and sensitivity, together with the favourable diagnostic properties of acoustic imaging, endow PAT with unique advantages in the detection and assessment of breast lesions. In spite of these favorable properties, PAT has rarely been evaluated for surgical intervention and only recently for assessing breast lumpectomy margins. In a study performed at Indiana University, 12 lumpectomy tissue specimens were assessed by employing a commercially available ultrasonography system (Vevo 2100, FUJIFILM VisualSonics Inc.). By using a fiber optic bundle, a conventional 21 MHz center-frequency linear transducer was coupled to an optical parametric oscillator (OPO) pumped laser (NT 300, EKSPLA) delivering up to 100 mJ/pulse. The multispectral system was able to tune wavelengths in a range from 670 nm to 2300 nm, offering excellent spectral specificity. By implementing a sophisticated spectral un-mixing approach, together with illumination at 16 wavelengths, the study concluded with a reported 100% sensitivity and 75% specificity in identifying positive margins[62].

However, the investigation included a small number of samples and only (IDC) lesions, raising concerns over statistical significance as well as ability to evaluate other types of tumours, such as ductal carcinoma in situ (DCIS) and invasive lobular carcinoma (ILC), which currently represent a substantial clinical problem.[63–65] Furthermore, depending on the standard of practice employed in a particular region or country, the reported 3 mm imaging penetration may or may not be enough to examine the margin to sufficient depth.[13,14,63] From a technical perspective, the limited view reflection mode imaging geometry, employed in that study, combined with a high frequency transducer, invited well documented photoacoustic imaging problems such as limited view and reflection artefacts, as well as shallow tissue penetration.[66,67] And finally, the study utilized BCS specimens that were fixed in 10% formalin as well as embedded in 2.5 % gelatin; these are both time consuming procedures, and hence, unrealistic with respect to clinical intraoperative applications. Extension of the results should therefore be made with caution since the effect of sample preparation on sensitivity and specificity is unknown. Nevertheless, the highly encouraging results highlighted the potential of a dedicated intraoperative lumpectomy margin evaluation system based on photoacoustic tomography (PAT).

1.5 Motivation and Objectives

The preceding discussion outlined unmet needs in areas of clinical breast cancer imaging and concluded with promising alternatives. Specifically, it was made clear that current diagnostic imaging methods suffer from insufficient specificity and sensitivity to a variety of breast abnormalities, especially as it pertains to in-situ lesions and dense breasts. This is likely the result of over-dependence of current methods on tissue physical density. Unfortunately, tissue-density based contrast, as a sole discriminator of tissue types, has been shown to be too vague in many cases and not applicable in dense breasts. On the other hand, in differentiating malignancy in the breast, recent developments in optical imaging techniques have demonstrated molecular-based contrast leading to outstanding sensitivity and specificity, and perhaps most importantly, independence from breast density.

Logically, numerous groups have investigated a variety of breast-tissue optical-imaging approaches, with a wide range of success. On the downside, most of these attempts resulted in demonstrating either limited imaging depth, or low resolution, ultimately preventing widespread clinical applicability. However, one particular optical technique distinguished itself by embodying the clinically desirable attributes of deep tissue penetration and high resolution along with pure optical contrast. Indeed, PA imaging, and especially 3D tomography, currently appears to be the best candidate as a superior stand-alone replacement of currently employed diagnostic imaging modalities.

A review of literature on the subject of PA imaging of breast tissue, *in-vivo* as well as *ex-vivo,* reveals a number of possible approaches with inherent strengths and weaknesses. Intriguingly, in spite of the volume of work completed to-date, it seems that a PA system capitalizing on the whole sum of knowledge in the field has yet to be realized. For example, some groups implemented state-of-the-art acoustic transducer technology, demonstrating high-sensitivity to bulk tissue properties, but failed to complement the detection scheme with an equally optimized multispectral illumination strategy[56,58]. Other groups employed excellent illumination technology, along with sophisticated spectral un-mixing methods with sensitivity to multiple tissue chromophores, including lipid and hemoglobin, but neglected to implement a complimentary PA-signal detection strategy, with an appropriate sensitivity, bandwidth, or scan geometry[60–62]. Consequently, this approach prevented efficient generation or detection of relevant PA-signals, resulting in poor image quality or lack of tumour-related sensitivity.

Another potential shortcoming of currently ongoing PA investigations into breast imaging has been the adoption of inflexible design methods, as well as in-vivo system testing. As a result, experimentation and system optimization via modification of system parameters, was likely difficult, and this is reflected in the many years seen between publications of results from newer generation systems. In light of these lessons, an optimized approach to investigation of PAT of breast abnormalities should ideally be flexible to various system and study design parameters. This strategy will allow rapid progress towards optimization

of a breast-cancer-dedicated imaging system based on PAT. Below is a summary of desirable features of an investigation into PAT of breast cancer.

Rather than beginning with *in-vivo* PAT imaging, the study of freshly excised breast tissue specimens is preferable. This stems from the fact that an excised specimen allows access for imaging scans from a full 360-degree range of angles. Consequently, this approach will enable direct testing of various scan and illumination geometries. Furthermore, the investigation should permit a relevant range of illumination wavelengths, particularly those related to lipid and hemoglobin absorption. This will reveal empirical evidence behind the selected illumination strategy. Finally, wide-band, relatively low frequency transducers should be implemented, permitting the interrogation of bulk-size tissue, typical of breast tumours at diagnosis.

In the following chapters, these attributes are exploited to determine the capability of PAT to visualize breast abnormalities in a true clinical setting through imaging of freshly excised lumpectomy specimens from 100 patients. Chapter 2 outlines the intraoperative nature of the study and describes the technical parameters of the employed PAT instrument. Moreover, through multispectral PAT imaging of fresh human as well as animal tissues, Chapter 2 dives into exploration of various cancer-related optical contrast mechanisms.

After optimization of the PAT imaging protocol from a technical and clinical perspective, a rich source of clinically-relevant data into visualization of malignancy by PAT was gathered. This data is used in Chapter 3 to compare the performance of volumetric visualization of IDC lesions by PAT, DCE-MRI, and pathology. This chapter also investigates the dependence of breast tumour contrast on wavelength and breast density. Finally, Chapter 3 includes a theoretical discussion about the underlying causes of artefacts in PAT.

In Chapter 4 the final results of the 100-patient study are summarized. The analysis includes comparison of breast lesion size as well as extent within freshly excised specimens. The included lesions belong to a

variety of histologic sub-types, such as IDC, DCIS, ILC as well as lesions with extensive intraductal component. The lesion size comparisons between PAT, DCE-MRI, and pathology are done through linear regression analysis. On the other hand, to compare lesion extent estimates by PAT to gold standard histopathology, positive and negative predictive values for lumpectomy margin status are calculated. This enables the effectiveness of PAT to detect positive margins to be evaluated, leading to estimates of the sensitivity and specificity of this technique. Chapter 4 includes a breakdown of these performance measures based on the utilized scan geometry, facilitating further performance optimization. The chapter closes with a variety of case studies, illustrating some of the most clinically confounding scenarios typically found in practice.

1.6 References

1. Hanahan D, Weinberg RA, Francisco S. The Hallmarks of Cancer Review University of California at San Francisco. 2000;100:57-70.
2. Siegel RL, Miller KD, Jemal A. Cancer Statistics , 2015. *CA Cancer J Clin*. 2015;65(1):5-29. doi:10.3322/caac.21254.
3. Lynch PJ. Breast anatomy. https://en.wikipedia.org/wiki/Breast#/media/File:Breast_anatomy_normal_scheme.png.
4. Green VL. Mammographic Breast Density and Breast Cancer Risk : Implications of the Breast Density Legislation for Health Care Practitioners. 2016;59(2):419-438.
5. Hermann KP. Applications and literature review of the BI-RADS classification. 2005:1027-1036. doi:10.1007/s00330-004-2593-9.
6. Chiarelli AM, Halapy E, Nadalin V, Shumak R, Malley FO, Mai V. Performance measures from 10 years of breast screening in the Ontario Breast Screening Program , 1990 / 91 to 2000. 2000:34-42.
7. Yaffe MJ, Bloomquist AK, Hunter DM, Mawdsley GE, Chiarlli AM, Muradali D, Mainprize JG. Comparative performance of modern digital mammography systems in a large breast screening program Comparative performance of modern digital mammography systems in a large breast screening program. *Med Phys*. 2013;40(112):121915. doi:10.1118/1.4829516.
8. Balleyguier C, Ayadi S, Van Nguyen K, Vanel D, Dromain C, Sigal R. BIRADS??? classification in mammography. *Eur J Radiol*. 2007;61(2):192-194. doi:10.1016/j.ejrad.2006.08.033.
9. Tardivon AA, Athanasiou A, Thibault F, El Khoury C. Breast imaging and reporting data system (BIRADS): Magnetic resonance imaging. *Eur J Radiol*. 2007;61(2):212-215. doi:10.1016/j.ejrad.2006.08.036.

10. Yang WT, Lam WWM, Cheung H, Suen M, King WWK, Metreweli C. Sonographic, magnetic resonance imaging, and mammographic assessments of preoperative size of breast cancer. *J Ultrasound Med*. 1997;16(12):791-797. http://www.scopus.com/inward/record.url?eid=2-s2.0-0000202613&partnerID=tZOtx3y1.

11. American joint committee on Breast Cancer Staging.

12. Ananthakrishnan P, Balci FL, Crowe JP. Optimizing Surgical Margins in Breast Conservation. *Int J Surg Oncol*. 2012;2012. doi:10.1155/2012/585670.

13. Lagios MD, Silverstein MJ. Ductal Carcinoma In Situ: Recent History and Areas of Controversy. *Breast J*. 2015;21(1):21-26. doi:10.1111/tbj.12359.

14. Silverstein MJ, Lagios MD. Treatment Selection for Patients with Ductal Carcinoma In Situ (DCIS) of the Breast Using the University of Southern California/Van Nuys (USC/VNPI) Prognostic Index. *Breast J*. 2015;21(2):127-132. doi:10.1111/tbj.12368.

15. Waljee JF, Hu ES, Newman LA, Alderman AK. Predictors of Re-excision among Women Undergoing Breast-Conserving Surgery for Cancer. *Ann Surg Oncol*. 2008;15(5):1297-1303. doi:10.1245/s10434-007-9777-x.

16. Schiller DE, Le LW, Cho BCJ, Youngson BJ, Mccready DR. Factors Associated with Negative Margins of Lumpectomy Specimen: Potential Use in Selecting Patients for Intraoperative Radiotherapy. *Ann Ourgical Oncol*. 2007;15(3):833-842. doi:10.1245/s10434-007-9711-2.

17. Hall FM, Kopans DB, Sadowsky NL, Homer MJ. Development of Wire Localization for Occult Breast. *Radiology*. 2013;268(3).

18. Gennari R, Galimberti V, Cicco C De, Zurrida S, Veronesi U, Hon F. Use of Technetium-99m – Labeled Colloid Albumin for Preoperative and Intraoperative Localization of Nonpalpable. 7515(0):692-698.

19. Bosch AM, Kessels AGH, Beets GL, Rupa JD, Koster D, van Engelshoven JMA, von Meyenfeldt MF. Preoperative estimation of the pathological breast tumour size by physical examination, mammography and ultrasound: A prospective study on 105 invasive tumours. *Eur J Radiol*. 2003;48(3):285-292. doi:10.1016/S0720-048X(03)00081-0.

20. Schaefgen B, Mati M, Sinn HP, et al. Can Routine Imaging After Neoadjuvant Chemotherapy in Breast Cancer Predict Pathologic Complete Response? *Ann Surg Oncol*. 2015;23(3):789-795. doi:10.1245/s10434-015-4918-0.

21. Gruber I V, Rueckert M, Kagan KO, Staebler A, Siegmann KC, Hartkopf A, Wallwiener D, Hahn M. Measurement of tumour size with mammography, sonography and magnetic resonance imaging as compared to histological tumour size in primary breast cancer. *BMC Cancer*. 2013;13(June 2005):328. doi:10.1186/1471-2407-13-328.

22. Gu Y-L, Pan S-M, Ren J, Yang Z-X, Jiang G-Q. Role of Magnetic Resonance Imaging in Detection of Pathologic Complete Remission in Breast Cancer Patients Treated With Neoadjuvant Chemotherapy: A Meta-analysis. *Clin Breast Cancer*. 2017. doi:10.1016/j.clbc.2016.12.010.

23. Menezes GL, Knuttel FM, Stehouwer BL, Pijnappel RM, van den Bosch MA. Magnetic resonance imaging in breast cancer: A literature review and future perspectives. *World J Clin Oncol*. 2014;5(2):61-70. doi:10.5306/wjco.v5.i2.61.

24. Siegmann-Luz KC, Bahrs SD, Preibsch H, Hattermann V, Claussen CD. Management of Breast Lesions Detectable Only on MRI. *Rofo*. 2014;186(1):30-36. doi:10.1055/s-0033-1335972.

25. Weir L, Worsley D, Bernstein V. The value of FDG positron emission tomography in the management of patients with breast cancer. *Breast J*. 2005;11(3):204-209. doi:TBJ21625 [pii]\r10.1111/j.1075-122X.2005.21625.x.

26. Britton PD, Sonoda LI, Yamamoto AK, Koo B, Soh E, Goud A. Breast surgical specimen radiographs : How reliable are they ? *Eur J Radiol*. 2011;79(2):245-249. doi:10.1016/j.ejrad.2010.02.012.

27. Eggemann H, Ignatov T, Dan S. Accuracy of ultrasound-guided breast-conserving surgery in the determination of adequate surgical margins. *Breast Cancer Res Treat*. 2014;145(1):129-136. doi:10.1007/s10549-014-2932-8.

28. Krekel NMA, Haloua MH, Cardozo AMFL, de Wit RH, Bosch AM, de Widt-Levert LM, Muller S, van der Veen H, Bergers E, de Lange de Klerk ESM, Meijer S, Petrousjka van den Tol M. Intraoperative ultrasound guidance for palpable breast cancer excision (COBALT trial): a multicentre , randomised controlled trial. *Lancet Oncol*. 2013;14(1):48-54. doi:10.1016/S1470-2045(12)70527-2.

29. Emmadi R, Wiley EL. Evaluation of Resection Margins in Breast Conservation Therapy : The Pathology Perspective — Past , Present , and Future. *Int J Surg Oncol*. 2012;2012:180259. doi:10.1155/2012/180259.

30. Esbona K, Li Z, Wilke LG. Intraoperative Imprint Cytology and Frozen Section Pathology for Margin Assessment in Breast Conservation Surgery : A Systematic Review. *Ann Surg Oncol*. 2012;19(10):3236-3245. doi:10.1245/s10434-012-2492-2.

31. Thill M, Dittmer C, Baumann K, Friedrichs K, Blohmer J. MarginProbe- Final results of the German post-market study in breast conserving surgery of ductal carcinoma in situ. *The Breast*. 2014;23(1):94-96. doi:10.1016/j.breast.2013.11.002.

32. Elston CW, Ellis O. Pathological prognostic factors in breast cancer . I . The value of histological grade in breast cancer : experience from a large study with long-term follow-up. 1991:403-410.

33. Koloydenko A, Notingher I. Towards intra-operative diagnosis of tumours during breast conserving surgery by selective-sampling Raman micro-spectroscopy. *Phys Med Biol*. 2014;59(20):6141-6152. doi:10.1088/0031-9155/59/20/6141.

34. Brown JQ, Bydlon TM, Richards LM, Yu B, Kennedy SA, Geradts J, Wilke LG, Junker MK, Gallagher J, Barry WT, Ramanujam N. Optical Assesssment of Tumor Resection Margins in the Breast. *IEEE J Sel Top Quantum Electron*. 2010;16(3):530-544.

35. Lue N, Kang JW, Yu C, Barman I, Dingari NC, Field MS, Dasari RR, Fitzmaurice M. Portable Optical Fiber Probe-Based Spectroscopic Scanner for Rapid Cancer Diagnosis : A New Tool for Intraoperative Margin Assessment. *PLoS One*. 2012;7(1). doi:10.1371/journal.pone.0030887.

36. Breslin TM, Xu F, Palmer GM, Zhu C, Gilchrist KW, Ramanujam N. Autofluorescence and Diffuse Reflectance Properties of Malignant and Benign Breast Tissues. *Ann Surg Oncol*. 2004;11(1):65-70. doi:10.1245/ASO.2004.03.031.

37. Nguyen FT, Zysk AM, Chaney EJ, Kotynek JG, Oliphant UJ, Bellafiore FJ, Rowland KM, Johnson PA,

Boppart SA. Intraoperative Evaluation of Breast Tumor Margins with Optical Coherence Tomography. *Cancer Res*. 2009;69(22):8790-8797. doi:10.1158/0008-5472.CAN-08-4340.

38. Jacques SL. Corrigendum : Optical properties of biological tissues : 2013;58:5007-5008. doi:10.1088/0031-9155/58/14/5007.

39. Cerussi AE, Berger AJ, Bevilacqua F, Shah N, Jakubowski D, Butler J, Holcombe RF, Tromberg BJ. Sources of Absorption and Scattering Contrast for Near-Infrared Optical Mammography 1. 2001:211-218.

40. Jakubowski D.B., Cerussi A. E., Bevilacqua F. SN. Monitoring neoadjuvant chemotherapy in breast cancer using quantitative diffuse optical spectroscopy: a case study. *J Biomed Opt*. 2003;9(1):230-238.

41. Anderson PG, Kainerstorfer JM, Sassaroli A, Krishnamurthy N, Homer MJ, Graham RA, Fantini S. Broadband optical mammography: Chromophore concentration and hemoglobin saturation contrast in breast cancer. *PLoS One*. 2015;10(3):1-23. doi:10.1371/journal.pone.0117322.

42. Bydlon TM, Barry WT, Kennedy S a, Brown JQ, Galagher JE, Wilke LG, Geradts J, Ramanujam N. Advancing optical imaging for breast margin assessment: an analysis of excisional time, cautery, and patent blue dye on underlying sources of contrast. *PLoS One*. 2012;7(12):e51418. doi:10.1371/journal.pone.0051418.

43. Papa M, Allweis T, Karni T, Sandbanks J, Konichezky M, Diment J, Guterman A, Shapiro M, Peles Z, Maishar R, Gur A, Kolka E, Brem R. An intraoperative MRI system for margin assessment in breast conserving surgery: Initial results from a novel technique. *J Surg Oncol*. 2016;114(1):22-26. doi:10.1002/jso.24246.

44. Balog J, Sasi-szabó L, Kinross J, Lewis MR, Muirhead LJ, Vesekov K, Mirnezami R, Dezso B, Damjanovich L, Darzi A, Nicholson JK, Takats Z. Intraoperative Tissue Identification Using Rapid Evaporative Ionization Mass Spectrometry. 2013;5(194).

45. Kim GR, Kang J, Kwak JY, Chang JH, Kim S Il, Youk JH. Photoacoustic Imaging of Breast Microcalcifications : A Preliminary Study with 8-Gauge Core-Biopsied Breast Specimens. *PLoS One*. 2014;9(8):8-10. doi:10.1371/journal.pone.0105878.

46. Wang B, Karpiouk A, Yeager D. In vivo intravascular ultrasound-guided photoacoustic imaging of lipid in plaques using an animal model of atherosclerosis. *Ultrasound Med Biol*. 2013;38(12):2098-2103. doi:10.1016/j.ultrasmedbio.2012.08.006.In.

47. Dogra VS, Chinni BK, Valluru KS, Joseph J V. Multispectral Photoacoustic Imaging of Prostate Cancer : Preliminary Ex - vivo Results. *J Clin Imaging Sci*. 2015;3(3):1-7. doi:10.4103/2156-7514.119139.

48. Kim C, Erpelding TN, Jankovic L, Pashley MD, Wang L V. Deeply penetrating in vivo photoacoustic imaging using a clinical ultrasound array system. *Biomed Opt Express*. 2010;1(1):335-340.

49. Song KH, Wang L V. Deep reflection-mode photoacoustic imaging of biological tissue. *J Biomed Opt*. 2007;12(December):1-3. doi:10.1117/1.2818045.

50. Wang L V, Hu S. Photoacoustic Tomography : In Vivo Imaging from Organelles to Organs. *Science (80-)*. 2012;335(March):1458-1462.

51. Bell AG. On the production and reproduction of sound by light. *Am J Sci*. 1880;20(118):305-324.

52. Xu M, Wang L V. Universal back-projection algorithm for photoacoustic computed tomography. *Phys Rev E*. 2005;71(1):16706. doi:10.1103/PhysRevE.71.016706.

53. Xia W, Piras D, Van Hespen JCG, van Velhdhoven S, Prins C, van Leeuwen TG, Steenbergen W, Manohar S. An optimized ultrasound detector for photoacoustic breast tomography. *Med Phys*. 2012;40(3):1-37. doi:10.1118/1.4792462.

54. Strohm EM, Moore MJ, Kolios MC. Single Cell Photoacoustic Microscopy : A Review. 2016;22(3).

55. Oraevski AA, Andreev VG, Karabutov AA, RD Fleming, Z Gatalica, H Singh, RO Esenaliev. Laser opto-acoustic imaging of the breast: detection of cancer angiogenesis. *Proc SPIE*. 1999;3597:352-363.

56. Ermilov S a., Khamapirad T, Conjusteau A, Leonard MH, Lacewell R, Mehta K, Miller T, Oraevski AA. Laser optoacoustic imaging system for detection of breast cancer. *J Biomed Opt*. 2009;14(2):24007. doi:10.1117/1.3086616.

57. Manohar S, Vaartjes SE, van Hespen JCG, Klasse JM, van den Engh FM, Steenbergen W, van Leeuwen TG. Initial results of in vivo non-invasive cancer imaging in the human breast using near-infrared photoacoustics. *Opt Express*. 2007;15(19):12277-12285. doi:10.1364/OE.15.012277.

58. Heijblom M, Piras D, van den Engh FM, van der Schaaf M, Klasse JM, Steenbergen W, Manohar S. The state of the art in breast imaging using the Twente Photoacoustic Mammoscope: results from 31 measurements on malignancies. *Eur Radiol*. 2016;26(11):3874-3887. doi:10.1007/s00330-016-4240-7.

59. Kruger RA, Lam RB, Reinecke DR, SP Del Rio, Doyle RP. Photoacoustic angiography of the breast. doi:10.1118/1.3497677.

60. Kruger RA, Kuzmiak CM, Lam RB, Reinecke DR, SP Del Rio, Steed D. Dedicated 3D photoacoustic breast imaging. *Med Phys*. 2013;40(11):113301. doi:10.1118/1.4824317.

61. Deán-ben XL, Fehm TF, Gostic M, Razansky D. Volumetric hand-held optoacoustic angiography as a tool for real-time screening of dense breast. 2016;259(3):253-259. doi:10.1002/jbio.201500008.

62. Li R, Wang P, Lan L, Lloyd jr. FP, Goergen CJ, Chen S, Cheng J. Assessing breast tumor margin by multispectral photoacoustic tomography. *Biomed Opt Express*. 2015;6(4):1273. doi:10.1364/BOE.6.001273.

63. Hainsworth A, Fosh B, Raymond W, Eaton M, Mcleay W. Ductal carcinoma in situ : breast-conserving surgery without radiotherapy. *ANZ J Surg*. 2015;85(4):245-248. doi:10.1111/ans.12655.

64. Subhedar P, Olcese C, Patil S, Morrow M, Zee KJ Van. Decreasing Recurrence Rates for Ductal Carcinoma In Situ : Analysis of 2996 Women Treated with Breast-Conserving Surgery Over 30 Years. *Ann Surg Oncol*. 2015;(April):3273-3281. doi:10.1245/s10434-015-4740-8.

65. Newcomb P a., Trentham-Dietz A, Hampton JM, Egan KM, Titus-Ernstoff L, Andersen SW, Greenberg ER, Willett WC. Late age at first full term birth is strongly associated with lobular breast cancer. *Cancer*. 2011;117:1946-1956. doi:10.1002/cncr.25728.

66. Ellwood R, Cox B, Zhang E, Beard P. Photoacoustic imaging using acoustic reflectors to enhance planar arrays. *J Biomed Opt*. 2014;19(12):126012. doi:10.1117/1.JBO.

67. Jaeger M, Harris-Birtill D, Gertsch A, O'Flynn E, Bamber J. Deformation-compensated averaging for clutter reduction in epiphotoacoustic imaging in vivo. *J Biomed Opt*. 2012;17(6):66007. doi:10.1117/1.JBO.17.6.066007.

Chapter 2: Intraoperative photoacoustic tomography (iPAT) of breast cancer: a novel imaging instrument and preliminary results

2.1 Introduction

The motivation behind selecting photoacoustic tomography as the technology of choice in BCS guidance is only briefly discussed below. For a better understanding of how iPAT technology fits within the broader context of breast cancer care, please see sections 1.1.4, 1.2.2-1.2.4, 1.3.2, 1.3.3 and 1.4.4 of the introduction chapter.

2.1.1 Overview

The past few decades witnessed the introduction of advanced imaging methods, regular screening programs and novel therapies causing breast cancer survival rates to improve significantly; however, it still remains as the most common cancer to affect women. Today, it is estimated that about 25% of new cancer cases in women will be breast cancer, resulting in 15% of all cancer mortalities. [1]

Typically, treatment of stage 1 and 2 diagnoses of breast cancer includes breast conserving surgery (BCS), sometimes referred to as lumpectomy. The procedure aims to remove all malignant tissue from the breast, however, the current success rates of BCS vary depending on the employed lesion localization techniques and equipment, as well as surgical team experience. Nevertheless, failure rates of 20% to 50% are common, resulting in repeat surgeries and degraded quality of care[2–6].

Clearly, a supplemental intraoperative margin assessment method could be of great benefit if it is able to quickly detect and visually guide the operating surgeon towards missed malignant tissue. There are several techniques that have been investigated in clinical practice as well as in the research setting[7-12]. Among these methods, optical techniques, have demonstrated superior soft tissue contrast resulting in margin assessment sensitivity as high as 100% and specificity near 92%[13–17]. Unfortunately, the desirable diagnostic properties of these methods are offset by either their limited penetration depth or insufficient

resolution. A margin evaluation method encompassing the specificity and sensitivity of optical imaging but with deep tissue penetration (i.e. > 10 mm) and sufficient resolution, would therefore offer substantial advantages over currently employed techniques.

3D photoacoustic tomography (PAT) has recently been used to demonstrate highly desirable capabilities in the arena of *ex vivo* and *in vivo* soft tissue visualization. The success of this technique is in large part due to its ability to sway contrast towards specific tissue chromophores, such as oxyhemoglobin, deoxyhemoglobin, lipid or calcium oxalate and hydroxyapatite (i.e. microcalcifications).[18–20] Furthermore, PAT overcomes limited depth penetration by ultrasonically encoding deep tissue optical contrast, and therefore, similarly to diagnostic ultrasound, is able to achieve several centimeters of penetration and near millimeter, or sub-millimeter, resolution[21–23].

In spite of these favorable properties, PAT has rarely been evaluated for surgical intervention and only recently for assessing breast lumpectomy margins. In a study performed at Indiana University, 12 lumpectomy tissue specimens were assessed by employing a commercially available hybrid US and photoacoustic imaging system with reported 100% sensitivity and 75% specificity[24]. However, the investigation included a small number of samples and only invasive ductal carcinoma (IDC) lesions, raising concerns over statistical significance as well as ability to evaluate other types of tumours, such as ductal carcinoma in situ (DCIS) and invasive lobular carcinoma (ILC), which currently represent a substantial clinical problem[25–27]. Other potential shortcomings of that investigation included insufficient imaging depth, sub-optimal scan geometry as well as extensive and time-consuming specimen processing[3,4,25,28,29]. Extension of the results should, therefore, be made with caution since the effect of sample preparation on sensitivity and specificity is unknown. Nevertheless, the results were highly encouraging highlighting the potential of a dedicated intraoperative lumpectomy margin evaluation system based on photoacoustic tomography (PAT).

2.1.2 Objectives

Here we report on results from BCS patients using a custom built intraoperative photoacoustic tomography (iPAT) lumpectomy evaluation system. The results include all major breast cancer related lesions such as IDC, DCIS, multifocal, IDC with extensive intraductal component as well as benign, non-palpable and occult lesions. These findings provide an evaluation of the capabilities of iPAT to assess the extent and composition of breast abnormalities during lumpectomy surgery.

2.2 Materials and methods

2.2.1 The iPAT imaging system

Figure 2.1(a) shows a schematic of the imaging system constructed for and employed in this investigation, while 2.1(b) depicts the system within the surgical suite. The imager is a hybrid photoacoustic/ultrasound (PA/US) system, dedicated to BCS imaging applications. It is designed to provide 3D photoacoustic images with co-registered 3D US images of surgical samples. The diagram shows a water tank used for acoustic coupling between the sample and PA/US transducer arrays. The 30 cm-diameter PA array was mounted on the effector of a 4-axis robot (Epson, Japan), as depicted in Figure 2.1(c). To perform imaging, a breast tissue sample was positioned in the tank between the robotically guided fused optical fiber and the PA/US arrays. This was accomplished using a custom designed lumpectomy specimen holder, seen in Figure 2.1(e). The approximately 30 mJ pulsed output of the tunable (680 – 950 nm) laser (Phocus InLine, Opotek Inc., CA, USA) was injected into the fiber and synchronized with the custom-designed 24-channel, 50 MHz data acquisition system (DAQ), so that the laser induced signals originating from the sample were recorded. The PA/US arrays and fused fiber bundle assembly was then moved to a new scan position using the high-precision 4-axis robot, which was controlled using the robot PC. The overall scan was coordinated using a PC with LabVIEW software

(National Instruments, Austin, TX), which controlled the synchronization of the DAQ, robot PC, and laser. The 3D US scan was carried out using a robot-synchronised clinical US scanner (Sonix Touch, Ultrasonix, BC, Canada).

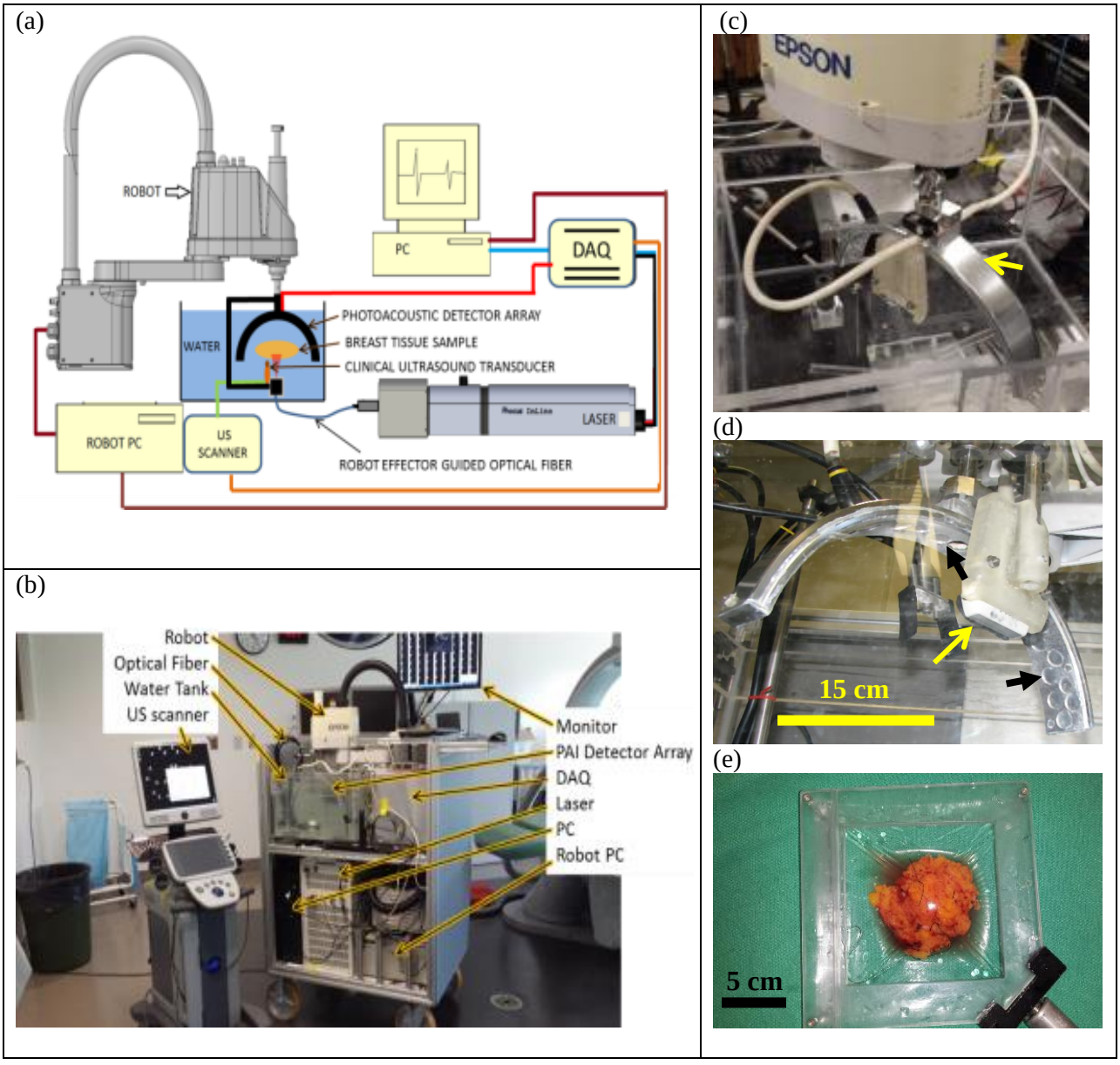

Figure 2.1. Major components of the iPAT system for intraoperative lumpectomy margin evaluation during BCS are depicted schematically in (a). Figure (b) is a labeled photograph of the intraoperative system within surgical suite, consisting of US system on the left and iPAT system on the right. The front panel of the iPAT system is removed to facilitate convenient viewing of internal components. Figure (c) shows a close-up photograph of the arc-shaped 24-channel PA transducer array (arrow) mounted on the effector of the Epson SCARA robot. Figure (d) depicts the PA array from below, along with scale bar indicating dimensions and the location of the conventional 6.6 MHz linear ultrasound transducer array (yellow arrow). Figure (d) also indicates the positioning of the individual transducer elements on the array chassis (black arrows). Figure (e) shows the custom-built lumpectomy specimen holder which contains a freshly excised compressively restrained lumpectomy specimen.

2.2.2 The PA array, calibration, illumination, and scan synergy

The custom designed and built, 30 cm diameter PA transducer array consisted of 24 disk-shaped PVDF elements measuring 15 mm in diameter each. The elements were positioned and secured in an arc shaped aluminum housing (Fig. 2.1d) such that the focus of the array was concentric with respect to the center of curvature. This arrangement, along with the approximately 15 degree angular acceptance of each transducer element, measured at -6dB, allowed for an effective isotropic imaging sub-volume of 3 cm x 3 cm x 3 cm. Near complete angular coverage of the imaging sub-volume was achieved by rotation of the arc array through 10 steps of 18 degrees each. This resulted in 240 projections per sub-volume and mimicked the performance of a staring and sparse 240-channel hemispherical array. The spatial locations of the transducers, with respect to the 3 cm^3 imaging sub-volume, were determined experimentally via robotic calibration scan, developed previously and detailed elsewhere[30–33]. Importantly, this approach eliminated the dependence of image reconstruction accuracy on array fabrication precision.

To complement the transducer-derived 3 cm x 3 cm x 3 cm imaging sub-volume, a high-power fused-input optical fiber bundle (Lumen Dynamics Group Inc., Mississauga, ON, Canada) was positioned 6 cm below the imaging volume (Fig 2.1a), such that the minimum beam diameter intersecting the volume was also 3 cm. The resulting maximum tissue surface fluence was approximately 4 mJ/cm^2, which is well below the damage threshold and well below the maximum permissible exposure for *in vivo* applications.[34] Crucially, this trans-illumination imaging mode combined with a delay generator (TCU-1, Continuum, Santa Clara, California) allowed the time-gated detection of laser induced PA signals so that strongest signals originating at tissue surface would not be permitted to interact with the detector array until the deeply sourced, weak signals, were recorded. This approach preserved the full dynamic range of the detection electronics and prevented back-scattered US “clutter” signals from interfering with direct time-

of-flight PA signal measurements. In this way, reflection artefacts commonly associated with deep tissue reflection mode PA imaging, were addressed [29].

In order to facilitate scans of specimens up to 11 cm in diameter, the total imaging volume was expanded by horizontal translation of the PA array and fiber bundle assembly along with the 3 cm^3 imaging sub-volume. This was implemented along a square x-y coordinate grid of 100 horizontal scan positions centered 9 mm apart. Consequently, the imaging scan amounted to 24,000 projections per total imaging volume (i.e. 240/sub-volume x 100 sub-volumes). The 9 mm horizontal step size was experimentally found to be close to an optimal compromise between scan speed and sufficient sampling. The 24-channel iPAT system combined with a 20 Hz laser was capable of scanning this total volume of 11 cm x 11 cm x 3 cm (L x W x H) in under 6 minutes. The iPAT scan was followed by a robotically guided 6.6 MHz US scan, which took approximately 90 seconds and examined the equivalent volume. This volume capacity encompasses the vast majority of lumpectomy specimens, as was indicated by the collaborating surgeon. However, due to a reduction in the iPAT system's signal-to-noise-ratio (SNR), experienced beyond 2 – 3 cm of imaging depth, the imaging protocol was to invert, or flip the specimen and repeat the scan for the opposite side. Nevertheless, this dual side scan imaging protocol was only implemented when intraoperative time constrains permitted.

Due to the 20 minute time constraint imposed by the intraoperative nature of the imaging protocol, only 2 wavelengths were able to be utilized in most cases. The expected dominant chromophore distribution inside lumpectomies, namely adipose tissue and deoxyhemoglobin, motivated use of 930 nm and 690 nm wavelengths, respectively.

2.2.3 Image reconstruction, image stitching, co-registration and resolution

To generate sub-volume images using the acoustic time-of-flight measurements performed by the iPAT system, the recorded pressure signals were first passed through a Butterworth bandpass filter (100 kHz –

3 MHz). The universal filtered backprojection (FBP) algorithm was then implemented[35]. The FBP method preserved the rich frequency content of broadband PA signals, necessary for generating boundary-enhanced images. It essentially related the acoustic amplitude measured at the transducer positions, to the initial pressure at each voxel position in the imaging volume at the moment of illumination. The approach assumed a spherical detection surface geometry with 240 measurement locations. It also included a simple apodization function that limited the contribution of each amplitude projection to a solid angle corresponding to 10 degrees. While image reconstruction using time reversal is probably more physically accurate, we found the computational needs of that method to be too great in the context of practical and time sensitive applications.

The full imaging volume was composed of 100 individual sub-volumes measuring 3 cm^3 each, and centered 9 mm apart. Consequently, stitching these sub-volumes together resulted in significant overlap, or heterogeneous spatial oversampling. This effect, combined with the laser output variability from shot to shot, manifested in the final composite image as a noticeable grid pattern. To compensate for the resulting uneven bulk-voxel intensity between neighboring sub-volumes, image stitching was carried out in the gradient domain using the Haar wavelet 2D integration method[36]. A disk-shaped 1% agar concentration phantom with radially directed graphite spokes was prepared to evaluate the performance of gradient domain stitching versus spatial domain stitching. The graphite concentration in the spokes was 1 g/L. After the phantom was fully cured it was secured in the iPAT water tank and scanned at a wavelength of 690 nm.

Co-registration of the iPAT and US images was performed using Horn's absolute orientation method.[37] The method called for a minimum of 3 known coordinates in each of the two (PA and US) Cartesian coordinate systems. An agar gel phantom, with 4 spherical graphite-containing inclusions, was prepared in order to calibrate the two systems. The inclusions were clearly visualized and the center coordinates of the spheres were selected for co-registration.

An imaging target consisting of a black surgical suture was selected to determine the iPAT system resolution. Full-width-half-max (FWHM) analysis of the line profile of the suture target was carried out to estimate the effective resolution value. The FBP, image stitching, and co-registration were all performed in MATLAB.

2.2.4 iPAT imaging of ex-vivo tissue

In order to evaluate iPAT's ability to differentiate various ex-vivo soft tissues, three tissue types were selected for imaging system testing. Based on their differing lipid and hemoglobin concentrations, poultry cuts of thigh fat and muscle tissue, as well as breast muscle, were used to produce a soft tissue specimen measuring approximately 6 cm in diameter. Specifically, breast muscle was used as the background, or tissue bed, while small cuts of thigh muscle and fat were used as inclusions. Two sections of the breast muscle tissue bed were excised and the thigh and fat tissue inclusions were inserted into the resulting surgical cavity. The specimen was then scanned using a wavelength of 690 nm to detect deoxyhemoglobin contrast, 930 nm for lipids, and 1064 nm due to its frequent use in near infrared photoacoustic imaging research.

2.2.5 Lumpectomy specimen collection and preparation

Patients diagnosed by biopsy with breast cancer or a related breast abnormality, and scheduled to undergo BCS, were asked to participate in the study according to the institutional review board of the University of Western Ontario (UWO Research Ethics Board # 105467; LHSC Tissue Archive # 888; Lawson Approval #R-14-311). The intraoperative imaging protocol permitted the surgical standard of care to be unaffected by the iPAT and US imaging scans. The freshly excised lumpectomy specimens were placed inside a customized saline filled Ziploc® bag and handed to the iPAT specialist for scanning. In the

meantime, the patient was sutured and prepared for surgical suite discharge. Prior to discharge the specimen was handed back to the surgeon, who then passed it on to pathology.

2.3 Results

2.3.1 Image reconstruction, stitching, and system resolution

The result of image reconstruction and stitching in the gradient domain, as compared to the spatial domain, can be appreciated in Figure 2.2. The figure shows outcome of scanning the spoked agar/graphite gel phantom followed by FBP reconstruction and sub-volume stitching in the spatial domain (a), as well as in the gradient domain (b). The relative brightness intensity in the images is proportional to the optical absorption coefficient of the phantom, and has been normalized with respect to the average pixel intensity within a particular slice. The selected z-slices are separated by 1 mm and depict the graphite spoke inclusions as hyper-intense on the iPAT scan. On the other hand, the photograph in (e) shows the same graphite inclusions as dark gray. The effect of uneven illumination and heterogeneous spatial sampling, between the stitched sub-volumes, manifested in the final composite image as a grid pattern, easier to see in the zoomed-in slice in (c). Intriguingly, the scan-grid artefacts appear to be effectively eliminated by implementing stitching in the gradient domain, as shown in (d). Equally important however, is the apparent lack of any significant side-effects on the final image results.

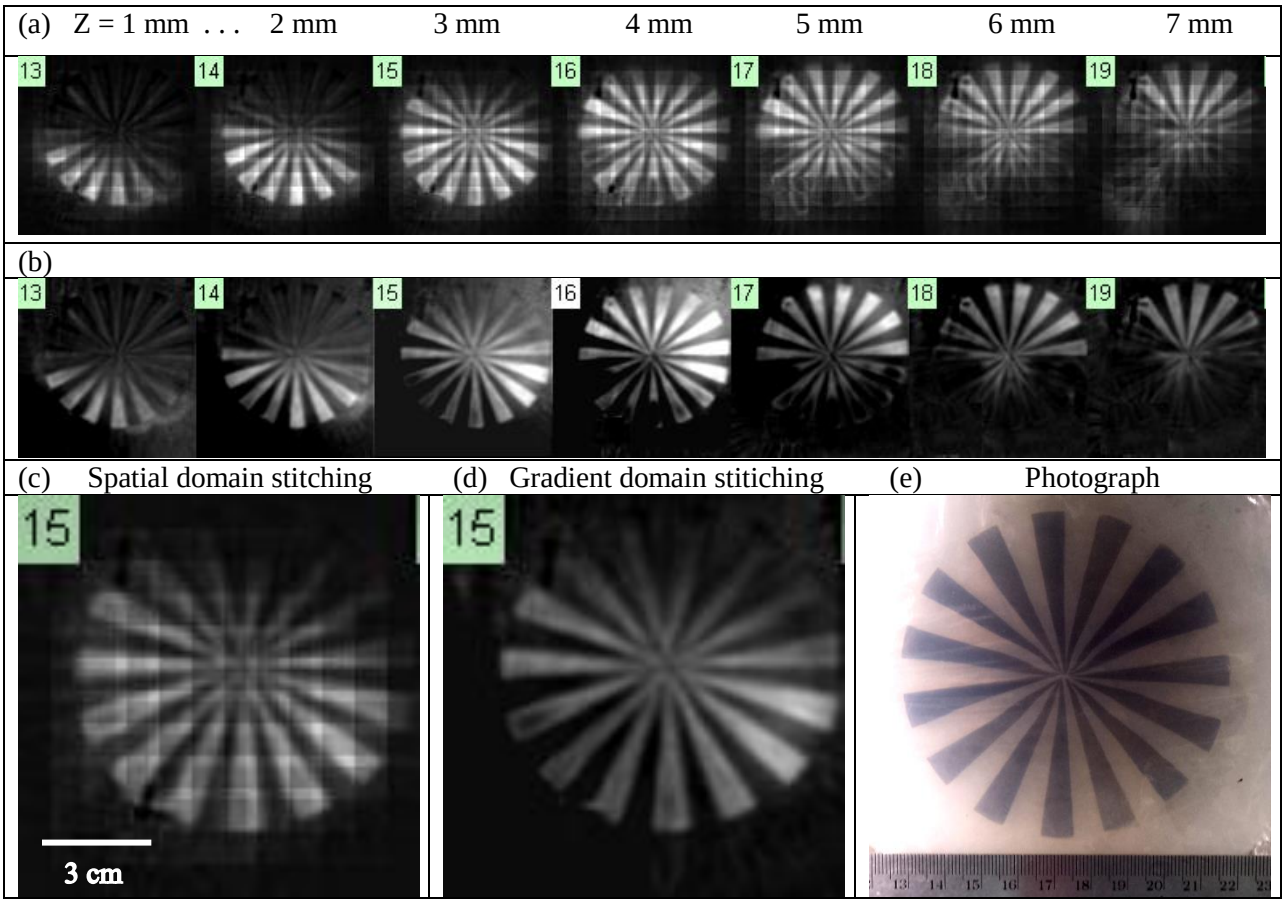

Figure 2.2. (a) Selected 690 nm iPAT z-slices showing a graphite/agar gel phantom reconstructed using spatial domain stitching, resulting in unwanted scan grid artefacts in the final composite image. Alternatively, Figure (b) shows the same scan data but with stitching implemented in the gradient domain, resulting in complete or near complete elimination of the grid artefacts. The larger images in Figures (c) and (d) allow for an easier appreciation of the result, while the photograph in (e) provides an effective gold standard reference.

Figure 2.3 shows the result of FWHM analysis of the line profile of a surgical suture. Figure 2.3(a) shows a photograph of a freshly excised lumpectomy specimen oriented with respect to the surgical cavity using approximately 100 µm-diameter black surgical sutures (white arrows), which have been attached to the specimen by the surgeon. The appearance of the black sutures, seen as hyper-intense on the 930 nm iPAT scan, can be appreciated on the selected iPAT slice in (b). The dashed line in the photograph, and on the iPAT slice, indicates the region that generated the line profile plot seen in Figure 2.3(c). Based on the FWHM of the pixel amplitudes, plotted as a function of distance along the line, a resolution of 2.5 mm was obtained.

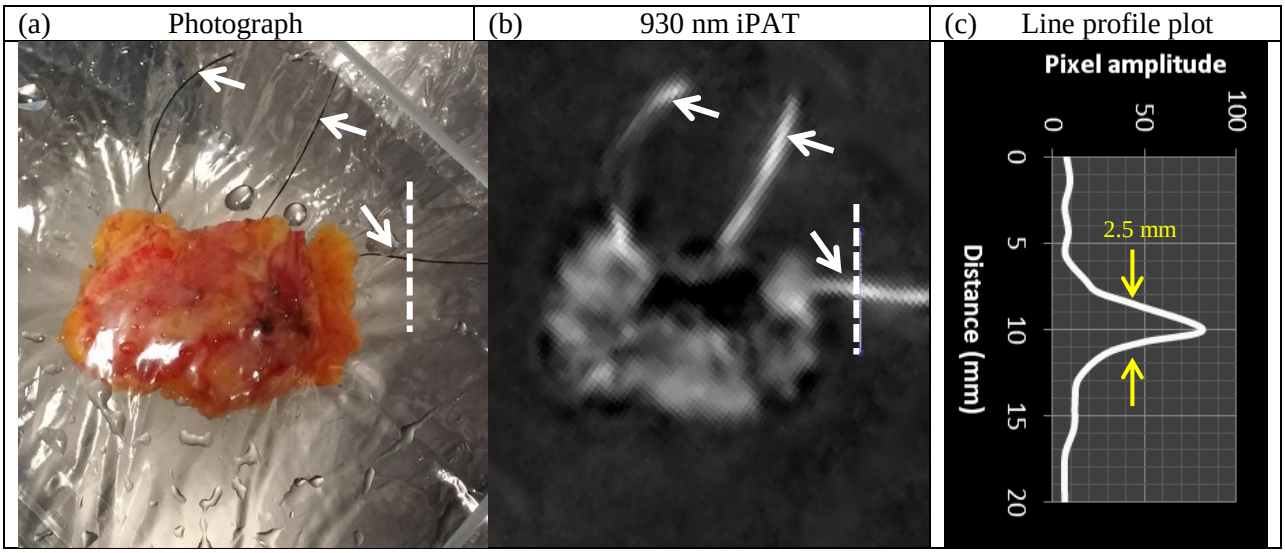

Figure 2.3. iPAT system resolution evaluation via line profile analysis of surgical suture image. The black sutures, seen in the Figure (a) photograph (arrows), were clearly visualized on the 930 nm iPAT scan result of Figure (b). The suture, indicated by an orthogonal 20 mm dashed line in the photo and iPAT image, was used to estimate the in-plane resolution of the imaging system. FWHM analysis indicated a resolution of approximately 2.5 mm.

2.3.2 iPAT imaging of ex-vivo tissue

Figure 2.4 shows selected slices generated by the iPAT system after scanning the ex-vivo poultry tissue specimen. The images correspond to an imaging depth of 5 mm below the illuminated surface and the figure also includes a photograph for reference. The three tissue types, namely thigh fat (black arrow), thigh muscle (white arrow), and breast muscle (yellow dashed perimeter), were clearly differentiated by use of just two of the three utilized wavelengths. In particular, the 690 nm derived image in (a) depicts thigh muscle tissue as hyper-intense due to its relatively high concentration of hemoglobin, as compared to the breast tissue bed. Conversely, thigh fat tissue appears hypo-intense on the 690 nm image, but hyper-intense on the 930 nm image in (b), due to its low concentration of hemoglobin and high concentration of lipids, as compared to the breast background. Finally, the 1064 nm derived image in (c) largely appears to fail to unambiguously differentiate the various tissues types.

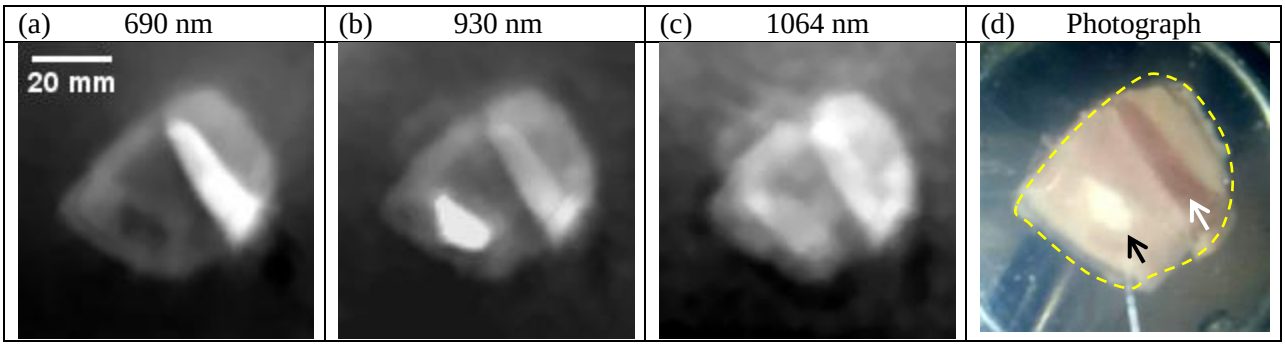

Figure 2.4. Representative iPAT slices of poultry tissue taken from 3D stacks corresponding to an imaging depth of 5 mm below the illuminated surface. The photograph (d) shows the tissue bed consisting of poultry breast tissue (yellow dashed perimeter) as well as thigh fat (black arrow) and thigh muscle (white arrow) inclusions. The fat and muscle inclusions appear light yellow and dark red in the photo due to having less and more hemoglobin concentration, respectively, compared to the breast tissue bed. As expected, the 690 nm scan result in (a) depicts the hemoglobin rich thigh muscle as hyper-intense while the 930 nm scan in (b) does so for the lipid-rich thigh-fat. On the other hand the 1064 nm scan in (c) reveals little differentiation of the three tissue types.

2.3.3 iPAT imaging of freshly excised lumpectomies

Case study 1. IDC excision with radioactive seed localization

A 69 year old patient presented with an architectural distortion on screening mammography and subsequently underwent an US exam of the whole right breast. The exam revealed an approximately 16 mm-diameter hypoechoic mass which demonstrated irregular margins and posterior acoustic shadowing. An US-guided biopsy was carried out and resulted in an IDC diagnosis (BIRADS-6). The patient underwent BCS with radioactive seed localization. Postoperative pathology discovered an 18 mm-diameter, grade 2, IDC lesion with the radioactive localization seed embedded within. The lesion and localization seed (arrow) can be appreciated in Figure 2.5(e), which depicts an intraoperative transmission X-ray image of the specimen. Figures 2.5(a-d) show representative z-slice image stacks of the freshly excised breast lumpectomy specimen at the indicated depths. Images in 2.5(a) and 2.5(b) were acquired using the iPAT scanner at 690 nm and 800 nm, respectively. Surprisingly, little or no correlation of internal structure was found when comparing the 690 nm and 800 nm hemoglobin-enhanced iPAT images, to the US results of Figure 2.5(d). In contrast, the 930 nm lipid-enhanced iPAT images in (c) clearly show a dark central mass corresponding to the hypoechoic region found in the US images of

Figure (d). This is easier to confirm in the zoomed-in images of Figures 2.5(f) and (g), where the US and the 930 nm iPAT slices show a hypo-intense region measuring approximately 20 mm in diameter. Furthermore, these findings were found concordant with the intraoperative X-ray image in (e) and pathology, as both confirmed the central location of the IDC tumour within the lumpectomy specimen. For reference, Figure 2.5(h) shows a colour photograph of the specimen (not co-registered), taken immediately prior to the iPAT scans.

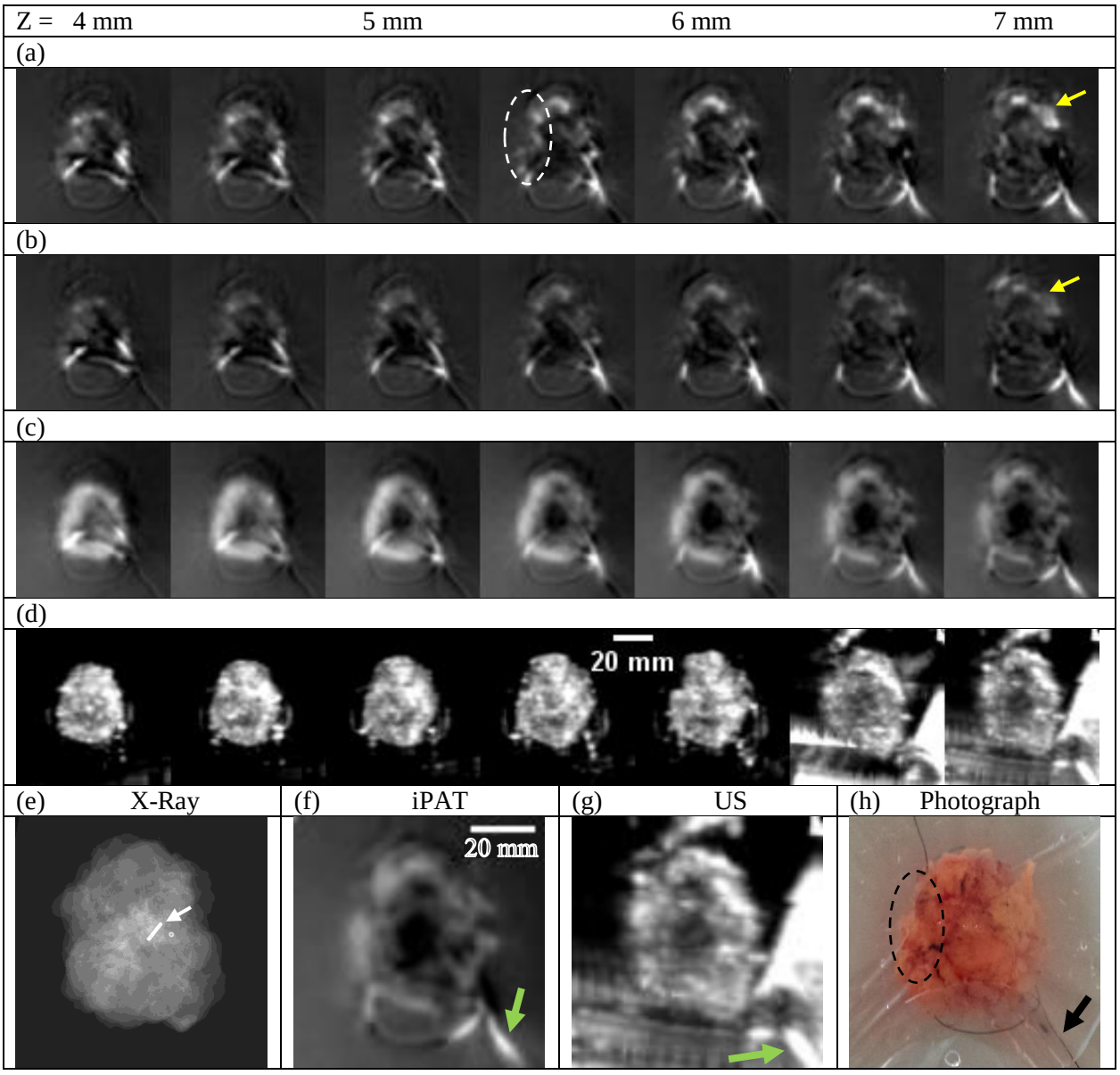

Figure 2.5. Image stacks of lumpectomy specimen containing an 18 mm diameter, grade 2 IDC, aquired using the iPAT system at the indicated Z-depths below illuminated surface. Figures (a) and (b) show iPAT results for 690 nm and 800 nm scanns, respectively, illustrating the small difference between targeting deoxy-hemoglobin (690 nm) vs total hemoglobin (800 nm). The increased intensity of the 690 nm scan results, compared to 800 nm (yellow arrows), likely indicate the presence of mostly deoxygenated blood in the excised specimen. For example, the dashed oval area in the photo (h) shows area of higher blood concentration, which is confirmed in the corresponding slice indicated by the dashed oval in the 690 nm iPAT stack (a). However, notice that the intensity of the corresponding feature at 800 nm is reduced, consistent with deoxygenated blood. Nonetheless, both wavelengths failed to unambiguaously differentiate the malignacy region, best indicated in the near 7 mm deep slice of the 6.6 MHz US scan shown (d) and (g), as well as in the X-ray image found in (e). On the other hand, the iPAT slices in (c) and (f), aquired using lipid weighted 930 nm scanns, clearly show a 20 mm-diameter centrally located hypo-intense area corresponding to the X-ray and US findings.

Case study 2. Failed lumpectomy surgery: Margin positive for DCIS

Figure 2.6 summarizes results of imaging a lumpectomy specimen which was confirmed by pathology to contain a positive margin and resulted in a repeat surgery. A 63 year old patient was diagnosed with a left sided IDC via US-guided biopsy (BIRADS-6), and underwent BCS. Excision without seed or wire guided localization produced the specimen shown in the photograph of Figure 2.6(e). Figures 2.6(a) and (c) depict selected 930 nm iPAT slices at the indicated depths and orientation, with superior at the top and anterior to the right (yellow arrows). Inspection of Figure 2.6(a) demonstrates a large hypo-intense mass located centrally through to a depth of about 10 mm. However, at a depth of 11 mm, an apparent extension of the mass reaches towards the superior margin. This is best visualized in (c) where the affected margin is indicated (white arrow). Interestingly, the co-registered US results of Figures 2.6(b) and (d) also indicate concordant hypo-intensities, nonetheless, the superior margin there appears intact. Postoperative pathologic examination of the specimen revealed a grade 2 IDC lesion measuring 40 mm in diameter and reaching within 2.5 mm of the superior margin. Moreover, pathology further discovered an extension of DCIS tumour which infiltrated the superior margin, resulting in a failed excision. To minimize the risk of recurrence, the patient underwent a second procedure approximately one month later.

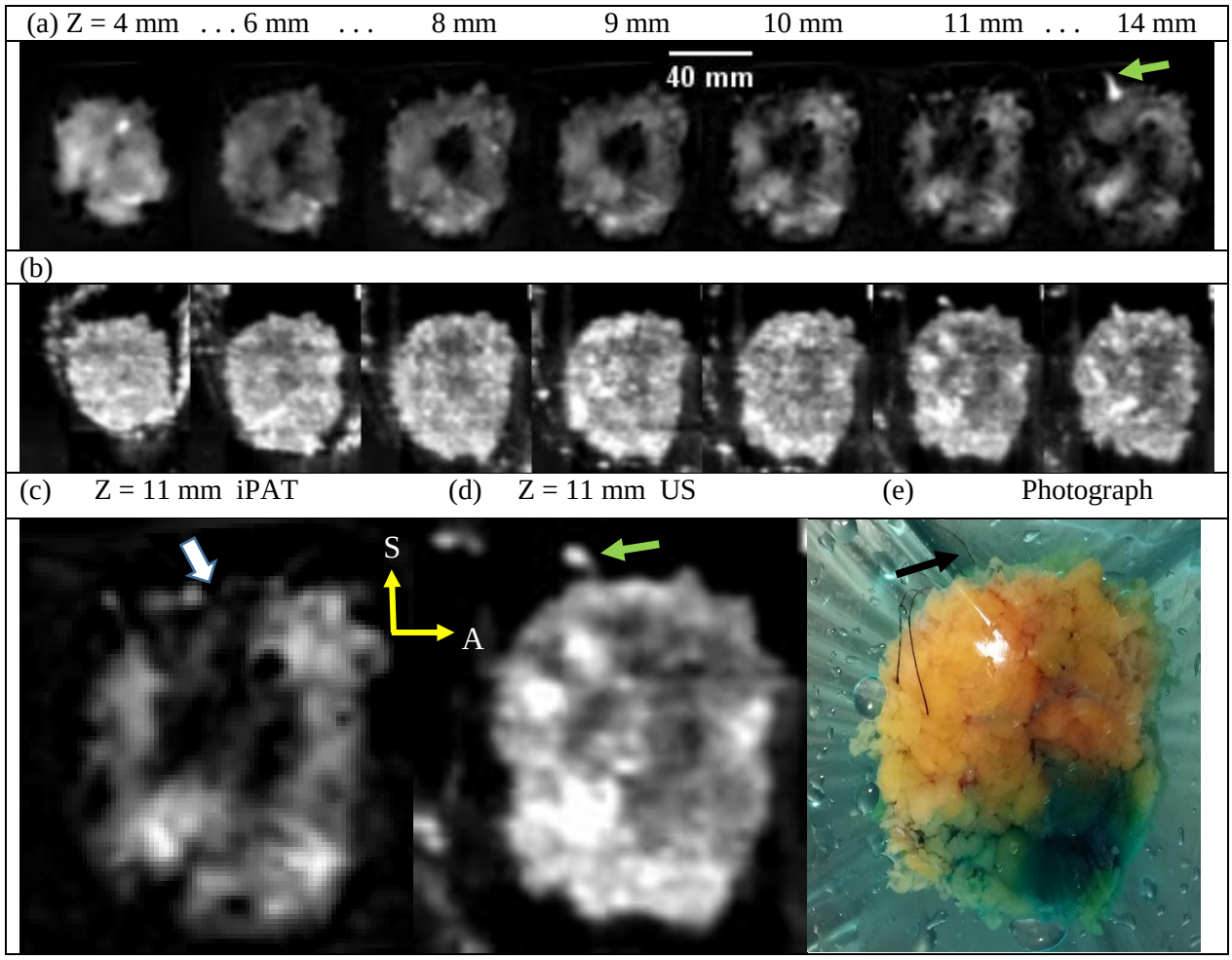

Figure 2.6. (a). 930 nm iPAT slices corresponding to the indicated depth bellow illumination surface, showing a grade 2 IDC along with a grade 2 DCIS- containing specimen, found by postoperative pathology to have a positive margin. (b) Co-registerd slices aquired using a 6.6 MHz conventional US scanner. Figures (c) and (d) show a larger view of the slice near Z=11 mm for iPAT and US, respectively. The iPAT slice in (c) clearly shows intrusion of the specimen edge by the hypo-intense extension (white arrow). For reference a photograph is included in (e), which, along with the 14 mm iPAT and US slices show the superior orientation suture (black and green arrows). The sutures facilitated the orietation of the specimen with superior (S) at the top and anterior (A) to the right (yellow arrows).

In addition to visualization of malignant tissue within the lumpectomy specimen, two imaging features exemplified by results shown in Figures 2.5 and 2.6, should be pointed out. First, notice the bright streaks especially apparent near the bottom and on the right of the US slices, near the 7 mm depth in Figures 2.5(d) and (g). These streaks were caused by US visualization of the ~40 µm-thick polyethylene Ziploc® bag, which was used to restrain the lumpectomy specimen. The streaks typically became apparent near the mid-plane of the specimen where the thin bag material obliquely intersected the imaging plane.

Because of the low NIR absorption coefficient of the optically clear Ziploc® bag material, it was not visualized in the iPAT images. Second, inspection of the photographs in Figures 2.5 and 2.6 reveals the presence of black surgical sutures (black arrows), which were used by the surgeon to mark the orientation of the specimen with respect to the patient's body. These were also visualized in the iPAT and US images (green arrows).

Figure 2.7 depicts selected slices demonstrating the iPAT visualization of 4 types of lesions frequently encountered in BCS. The figure contains intraoperative X-ray images as well as iPAT and US results for the selected specimens. The shown slides have been co-oriented to allow comparison of feature locations. Briefly, shown in Figure 2.7(a) is an example of a BCS specimen containing a biopsy proven 17 mm-diameter grade 1 IDC tumour. Results of inspecting the US image seem to be inconclusive as just a few contrasting features are present (arrows) in the area marked by the radioactive localization seed and architectural distortion, seen in the X-ray image (dashed circle). On the other hand, the 930 nm iPAT image illustrates a specimen with an approximately 20 mm-diameter hypo-intense mass surrounded by a hyper-intense cuff produced by the high lipid content of the healthy margin enclosing the tumour. The last column shows the corresponding photograph, which, along with the X-ray, is not co-registered. Figure 2.7(b) shows similar results, however, in this case the lesion was composed of a combination of an 8 mm-diameter grade 1 IDC and a grade 2 DCIS tumour. Again, in comparison to the X-ray results, the iPAT image appears to indicate more concordant contrasting features while US fails to unambiguously define the extent of the lesion. The specimen shown in Figure 2.7(c) was described by the pathologist as containing two apparently separate foci of grade 1 IDC tumour invasion, measuring 16 mm and 15 mm in diameter each, contiguously located with high-grade (III) DCIS. Interestingly, the 930 nm iPAT image in this case agrees with X-ray and also US, as all show extensive contrasting features extending through much of the specimen. Finally, Figure 2.7(d) depicts a specimen containing a pure DCIS lesion, measured on pathology to be at least 18 mm in extent. The lesion was excised using wire guided localization, appreciated in the X-ray and photograph, which show the hooked localization wires inserted

in the lesion (arrows). As consistent with previous performance, the iPAT image shows hypo-intense features whose location coincides with the apparent lesion location in the X-ray image, marked by the hooked wire ends. Again, the US results are inconclusive as there are few definite contrasting areas in the image.

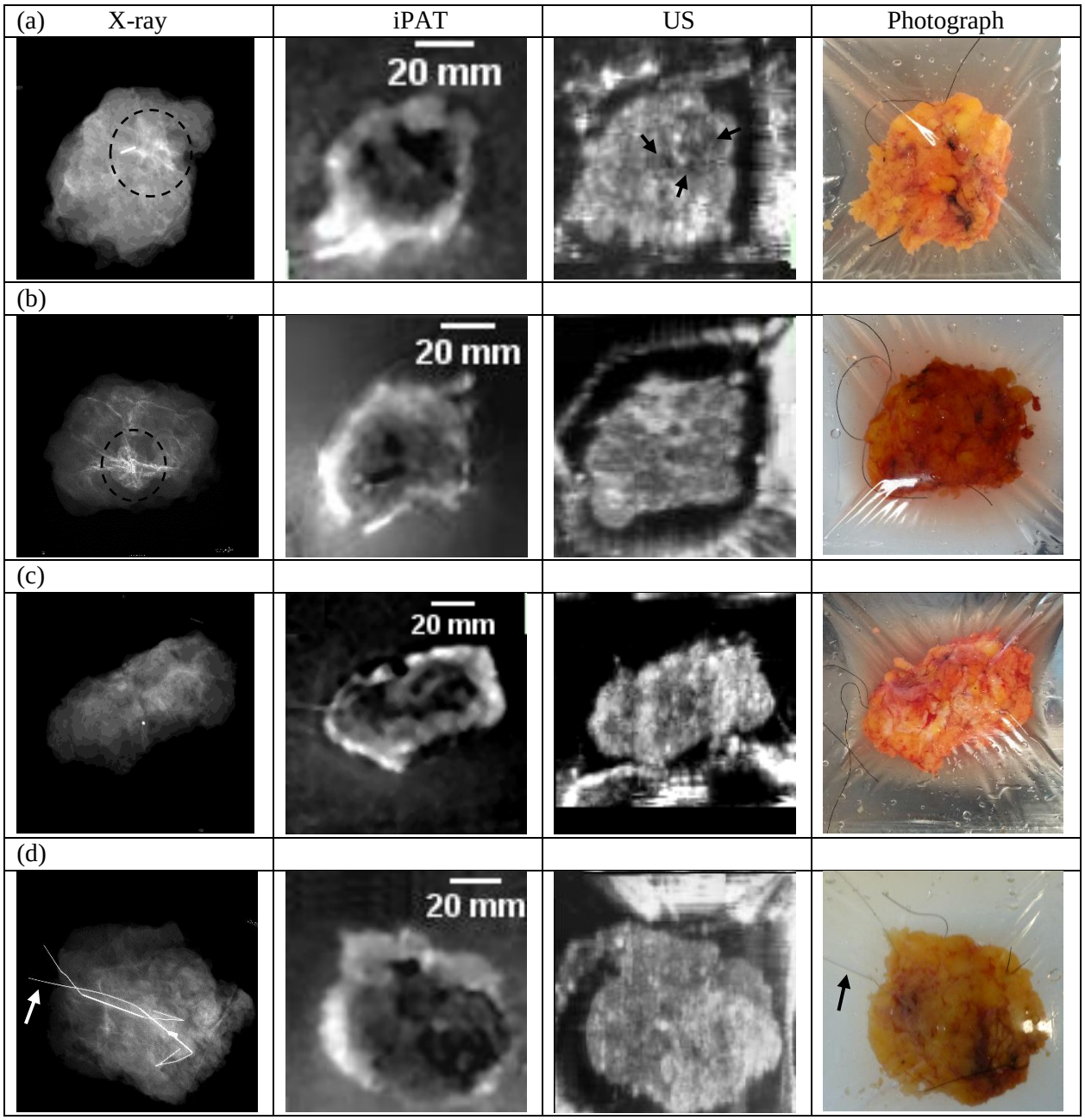

Figure 2.7. Representative montage with slides of commonly encountered BCS lesions, acquired using the iPAT lumpectomy evaluation system. The first column shows intraoperative transmission X-ray images. The second column depicts the corresponding 930 nm iPAT slices, which are co-registered to the US slices shown in the third column. Finally, the last column shows specimen photographs, which, along with the X-ray images, are not co-registered. The specimen in (a) contained a pathologically confirmed 17 mm IDC with concordant findings on iPAT and X-ray (dashed circle), and to a lesser degree, US. Figure (b) shows a specimen which contained a lesion composed of an 8 mm IDC with an extension of DCIS. Figure (c) represents a lumpectomy specimen found by pathology to contain two adjacent foci of IDC, measuring 16 mm and 15 mm each, along with high-grade DCIS. Lastly, the lumpectomy found in (d) was confirmed to be a pure DCIS lesion measuring at least 18 mm in diameter and was removed using wire guided excision. The hooked localization wires can be appreciated in the photograph and on the X-ray image (arrows). The iPAT results appear to be in agreement as they show hypo-intense areas corresponding to the lesion location in the X-ray.

2.4 Discussion

2.4.1 Lipid vs hemoglobin in ex vivo applications

A survey of photoacoustic imaging literature suggests that the primary contrast of tumours is provided by elevated hemoglobin concentration associated with cancer induced angiogenesis[20,23,38–40]. Consequently, it was expected that 690 nm imaging would show increased signal intensity originating from periphery of tumour regions. However, contrary to this hypothesis, this investigation found evidence that 690 nm deoxyhemoglobin weighted images generally showed little or no correlation with hypoechoic US regions inside *ex vivo* specimens. This was the case for most of the specimens encountered in this study and is exemplified in Figure 2.5. Therefore, the extendibility of documented *in vivo* results to *ex vivo* applications must be questioned. The extendibility hypothesis rests upon two assumptions. First, it was assumed that a freshly excised tissue specimen will quickly reach low blood oxygenation levels due to a lack of blood supply. This motivated the 690 nm wavelength selection, where deoxyhemoglobin dominates tissue absorption. The validity of this assumption was corroborated by the increased signal intensity, seen in the 690 nm slices compared to the 800 nm slices of Figure 2.5 (yellow arrows). Specifically, one can infer that the blood content in the excised tissue is dominated by deoxyhemoglobin since the 800 nm wavelength is absorbed equally by both deoxy- and oxy-hemoglobin while the 690 nm wavelength is primarily absorbed by only deoxy-hemoglobin. Indeed, upon closer inspection of the 690 nm iPAT imaging results of Figure 2.5, it can be seen that areas with higher blood concentration produce high intensity features. For example, the area of high blood content marked in the photograph of Figure 2.5(h) by a dashed oval, corresponds well to the iPAT 690 nm image in 2.5(a), near the periphery of the specimen (dashed oval). The second assumption is that blood distribution inside the specimen will remain relatively unchanged after excision. However, the blood distribution depends on ability of the vascular network to maintain blood vessel volume, which in turn depends on blood pressure, provided by cardiac output. Because an excised specimen is no longer connected to the cardiovascular system, it is

possible that many of its blood vessels collapsed during surgery, leading to a heterogeneous reduction in blood volume. Therefore, hemoglobin distribution inside *excised* tissue specimens may not a good biomarker of malignancy.

Alternatively, low lipid concentration has been well documented by optical methods as being a significant indicator of breast abnormalities[41]. Furthermore, the lipid concentration within breast tissue, including the parenchyma and adipose tissue, is unaffected by surgical excision. Consequently, it is possible that low lipid concentration is a good indicator of tumour location, and extent, in excised tissue. Moreover, lipid may be a more effective biomarker for *in vivo* tumour mapping as well, and going forward, researchers with access to high-fidelity photoacoustic imaging systems should make an effort to examine this approach. The preliminary results of the study presented here, provide motivation for this direction.

Finally, the results outlined in the case study sections provided confidence that photoacoustic imaging may have a significant role to play in soft tissue visualization and assessment, especially as pertains to malignancy visualization. The high concordance of iPAT results with established X-ray and US technology, in terms of tumour location and extent, were encouraging. Furthermore, the agreement between iPAT derived indications and the gold standard postoperative pathologic examination, indicate that molecular specificity of optical imaging may give iPAT an edge over existing lumpectomy margin assessment methods. In particular, the positive margin case illustrated a possible opportunity to intervene intraoperatively, potentially sparing the patient a repeat surgery, however, substantially more data must be gathered before conclusions are made.

2.4.2 Enabling intraoperative surgical intervention

Mapping 3D spatial coordinates of detected positive margins to the surgical cavity where missed malignant tissue needs to be excised, is not trivial. Fortunately, the current standard of practice for BCS surgery includes specimen orientation sutures, which are used by the surgeon to mark the lateral (long

suture) and superior (short suture) orientation of the specimen with respect to the patient. These can be seen in the specimen photographs. Even more importantly, the high contrast appearance of black colour sutures in the iPAT images promises convenient referencing of the specimen orientation with respect to the surgical cavity, enabling intraoperative intervention in cases of positive margin detection.

As outlined in the introduction, most novel systems currently being considered for intraoperative margin assessment applications do not provide the surgeon with a full view of the tumour, and at worst, only examine the surface. In some cases, this approach may not meet the needs of the standard of care, but perhaps even more importantly, it may hinder the translation of the technology to the clinic. Complete visualization of the specimen, which is the current intraoperative standard provided by x-ray imaging, allows evaluation of the tumour extent, shape, morphology and position within the specimen. The information is provided simultaneously, giving the surgeon confidence about the assessment results, and this likely plays a role in enabling effective intervention. The iPAT system was able to deliver this familiar functionality, but with the enhanced sensitivity and specificity of optical spectroscopy.

2.4.3 System resolution and scan speed

The estimated 2.5 mm resolution of the iPAT system is sufficient for most intraoperative applications. The present surgical standard of a minimum 2 mm clear margin is potentially practicable with the current version of the iPAT system. However, the ongoing debate about the minimum margin width necessary for recurrence prevention may establish a new standard of less than 2 mm, in the near future. Fortunately, this trend would not render iPAT ineffective because the system resolution can be readily increased by use of higher frequency PA transducer arrays.

The scan time of 6 minutes per side means that scanning both sides will require about 12 minutes, not including sample preparation and inversion. This is substantially longer than just a few seconds needed by current x-ray technology. However, we used a 24-channel PA array and, consequently, the system

spent most of its time rotating and translating the array over the imaging volume. An array with 240-elements can be constructed using a straight forward extension of existing technology. This would result in a scan time of less than 40 seconds, on par with current x-ray technology.

2.5. Conclusion

We have presented preliminary results of intraoperative photoacoustic imaging of breast lumpectomy specimens using a novel iPAT scanner, clearly showing whole tumours in a true clinical setting. This was accomplished via construction of a medical grade carted photoacoustic imager. A key aspect of PAT system design is the use of transducer array technology specialized for a specific imaging task. Detecting signals from large tissue specimens requires highly sensitive detectors with frequency bandwidth extending over an ultra-broad range, typically unavailable commercially. Furthermore, accurate reconstruction of PA images requires full view PA detection geometry. By addressing these common pitfalls of PAT system design we have successfully constructed an intraoperative photoacoustic tomography lumpectomy evaluation system allowing us to pursue practical imaging studies within clinical conditions. We found that targeting surgical margins during BCS imaging is advantageous over targeting the tumour due to the consistent presence of lipids in healthy breast tissue. This approach shines a light towards novel soft tissue abnormality assessment, potentially leading to improved intraoperative instrumentation and higher surgical success rates.

Future work consists of system resolution and imaging speed improvements, regular imaging of fresh lumpectomy specimens and extension to a clinical trial. Also, development of a segmentation technique to differentiate healthy from malignant tissue is needed. Such extensions to the current work will result in a statistical database linking the iPAT results to pathology and re-excision surgery rates.

2.6. References

1. Siegel RL, Miller KD, Jemal A. Cancer Statistics , 2015. *CA Cancer J Clin*. 2015;65(1):5-29.

doi:10.3322/caac.21254.

2. Ananthakrishnan P, Balci FL, Crowe JP. Optimizing Surgical Margins in Breast Conservation. *Int J Surg Oncol*. 2012;2012. doi:10.1155/2012/585670.

3. Lagios MD, Silverstein MJ. Ductal Carcinoma In Situ: Recent History and Areas of Controversy. *Breast J*. 2015;21(1):21-26. doi:10.1111/tbj.12359.

4. Silverstein MJ, Lagios MD. Treatment Selection for Patients with Ductal Carcinoma In Situ (DCIS) of the Breast Using the University of Southern California/Van Nuys (USC/VNPI) Prognostic Index. *Breast J*. 2015;21(2):127-132. doi:10.1111/tbj.12368.

5. Waljee JF, Hu ES, Newman LA, Alderman AK. Predictors of Re-excision among Women Undergoing Breast-Conserving Surgery for Cancer. *Ann Surg Oncol*. 2008;15(5):1297-1303. doi:10.1245/s10434-007-9777-x.

6. Schiller DE, Le LW, Cho BCJ, Youngson BJ, Mccready DR. Factors Associated with Negative Margins of Lumpectomy Specimen : Potential Use in Selecting Patients for Intraoperative Radiotherapy. *Ann Ourgical Oncol*. 2007;15(3):833-842. doi:10.1245/s10434-007-9711-2.

7. Emmadi R, Wiley EL. Evaluation of Resection Margins in Breast Conservation Therapy : The Pathology Perspective — Past , Present , and Future. *Int J Surg Oncol*. 2012;2012:180259. doi:10.1155/2012/180259.

8. Esbona K, Li Z, Wilke LG. Intraoperative Imprint Cytology and Frozen Section Pathology for Margin Assessment in Breast Conservation Surgery : A Systematic Review. *Ann Surg Oncol*. 2012;19(10):3236-3245. doi:10.1245/s10434-012-2492-2.

9. Britton PD, Sonoda LI, Yamamoto AK, Koo B, Soh E, Goud A. Breast surgical specimen radiographs : How reliable are they ? *Eur J Radiol*. 2011;79(2):245-249. doi:10.1016/j.ejrad.2010.02.012.

10. Thill M, Dittmer C, Baumann K, Friedrichs K, Blohmer J. MarginProbe- Final results of the German post-market study in breast conserving surgery of ductal carcinoma in situ. *The Breast*. 2014;23(1):94-96. doi:10.1016/j.breast.2013.11.002.

11. Eggemann H, Ignatov T, Dan S. Accuracy of ultrasound-guided breast-conserving surgery in the determination of adequate surgical margins. *Breast Cancer Res Treat*. 2014;145(1):129-136. doi:10.1007/s10549-014-2932-8.

12. Krekel NMA, Haloua MH, Cardozo AMFL, de Wit RH, Bosch AM, de Widt-Levert LM, Muller S, van der Veen H, Bergers E, de Lange de Klerk ESM, Meijer S, Petrousjka van den Tol M. Intraoperative ultrasound guidance for palpable breast cancer excision (COBALT trial): a multicentre , randomised controlled trial. *Lancet Oncol*. 2013;14(1):48-54. doi:10.1016/S1470-2045(12)70527-2.

13. Koloydenko A, Notingher I. Towards intra-operative diagnosis of tumours during breast conserving surgery by selective-sampling Raman micro-spectroscopy. *Phys Med Biol*. 2014;59(20):6141-6152. doi:10.1088/0031-9155/59/20/6141.

14. Brown JQ, Bydlon TM, Richards LM, et al. Optical Assesssment of Tumor Resection Margins in the Breast. *IEEE J Sel Top Quantum Electron*. 2010;16(3):530-544.

15. Lue N, Kang JW, Yu C, et al. Portable Optical Fiber Probe-Based Spectroscopic Scanner for Rapid Cancer Diagnosis : A New Tool for Intraoperative Margin Assessment. *PLoS One*. 2012;7(1). doi:10.1371/journal.pone.0030887.

16. Breslin TM, Xu F, Palmer GM, Zhu C, Gilchrist KW, Ramanujam N. Autofluorescence and Diffuse Reflectance Properties of Malignant and Benign Breast Tissues. *Ann Surg Oncol*. 2004;11(1):65-70. doi:10.1245/ASO.2004.03.031.

17. Nguyen FT, Zysk AM, Chaney EJ, Kotynek JG, Oliphant UJ, Bellafiore FJ, Rowland KM, Johnson PA, Boppart SA. Intraoperative Evaluation of Breast Tumor Margins with Optical Coherence Tomography. *Cancer Res*. 2009;69(22):8790-8797. doi:10.1158/0008-5472.CAN-08-4340.

18. Kim GR, Kang J, Kwak JY, Chang JH, Kim S Il, Youk JH. Photoacoustic Imaging of Breast Microcalcifications : A Preliminary Study with 8-Gauge Core-Biopsied Breast Specimens. *PLoS One*. 2014;9(8):8-10. doi:10.1371/journal.pone.0105878.

19. Wang B, Karpiouk A, Yeager D. In vivo intravascular ultrasound-guided photoacoustic imaging of lipid in plaques using an animal model of atherosclerosis. *Ultrasound Med Biol*. 2013;38(12):2098-2103. doi:10.1016/j.ultrasmedbio.2012.08.006.In.

20. Dogra VS, Chinni BK, Valluru KS, Joseph J V. Multispectral Photoacoustic Imaging of Prostate Cancer : Preliminary Ex - vivo Results. *J Clin Imaging Sci*. 2015;3(3):1-7. doi:10.4103/2156-7514.119139.

21. Kim C, Erpelding TN, Jankovic L, Pashley MD, Wang L V. Deeply penetrating in vivo photoacoustic imaging using a clinical ultrasound array system. *Biomed Opt Express*. 2010;1(1):335-340.

22. Song KH, Wang L V. Deep reflection-mode photoacoustic imaging of biological tissue. *J Biomed Opt*. 2007;12(December):1-3. doi:10.1117/1.2818045.

23. Wang L V, Hu S. Photoacoustic Tomography : In Vivo Imaging from Organelles to Organs. *Science (80-)*. 2012;335(March):1458-1462.

24. Li R, Wang P, Lan L, et al. Assessing breast tumor margin by multispectral photoacoustic tomography. *Biomed Opt Express*. 2015;6(4):1273. doi:10.1364/BOE.6.001273.

25. Hainsworth A, Fosh B, Raymond W, Eaton M, Mcleay W. Ductal carcinoma in situ : breast-conserving surgery without radiotherapy. *ANZ J Surg*. 2015;85(4):245-248. doi:10.1111/ans.12655.

26. Subhedar P, Olcese C, Patil S, Morrow M, Zee KJ Van. Decreasing Recurrence Rates for Ductal Carcinoma In Situ : Analysis of 2996 Women Treated with Breast-Conserving Surgery Over 30 Years. *Ann Surg Oncol*. 2015;(April):3273-3281. doi:10.1245/s10434-015-4740-8.

27. Newcomb P a., Trentham-Dietz A, Hampton JM, et al. Late age at first full term birth is strongly associated with lobular breast cancer. *Cancer*. 2011;117:1946-1956. doi:10.1002/cncr.25728.

28. Ellwood R, Cox B, Zhang E, Beard P. Photoacoustic imaging using acoustic reflectors to enhance planar arrays. *J Biomed Opt*. 2014;19(12):126012. doi:10.1117/1.JBO.

29. Jaeger M, Harris-Birtill D, Gertsch A, O'Flynn E, Bamber J. Deformation-compensated averaging for clutter reduction in epiphotoacoustic imaging in vivo. *J Biomed Opt*. 2012;17(6):66007. doi:10.1117/1.JBO.17.6.066007.

30. Roumeliotis M, Ephrat P, Patrick J, Carson JJL. Development and characterization of an omnidirectional photoacoustic point source for calibration of a staring 3D photoacoustic imaging system. *Opt Express*. 2009;17(17):15228-15238. doi:10.1364/OE.17.015228.

31. Roumeliotis MB, Kosik I, Carson JJL. 3D photoacoustic imaging using starting, sparse array with 60 transducers. 2012;8223:82233F-82233F-6. doi:10.1117/12.908841.

32. Kosik I, Carson JJL, Program I, Health L, Joseph S. Combined 3D photoacoustic and 2D fluorescence imaging of indocyanine green contrast agent flow. *Proc SPIE*. 2013;8581:1-8. doi:10.1117/12.2005269.

33. Wong P, Kosik I, Raess A, Carson JJL. Objective Assessment and Design Improvement of a Staring, Sparse Transducer Array by the Spatial Crosstalk Matrix for 3D Photoacoustic Tomography. *PLoS One*. 2015;10(4):e0124759. doi:10.1371/journal.pone.0124759.

34. *American National Standard for Safe Use of Lasers*, ANSI Z136.1, Washington, DC (2007).

35. Xu M, Wang L V. Universal back-projection algorithm for photoacoustic computed tomography. *Phys Rev E*. 2005;71(1):16706. doi:10.1103/PhysRevE.71.016706.

36. Sevcenco IS, Hampton PJ, Agathoklis P. Seamless stitching of images based on a Haar Wavelet 2D integration method. In *17th International conference on digital signal processing*. 2011, (DSP) pp. 1-6. doi:10.1109/ICDSP.2011.6004934

37. Horn BKP. Closed-form solution of absolute orientation using unit quaternions. *J Opt Soc Am A*. 1987;4(4):629. doi:10.1364/JOSAA.4.000629.

38. Ermilov S a., Khamapirad T, Conjusteau A, Leonard MH, Lacewell R, Mehta K, Miller T, Oraevski AA. Laser optoacoustic imaging system for detection of breast cancer. *J Biomed Opt*. 2009;14(2):24007. doi:10.1117/1.3086616.

39. Manohar S, Vaartjes SE, van Hespen JCG, Klasse JM, van den Engh FM, Steenbergen W, van Leeuwen TG. Initial results of in vivo non-invasive cancer imaging in the human breast using near-infrared photoacoustics. *Opt Express*. 2007;15(19):12277-12285. doi:10.1364/OE.15.012277.

40. Xie Z, Hooi FM, Fowlkes JB, Pinsky RW, Wang X, Carson PL. Combined photoacoustic and acoustic imaging of human breast specimens in the mammographic geometry. *Ultrasound Med Biol*. 2013;39(11):2176-2184. doi:10.1016/j.ultrasmedbio.2013.05.018.

41. Anderson PG, Kainerstorfer JM, Sassaroli A, Krishnamurthy N, Homer MJ, Graham RA, Fantini S. Broadband optical mammography: Chromophore concentration and hemoglobin saturation contrast in breast cancer. *PLoS One*. 2015;10(3):1-23. doi:10.1371/journal.pone.0117322.

Chapter 3: Comparison of breast tumor size by intraoperative photoacoustic tomography, magnetic resonance imaging and pathology

3.1 Introduction

A relatively brief discussion of the many roles that medical imaging plays in the breast cancer treatment process is outlined below. For a more detailed examination please see sections 1.1.3, 1.2.1 and 1.2.2.

This chapter also includes investigation of multispectral optical-contrast mechanisms that lead to a new method of PA tumour visualization. Review of the topics covered in sections 1.3.1 and 1.4.3 may aid in a more thorough appreciation of this subject.

3.1.1 Overview

Breast cancer is one of the most common cancers to affect women, exhibiting an average lifetime risk of 1 in 8 [1]. It is a complex disease that is of particular concern for aging women and those with family history of cancer. In spite of rising incidence of breast cancer, the prognosis of patients diagnosed with the disease is much better today compared to the past. These improvements are largely due to the early detection of breast tumours, often at stage I and II, facilitated by the rapid development of medical imaging technology and widespread screening programs[2-7].

By monitoring neoadjuvant therapy, medical imaging continues to play a vital role in the treatment of stage 3 and higher breast cancers, as well as tumors which are inoperable due to location or extent [8]. This therapy is administered in the time between initial diagnosis and surgical intervention, which may be radical mastectomy or BCS. The aim of neoadjuvant therapy is to reduce the cancer extent, known as the residual tumor burden (RTB), and potentially down-stage the cancer. In responding patients this treatment course may open up new surgical options such as BCS versus mastectomy, or even facilitate a

surgical option when there was none before. Furthermore, depending on the estrogen receptor (ER), progesterone receptor (PR), or human epidermal growth factor receptor (HER-2) status of the primary tumor, this therapy is usually tailored as neoadjuvant hormone therapy, targeted therapy, chemotherapy or radiation therapy. In some cases, it may be appropriate to select a combination of these therapies.

Regardless of which therapy avenue is chosen, one of the most critical aspects of treatment is accurate and repeatable RTB assessment. Indeed, the size of the tumor in breast cancer is the single most important factor determining the cancer stage [9]. As a result, the accuracy of tumor measurement can have a significant effect on selecting an appropriate course of action. Measurement errors of just a few mm, can, in some cases, alter the course of treatment. The need for high precision RTB assessment is further highlighted by the widely adopted revised Response Evaluation Criteria in Solid Tumors (RECIST v1.1, released 2009) originally prepared by the International Working Group.[10] Amongst other changes, the updated definition of "tumor progression" now includes an absolute increase of the largest tumor diameter by a minimum of 5 mm. Compared to the previous criteria of a minimum 20% increase in size, this new standard places a premium on medical imaging precision and accuracy, especially in cases with multiple lesions where the sum of diameters must be calculated.

Beyond the responsibility of determining the stage of the cancer, tumor extent assessment, therefore, also continues to play a vital role in treatment efficacy monitoring during neoadjuvant therapy. The importance of this cannot be overstated since ineffective therapies can subject patients to prolonged as well as potentially toxic treatments, with no added survival benefit. Even more significant to patient well-being, however, is the possibility that with periodic RTB assessment, a patient with a non-responding tumor could be switched to a different neoadjuvant therapy, which may in some cases be more effective, thereby maximizing patient survival and recovery. From the perspective of the cancer therapy researcher who is armed with an efficient and accurate RTB monitoring tool, the time between diagnosis and surgery represents an opportunity to examine a number of different neoadjuvant therapies, potentially tailoring the optimum therapy for each patient. Finally, employing an approach featuring accurate and efficient RTB

monitoring, could yield a wealth of knowledge about the relationship between various disease and therapy models. This information has been shown to be useful in predicting patient response to post-surgical therapy, further maximizing survival, especially for stage 3 and higher cancers[11].

Aside from facilitating breast cancer screening, staging, and therapy monitoring, clinical imaging modalities such as DCE-MRI, sonography, as well as X-ray mammography and radiography, also facilitate pre-operative and intraoperative lesion localization, making them invaluable tools in the overall treatment process[2,5,8,12-16].

The debate about how best to perform tumor extent assessment, in general as well as in the neoadjuvant setting, is ongoing. However, there is broad agreement on several fronts. For example, the current standard of unidimensional tumour measurement is likely to change in the near future due to the clinically demonstrated superiority of 3-dimensional assessment. In fact, the International Working Group, while preparing the revised version of RECIST (v1.1, 2009), noted that, in regards to volumetric tumor assessment, they "did not believe that there is at present sufficient standardization and widespread availability to recommend adoption." [10] This conclusion suggests that RECIST guidelines will reflect a technologically viable solution once it is available and sufficiently standardized. Beyond 3D visualization, other desirable features of such a potentially viable breast imaging solution include simplicity, low cost, operator independence and breast density independence.

Photoacoustic tomography (PAT) is a relatively new imaging modality with limited clinical experience[17–20]. Nevertheless, it has demonstrated highly desirable features, especially with respect to breast cancer imaging. It appears to meet many of the desired properties required for widespread practical implementation in the breast abnormality assessment arena [18]. For example, PAT employs tissue-safe near infrared laser illumination thereby avoiding problems associated with ionizing radiation such as in mammography. PAT is also a relatively inexpensive imaging technique, especially compared to MRI where the cost and complexity of maintaining superconducting magnets makes the installation of MRI systems rather involved and unaffordable to all but larger hospitals. Moreover, PAT makes use of

endogenous optical contrast of blood, lipids and other soft tissues, eliminating the need for exogenous contrast agents, and hence, speeding up and simplifying the imaging protocol.[21,22] Because the basis of PAT is an intrinsically 3D phenomenon, called the photoacoustic effect, it is easily implemented as a 3D imaging modality, eliminating the concern for operator dependence.[18,23] And finally, PAT sensitivity has been shown to be breast density independent.[17,19] Breast density independence is again owing to the optical nature of its contrast mechanism, as opposed to mammography and US which derive contrast based on tissue density.

3.1.2 Objectives

The purpose of this study was to determine the viability of intraoperative PAT (iPAT), as a breast tumor assessment method by comparison of tumour volumes determined by iPAT to DCE-MRI and pathology. Also, informal comparison of iPAT imaging to ultrasonography and intraoperative X-ray imaging is presented. Finally, an investigation was carried out to examine how tumor contrast in iPAT images depended on illumination wavelength, fibro-glandular density of tumor bed as well as tumor grade, receptor status, and presence of *in-situ* components.

3.2. Materials and Methods

3.2.1 iPAT Scans and patient selection

Seventeen patients undergoing diagnostic imaging studies in preparation for BCS were recruited for this iPAT imaging study. In brief, a novel and portable iPAT scanner was used to generate 3D image volumes of freshly excised breast lumpectomy specimens. Figure 3.1(a) shows a photograph of the system inside a surgical suite. The front cover panel of the system was removed to expose the major components, which are labeled. The device was a hybrid photoacoustic/ultrasound (PA/US) system, dedicated to BCS imaging applications. It was designed to provide 3D photoacoustic images with co-registered 3D US

images of surgical samples. The photo shows a water tank used for acoustic coupling between the sample and photoacoustic detector array. To perform imaging, a breast tissue sample was positioned in the tank using a custom designed lumpectomy specimen holder, seen in Figure 3.1(b). Following specimen positioning, a SCARA robot (Epson, Japan) was used to scan the custom designed 24-channel arc-shaped PA transducer array using a combination of rotational and translational motion. Illumination was provided by a pulsed laser system delivering approximately 30 mJ of output in the 680 nm to 950 nm wavelength range (Phocus In-line, Opotek, Carlsbad, CA, USA). The laser induced signals were detected and digitized using a custom fabricated 50-MHz data acquisition system (DAQ). The overall scan was coordinated using a PC with LabVIEW software, which oversaw the synchronization of the DAQ, robot PC and laser. Following the iPAT scan a co-registered 3D US scan was carried out using a robot-synchronized 6.6 MHz clinical US scanner (Sonix Touch, Ultrasonix, BC, Canada). In some cases, due to concern over specimen thickness and artefacts, a scan of the opposite face was performed after flipping the specimen 180° with respect to the diagonal axis of the holder (see dotted line in Figure 3.1(b)).

Patient eligibility consisted of biopsy confirmed breast cancer cases with at least an invasive component. Patient recruitment and study procedures were performed at a university affiliated hospital and regional breast cancer center. Results were retrospectively examined to obtain imaging data for patients who also received a preoperative bilateral DCE-MRI scan. The study was carried out with approval of the Institutional Review board of The University of Western Ontario (HSREB# 105467).

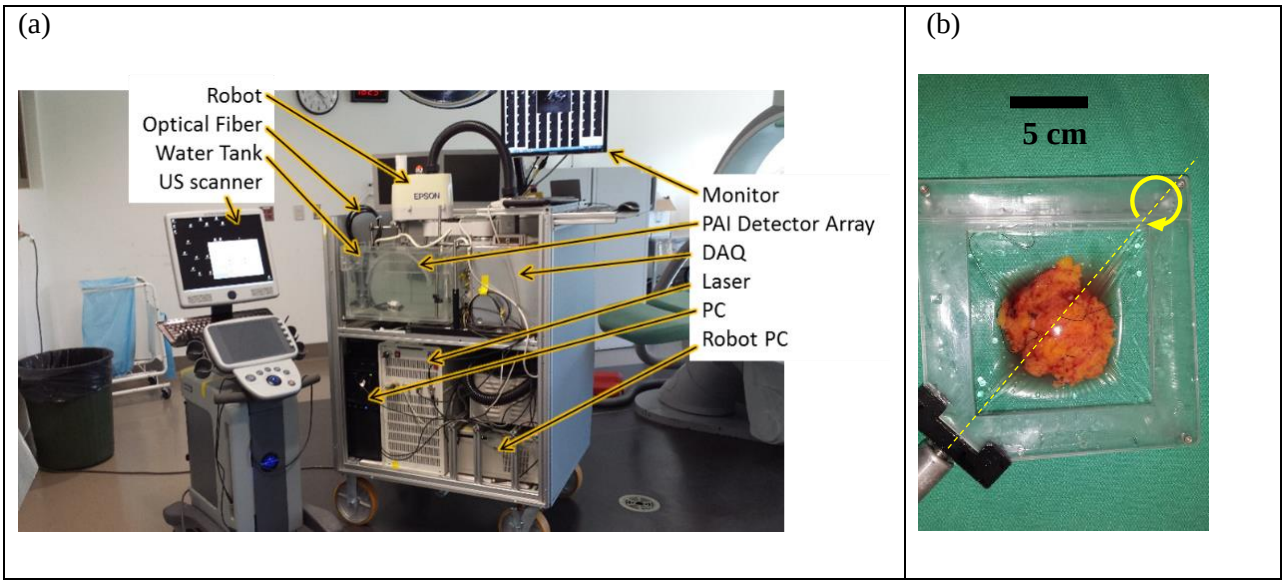

Figure 3.1. (a) Photograph of iPAT system (center) within surgical suite as well as conventional ultrasonography system (left). Major components of iPAT scanner are labeled, including water tank which contains a fused fiber-optic bundle assembly that is used to direct near infrared laser pulses toward lumpectomy specimens restrained in the specialized lumpectomy holder seen in (b). The water in the tank facilitates acoustic coupling between the lumpectomy specimen and the 24-channel arc-shaped photoacoustic detector array. The array and fiber-optic assembly is mounted to the effector of a 4-axis SCARA robot which is controlled by the robot PC. The laser induced signals detected by the transducer array are transferred to the 50 MHz data acquisition system (DAQ) where they are digitized and sent to the workstation PC for processing and visualization on the video monitor. Figure 3.1(b) is a photograph of the iPAT compatible lumpectomy holder showing a compressively restrained surgical specimen.

3.2.2 iPAT Image Volume Reconstruction and Processing

All volumes were processed using a consistent procedure, eliminating subjective bias and therefore standardizing the process similarly to clinically acceptable methods. The iPAT volumes were reconstructed using filtered back projection (FBP), detailed previously.[24] Following FBP, the volumetric results were processed through 5 iterations of K-Wave iterative image improvement using time reversal, adapted for volumetric results and described by Treeby and Cox.[25] This procedure partially restores the amplitude of voxels by use of virtual detectors in locations where detectors were absent in the original iPAT scan, thereby mimicking the coverage of a fully enclosed signal-detection geometry.

Next, to enhance contrast prior to segmentation, the minimum (0) to maximum (255) window and level of the resulting 8-bit RGB image volumes was set to 110-255. Image noise reduction was carried out by use

of a 2-voxel wide median filter to de-speckle and preserve sharp boundaries. Uneven illumination, caused by illumination gradients, was addressed by implementation of a pseudo-flat-field background correction available in ImageJ (1.49v, National Institutes of Health, USA). The final window and level were set by excluding very bright objects, such as black sutures, and saturating 1% of voxels so that the contrast stretching was not influenced by outliers. Image reconstruction and K-Wave correction was implemented in Matlab (MATLAB and K-wave Toolbox Release 2013a, The MathWorks, Inc., Natick, Massachusetts, United States) and image processing was carried out using ImageJ (1.49v, National Institutes of Health, USA).

3.2.3 Volumetric segmentation and maximum diameter measurements of iPAT results

Prior to segmentation of the tumor volumes in iPAT, co-registered 3D-US imaging was used to identify specimen edges, which were in some cases difficult to delineate using iPAT alone due to shadowing edge artefacts. Furthermore, specimen x-ray images obtained using a dedicated 2-D intraoperative scanner (Faxitron, Faxitron Bioptics, Tucson, Arizona, USA), were examined, and the tumor location was correlated to the tumor location in the iPAT volumes. Importantly, while specimen edges and tumour locations were correlated with US and X-ray images, tumour measurements themselves were performed using only iPAT visualization. To aid in visual referencing, image volumes from all 3-D modalities (iPAT, DCE-MRI, US) were reoriented to coincide with each other, as well as with images from the 2-D modalities (intraoperative X-ray, photography). This was done with help of surgical specimen orientation sutures, used by the surgeon to orient specimens with respect to the surgical cavity. The sutures indicated the superior aspect (short suture) and the lateral aspect (long suture).

The identified tumor masses were segmented manually by an experienced operator, who trained on images of phantoms. In the case of multi-focal cancer, the largest tumor was measured for

unidimensional measurement and all lesions were summed for volumetric measurements. Tumors presenting as stellate or spiculated lesions were measured as the longest contiguous dimension and total apparent contiguous volume. The resulting segmented areas were used to calculate the total volume, based on slice thickness, as well as the maximum in-slice diameter. The segmentation was carried out in ImageJ.

To account for specimen shape distortion between formalin-fixed samples and samples compressed inside the specialized lumpectomy holder, whole lumpectomy specimen size measurements from pathology were compared to measurements from the iPAT and US scans. The findings were then correlated with tumor size and shape to determine possible effect of specimen preparation on tumor measurements.

3.2.4 Statistical Analysis

A linear regression analysis was carried out to determine the relationship between measured quantities. Comparison of tumor maximum diameter and volume was done by calculation of Pearson's correlation coefficients, and the non-parametric Wilcoxon signed-rank test. P=0.05 was considered as the significance threshold. iPAT derived volumes were compared to DCE-MRI volumes. Maximum diameters determined by iPAT were compared to DCE-MRI diameters, and separately, to pathology derived diameters. Finally, DCE-MRI diameters were also compared to diameters reported by pathology. Imaging-derived maximum diameters were measured on a single slice, and pathologic diameters were measured on a single slide. The statistical analysis was carried out using the Statistics Toolbox in Matlab (MATLAB and Statistics Toolbox Release 2013a, The MathWorks, Inc., Natick, Massachusetts, United States).

3.2.5 Tumor-contrast spectral dependence

On two occasions, cosmetic breast-reconstruction procedures delayed patient discharge from the surgical suite, allowing extra scanning time with the fresh lumpectomy specimen. The extended access allowed 6 wavelengths in one case and 5 wavelengths in the other, to be utilized. The wavelengths ranged from 690 nm to 950 nm. This opportunity facilitated a small multispectral iPAT study to be carried out by comparing the average contrast *C, between* the tumor and background breast tissue, defined by equation 1.

$$C = (I_t - I_b)/I_b \quad (1)$$

Where I_t is the average voxel intensity in the tumor area, and I_b is the average intensity in the normal breast tissue. The tumor area was defined as a 1 cm diameter disk, which simultaneously overlapped apparent tumor tissue found in iPAT, US and X-ray images. The background breast tissue was defined by segmenting out the entire specimen. The *C* values were then plotted against the corresponding wavelength. The average intensities were extracted using ImageJ after images were scaled from 0 (black) to 255 (white). While an investigation with only 2 specimens and 5/6 wavelengths cannot present statistically significant findings, we nevertheless include it here as a possible motivator for future PAT research.

3.2.6 Breast density dependence

To investigate the relationship between breast density and iPAT performance, tissue-density surrounding the tumors was classified according to the ACR BI-RADS ATLAS for breast MRI.[26] For comparison, information from the pathology report regarding the tumor bed was also classified using the same categories. These findings were then correlated to visualization contrast and quality of the tumor masses on iPAT.

3.2.7 MR imaging and pathology

Gradient-echo 3D T1-weighted images were obtained in an axial and sagittal plane with and without Gadovist injection. Tumors, identified by a radiologist with extensive experience (>10 years), were manually segmented in the axial plane based on their contrast enhancement. The segmented areas were used to calculate the total volume, as well as the maximum diameter.

Pathological examination was completed, and a breast invasive carcinoma synoptic report was generated, according to AJCC/UICC TNM 7th edition, CAP Version 3.1.0.0 (June 2012). The work was completed by, or under supervision of, a senior pathologist with more than 10 years of experience. The synoptic report was used to determine the following tumor specific information: maximum diameter, histologic type and grade, receptor status, presence of extensive intra-ductal component and presence of *in situ* disease. These properties were then compared with the photoacoustic appearance of the lesion to discover potential relationships.

3.3 Results

3.3.1 iPAT Scans and patient selection

Seventeen out of the 100 patients who participated in the intraoperative photoacoustic imaging study of breast lumpectomy assessment were found to have received a DCE-MRI scan. One patient had a DCE-MRI occult tumor due to contrast enhancement which was not significantly different from background. One patient received a second BCS, having had the main tumor mass removed previously. One patient had received neoadjuvant therapy and was found on pathology to be a pathologically complete responder, with no malignancy remaining. One patient presented with pure in-situ disease and no invasive tumor. And finally, one patient was found to have a pure radial scar. The remaining 12 patients were included in

the study with informed consent and approval of the institutional review board of The University of Western Ontario.

The imaging scan duration was 6 minutes and 1.5 minutes for the iPAT and US scan, respectively. In cases where multiple wavelengths were used, or specimen was scanned from two sides, the scan duration was extended by 6 minutes per side/wavelength. The iPAT/US intraoperative imaging protocol did not interfere with the standard of care as maximum ischemic time prior to formalin fixation never exceeded 60 minutes.

Table 3.1 contains a tabulated summary of patient and tumor specific information. The average age of the patients was 49.5 with a range of 33 to 75 and the median age was 50.

Table 3.1. Patient and tumor information

Specimen number	Patient age	Tumor histologic type	Tumor histologic grade	Tumor receptor status ER	PR	HER2	Extensive intra-ductal component	*In-situ* disease (nuc. grade)
AF012	53	IDC	3	+	+	+	n/a	no
AF018	75	IDC	2	n/a	n/a	n/a	n/a	Yes (3)
AF024	53	IDC	2	+	+	-	YES	Yes(2-3)
AF029	33	IDC	1	+	+	-	No	Yes(1-2)
AF032	45	ILC (lobular)	2	+	+	-	n/a	Yes(n/a)
AF033	46	IDC	1	+	+	-	n/a	Yes(1-2)
AF043	53	IDC(multifocal)	2	+	+	+	n/a	Yes(2-3)
AF046	50	IDC(tubular)	1	+	+	-	No	Yes(1)
AF047	50	IDC(crush artefact)	1	+	+	-	n/a	no
AF072	50	IDC(tubular)	1	+	+	-	n/a	Yes(1-2)
AF089	45	IDC	1	+	+	-	n/a	no
AF096	42	IDC	3	-	-	+	YES	Yes(3)

3.3.2 iPAT Image Volume Reconstruction and Processing

Figure 3.2(a) shows the initial image reconstruction results obtained by FBP. It depicts a representative slice taken from a 3D stack of a freshly excised lumpectomy specimen containing an invasive ductal

carcinoma tumour scanned at a wavelength of 930 nm. The effect of applying the K-wave iterative image improvement algorithm using time reversal is shown in Figure 3.2(b). Figures 3.2(c) and 3.2(d) show the impact of a 2-voxel wide median filter, and a pseudo-flat-field background image correction, respectively. Finally, Figure 3.2(e) shows the corresponding slice taken from a 3D ultrasound stack. The top row represents a reflection-mode image, as the illumination and subsequent ultrasound signal detection occurred on the same side. The bottom row is analogous to transmission mode imaging, because illumination and signal collection was implemented on opposite sides. Each slice was acquired approximately 7 mm below the illuminated surface and the total specimen thickness was 21 mm.

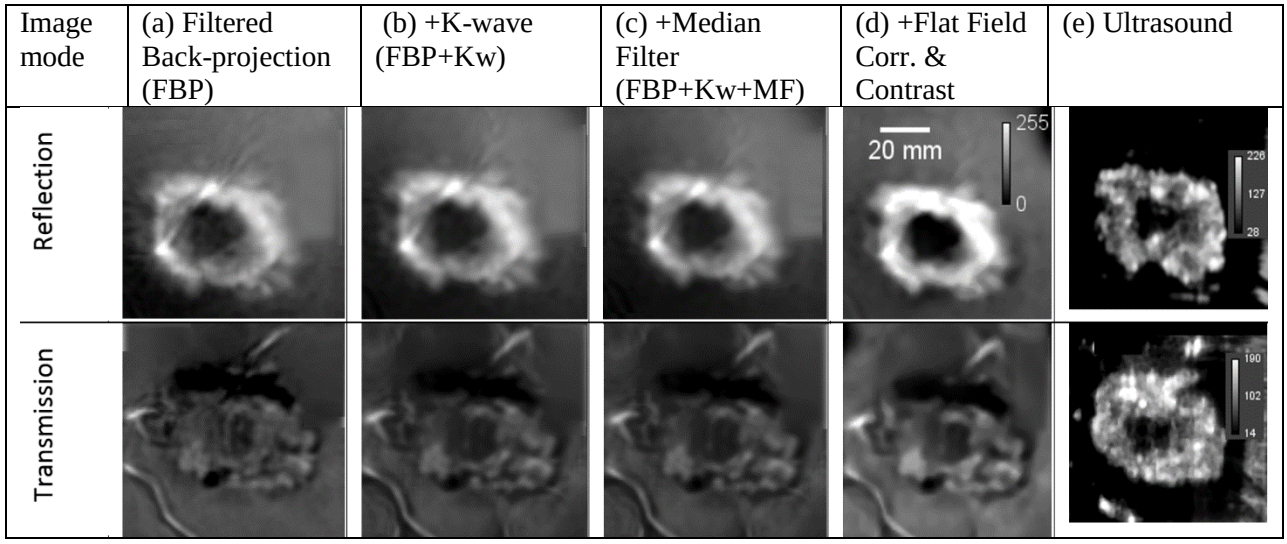

Figure 3.2. Slices representative of reflection and transmission mode iPAT, showing compounding impact of (a) Back-projection, (b) K-wave iterative image improvement, (c) 2-voxel wide median filter and (d) pseudo-flat-field correction combined with contrast adjustment. (e) Corresponding US image.

Figure 3.3 is a visual summary of the imaging results for the 12 lumpectomies investigated in this work. The 3D imaging results (iPAT, DCE-MRI, US) have been reoriented to approximately coincide with the intraoperative X-ray and photograph, where available. The specific slices shown here were selected due to the apparent good co-visualization of tumors in most of the imaging modalities used. The specimen thickness at iPAT/US imaging ranged from 9 mm to 22 mm, and the selected slice depth ranged from 4 mm to 9 mm below surface.

Intraoperative 930 nm iPAT	Intraoperative X-ray	Intraoperative US	Preoperative DCE-MRI	Photograph
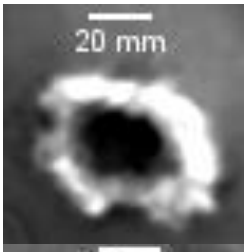	NOT AVAILABLE	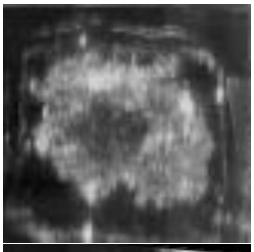	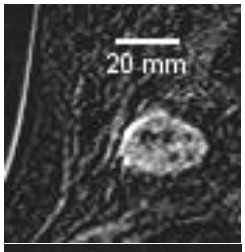	
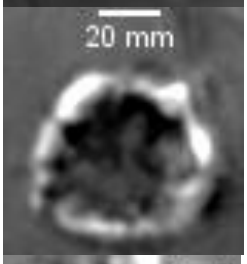	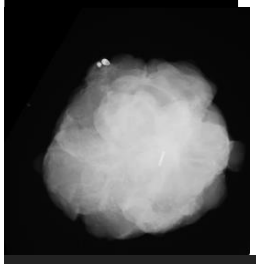	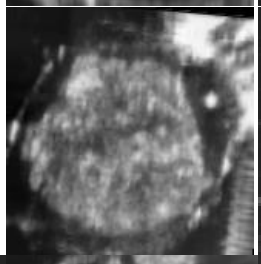	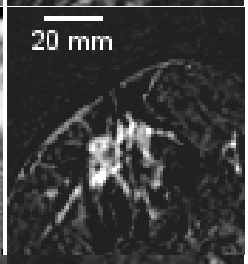	NOT AVAILABLE
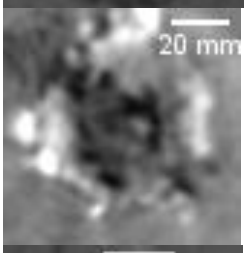	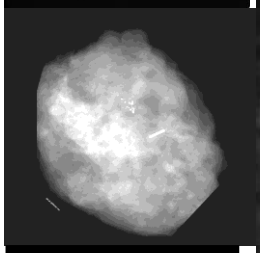	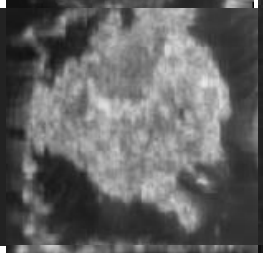	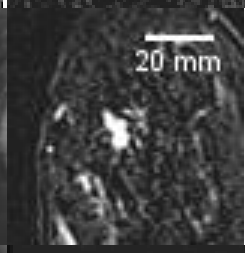	
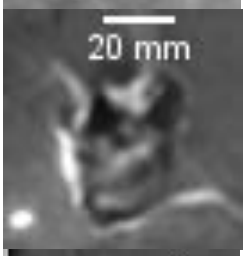	NOT AVAILABLE	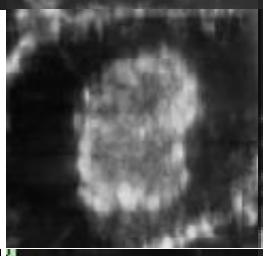	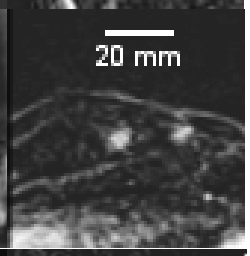	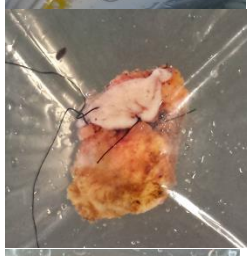
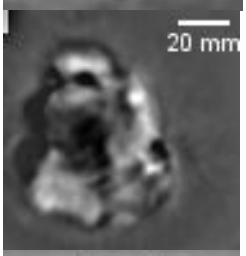	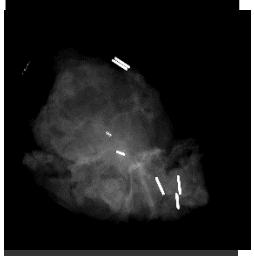	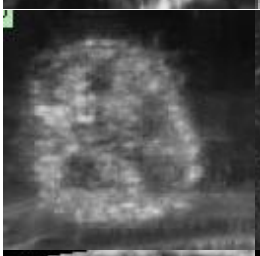	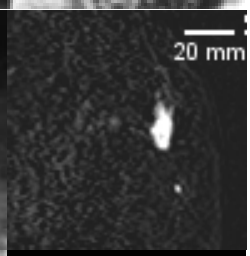	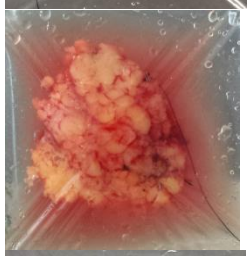
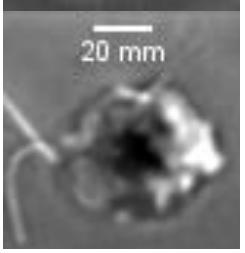	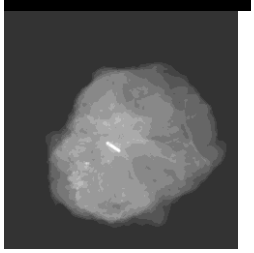	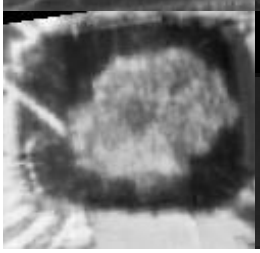	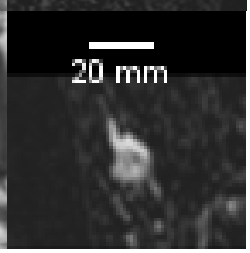	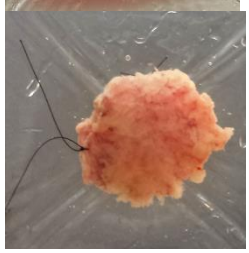

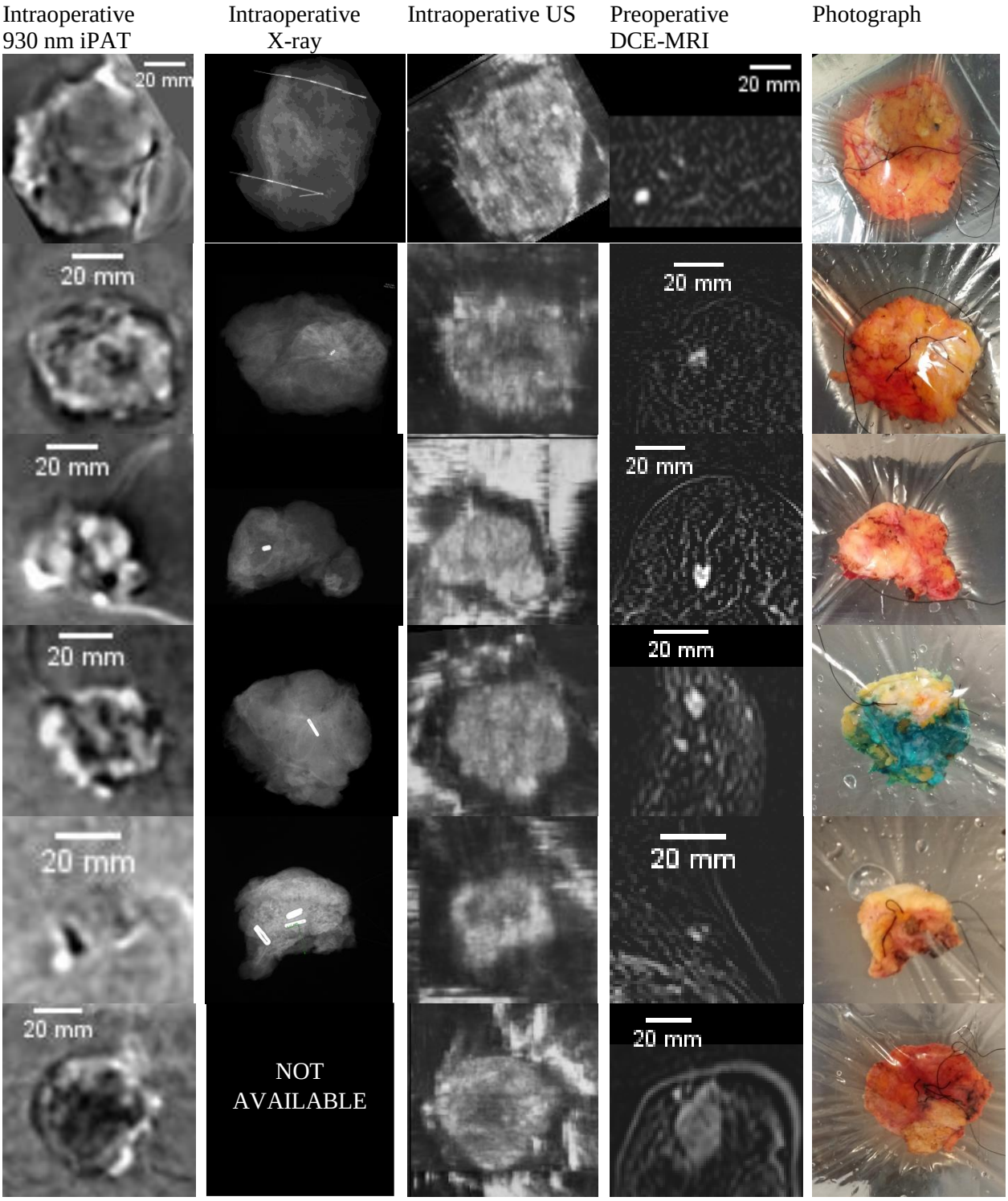
Intraoperative 930 nm iPAT
Intraoperative X-ray
Intraoperative US
Preoperative DCE-MRI
Photograph
20 mm
NOT AVAILABLE

Figure 3.3. Representative slices of specimens containing at least an invasive component of breast carcinoma. Each row represents a single case. Going from left to right, tumors are visualized by iPAT, X-ray, US, DCE-MRI and photograph. Specimens in each row have been reoriented to represent approximately the same perspective. For easy referencing, specimens are listed in the same order as in Tables 1 – 3. The first column represents selected iPAT slices acquired at 930 nm. The second column indicates the result of a transmission X-ray image of the specimen and shows any surgical aides such as radioactive localization seeds and localization wires. The third column shows co-registered US slices of the specimen taken using a conventional 6.6 MHz US system. The fourth column indicates the area of interest on a preoperative DCE-MRI scan and has been scaled and re-oriented to approximately correspond to the iPAT and US results. Finally, the fifth column shows a photograph of each specimen contained within a saline filled bag and compressively restrained by the lumpectomy holder. The photo also demonstrates the visualization of the black surgical orientation sutures attached by the surgeon to establish specimen orientation with respect to the surgical cavity and patient.

3.3.3 Volumetric segmentation and maximum diameter measurements

The maximum diameter measurements for pathology, DCE-MRI, and iPAT are listed in Table 3.2. The table also shows results for volumetric measurements derived from DCE-MRI and iPAT. The mean tumor volume based on DCE-MRI was 1426 mm^3 (range of 94 – 5509 mm^3) with a median of 610 mm^3. In comparison, the mean volume from iPAT measurements was 1169 mm^3 (range of 41 – 4705 mm^3) and median was 757 mm^3. In terms of mean maximum tumor diameter, the measurement for pathology was 14.8 mm (range 4 – 39 mm) with median 13.5 mm, DCE-MRI produced 18 mm (range 7 -43 mm) with median 16 mm, and finally iPAT mean maximum diameter was 23.1 mm (range 9 – 46 mm) with median of 23 mm.

Table 3.2. Maximum tumor diameters and volumetric measurements

Specimen number	Maximum tumor diameter (mm)			Tumor volume (mm^3)	
	Pathology	DCE-MRI	iPAT	DCE-MRI	iPAT
AF012	39	27	46	5509	4705
AF018	24	36	38	2583	2930
AF024	12	17	23	517	573
AF029	15	9	31	263	1028
AF032	18	18	26	1240	1206
AF033	13	18	23	1407	1199
AF043	15	15	13	703	929
AF046	9	9	13	149	261
AF047	4	9	8	213	41
AF072	8	8	24	327	459
AF089	7	7	9	94	115
AF096	14	43	23	4109	585
Mean	14.8	18	23.1	1426	1169
Median	13.5	16	23	610	757

Table 3.3 shows three orthogonal measurements of the whole lumpectomy specimens, taken from iPAT/US imaging, as well as measurements of the formalin fixed specimens, taken from the pathology report. For comparison, the table also includes ellipsoid volumes calculated using these diameters.

Table 3.3. Specimen diameters and corresponding ellipsoid volumes determined by pathology and iPAT

Specimen number	Specimen diameters (D) from pathology				Specimen diameters from iPAT/US* imaging (mm)			
	Max D (mm)	D2 (mm)	D3 (mm)	Ellipsoid Volume (cm^3)	Max D (mm)	D2 (mm)	D3 (mm)	Ellipsoid volume (cm^3)
AF012	65	45	30	45.9	75	51	21	42.0
AF018	55	55	30	47.5	66	63	22	47.9
AF024	62	55	25	44.6	63	60	19	37.6
AF029	40	25	15	7.85	51	34	13	11.8
AF032	67	54	31	58.7	77	63	19	48.2
AF033	48	37	23	21.4	58	47	15	21.4
AF043	67	60	25	52.6	81	63	18	48.1
AF046	50	45	25	29.4	59	49	14	21.2
AF047	35	35	25	16.0	50	31	9	7.30
AF072	42	33	18	13.1	50	42	11	12.1
AF089	25	22	10	2.88	31	24	9	3.50
AF096	44	44	14	14.2	53	49	10	13.6

*Specimen perimeter was outlined using iPAT images unless artefacts obscured edge, in which case US was used.

3.3.4 Statistical Analysis

Table 3.4. lists the Pearson correlation coefficients and Wilcoxon signed-ranked-test results between the imaging modalities and pathology, as well as the related significance values. This table also relates the mean and median volumetric size differences between DCE-MRI and iPAT and unidimensional size differences between DCE-MRI, iPAT and pathology. To account for the broad range of tumor sizes in this study, the sizes were compared in terms of absolute as well as relative differences.

iPAT vs DCE-MRI tumor volumes:

The regression analysis indicated a statistically significant correlation between iPAT and DCE-MRI for derived volumetric tumor size ($r=0.78$, $p=0.003$). Moreover, the mean difference in derived volumetric tumour size estimated from these two modalities was not significantly different according to the Wilcoxon signed-ranked-test ($p=0.97$). In other words, this indicates that the median of the differences of the two data sets (iPAT and MRI volumes) was zero (i.e. the null hypothesis), implying that the measurements were likely of the same sample population. The mean volume difference and its standard deviation were -257 ± 1093 mm^3, while the median difference was 38.6 mm^3. Compared to DCE-MRI, volume estimates by iPAT were misestimated by a mean -3.6% and by a median +11%.

iPAT vs DCE-MRI tumor diameters:

The regression analysis indicated a moderately significant correlation between iPAT and DCE-MRI for maximum tumor diameters ($r=0.54$, $p=0.07$). Furthermore, the mean difference in derived unidimensional tumour size estimated from these two modalities was not significantly different according to the Wilcoxon signed-ranked-test ($p=0.064$). Compared to DCE-MRI this corresponded to a mean overestimate of maximum diameters by iPAT of 5.1 ± 11.1 mm and a median overestimate of 4.5 mm. In terms of percent difference, iPAT overestimated maximum diameters by an average 28% and a median of 28%.

iPAT vs pathology tumor diameters:

In comparing iPAT tumour diameters to pathology, the regression analysis showed a very strong and significant correlation ($r=0.87$, $p=0.0002$), but according to the Wilcoxon signed-rank-test, also a significant difference ($p=0.0015$). The results indicated a mean 8.3 ± 5.6 mm and median 8.5 mm overestimate of maximum diameters by iPAT versus pathology. In terms of percent difference, an average 46% overestimate of maximum diameters was found with a median 47%.

DCE-MRI vs pathology tumour diameters:

Comparison of DCE-MRI and pathology tumour diameter measurements revealed a moderate correlation ($r=0.56$, $p=0.06$), but, according to the Wilcoxon test, no significant difference in size ($p=0.55$). DCE-MRI overestimated the maximum diameters by a mean 3.2 ± 10.1 mm corresponding to 17% of the average tumour diameter. However, when using the median, DCE-MRI was no different from pathology (median = 0 mm).

iPAT vs pathology specimen diameters:

In terms of whole specimen measurements, the analysis showed a significant and strong correlation between maximum specimen diameters determined by iPAT/US and pathology ($r=0.97$, $p<0.0001$). However, in comparing the two measurement methods, the Wilcoxon signed-rank-test indicated a significant difference in diameter size ($p=0.0005$). The iPAT/US-measured maximum diameters overestimated the pathology measurements by a mean value of 9.5 ± 3.6 mm and a median value of 10 mm, or 18% and 19%, respectively.

iPAT vs pathology specimen ellipsoid volume:

Ellipsoid volumes based on three orthogonal-diameter measurements were also compared. iPAT-derived specimen ellipsoid volumes were positively correlated ($r=0.98$, $p<0.0001$) and based on the Wilcoxon test not significantly different from pathology derived volumes ($p=0.052$). iPAT ellipsoid volumes

underestimated the pathology results by a mean -3.29 ± 4.54 cm^3, with a median -2.43 cm^3, corresponding to 14 % and 10%, respectively.

Table 3.4. Correlation coefficients and statistical assessment between the imaging modalities for tumor size and whole specimen size.

Comparison pairs	Pearson correlation R-value	Wilcoxon signed rank test	Mean (S.D.) difference		Median difference	
			(dimension)	(%)	(dimension)	(%)
iPAT vs DCE-MRI tumor volumes	0.78 (p=0.003)	p=0.97	-257 (1093) mm^3	3.6 (15)	38.6 mm^3	11
iPAT vs DCE-MRI tumor max diameter	0.54 (p=0.07)	p=0.064	5.1 (11.1) mm	28 (61)	4.5 mm	28
iPAT vs pathology tumor max diameter	0.87 (p=0.0002)	p=0.0015*	8.3 (5.61) mm	46 (31)	8.5 mm	47
DCE-MRI vs pathology tumor max diameter	0.56 (p=0.06)	p=0.55	3.2 (10.1) mm	17 (54)	0 mm	0
iPAT vs pathology specimen max diameter	0.97 (p<0.0001)	p=0.00049*	9.5 (3.61) mm	18 (6.8)	10 mm	19
iPAT vs pathology specimen ellipsoid Volume	0.98 (p<0.0001)	p=0.052	-3.29 (4.54) cm^3	14 (19)	-2.43 cm^3	10

*Indicates significant difference

The regression analysis resulted in four scatter plots depicting the correlation of volumetric and maximum-diameter measurements by pathology and DCE-MRI, to measurements by iPAT. Also, correlation between DCE-MRI and pathology measurements was examined. Figure 3.4(a-d) shows the plots along with a line of best fit and the associated 95% confidence intervals.

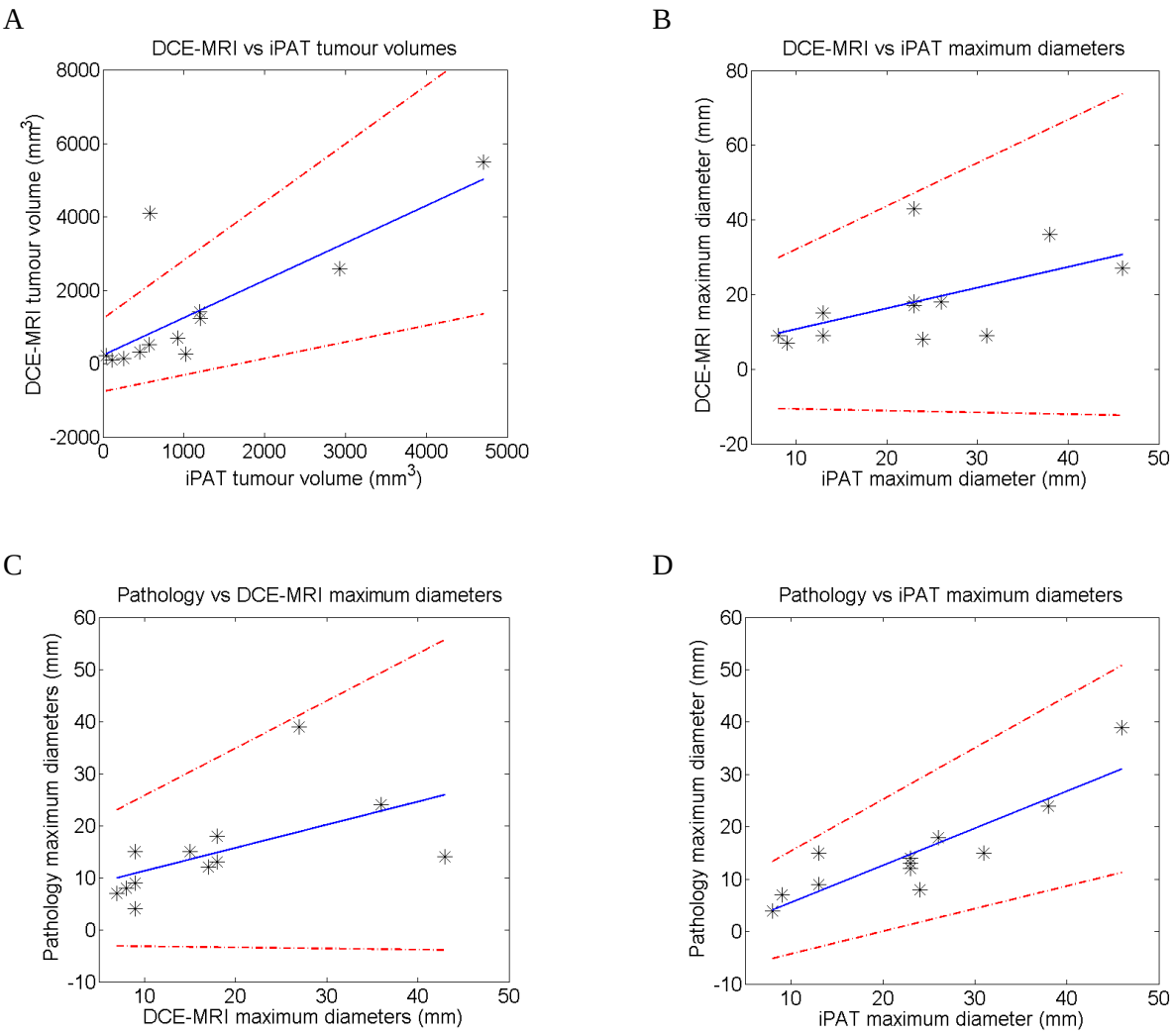

Figure 3.4. Regression analysis and scatter plots with line of best fit (blue) and 95% confidence intervals (red dashed) for comparing volumes (A) and maximum diameters (B, C and D) measured by iPAT, pathology and DCE-MRI.

3.3.5 Tumor-contrast spectral dependence

Figure 3.5 includes slices selected for contrast comparison of tumor and normal tissue types, as well as corresponding US and X-ray images, where available. The figure represents a lumpectomy containing a pathologically-measured 30-mm diameter IDC tumor, described by the pathologist as centrally located within the specimen. The location of the tumor is confirmed in the US image, however, the extent of the tumor is significantly underestimated. Also indicated are areas that were used to sample tumor and

normal tissue. When considering the normal tissue area in Figure 3.5, note the exclusion of shadow-artefact, seen in the image as a hypo-intense area surrounding the specimen. Furthermore, the excluded area in Figure 3.5 also included incidental lymphatic tracer excitation, seen in the 690 nm image as a hyper-intense region near the bottom-right. This effect was caused by the close spectral proximity of the 690 nm laser used during the iPAT scan to the 670 nm peak absorption wavelength of the lymphatic tracer dye (Methylene blue) used during sentinel lymph node excision.

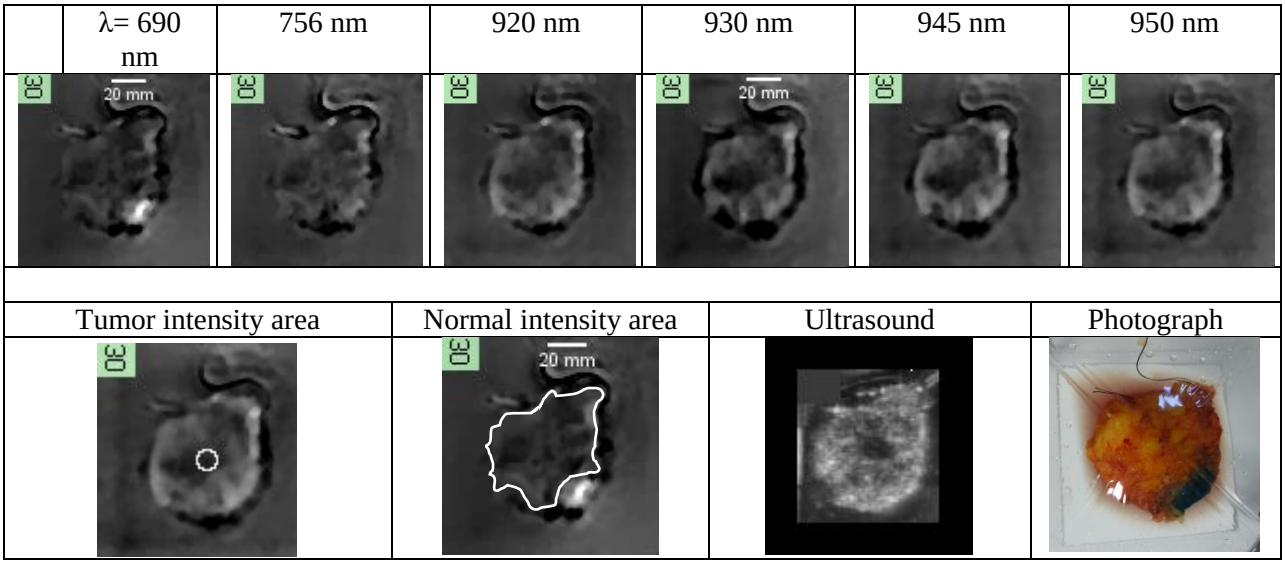

Figure 3.5. (Top row) Representative slices taken from stacks of a specimen containing a 30 mm diameter centrally located IDC, acquired at the 6 indicated wavelengths. (Bottom row) Segmented areas showing how tumor area and normal area were defined. 6.6 MHz specimen US is included for reference showing the centrally located hypo-intense suspicious lesion. The photograph indicates the orientation sutures as well as the lymphatic system tracer at the bottom right.

Figure 3.6 depicts a specimen that was described by the pathologist as containing an 18 mm-diameter IDC with a radioactive I-125 seed embedded within the tumor. The seed is clearly visualized in the x-ray image. The tumor can also be seen on the x-ray slide, and to a limited extent, in the US slice.

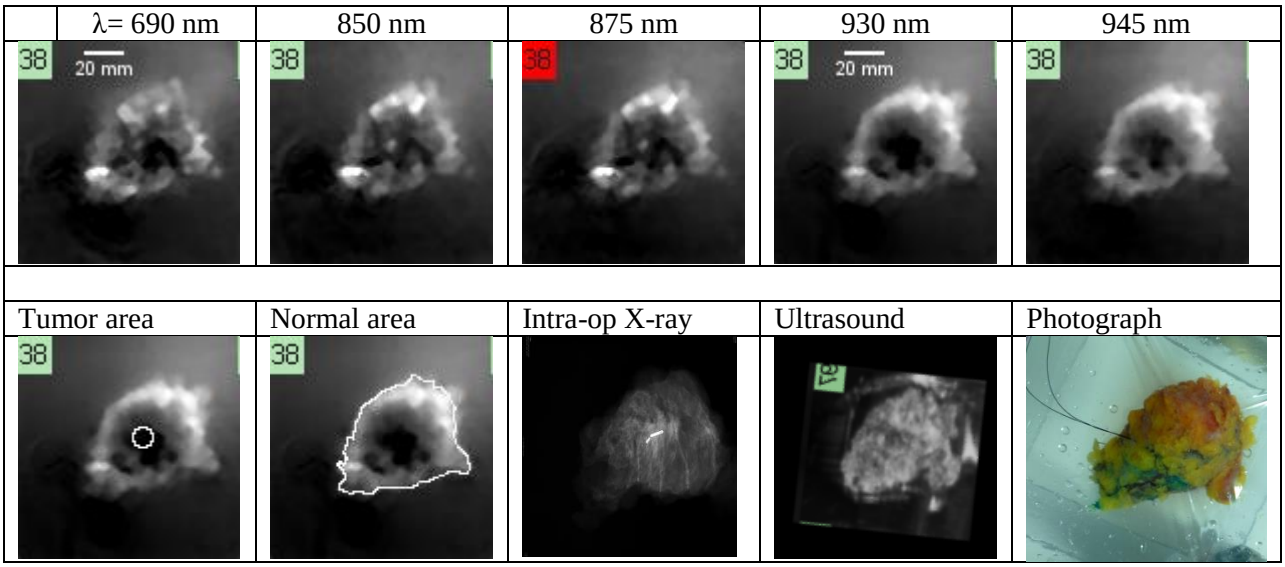

Figure 3.6. Multispectral iPAT results similar to Figure 3.5, but for a specimen containing an 18 mm diameter IDC, acquired at the 5 indicated wavelengths. The top row shows the effect of different illumination wavelengths on the visualization of the tumour, which is assumed to be the centrally located hypo-intense area. The bottom row indicates how the normal tissue area and the tumour area were defined. Here an intraoperative X-ray image of the specimen is also included showing the radioactive localization seed, centrally coinciding with the suspicious lesion. The photograph shows the black orientation sutures as well as the lymphatic tracer dye (Methylene Blue)

Due to the hypo-intense nature of tumor tissue appearance in iPAT images, quantification of contrast according to Equation 1 was made in terms of absolute values. Figure 3.7 describes the relationship between tumor contrast and wavelength found from analysis of the selected IDC specimens. For the two lesions and selected wavelengths investigated, it was found that maximal tumor contrast occurred near a wavelength of 930 nm.

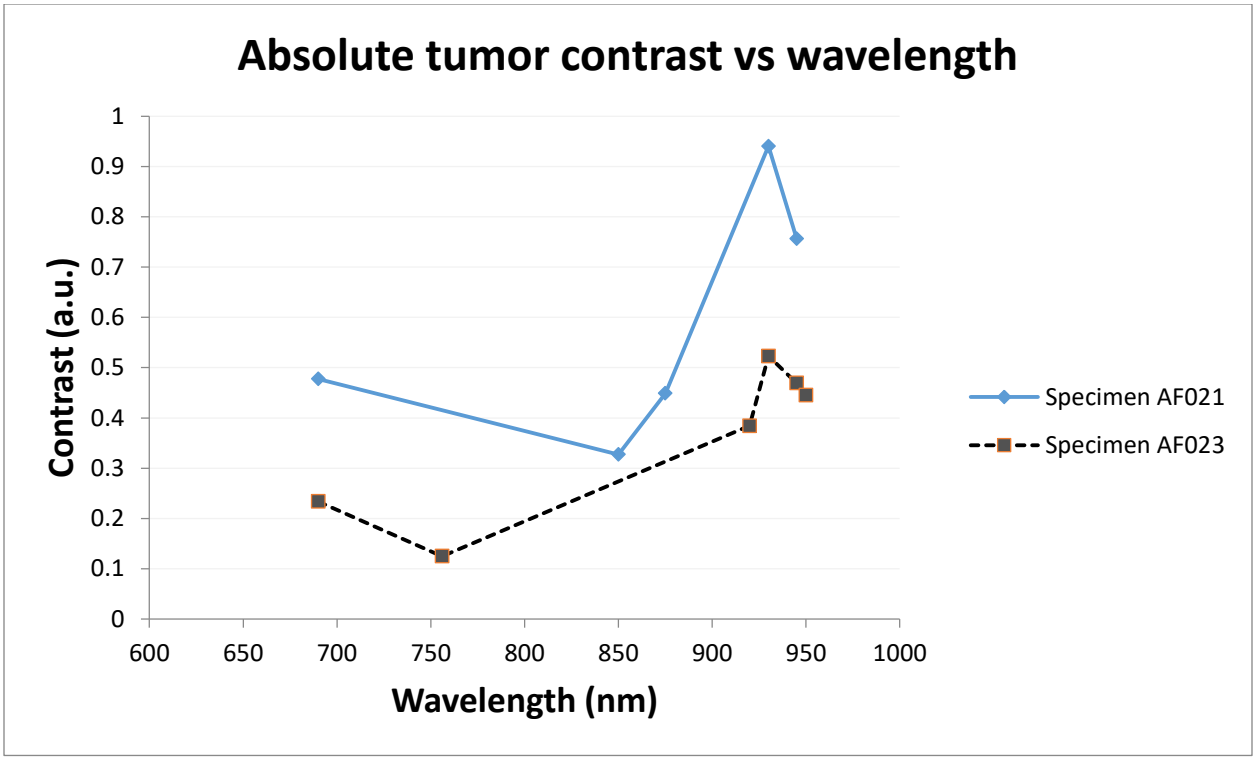

Figure 3.7. Absolute value of tumor contrast as a function of wavelength for two IDC specimens where contrast values were derived based on mean voxel intensity in predefined normal and tumour areas as described in Figures 3.5 and 3.6 and Equation 1. The measurements were taken at somewhat different wavelength intervals as limited time prevented a more comprehensive wavelength range to be used. Nevertheless, the two plots indicate that a wavelength of around 930 nm appeared to produce maximal contrast in both specimens.

3.3.6 Dependence of tumour contrast on breast density

IDC tumour in adipose breast tissue

A 53 year old patient presented with a palpable mass in the posterior-third lower inner quadrant of the left breast near the chest wall. Preoperative ultrasound examination showed a large (25 mm) hypo-intense region at the palpated location along with several indeterminate lesions. Bilateral DCE-MRI indicated a highly suspicious irregular enhancing mass at the same location measuring 27 mm in maximal dimension and a biopsy of the area confirmed an IDC diagnosis (BIRADS-6). The patient subsequently underwent BCS to remove the tumour. Intraoperative iPAT imaging of the excised specimen demonstrated a centrally located 46 mm-diameter hypo-intense mass while postoperative pathological examination

revealed a centrally located 39 mm-diameter grade 3 IDC tumour. Figure 3.8 summarizes MRI, US, and iPAT imaging findings and indicates the nature of the tumour bed for this case. Specifically, Figure 3.8(a) shows a pre-contrast T1-weighted MRI acquisition without fat subtraction indicating the non-dense adipose breast in bright white and the dense fibro-glandular tissue as dark gray. On the other hand, Figure 3.8(b) shows the same view acquired using a DCE-MRI sequence indicating contrast enhancement in bright white. While the breasts appear heterogeneously dense, the tumour bed location in this case coincided with mostly non-dense adipose tissue making the visualization of the hypo-intense lesion (yellow rectangle in 3.8(a)) possible without contrast dynamics. Alternatively, the tumour is clearly visualized as hyper-intense on the DCE-MRI acquisition image of Figure 3.8(b). These findings were found to be concordant with iPAT and US results shown on a larger scale in Figure 3.8(d) and 3.8(e), co-oriented to the MRI images. For reference a magnified image of the pre-contrast MRI and a photograph of the freshly excised specimen are included in Figures 3.8(c) and 3.8(f).

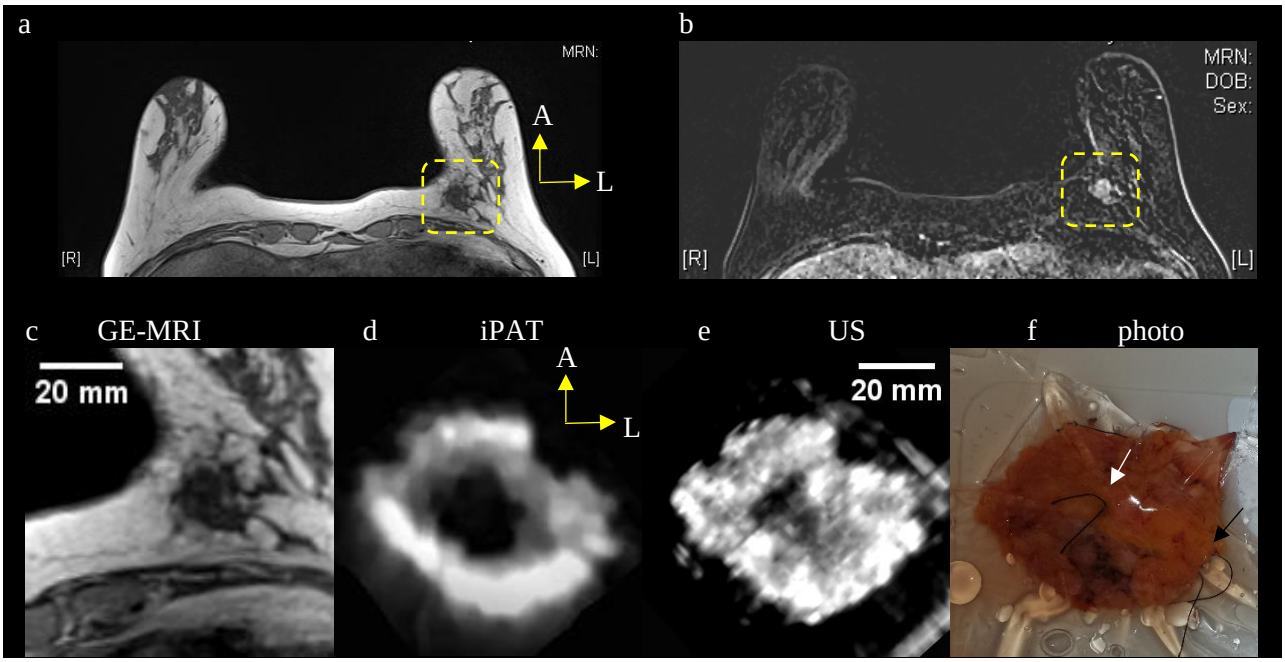

Figure 3.8. (a) Bilateral T1w pre-contrast GE-MRI without fat suppression and (b) DCE-MRI in axial view showing biopsy confirmed 39 mm IDC in the posterior-third lower inner quadrant of the left breast near the chest wall (yellow dashed box) as well as yellow orientation arrows indicating the anterior (A) and lateral (L) directions. (c) Zoomed in view of the T1w pre-contrast acquisition without fat subtraction showing tumor region coinciding with mostly bright fatty tissue, which makes the triangular tumour margins straight forward to delineate without contrast dynamics. (d) Selected co-oriented 930 nm iPAT slice showing the same triangular tumour with good contrast at all margins. (e) Co-registered 6.6 MHz US slice again showing the triangular tumour with good contrast. (f) Photograph of the freshly excised specimen showing the superior orientation suture (white arrow) and the lateral suture (black arrow). Note that for convenient referencing, the photograph has been digitally mirrored, or flipped, left-to-right.

IDC tumour in fibro-glandular breast tissue

Figure 3.9 is a representative case of tumour visualization when the tumour bed consisted of dense fibro-glandular tissue. A 53 year old patient presented with mammographic calcifications which subsequently resulted in a biopsy proven right-sided high-grade DCIS diagnosis (BIRADS-6). To rule out invasive component a bilateral DCE-MRI study was performed. The radiologist noted heterogeneous breast density, as depicted in Figure 3.9(a), along with marked background parenchymal enhancement (BPE). BPE is known to reduce the accuracy of image interpretation and can be appreciated in Figure 3.9(b). Nevertheless, a 17 mm diameter enhancing lesion whose location coincided with the area of mammographic calcifications was identified (yellow rectangle) as highly concerning for invasive carcinoma. Excision with radioactive seed localization was recommended and the patient subsequently underwent BCS. Intraoperative specimen US, shown in Figure 3.9(e), failed to identify a concerning

abnormality. On the other hand, iPAT of the specimen, depicted in Figure 3.9(d), indicated an irregular shaped hypo-intense lesion measuring 23 mm in maximum dimension seen approaching the anterior margin of the specimen (black arrow). Furthermore, the iPAT detected lesion was found to be located concordantly with the calcifications (black arrow) seen in the co-oriented intraoperative X-ray image of Figure 3.9(c). Figure 3.9(c) also indicates the location of the localization seed (white arrow). Postoperative pathological examination confirmed the presence of a lesion consisting of a grade 2 IDC measuring 12 mm in diameter, along with grade 3 DCIS exhibiting extensive intraductal component (EIC). Intriguingly, the pathologic examination was also found to be concordant with the iPAT results as it identified the lesion location as closest (3 mm) from the anterior margin of the specimen. For orientation purposes, a photograph of the co-oriented specimen is included in Figure 3.9(f) indicating the lateral suture (black arrow) and the superior suture (white arrow).

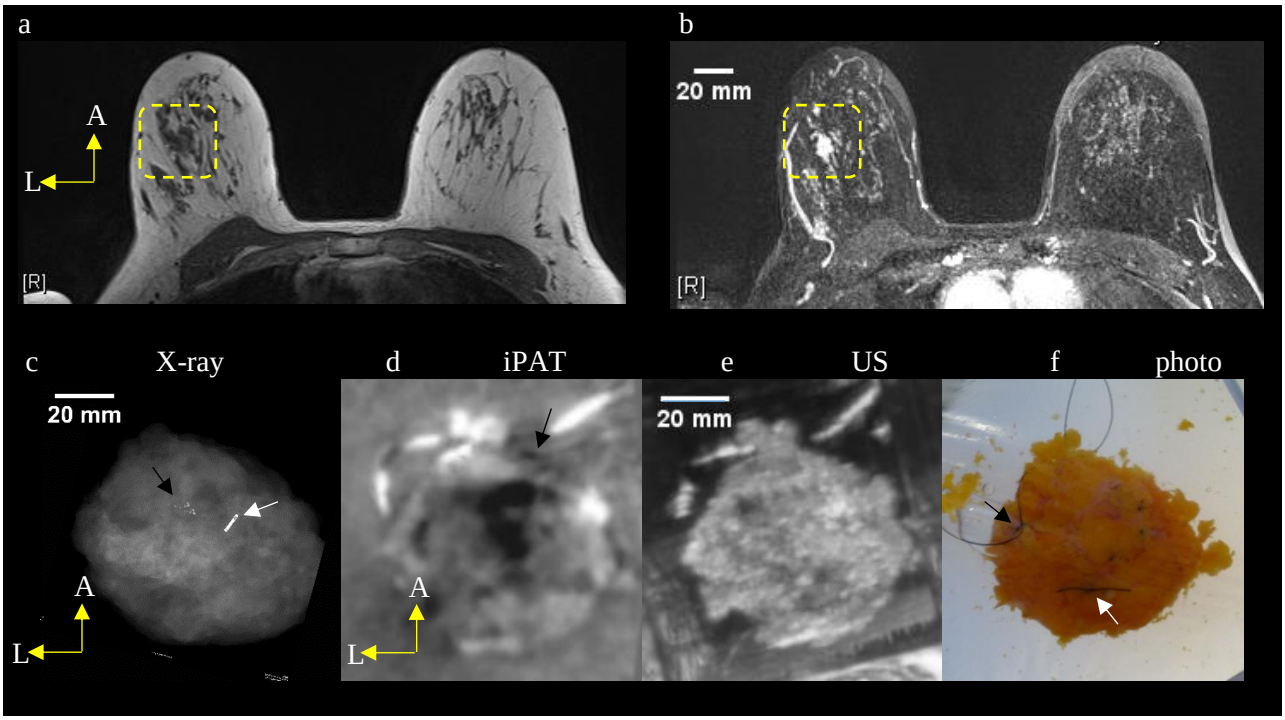

Figure 3.9. (a) Bilateral T1w pre-contrast without fat suppression and (b) DCE-MRI in axial view showing biopsy confirmed 12 mm grade 2 IDC with accompanied DCIS and EIC in the right breast (yellow dashed box) as well as yellow orientation arrows indicating the anterior (A) and lateral (L) directions. Due to the dense breasts, the tumour is difficult to delineate without contrast dynamics in (a) as it is contiguous with dense fibro-glandular tissue visualized as dark gray. (c) Co-oriented intraoperative transmission X-ray image of the specimen showing the radioactive localization seed (white arrow) along with an area of suspicious calcifications (black arrow). (d) Selected co-oriented 930 nm iPAT slice showing the hypo-intense tumour with good contrast approaching the anterior margin (black arrow) as indicated by postoperative pathologic examination. (e) Co-registered 6.6 MHz US slice failing to visualize any suspicious abnormality at the pathologically confirmed location of the lesion. (f) Photograph of the freshly excised specimen showing the superior orientation suture (white arrow) and the lateral suture (black arrow). Note that for convenient referencing, the photograph has been digitally mirrored, or flipped, left-to-right.

Table 3.5 lists the ACR BI-RADS ATLAS classification of breast tissue density, encountered in this study, and the same categories have been adopted for the corresponding pathological description. Table 5 also shows a breakdown of the DCE-MRI background parenchymal enhancement levels. While the pathological description corresponded to the limited breast tissue volume of the excised specimen, a good agreement was found with MRI, which described the entire breast. MRI breast density was extreme in 4 cases, while pathologic description indicated extreme density in 3 cases. Heterogeneous density was found to be present in 6 and 5 cases for MRI and pathology, respectively. Pathology indicated the remaining 4 specimens to be either mostly fatty or scattered fibro-glandular, while MRI found this for the

remaining 2 cases. Background parenchymal enhancement was minimal or mild in 9 cases, moderate in 1 case and extreme in the remaining 2 cases.

Table 3.5. Breast composition according to pathology and MRI. Also, level of background parenchymal enhancement in DCE-MRI is indicated.

Breast density/Background enhancement level	Density MRI	DCE-MRI Background enhancement	Density Pathology
Almost entirely fat/minimal	0	5	3
Scattered fibro-glandular tissue /mild	2	4	1
Heterogeneous fibro-glandular tissue/moderate	6	1	5
Extreme fibro-glandular tissue/marked	4	2	3

3.4 Discussion and future directions

3.4.1 Comparison of breast tumor measurements by iPAT, DCE-MRI and pathology

This investigation showed a significant and positive correlation ($r = 0.78$, $p = 0.003$) between volumetric assessment of tumors by iPAT and DCE-MRI, as seen in Table 3.4. The non-parametric Wilcoxon signed-ranked test showed no significant difference between the two measurements ($p = 0.97$). On the other hand, unidimensional maximum diameter measurements were found to be overestimated by 5.1 ± 10.1 mm on iPAT, although still significantly positively correlated to DCE-MRI. A similar trend was seen in comparison to unidimensional pathologic measurements, where correlations were positive but sizes were significantly overestimated. The average 3.2 ± 10.1 mm overestimation of tumor size on DCE-MRI compared to pathology is not unique and well documented in literature[15,16,27]. The leading theory for the overestimation by DCE-MRI is related to the lack of inclusion of DCIS components as part of standard pathologic measurements of breast tumors. The problem is further compounded by difficulty

in differentiating DCIS from IDC with current medical imaging technology. This study, being retrospective in nature, did not include special instructions to collect more detailed information on DCIS tumors. This is unfortunate because the maximum tumor diameter overestimate, found on both DCE-MRI and iPAT, is likely at least partially due to DCIS. Having DCIS size information would have allowed iPAT effectiveness for DCIS assessment to be estimated, and therefore, future studies focused on DCIS should ensure that detailed pathologic measurements are taken.

Tumor grade and receptor status was not found to significantly affect iPAT imaging findings or appearance. However, the two specimens found to contain extensive intra-ductal component, did appear to have many heterogeneously scattered focal hypo-intensities. This made tumor measurements somewhat difficult, compared to almost all other cases, and resulted in an above average overestimation of size by iPAT and DCE-MRI, compared to pathologic size.

3.4.2 Effect of lumpectomy holder on measurements

While the overestimate of maximum tumor diameters by iPAT versus pathology is partially explained by the lack of inclusion of DCIS, it does not explain the average 5.1 mm overestimate of diameters on iPAT compared to DCE-MRI. However, a compelling case can be made by considering the method by which the specimen was immobilized inside the iPAT scanner. The specialized lumpectomy specimen holder, that was used to restrain the samples, applied significant compressive pressure on the specimens. This had the effect of flattening out the samples, making them noticeably thinner, vertically, as well as wider, horizontally. Motivated similarly to x-ray mammographic breast compression, this method of sample immobilization is well suited to iPAT because it allows greater laser fluence to reach inside the thinner compressed specimen compared to an uncompressed specimen. Unfortunately, compression may skew non-volumetric unidimensional measurement results, due to specimen deformation, making maximum diameter correlations biased.

To establish a measure of specimen and tumor deformation, three orthogonal diameter measurements and associated ellipsoid volumes were calculated using pathologic and iPAT/US data. Similarly, to tumor maximum diameters, the resulting specimen maximum diameters were also positively correlated but significantly different. In fact, specimen maximum diameters were overestimated by an average 9.5 ± 3.6 mm, while ellipsoid volumes were not significantly different, a trend also seen with the tumor measurements tabulated in Table 3.4. Therefore, a reasonable explanation is that at least part of the specimen deformation, caused by the compressive nature of the lumpectomy holder, was imparted to the lesions contained within. This finding is not entirely new as mammographic and photoacoustic compression paddles, as well as MRI breast coils, have been blamed for tumor measurement discrepancies in previous studies[5,19,28]. Furthermore, the shape of specimens in the present investigation was likely even more affected by the compression of the holder because less tissue was present surrounding the tumor compared to *in-vivo* cases. In fact, the goal of BCS is to remove a minimum amount of surrounding normal tissue in order to achieve good cosmetic outcomes. With less tissue to cushion the compression of the holder, even more deformation should be expected, making the present investigation particularly vulnerable to systematic bias.

3.4.3 Participant and lesion characteristics

The selected participants in this first-of-a-kind investigation were not representative of an average breast cancer patient population. The most common reason for MRI examination in these cases was either occult nature of tumor on US and mammography, or generally ambiguous findings due to dense breasts. This is reflected in the low mean (49.5 years) and median (50 years) age of the participants. Compared to the full 100 participant cohort in our intraoperative study, the average age for the group reported here was approximately 10 years lower. For these reasons it is not surprising that the average breast density associated with the participants in this investigation was significantly higher, compared to a normal population. In fact, 10 out of 12, or 83%, of the participants had heterogeneous or extreme fibro-

glandular tissue. This is much higher than an average of 50% encountered in the normal population[29]. Furthermore, 75%, or 9 out of 12 invasive cancer cases studied contained *in-situ* components, which were not included in pathologic measurements, as per current standard of care. These statistics indicate that the cases are likely more challenging than what would be expected of the general population. Therefore, interpretation of the results should be made with these differences in mind.

3.4.4 Image reconstruction and processing

The specificity of iPAT is owed in large part to the relative quantification of dominant tissue chromophores, extracted from deep tissue via the photoacoustic effect. Filtered back-projection was found to be an efficient image reconstruction method to estimate the chromophore distribution inside the specimens. However, the limited aperture effect, which often plagues PAT results, likely distorted the true chromophore distribution due to the absence of sensors at key points[30,31]. We found that the K-wave image improvement method, described above, could at least partially restore voxel amplitudes in areas where intensity varied in a non-physical manner. The result was a smoother and more cohesive appearance of tumours. This can be appreciated in Figure 3.2 where the tumour-edge is significantly clearer in the K-wave improved image. The effect is especially noticeable in the transmission-mode image, which is consistent with the fact that the transmission mode side of the imaging volume is further out of the effective signal detection region. The improved images were found to better agree with correlated x-ray and US findings, and were easier to segment. The segmentation was further aided by use of a median filter, which is often invoked in US image processing because of its ability to smooth out speckle noise while preserving boundary features.[32]

The benefit of K-wave iterative image improvement on the imaging results of this study indicated that detector coverage was sub-optimal. While the method was able to partially mitigate transducer detection gaps by estimating forward model pressure measurements over a fully enclosing detection surface using time reversal, it was unable to provide any additional information. To minimize missing information

caused by aperture deficits, future investigations using PAT should pay close attention to scanning geometry and transducer detection coverage.

3.4.5 Shadowing artefacts

The vertical bidirectional illumination geometry, combined with an effectively hemispherical detection scheme, resulted in what can be considered a combination transmission/reflection/orthogonal mode image volume. It was important that image analysis and segmentation took this information into account, particularly near the edges of the specimen. Analogous to *acoustic shadowing* and *edge shadowing* artefacts in ultrasonography, sharp illumination gradients associated with iPAT imaging may also cause shadowing artefacts.[33] For example, in the case of the IDC shown in Figure 3.2, the transmission-mode panels show a hypo-intense band running along the top of the specimen. These shadow-like effects can interfere with the visualization of tumors, which also present as hypo-intense volumes. In cases where the tumor was abutting the margins, or was otherwise located peripherally, this interference caused the edges of the specimen to be difficult to delineate from the tumors. In this study, we partially overcame this difficulty by collecting co-registered US images to define the edges of the specimens prior to tumor segmentation. This approach was particularly useful in one case where a positive margin was detected on pathology. Nevertheless, if the shadowing artefacts were mistaken for tumour tissue, the delineation problem could still arise even with specimen edges predefined by US. However, notice the lack of shadowing artefacts in the reflection-mode image of the same IDC in Figure 3.2. More generally, we found that transmission mode iPAT imaging was prone to shadowing, while reflection mode appeared artefact-free. This points to a seemingly simple solution, but more investigation is needed to establish the superiority of reflection-mode iPAT, especially as it pertains to imaging depth and sensitivity of tumour imaging.

3.4.6 Breast density dependence

Our results indicated that tumour tissue may be distinguished from normal breast tissue using iPAT. The mechanism underlying this contrast difference was hypothesized to be due to the relatively low optical absorption coefficient of malignant tissue and subsequent hypo-intense imaging appearance on scans near a wavelength of 930 nm. However, a wavelength of 930 nm has been shown to be strongly absorbed by bulk-lipid, or, fat-containing tissue.[34] A possible concern with this inference, therefore, was that the hypo-intense regions in iPAT images were volumes of the breast with relatively low-fat content, and as such may simply have represented dense non-fatty fibro-glandular tissue. Indeed, dense fibro-glandular tissue is also often blamed for sensitivity and specificity deficits in conventional imaging methods, such as ultrasound and mammography, and are often overcome only by use of dynamic contrast enhancement in MRI.[12,15] It was therefore hypothesized that tumours which are visible on iPAT simply due to surrounding fat tissue should also be seen as surrounded by fat, visualized as hyper-intense on T1 weighted pre-contrast MRI. This situation is exemplified by the case in Figure 3.8. Surprisingly however, inspection of Figure 3.9 reveals that this may not always be the case, since a significant portion of that IDC was embedded in dense fibro-glandular tissue and was only delineated by use of dynamic contrast enhancement. Since most of the cases in this study involved relatively dense breasts, as seen in Table 3.5, the ability of iPAT to successfully visualize highly localized hypo-intense volumes with good contrast, hints at the independence of iPAT and breast density. Finally, the photoacoustic mammography, or PAM, study by Manohar et al. also reached the same conclusion, i.e. the optical contrast in PAT is largely independent of tissue density.[19]

3.4.7 Tumor-contrast spectral dependence

Figure 3.7 indicates that maximum apparent tumor contrast on iPAT scans occurs near a wavelength of 930 nm. As discussed above, this wavelength corresponded to the strong absorption band by fat, and

apparently, healthy fibro-glandular breast tissue. Therefore, the contrast mechanism came about by enhancement of non-malignant volumes, leaving tumours hypo-intense. However, beyond using 690 nm and 930 nm to map hemoglobin and lipids in lumpectomies, other wavelengths may offer further cancer relevant contrast. For example, the firm and fibrous tissue that is often associated with palpable tumour lumps, is known to contain elevated concentrations of water and collagen, both of which exhibit unique spectral features in the infrared wavelength range from about 900 nm to 1300 nm. Therefore, careful selection of key wavelengths in this range may offer further differentiation capability.

Interestingly, both lesions under the multispectral study had present within them volumes that were hypo-intense at multiple wavelengths. Even the deoxy-hemoglobin-sensitive wavelengths of 690 nm and 756 nm contained hypo-intense areas, some of which were contiguous with the tumor. These findings indicated that some malignant tissue may present as hypo-intense only on lipid-weighted 930 nm imaging, while other malignant tissue presents as hypo-intense on both 930 nm and hemoglobin-weighted 690 nm imaging. The heterogeneity of tumor areas, imaged at different wavelengths, indicates underlying compositional complexity, and this highlights the importance of multispectral assessment in furthering our understanding of the tumour environment.

3.5 Conclusion

This investigation presented a comparison of breast tumor size by intra-operative iPAT, pre-operative DCE-MRI and post-operative pathology. The strong positive correlations of up to $r = 0.78$ that were found between iPAT and other modalities as well as pathology provided confidence that iPAT has utility for imaging during breast surgery. We found that volumetric tumor measurements were more reliable than unidimensional measurements, echoing previous studies with established medical imaging technologies. These findings open a new window and a fresh perspective on malignancy visualization and assessment. Compelling future research directions were highlighted by brief examination of the nature of breast tumor contrast in iPAT, and its dependence on illumination wavelength. Finally, perhaps

the most impactful aspect of this investigation may be the apparent independence of iPAT tumour contrast and breast density. This finding implies that a breast imaging system based on iPAT technology may offer fast and safe high-contrast tumour visualization at low cost and without the need for contrast agents or ionizing radiation exposure. In addition to intraoperative applications, highlighted here, the potential impact of such technology on breast screening programs as well as preoperative imaging is significant.

3.6 References

1. Siegel RL, Miller KD, Jemal A. Cancer Statistics , 2015. *CA Cancer J Clin*. 2015;65(1):5-29. doi:10.3322/caac.21254.

2. Yaffe MJ, Bloomquist AK, Hunter DM, et al. Comparative performance of modern digital mammography systems in a large breast screening program Comparative performance of modern digital mammography systems in a large breast screening program. *Med Phys*. 2013;40(112):121915. doi:10.1118/1.4829516.

3. Balleyguier C, Ayadi S, Van Nguyen K, Vanel D, Dromain C, Sigal R. BIRADS??? classification in mammography. *Eur J Radiol*. 2007;61(2):192-194. doi:10.1016/j.ejrad.2006.08.033.

4. Tardivon AA, Athanasiou A, Thibault F, El Khoury C. Breast imaging and reporting data system (BIRADS): Magnetic resonance imaging. *Eur J Radiol*. 2007;61(2):212-215. doi:10.1016/j.ejrad.2006.08.036.

5. Yang WT, Lam WWM, Cheung H, Suen M, King WWK, Metreweli C. Sonographic, magnetic resonance imaging, and mammographic assessments of preoperative size of breast cancer. *J Ultrasound Med*. 1997;16(12):791-797. http://www.scopus.com/inward/record.url?eid=2-s2.0-0000202613&partnerID=tZOtx3y1.

6. Ananthakrishnan P, Balci FL, Crowe JP. Optimizing Surgical Margins in Breast Conservation. *Int J Surg Oncol*. 2012;2012. doi:10.1155/2012/585670.

7. Hargreaves AC, Mohamed M. Intra-Operative Guidance : Methods for Achieving Negative Margins in Breast Conserving Surgery. *J Surg Oncol*. 2014;110(1):21-25. doi:10.1002/jso.23645.

8. Gu Y-L, Pan S-M, Ren J, Yang Z-X, Jiang G-Q. Role of Magnetic Resonance Imaging in Detection of Pathologic Complete Remission in Breast Cancer Patients Treated With Neoadjuvant Chemotherapy: A Meta-analysis. *Clin Breast Cancer*. 2017. doi:10.1016/j.clbc.2016.12.010.

9. Groheux D, Cochet A, Humbert O, Alberini J-L, Hindié E, Mankoff D. 18F-FDG PET/CT for Staging and Restaging of Breast Cancer. *J Nucl Med*. 2016;57 Suppl 1:17S-26S. doi:10.2967/jnumed.115.157859.

10. Eisenhauer EA, Therasse P, Bogaerts J, et al. New response evaluation criteria in solid tumours: Revised RECIST guideline (version 1.1). *Eur J Cancer*. 2009;45(2):228-247. doi:10.1016/j.ejca.2008.10.026.

11. Waljee JF, Hu ES, Newman LA, Alderman AK. Predictors of Re-excision among Women Undergoing Breast-Conserving Surgery for Cancer. *Ann Surg Oncol*. 2008;15(5):1297-1303. doi:10.1245/s10434-007-9777-x.

12. Bosch AM, Kessels AGH, Beets GL, et al. Preoperative estimation of the pathological breast tumour size by physical examination, mammography and ultrasound: A prospective study on 105 invasive tumours. *Eur J Radiol*. 2003;48(3):285-292. doi:10.1016/S0720-048X(03)00081-0.

13. Weir L, Worsley D, Bernstein V. The value of FDG positron emission tomography in the management of patients with breast cancer. *Breast J*. 2005;11(3):204-209. doi:TBJ21625 [pii]\r10.1111/j.1075-122X.2005.21625.x.

14. Schaefgen B, Mati M, Sinn HP, et al. Can Routine Imaging After Neoadjuvant Chemotherapy in Breast Cancer Predict Pathologic Complete Response? *Ann Surg Oncol*. 2015;23(3):789-795. doi:10.1245/s10434-015-4918-0.

15. Gruber I V, Rueckert M, Kagan KO, et al. Measurement of tumour size with mammography, sonography and magnetic resonance imaging as compared to histological tumour size in primary breast cancer. *BMC Cancer*. 2013;13(June 2005):328. doi:10.1186/1471-2407-13-328.

16. Menezes GL, Knuttel FM, Stehouwer BL, Pijnappel RM, van den Bosch MA. Magnetic resonance imaging in breast cancer: A literature review and future perspectives. *World J Clin Oncol*. 2014;5(2):61-70. doi:10.5306/wjco.v5.i2.61.

17. Manohar S, Vaartjes SE, van Hespen JCG, et al. Initial results of in vivo non-invasive cancer imaging in the human breast using near-infrared photoacoustics. *Opt Express*. 2007;15(19):12277-12285. doi:10.1364/OE.15.012277.

18. Kruger RA, Kuzmiak CM, Lam RB, et al. Dedicated 3D photoacoustic breast imaging Dedicated 3D photoacoustic breast imaging. *Med Phys*. 2013;40(11):113301. doi:10.1118/1.4824317.

19. Heijblom M, Piras D, van den Engh FM, et al. The state of the art in breast imaging using the Twente Photoacoustic Mammoscope: results from 31 measurements on malignancies. *Eur Radiol*. 2016;26(11):3874-3887. doi:10.1007/s00330-016-4240-7.

20. Ermilov S a., Khamapirad T, Conjusteau A, et al. Laser optoacoustic imaging system for detection of breast cancer. *J Biomed Opt*. 2009;14(2):24007. doi:10.1117/1.3086616.

21. Wang L V, Hu S. Photoacoustic Tomography : In Vivo Imaging from Organelles to Organs. *Science (80-)*. 2012;335(March):1458-1462.

22. Dogra VS, Chinni BK, Valluru KS, Joseph J V. Multispectral Photoacoustic Imaging of Prostate Cancer : Preliminary Ex - vivo Results. *J Clin Imaging Sci*. 2015;3(3):1-7. doi:10.4103/2156-7514.119139.

23. Kosik I, Carson JJL, Program I, Health L, Joseph S. Combined 3D photoacoustic and 2D fluorescence imaging of indocyanine green contrast agent flow. *Proc SPIE*. 2013;8581:1-8. doi:10.1117/12.2005269.

24. Xu M, Wang L V. Universal back-projection algorithm for photoacoustic computed tomography. *Phys Rev E*. 2005;71(1):16706. doi:10.1103/PhysRevE.71.016706.25. Treeby B, Cox B. Iterative Image Improvement Using Time Reversal. http://www.k-wave.org/documentation/example_pr_2D_tr_iterative.php. Published 2016.

26. CJ D, EA S, EB M, EA M. ACR BI-RADS® Atlas, Breast Imaging Reporting and Data System. *Am Coll Radiol*. 2013.

27. Lai H-W, Chen D-R, Wu Y-C, et al. Comparison of the Diagnostic Accuracy of Magnetic Resonance Imaging with Sonography in the Prediction of Breast Cancer Tumor Size: A Concordance Analysis with Histopathologically Determined Tumor Size. *Ann Surg Oncol*. 2015;(August 2014):3816-3823. doi:10.1245/s10434-015-4424-4.

28. El Khouli RH, Macura KJ, Kamel IR, Bluemke D a, Jacobs M a. The effects of applying breast compression in dynamic contrast material-enhanced MR imaging. *Radiology*. 2014;272(1):79-90. doi:10.1148/radiol.14131384.

29. Radiology AC of. Breast Density Breast cancer screening. https://www.acr.org/~/media/ACR/Documents/PDF/QualitySafety/Resources/Breast-Imaging/Breast-Density-bro_ACR_SBI_lores.pdf.

30. Yao L, Jiang H. Photoacoustic image reconstruction from few-detector and limited-angle data. *Biomed Opt Express*. 2011;2(9):2649. doi:10.1364/BOE.2.002649.

31. Paltauf G, Nuster R, Burgholzer P. Weight factors for limited angle photoacoustic tomography. 2011;54(11):3303-3314. doi:10.1088/0031-9155/54/11/002.Weight.

32. Shibin Wu, Qingsong Zhu, Yaoqin Xie. Evaluation of various speckle reduction filters on medical ultrasound images. *2013 35th Annu Int Conf IEEE Eng Med Biol Soc*. 2013:1148-1151. doi:10.1109/EMBC.2013.6609709.

33. Feldman MK, Katyal S, Blackwood MS. US artifacts. *Radiographics*. 2009;29(4):1179-1189. doi:10.1148/rg.294085199.

34. Anderson PG, Kainerstorfer JM, Sassaroli A, et al. Broadband optical mammography: Chromophore concentration and hemoglobin saturation contrast in breast cancer. *PLoS One*. 2015;10(3):1-23. doi:10.1371/journal.pone.0117322.

Chapter 4: Intraoperative photoacoustic imaging of breast cancer: a new perspective on malignancy visualization and surgical guidance

4.1 Introduction

This chapter presents results from a variety of diagnostic and intraoperative imaging modalities. A detailed discussion on this subject can be found in section 1.2.1.

The discussion below also includes assumed knowledge relating to current histopathological tissue examination standards as well as emerging intraoperative alternatives. Sections 1.2.4, 1.3.2, 1.3.3 and 1.4.4 provide a brief primer into these areas.

4.1.1 Overview

Breast cancer is a serious problem, especially for aging women and those with a family history of the disease. It represents nearly one quarter of new cancer cases in women. Estimates indicate that one in eight women will be affected by the disease during her lifetime and this is projected to be a major health care challenge in the future[1]. Nearly everyone will be either directly impacted, or will have family members who are. Incidence of breast cancer has been steadily rising over the past several decades, and this trend is expected to continue. In spite of this trend, receiving a diagnosis of breast cancer today often comes with a much better prognosis than in the past thanks to innovative treatment strategies and advances in medical science, particularly imaging[2].

Treating breast cancer is a complicated process, however almost all cases involve surgery[3]. A successful surgery depends on many factors. Ideally, the surgical team is equipped with state-of-the-art tools, allowing them to operate with precision and confidence. Amongst the most important of these are medical imaging systems such as mammography, ultrasonography (US) and dynamic contrast enhanced magnetic resonance imaging (DCE-MRI)[2,4–6]. These modalities provide the radiologist and surgeon with

critical information about the location and extent of disease. Consequently, medical imaging is instrumental in selecting the most appropriate therapy and surgical avenue, be it breast conserving surgery (BCS) or mastectomy.

Precision breast cancer imaging is becoming even more important in recent years due to the increasing popularity of BCS compared to more invasive procedures such as radical mastectomies. Large multicenter trials have been completed, catalyzing confidence in BCS by demonstrating comparable long-term disease recurrence rates to mastectomies, particularly in conjunction with advanced adjuvant and neo-adjuvant therapies[7,8]. However, BCS is fundamentally more challenging. The surgeon is charged with minimizing the volume of excised tissue while ensuring complete tumor excision. Finding the right balance is necessary to produce desirable cosmetic results in conjunction with minimal disease recurrence rates.

Placing a premium on breast conservation has also increased the demands on imaging versatility. For example, in cases of close areolar complex involvement, surgeons and radiologists are now more encouraged to consider nipple sparing procedures. By facilitating oncoplastic surgery, these procedures offer real benefits for the patient with the possibility of improving quality of life, particularly for younger women[9]. Since the areolar and retro-areolar region accounts for about 8 percent of breast cancers, this represents a considerable clinical problem[10]. Furthermore, due to the typically increasing ductal density near the nipple, this area of the breast challenges even the most advanced imaging methods. This is particularly problematic for conventional imaging modalities, such as mammography and US, which rely on density-based contrast. Often in these cases, DCE-MRI is used in the assessment; however, the areolar complex may still be problematic due to benign ductal enhancement caused by increased vascularity in this region. One DCE-MRI study of 427 lesions found that ductal enhancement was associated with benign findings in 55 percent of cases, and resulted in a positive predictive value (PPV) of only 26 percent[11]. Finally, the large prevalence of ductal carcinoma *in-situ* tumors (DCIS) mixed with invasive

ductal carcinoma (IDC) tumors means that imaging of ductal tissue represents a challenging clinical problem.

In light of these technological shortcomings it is perhaps not surprising that a statistical examination of success rates of BCS indicate that nearly one in four procedures fail to remove all malignant tissue[12,13]. Further complicating the situation is the fact that these failures are usually discovered post-operatively, at the pathology level. Typically, pathologic examination of a formalin fixed lumpectomy specimen is performed days after surgery. At that point in time, the discovery of tumor tissue at the edge of the specimen, referred to as a positive margin, means that the surgery must be repeated in order to achieve complete excision. Currently, repeat surgeries constitute a serious setback for patients due to extensive leave from employment, as well as emotional and physical hardship. In terms of health care administration, repeat surgeries negatively impact hospital resources, however, the associated delays in therapies and increased surgical wait times also negatively impact treatment efficacy.

The high monetary and personal burden of repeat surgeries is perhaps best highlighted by the recent increase in adoption of the more relaxed "no-ink-on-tumor" definition of a clear margin[14]. The new definition means that it is now considered sufficient for there to be a single layer of normal cells between the tumor and margin. While this new standard has reduced re-excision rates due to close margins by almost 14 percent, it throws into question whether there will be any associated effect on long term recurrence rates[14]. On the one hand, recent meta-analysis studies assessing the new guideline show acceptable disease control as long as radiation therapy is administered[15]. However, adopting such narrow margins on the surgical side in conjunction with errors arising from under-sampling on the pathology side may result in an increase in undetected disease remaining near the post-surgical cavity. This outcome could prove problematic due to the theoretically increased radiation-therapy resistance of aggressive tumour cells within the typically hypoxic environment of the lumpectomy scar bed[16]. Finally, breast radiation therapy is associated with negative side-effects, morbidity, and in cases of small low-grade tumours as well as DCIS lesions, no significant improvement in survival compared to radiation-free

BCS[17,18]. Alternatively, studies show that advanced oncoplastic techniques aided by pre-operative and intra-operative imaging can produce similar ipsilateral recurrence rates without the use of radiation therapy[18,19]. Therefore, eliminating at least some post-operative radiation treatments via high-precision malignancy visualization could translate to a better BCS experience for the patient without sacrificing long term results.

The reasons outlined above indicate that technological improvement is needed on two fronts. First, radiologists and surgeons are in need of better pre-operative malignancy visualization systems, allowing them to quickly assess the position and extent of breast lesions with high sensitivity and specificity. A strong contender would ideally offer visualization in 3-dimensions and be independent of tissue density as well as lesion type and location. Its implementation in the pre-surgical work-up would likely significantly reduce rates of positive margins. The second improvement can be thought of as a last line of defense against failed surgeries. It would implement a lumpectomy margin assessment system within the intra-operative setting. The actionable information, provided by the system in real-time, would allow the surgeon to intervene prior to patient discharge, thereby sparing them a second procedure.

The needs of clinical pre-operative malignancy visualization are currently addressed in practice by the medical imaging systems discussed above. However, some cases of advanced disease or ambiguous findings indicate that unique information provided by other modalities may be useful. These include Positron Emission Tomography (PET) and Computed Tomography (CT), as well as hybrid varieties such as PET-CT and PET-MRI. The strengths and weaknesses of these systems have been extensively discussed, but briefly put, sensitivity and specificity deficits remain, especially related to breast density and small (< 2 cm) tumour size [5,20-22]. In terms of intra-operative margin assessment, there are numerous possible approaches. Many of these are based on the same familiar imaging modalities, such as X-ray (Faxitron), US and MRI, meaning that they suffer similar shortcomings[23–26]. Others, such as frozen sectioning, contact cytology and radiofrequency spectroscopy have been shown to be somewhat effective but are considered too labour intensive and time consuming by most busy surgical centers[27,28].

However, because part of the goal of intraoperative lumpectomy assessment is to examine the surface of the excised specimen, optical imaging systems offer unique opportunities. Optical imaging methods include Raman spectroscopy, autofluorescence spectroscopy, optical coherence tomography (OCT) and diffuse reflectance spectroscopy[29–33]. Once again, these methods have been previously discussed, and it was demonstrated that in differentiating normal tissue from malignancy, optical contrast produced superior sensitivity and specificity values. In spite of these successes, limitations in either resolution or imaging depth have prevented optical-based systems from enjoying wide-spread adoption.

A highly promising approach, called Photoacoustic Tomography (PAT), capable of overcoming these limitations by ultrasonically encoding optical contrast from deep tissue, has been described in a number of studies[34–37,38–41]. PAT is a hybrid optical-acoustic imaging method used to interrogate soft tissues to a depth of several centimeters. The imaging procedure typically begins with pulsed laser illumination of a tissue sample, resulting in absorption of light within the tissue. The absorption leads to the emission of an acoustic wave via the photoacoustic effect. Finally, the time-resolved intensity of the acoustic wave can be detected by US transducers surrounding the sample. Such measurements can be used with a number of image reconstruction methods to generate a 2D or 3D image. Of particular significance, PAT images appear to be insensitive to breast tissue density[42]. To our knowledge, one study of lumpectomy assessment via PAT has been carried out to date[43]. However, the study involved extensive sample preparation, including formalin fixation, and therefore was not realistic with respect to real-time intraoperative surgical guidance. Also, that investigation used a detection scheme permitting only a few mm of imaging depth, and hence failed to visualize complete lesions. Here we show for the first time that high contrast visualization of whole tumors within freshly excised specimens is feasible in a clinical setting via PAT imaging. Studies showing low 10 year recurrence rates of 2.8 % when intraoperative ultrasonography was combined with wide excision, motivated this investigation to be carried out in the setting of intraoperative breast abnormality assessment and lumpectomy margin evaluation[44]. We present intraoperative PAT imaging from 100 patients who underwent BCS.

4.1.2 Objectives

This report summarizes results of a 100-patient pilot study aimed to investigate the capabilities of a PAT-based imaging system, which we dubbed intraoperative Photoacoustic Tomography (iPAT). By comparing iPAT derived results to pathology, this study aims to estimate the accuracy of iPAT with respect to breast tumour sizing and localization within freshly excised specimens. Furthermore, we present a case study example of areolar-complex invasion, and compare the performance of iPAT to conventional US. Similarly, another case study is used to compare visualization of Ductal Carcinoma in Situ (DCIS) using iPAT, US, DCE-MRI and X-ray imaging. A third study demonstrates the independence of iPAT tumour contrast and breast density. Finally, we close with a case study of a failed lumpectomy surgery, exemplifying the visualization of a positive margin on iPAT and US.

4.2 Materials and Methods

4.2.1 Imaging system, image reconstruction, and intraoperative protocol

A custom designed and built photoacoustic imaging system was deployed in an intra-operative setting of a university-affiliated hospital breast surgical suite. Figure 4.1(a) shows the iPAT system within the surgical suite and Figure 4.1(b) and (c) shows the system schematic diagram with major components exposed for convenient viewing. The protocol for imaging a specimen was as follows: First, a surgeon presented a freshly excised lumpectomy. The specimen was immediately immersed in a saline solution contained within a specialized zipploc® bag. The bag was carefully sealed, making sure no air bubbles were present. Next, the bag was mounted on a custom-designed iPAT compatible lumpectomy holder, seen in Figure 4.1(d), and inserted inside the scanner water tank at the location marked by the red ellipsoid in Figure 4.1(b). This location coincides with the active sensor area of the arc-shaped 24-channel photoacoustic transducer array, seen inside the tank. The water in the tank provided acoustic

coupling between the array and the sample, enabling signal detection and playing a similar role to conventional US gel.

Once the sample was secured in position, two iPAT scans were carried out at wavelengths of 930 nm and 690 nm. When intraoperative time constraints permitted, concerns about imaging depth penetration and artefacts were addressed by implementing a "transmission-mode" imaging protocol. This protocol consisted of scanning the two compressed sides of the specimen separately by inverting the sample and scanning the other side. Otherwise, a "fast" protocol was implemented which consisted of scanning the entire specimen in one pass. The trade-off of the "fast" protocol was the multimode nature of the resulting image volume which was more difficult to interpret. The protocol concluded with a 6.6 MHz ultrasound scan of the sample, performed using the conventional US system seen on the left in Figure 4.1(a), which examined the equivalent volume.

Each scan resulted in 24,000 acoustic time-of-flight measurements, or projections. These measurements were used in conjunction with a filtered-back-projection (FBP) image reconstruction algorithm to generate 3D images representing the relevant chromophore distribution within the sample. For the 930 nm wavelength, the targeted tissue was healthy breast parenchyma and fat, while the 690 nm scan corresponded to hemoglobin distribution. After initial FBP reconstruction, image post-processing was carried out to aide image interpretation. Post-processing consisted of K-Wave iterative image improvement using time reversal, which was adapted for volumetric results. This procedure partially corrected the amplitude of voxels by use of virtual photoacoustic signal detectors in locations where detectors were absent in the original iPAT scan. Therefore, implementation of this procedure simulated the coverage of fully enclosing signal-detection geometry[45]. Image noise reduction was carried out by use of a 2-voxel wide median filter which de-speckled the images while preserving sharp boundaries. In a few cases of low SNR due to deep imaging demands or low laser output, contrast enhancement was done by narrowing of the minimum (0) to maximum (255) window of the 8-bit RGB image volume. Image reconstruction was carried out in Matlab (MATLAB and K-wave Toolbox Release 2013a, The

MathWorks, Inc., Natick, Massachusetts, United States) and image processing was carried out using ImageJ (1.49v, National Institutes of Health, USA).

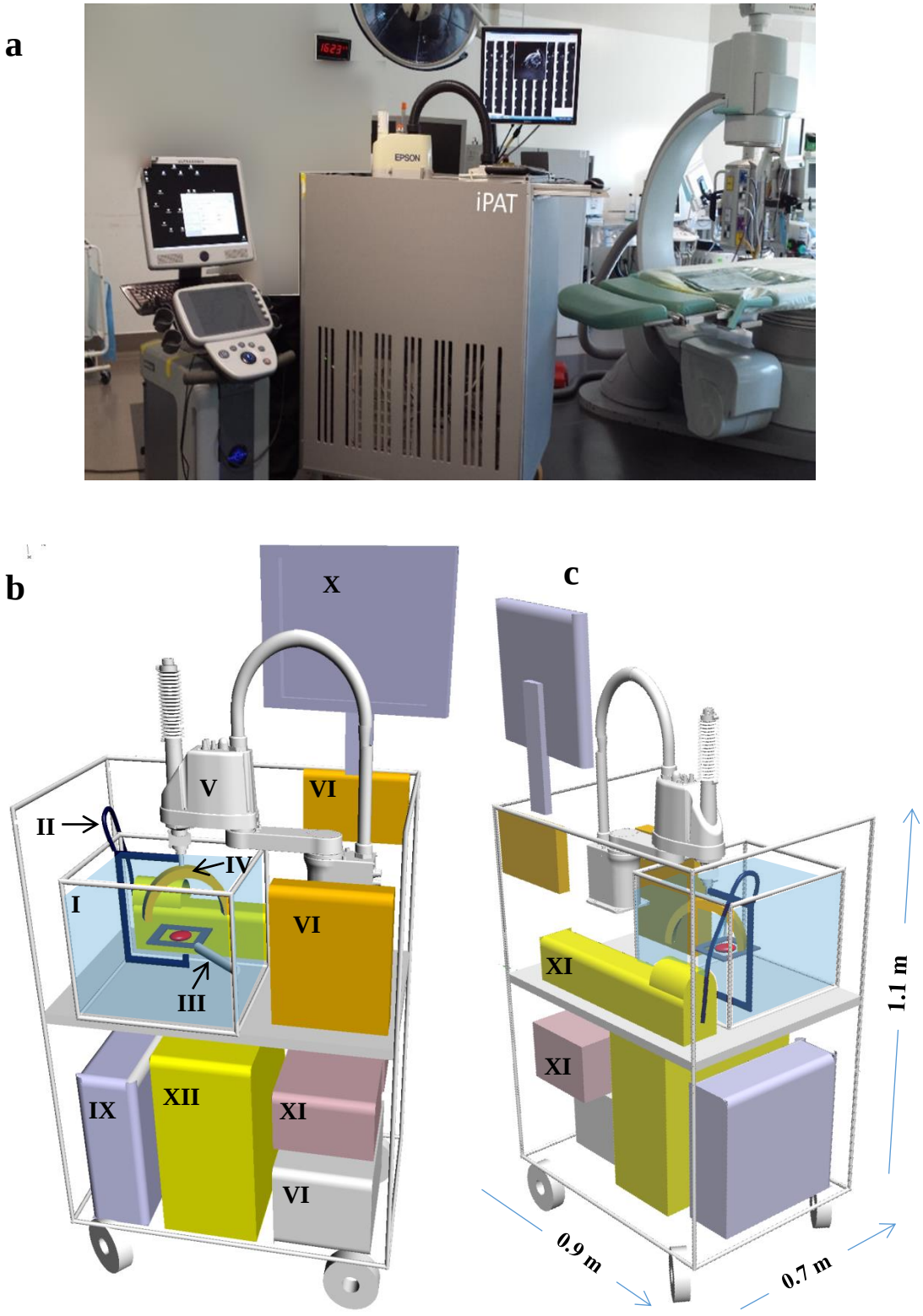

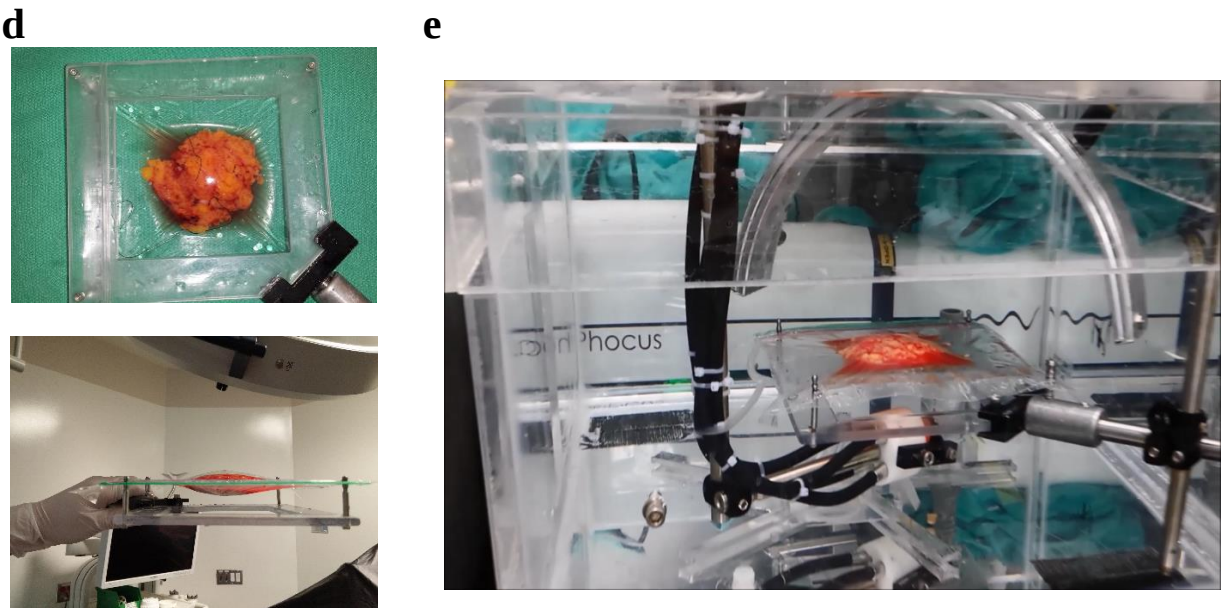

Figure 4.1. (a) Photograph of iPAT system (center) within surgical suite as well as conventional ultrasonography system (left). (b) Three dimensional schematic showing major components of iPAT scanner, including water tank (I) which contains a fused fiber-optic bundle assembly (II) that is used to direct near infrared laser pulses toward the lumpectomy specimen seen restrained in the specialized lumpectomy holder (III). The water in the tank facilitates acoustic coupling between the lumpectomy specimen and the 24 channel arc-shaped photoacoustic transducer array (IV). The array and fiber-optic assembly is mounted to the effector of a 4-axis SCARA robot (V) which is controlled by the robot PC (VI). The laser induced signals detected by the transducer array are synchronized using the time delay generator (VII) and transferred to the 50 MHz data acquisition system (VIII) where they are digitized and sent to the workstation PC (IX) for processing and visualization on the video monitor (X). General power to the system is provided through a hospital grade isolation transformer (XI) which also feeds the laser power supply (XII). Figure 4.1(c) depicts the back of the iPAT system including the auxiliary hospital grade uninterruptible power supply (XIII) and the laser system (XIV) as well as scale bars indicating the system dimensions. Figure 4.1(d) consists of photographs of the iPAT compatible lumpectomy holder with 2 mutually orthogonal views showing a compressively restrained surgical specimen. Figure 4.1(e) is a close up photograph of the iPAT system's water tank during an intraoperative specimen scan showing the specimen near the center, the arc-shaped transducer array above, and the fiber-optic bundle below.

4.2.2 Patient selection

One hundred women undergoing BCS between June 2015 and May 2016 were asked to participate in this study with informed consent and the approval of the institutional review board of The University of Western Ontario (UWO Research Ethics Board # 105467; LHSC Tissue Archive # 888; Lawson Approval #R-14-311). Inclusion criteria consisted of pathology proven invasive or *in-situ* lesions of at least 3 mm in maximum dimension, including IDC, DCIS, Invasive Lobular Carcinoma (ILC), Lobular Carcinoma in Situ (LCIS), Invasive Mucinous Carcinoma (IMC), Invasive Tubular Carcinoma (ITC), as

well as lesions exhibiting extensive intra-ductal component (EIC). Finally, lesions consisting of combinations of these were also included.

4.2.3 Lesion maximum diameters comparison to pathology and Statistical Analysis

Tumour masses were identified on 930 nm iPAT scans as hypo-intense volumes. The maximum diameter of the volumes was measured on a single imaging slice that presented the largest contiguous lesion profile. Correspondingly, maximum diameters were pathologically measured within a single histology slide presenting the largest profile. The relationship between diameters was then examined. Furthermore, to establish the relationship between total amount of excised tissue and tumour size, maximum pathologically measured tumour diameters were also compared to whole specimen diameters. Statistical examination consisted of linear regression analysis and the non-parametric Wilcoxon signed-rank test. These resulted in a Pearson's correlation coefficient (R-value) and the Wilcoxon probability value (p-value) for estimating equivalency of the two data sets. The analysis was carried out using the Statistics Toolbox in Matlab (MATLAB and Statistics Toolbox Release 2013a, The MathWorks, Inc., Natick, Massachusetts, United States). Tumour maximum diameter measurements were performed using ImageJ (1.49v, National Institutes of Health, USA). A value of $p=0.05$ was considered statistically significant.

4.2.4 Lesion localization and iPAT predictive values

Pathological examination was carried out resulting in a breast invasive carcinoma synoptic report. This was done according to AJCC/UICC TNM 7th edition, CAP Version 3.1.0.0 (June 2012). A pathologist with extensive experience (>10 years) performed or supervised the examination. To estimate how tumour localization of iPAT compared to pathology, image volumes resulting from 930 nm iPAT scans were first oriented using intraoperative photographs in conjunction with surgical orientation sutures. The sutures

are placed by the surgeon to orient the specimen with respect to the surgical cavity. The sutures indicate the superior aspect (short suture) and the lateral aspect (long suture), and are visualized on iPAT. The six margins (superior, inferior, medial, lateral, anterior and posterior) of the specimen were identified through interpretation of the sutures in the iPAT and US images. Hypo-intense regions within the iPAT image volumes were considered representative of malignant lesions. The extent of the hypo-intense lesions in the oriented images was used to find all iPAT-positive margins. If no margins appeared positive, the closest uninvolved margin was measured. These findings were then compared to the positive or closest uninvolved margins noted by the pathologist. As described in literature, gross pathologic measurements were used unless microscopic measurements were available[46].

Positive Predictive Values (PPV) and Negative Predictive Values (NPV) were established for two paradigms. First, given a particular lumpectomy specimen, we assessed the ability of iPAT to predict which margins the pathologist would measure as closest, whether involved or not. And second, given an iPAT-specific definition of a pathologically-measured positive margin, how accurately did the system predict margin status. Finally, the potential effect of iPAT on preventing positive margins at pathology was determined. The "no-ink-on-tumour" definition was adopted.

To achieve the first task, each of the six margins was placed into one of two categories. This was done based on iPAT imaging results, and separately, based on pathology measurements. Specifically, if iPAT indicated that a margin was positive or closest, it was placed into the close margin category (CMC). The remaining margins of that lumpectomy specimen were then placed in the wide margin category (WMC). Separation of the six margins into these binary categories established a proportion of close-to-wide margins for each lumpectomy specimen, and this proportion was maintained during the pathologic categorization. For example, if after assessing a particular lumpectomy specimen, iPAT placed x-number of margins into the CMC, this would subsequently guide the pathologic examination to also place the closest x-number of pathologically measured margins into the CMC. The remaining margins in both assessments were placed into the WMC.

Following this categorization, PPV were calculated by defining true positives (TP) as cases where a margin, placed in the CMC by iPAT, was also placed there by pathology. Correspondingly, false positives (FP) were defined as cases where a margin, placed in the CMC by iPAT, was placed in the WMC by pathology. Similarly, NPV were calculated by defining true negatives (TN) as cases where a margin placed in the WMC by iPAT, was also placed in the WMC by pathology. Finally, false negatives (FN) were cases where a margin was placed in the WMC by iPAT, but was placed into the CMC by pathology or was the same pathologic size as the margin(s) in the CMC.

For margin status prediction, we emulated previous intraoperative US studies where PPV and NPV were determined[47]. These recognized frequent underestimation of lesion size, and hence overestimation of margin size, and compensated for this by calibrating their US margin measurements (e.g. US = Path + 8 mm). Therefore, to achieve an expected 2 mm histologically-measured negative margin, they adopted a minimum 10 mm US-measured negative margin. In contrast, results relating iPAT to pathologic tumour sizes, as described in section 2.3 above, demonstrated a possible overestimation of lesion size, and therefore underestimation of margin-width. This motivated defining positive iPAT-determined margins as ones that are pathologically-measured to be 5 mm or less (e.g. iPAT = Path – 5 mm). PPV, NPV, sensitivity and specificity for margin status were then calculated. This was done by defining TP as cases where positive iPAT-determined margins were found to be 5 mm or less on pathology. FP were therefore considered cases where iPAT-determined positive margins were found to be larger than 5 mm on pathology. Similarly, TN were counted for cases where iPAT indicated a negative margin which was found to be larger than 5 mm on pathology, and FN were cases where iPAT indicated a negative margin which was found to be 5 mm or less on pathology.

4.2.5 Areolar invasion, DCIS, breast density dependence and positive margin investigation

Four representative cases of common clinically-problematic situations were selected. Inclusion in the Areolar-complex invasion case-study depended on excision of nipple, the areola, a significant area of the surrounding skin as well as dermal or epidermal tumour invasion. The DCIS case was selected based on excision of at least several cm of ductal tissue, good visualization on imaging and evidence of extensive DCIS involvement. The breast density case was included due to documented presence of dense fibro-glandular tumour bed. Finally, the positive margin case consisted of a pathologically confirmed invasion of a lumpectomy specimen margin by an IDC, as well as concordant findings on iPAT imaging.

4.3 Results

4.3.1 Imaging system and intraoperative protocol

Of the 100 women that agreed to participate in the study, the first 11 cases were used to optimize the imaging system, the iPAT detector array, imaging parameters, appropriate lumpectomy specimen holder, and the general intraoperative protocol. Seven attempts were prevented by technical failures including laser malfunctions, insufficient time to complete scan, and failure to capture photographs resulting in un-oriented lumpectomy specimens. Preparation of the lumpectomy specimen and insertion of the lumpectomy holder into the iPAT scanner consumed approximately 5 minutes. The iPAT scan was 6 minutes in duration per side per wavelength and the US scan was approximately 90 seconds. Therefore, in cases where the sample was imaged using the "fast" protocol, the duration of the full imaging procedure was under 20 minutes. Alternatively, when time permitted "transmission-mode" scans, the procedure took approximately 35 minutes.

4.3.2 Patients and clinical information

Eighty-two specimens were successfully imaged. Nineteen lesions consisting of 8 fibroadenomas, 3 post-surgical healing changes, 2 hyperplasias, 2 rare atypias, a smooth muscle tumor, a lymph node and two lesions under 3 mm in diameter, were excluded. The remaining 63 cases were included in the study, with informed consent and approval of the institutional review board. The "fast" protocol was implemented in 37 cases, while the remaining 26 were scanned using the "transmission-mode" protocol. Table 4.1 is a summary of patient and tumour type information. Our cohort of women presented with an average age of 63 and a range of 33 to 94 years. As consistent with other studies, the majority of cases involved IDC (81%) and mixed invasive and *in-situ* lesions (57%). Lobular type lesions were seen in 8% of the participants.

Table 4.1. Patient and tumor information

Measure	Patient age			*In-situ* + Invasive Tumour	Tumor histologic type				Tumor histologic grade			EIC[1]	NAT[2]
	Mean	Med	Range		IDC	ILC	DCIS	Other[3]	1	2	3		
N	63	63	33-94	36	51	5	4	3	22	29	12	3	4
%				57	81	8	6	5	35	46	19	5	6

1. Extensive Intraductal Component
2. Neoadjuvant Therapy
3. Invasive Mucinous Carcinoma, Invasive Tubular Carcinoma

4.3.3 Lesion localization and iPAT predictive values

As outlined in section 2.4, photographs showing surgical orientation sutures of lumpectomy specimens were used to orient the iPAT image volumes. This procedure can be appreciated in Figure 4.2 which shows a representative case depicting a left sided lumpectomy specimen that contained a pathologically measured 23 mm diameter IDC. The selected slices, ranging in depth from 11 mm to 14 mm below

illuminated surface, were taken from a 3-D iPAT image stack and clearly show the orientation sutures (arrows), which can also be seen in the photograph. The co-visualization of sutures facilitated the orientation of the specimen with superior aspect on the top and lateral to the right. The sutures were also visible in the corresponding US slices, although the echogenic nature of the specimen bag often obscured the view. The X-Ray (Faxitron) image confirmed the central location of the IDC lesion within the specimen and also verified the presence of an I-125 radioactive localization seed.

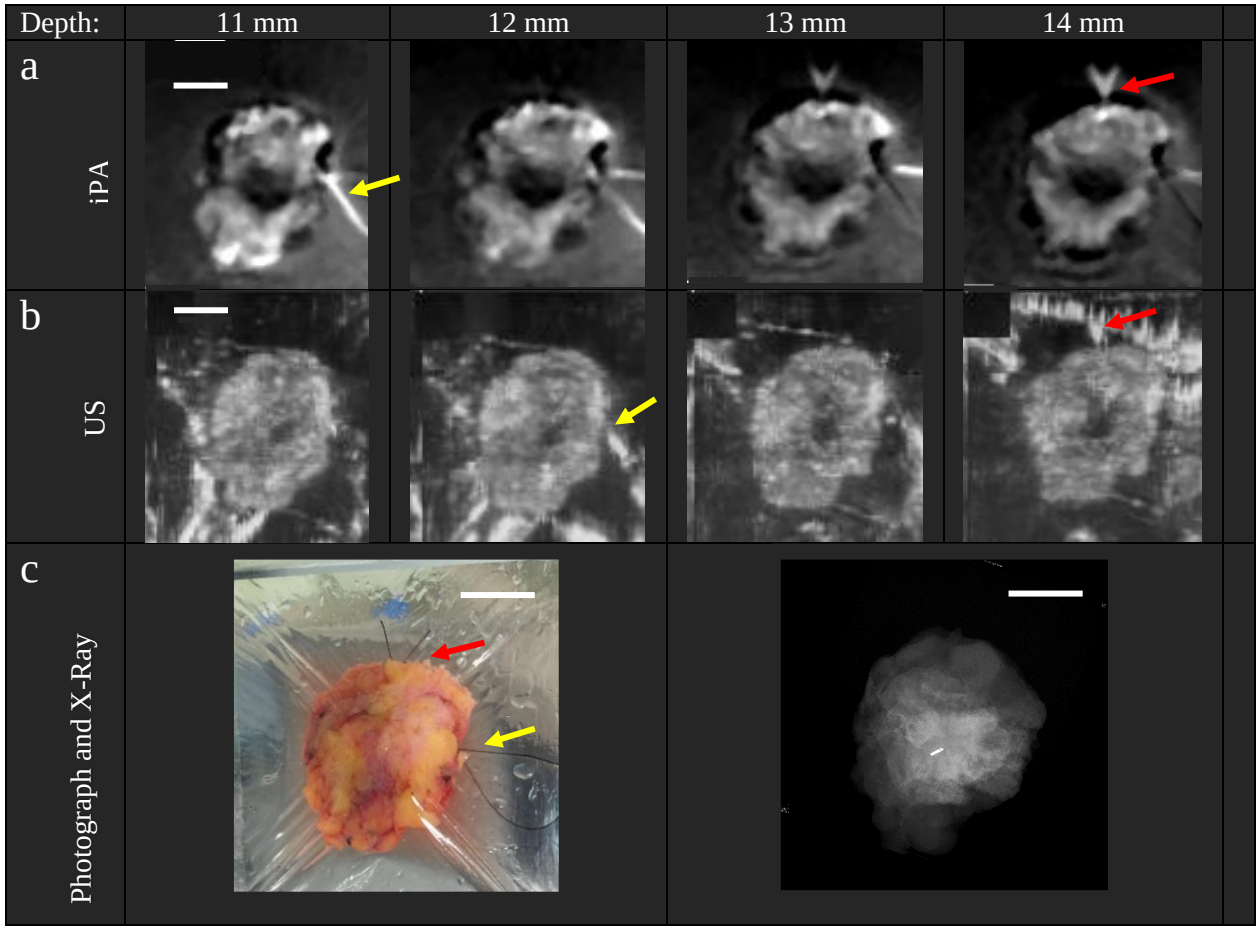

Figure 4.2. Representative lumpectomy specimen illustrating orientation procedure by visualization of surgical sutures on iPAT images and photograph. The top row of images (a) represent xy-slices in the iPAT 3D stack of images showing the lumpectomy specimen cross sections at the indicated depths below the surface. The middle row (b) shows the corresponding US slices. The yellow arrows indicate the long suture representing the lateral direction, and the red arrows indicate the short suture representing the superior direction. The long and short sutures are clearly visible in the photograph of the lumpectomy specimen on the left of Figure (c). The radioactive seed is clearly visible in the X-ray transmission image near the center of the specimen on the right of Figure (c). The scale bars in each panel represent a dimension of 2 cm.

Fifty-three of the 63 cases under investigation included pathology measurements for all six margins, enabling the classification scheme outlined in section 2.4. Table 4.2 summarizes the predictive value results for both scan modes combined, as well as for "fast"-mode and transmission-mode scans independently. A total of 318 margins were investigated by both iPAT and pathology. Examining the number of iPAT-determined positive or closest margins for the whole cohort resulted in 112 margins being classified into the close margin category (CMC), with a mean pathology-measured margin size of 5.6 ± 6.1 mm (median 4 mm, range 0 mm – 44 mm) . On the other hand, the remaining 206 margins that were iPAT-allocated to the wide margin category (WMC) presented with a mean pathology margin of 13.2 ± 8.4 mm (median 12 mm, range 0 mm – 40 mm). Comparing the classification results to pathology yielded 79 true positives (TP), 33 false positives (FP), 170 true negatives (TN) and 36 false negatives (FN). This indicates that for a positive or close margin prevalence of 35.2%, the PPV, NPV, sensitivity and specificity for iPAT was 70.5%, 82.5%, 68.7%, and 83.7%, respectively.

Inclusion of only the transmission-mode scans revealed a total 114 margins on 19 specimens, with a positive or close margin prevalence of 37.7%. The PPV, NPV, sensitivity and specificity for transmission mode was 81.4%, 87.3%, 79.6%, and 88.6%, respectively. The "fast" scan alone produced data for 204 margins with a positive or close margin prevalence of 33.8%. The PPV, NPV, sensitivity and specificity for "fast" mode scan was 63.8%, 80.0%, 62.0%, and 81.2%, respectively.

As outlined above, for margin-status prediction we adopted a 5 mm threshold for positive margin definition. Therefore, margins measured to be 5 mm or less on pathology were considered positive, while margins measured to be 0 mm on iPAT were considered to be positive. The comparison between iPAT and pathology resulted in 75 true positives, 38 false positives, 170 true negatives and 36 false negatives. This paradigm established a positive margin prevalence of 34.8%, with PPV, NPV, sensitivity, and specificity of 66.4%, 82.5%, 67.6% and 81.7%, respectively. Considering only transmission-mode scans produced positive margin prevalence of 34.2%, with PPV, NPV, sensitivity, and specificity of 68.2%,

87.1%, 76.9% and 81.3%, respectively. Finally, the "fast" scan had a positive margin prevalence of 35.1%, with PPV, NPV, sensitivity, and specificity of 65.2%, 80.1%, 62.5% and 82.0%, respectively.

Table 4.2. Predictive values, specificity, and sensitivity for two paradigms aiming to achieve negative margins at pathology.

Margin classification	Prevalence (%)	PPV (%)	NPV (%)	Sensitivity (%)	Specificity (%)	TP (*N*)	FP (*N*)	TN (*N*)	FN (*N*)
Closest or positive (both scans)	35.2	70.5	82.5	68.7	83.7	79	33	170	36
Closest or positive (transmission-mode scan)	37.7	81.4	87.3	79.6	88.6	35	8	62	9
Closest or positive ("fast"-mode scan)	33.8	63.8	80.0	62.0	81.2	44	25	108	27
Positive (< 5 mm on pathology) (both scans)	34.8	66.4	82.5	67.6	81.7	75	38	170	36
Positive (< 5 mm on pathology) (transmission-mode scan)	34.2	68.2	87.1	76.9	81.3	30	14	61	9
Positive (< 5 mm on pathology) ("fast"-mode scan)	35.1	65.2	80.1	62.5	82.0	45	24	109	27

In considering individual lumpectomy specimens, the "no-ink-on-tumour" definition of positive pathological margin resulted in pathology discovering 12 positive specimens out of a total of 53, for a rate of 22.6%. Acting on the information provided by iPAT, detection of 9 out of the 12 positive specimens would have occurred. If all detected cases were successfully remedied intraoperatively, the positive specimen rate would have been 5.7%, a reduction of 74.8%.

4.3.4 Lesion maximum diameter comparison to pathology and statistical analysis

Tumour measurements of the 63 lesions assessed by iPAT produced a mean maximum diameter of 30.3 mm (median 30 mm, range 8 mm – 64 mm). In comparison, pathologic measurements on these lesions produced a mean diameter of 20.1 mm (median 18 mm, range 4 mm – 55 mm). As can be seen in Table 4.3, this represented a mean overestimate of 10.2 ± 9.9 mm and a median difference of 10 mm. In terms of percent difference, the iPAT measurements overestimated pathology results by a mean of 50.7% with a median of 49.8%. The regression analysis resulted in 4 scatter plots, shown in Figure 4.3, correlating the

maximum diameters measured by iPAT and pathology, as well as between specimen size and pathologic tumour size.

For “fast”-mode and transmission-mode iPAT scans combined, as well as separately, the non-parametric Wilcoxon signed-rank-test indicated a significant difference in measured diameters compared to pathology ($p<0.0001$). However, the Pearson correlation coefficient for the whole cohort showed a fairly strong positive correlation ($r = 0.61$, $p<0.0001$). Furthermore, the transmission-mode scan alone produced a significant and strong positive correlation ($r = 0.77$, $p<0.0001$) and the “fast”-mode scan alone resulted in a moderate positive correlation ($r = 0.52$, $p<0.001$). Compared to pathology, the transmission-mode scan delivered the smallest mean and median tumour diameter difference of 6.7 ± 6.9 mm and 4.5 mm, respectively. Finally, comparing pathologically measured specimen size and tumour size resulted in a somewhat weak positive correlation ($r = 0.43$, $p=0.0004$).

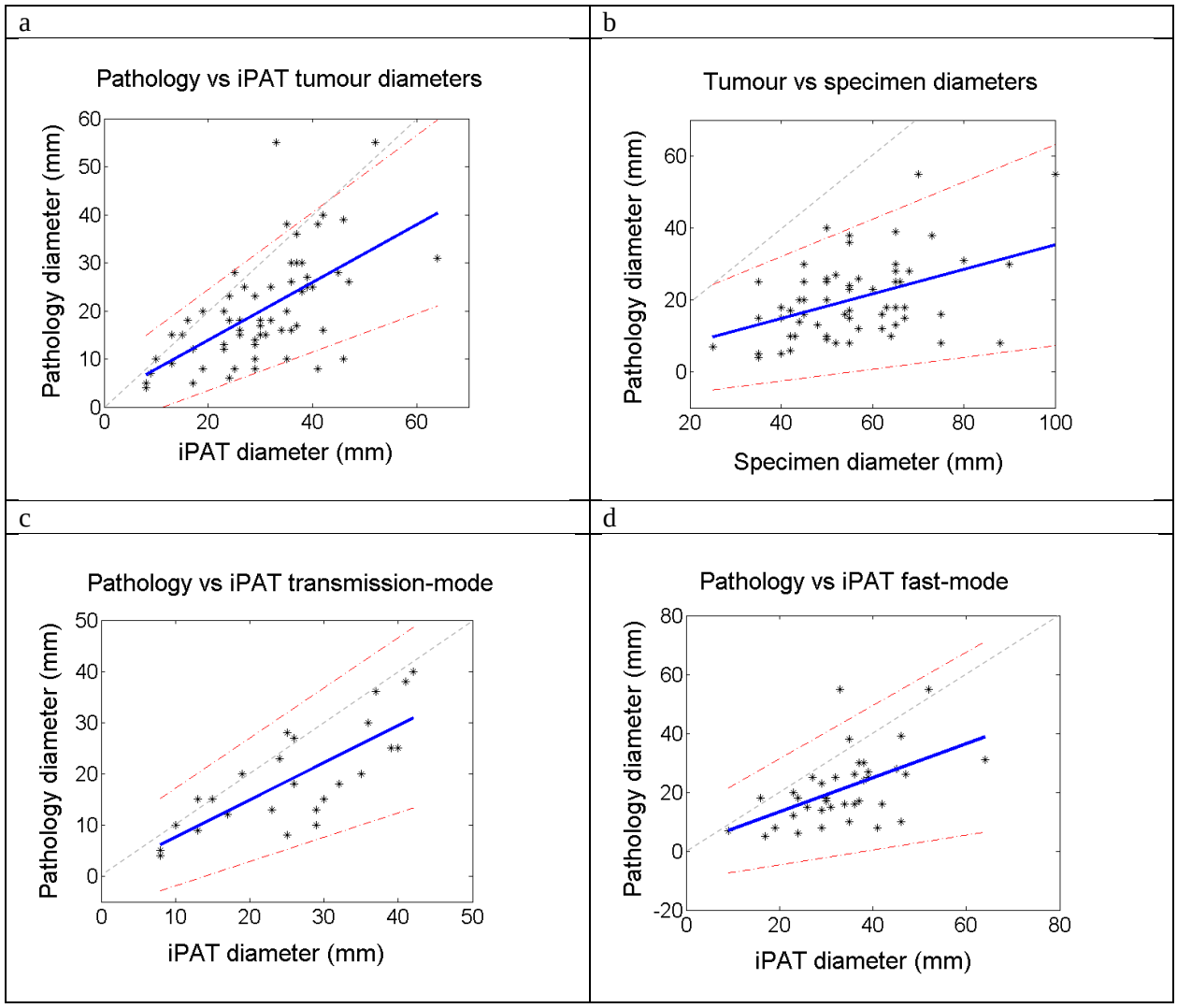

Figure 4.3. Regression analysis and scatter plots showing the line of best fit (solid blue), line of equality (dashed gray), and 95% confidence intervals (dashed red) for comparing (a) iPAT measured tumour diameters to pathology measured diameters, (b) tumour diameters on pathology to whole specimen diameters on pathology, (c) tumour diameters on pathology to iPAT measured diameters when only transmission-mode scan configuration was employed and finally (d) tumour diameters on pathology to iPAT measured diameters for fast-mode only scan configuration.

Table 4.3. Correlation coefficients and statistical difference assessment between iPAT and pathology, as well as between tumour size and specimen size by absolute as well as percent difference.

Comparison pairs	Pearson Correlation R-value	Wilcoxon signed rank test	Mean (S.D.) difference		Median difference	
			(mm)	(%)	(mm)	(%)
iPAT vs pathology tumor diameter (both scans)	0.61 (p<0.0001)	p<0.0001*	10.2 (9.9)	50.7 (49.2)	10	49.8
iPAT vs pathology (transmission-mode)	0.77 (p<0.0001)	p<0.0001*	6.7 (6.9)	34.9 (36.1)	4.5	23.6
iPAT vs pathology ("fast" mode scan)	0.52 (p<0.001)	p<0.0001*	12.4 (11.2)	58.5 (52.9)	12	56.9
Specimen vs tumour max diameter by pathology	0.43 (p=0.0004)	p<0.0001*	35.4 (13.6)	177.2 (68.3)	35	174.3

*Indicates significant difference

4.3.5 Areolar invasion, DCIS and positive margin investigation

Case 1: Areolar Complex

Figure 4.4 depicts the results of intra-operative imaging of a freshly excised lumpectomy specimen belonging to a 72-year-old patient with a biopsy proven cancer in the left breast (BIRADS-6). The top row shows selected slices produced by a 930 nm iPAT scan ranging in depth from 7 mm to 14 mm below the skin surface. The bottom row shows the corresponding US slices. Pathologic examination revealed a 25 mm, grade 2 IDC lesion that was described as having direct involvement of the dermis or epidermis without skin ulceration. Good agreement is found between iPAT, US, and pathology. Both imaging modalities clearly demonstrate intrusion of the hypo-intense mass towards the areolar complex and nipple. Careful examination of the iPAT slices ranging from 7 mm to 9 mm also provided visualization of the skin edge, which is more difficult to see in the US slices. The 14 mm iPAT slice shows a deeply infiltrating mass with spiculations. The corresponding US slice confirms the location of the mass but fails to visualize the spiculations. The arrow indicates an area of "shadowing" artefact.

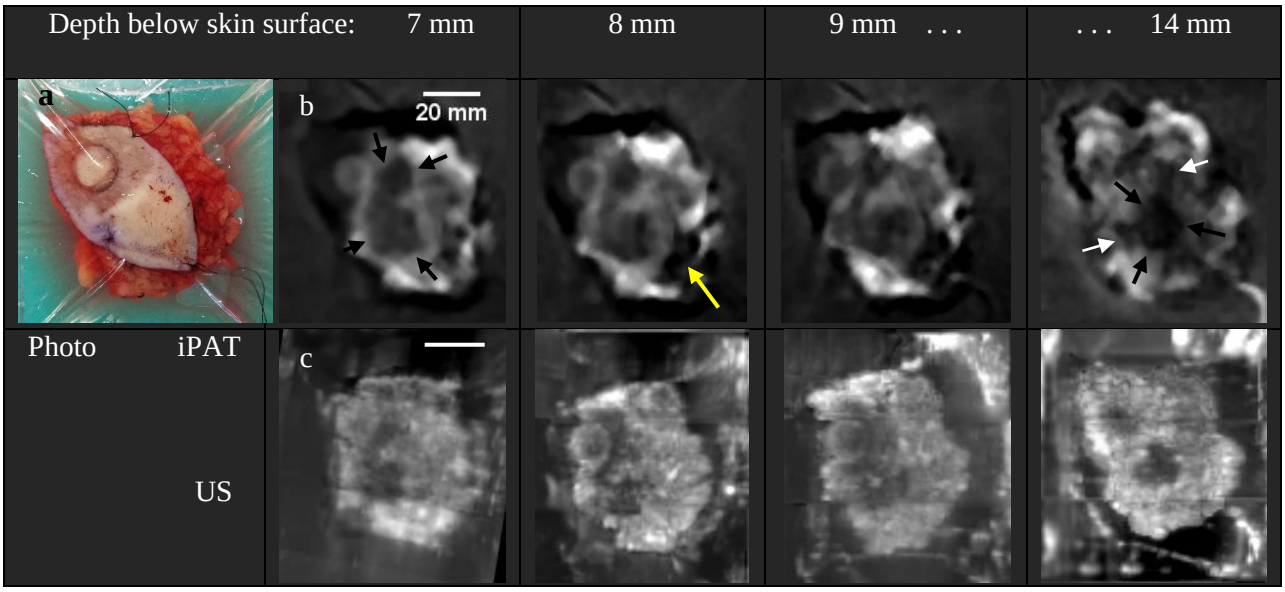

Figure 4.4. (a) Photograph of freshly excised specimen belonging to a 72 year old patient with biopsy proven 25 mm, grade 2 IDC. (b) Selected iPAT slices ranging from 7 mm to 9 mm below the skin surface showing intrusion of hypo-intense mass (black arrows) towards areolar complex and nipple. The 14 mm slice depicts a deeply infiltrating hypo-intense mass (black arrows) with spiculations (white arrows). The yellow arrow indicates an area of "shadowing artefact". Figure (c) consists of corresponding image slices from a conventional 6.6 MHz ultrasound scan indicating concordant findings but failing to visualize the deeply seeded spiculations. Subsequent pathology examination confirmed infiltration of dermis or epidermis by IDC. The white scale bars indicate a length of 2 cm.

Case 2: DCIS

A 57-year-old patient presented with indeterminate calcifications on mammogram, which subsequently resulted in a left-sided biopsy-proven IDC (BIRADS-6). The occult nature of the lesion prompted a DCE-MRI study which revealed both clumped and significant amounts of segmental enhancement. The radiology department reported an involved area measuring approximately 44 mm x 40 mm, and to aid excision, recommended wire localization via bracketing technique. This can be appreciated on the intraoperative X-ray in Figure 4.5(e), which shows the hooked localization wires bracketing the lesion. Post-operative pathologic examination discovered high and intermediate grade DCIS along with a grade 2 multifocal-IDC with 3 foci of invasion measuring 15 mm, 3 mm and 1 mm each. iPAT-930 nm images, shown in Figures 4.5(a) and (f), were found to be concordant with intraoperative X-ray (e), and pre-operative DCE-MRI, (g) and (h), as they revealed a suspicious lesion with segmental (black arrows) and clumped (white arrows) hypo-intensities. Localization of the lesion within the large 81 mm specimen was found to be in excellent agreement with X-ray. Satisfactory localization agreement was also found with

US; however, the appearance of the lesion was limited in extent compared to iPAT. Furthermore, compared to US the image quality of iPAT appeared superior, permitting the visualization of what appeared to be individual ductal structures. These can be appreciated in the selected iPAT slices at depths of 12 mm – 14 mm, which show segmental and branching hypo-intensities near the top of the image. At a depth of 14 mm, US also shows some concordant segmental structure (dashed box), but again, low image quality makes evaluation more difficult. Interestingly, the specimen under consideration also exhibited areas with elevated hemoglobin concentrations, which were also well co-located with the malignant lesion. These are visualized as hyper-intensities (yellow arrows and dashed box) on the 690 nm iPAT scan results, shown in Figure 4.5(c).

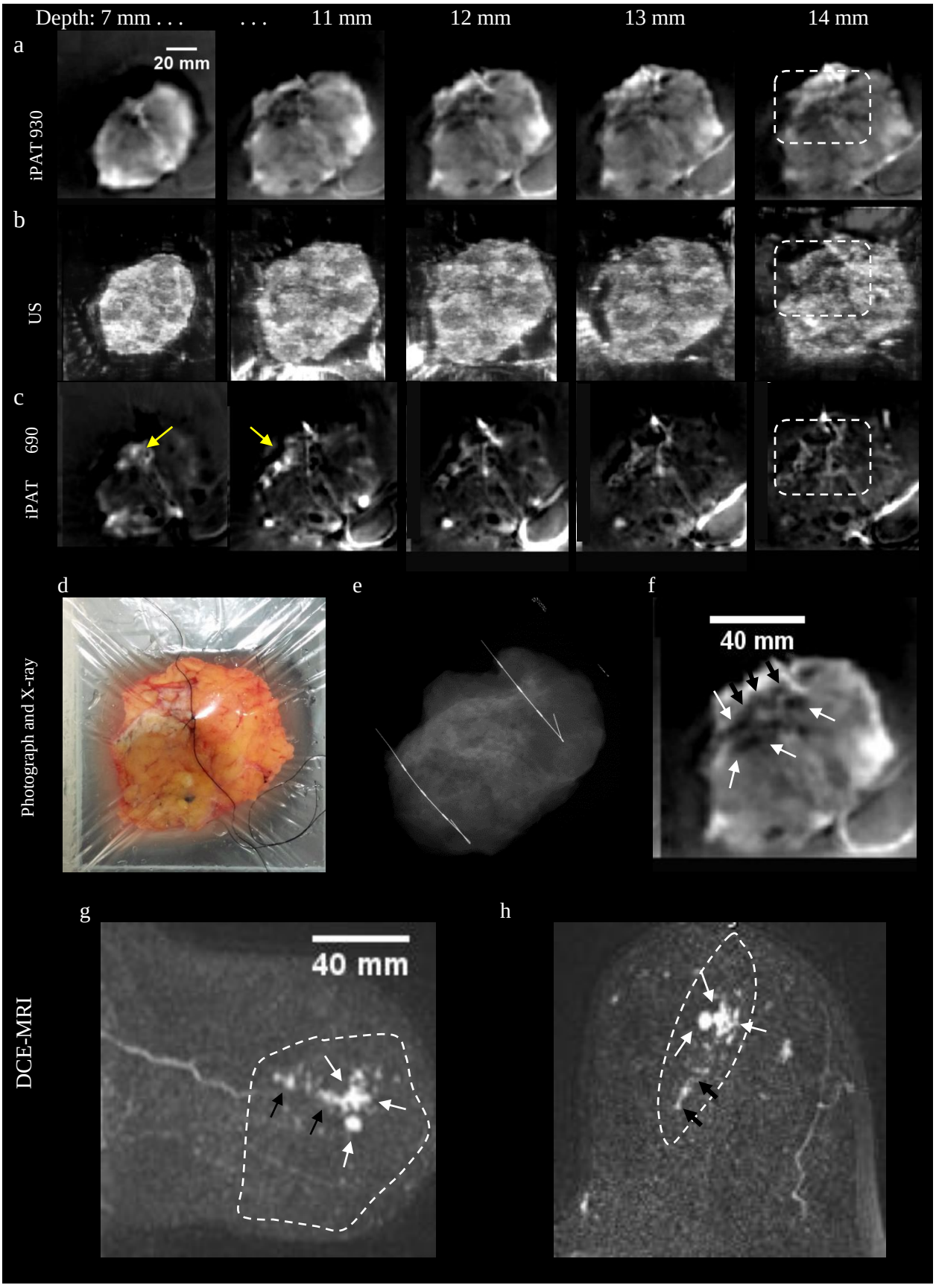
Depth: 7 mm . . .
. . . 11 mm
12 mm
13 mm
14 mm
a
20 mm
iPAT 930
b
US
c
iPAT 690
Photograph and X-ray
d
e
f
40 mm
DCE-MRI
g
40 mm
h

Figure 4.5. (a) Representative iPAT imaging slices of a lumpectomy specimen belonging to a 57 year old patient with pathology proven high and intermediate grade DCIS combined with multi-focal IDC, showing segmental and clumped hypo-intensities at radiographically confirmed location of lesion. (b) Corresponding US slices showing ambiguous results for depths 7 mm to 12 mm and some concordant hypo-intensities in the 13 mm and 14 mm slices (dashed box). (c) 690 nm iPAT scan representing hemoglobin distribution within specimen and exhibiting hyper-intensities at location of suspicious lesion (yellow arrows). (d) Photograph of the specimen showing black orientation sutures. (e) Co-oriented intraoperative digital X-ray radiograph indicating the two dimensional extent of the lesion along with hooked localization wires seen bracketing the lesion. The wires were inserted preoperatively for surgical guidance. Figure (f) is a zoomed in view of the 12 mm deep iPAT slice taken from stack above offering better visualization of the segmental (black arrows) and clumped (white arrows) hypo-intensities. Figure (g) shows a pre-operative DCE-MRI medio-lateral maximum intensity projection through the affected volume of the breast showing concordant clumped (white arrows) and segmental (black arrows) enhancement as well as an approximation of the excised area (dashed white line). Finally, Figure (h) shows the same features from a cranial-caudal perspective demonstrating the pancake shape of the large excised volume.

Case 3: Breast density dependence

Figure 4.6 is a representative case of invasive tumor visualization when tumor bed consisted of dense fibro-glandular tissue. A 46-year old patient was admitted due to a palpable mass in the upper outer right breast. A biopsy of the site indicated an IDC diagnosis (BIRADS-6). The patient underwent BCS with preoperative bilateral DCE-MRI and mammogram scans. Post-operative pathology found a 13 mm diameter IDC as well as low and intermediate grade DCIS. The tumour presented as an 18 mm diameter lesion on pre-operative DCE-MRI and as a 23 mm lesion on intra-operative 930 nm iPAT. Figures 4.6(a) and (b) clearly show that the tumor's inferior and posterior aspect is contiguous with dense fibro-glandular tissue, which makes delineation of those tumor margins difficult to evaluate without contrast dynamics (right). This is confirmed to be the case through all of the coronal slices shown in (c) and (d). On the other hand, the co-oriented slices in Figure (e) clearly show the same tumor on iPAT imaging without loss of contrast at the dense fibro-glandular margins (dashed box). The co-registered US slices in Figure (f) confirm the central location of the tumor. Figure (g) shows the results of intraoperative X-ray, further demonstrating the central location of the lesion, but also confirming the presence of the localization seed within the lesion as well as the spiculated nature of the tumour. For easier visualization, Figure (g) also includes selected zoomed in slices, taken from the iPAT and US stacks, indicating the extent of disease detected by those modalities.

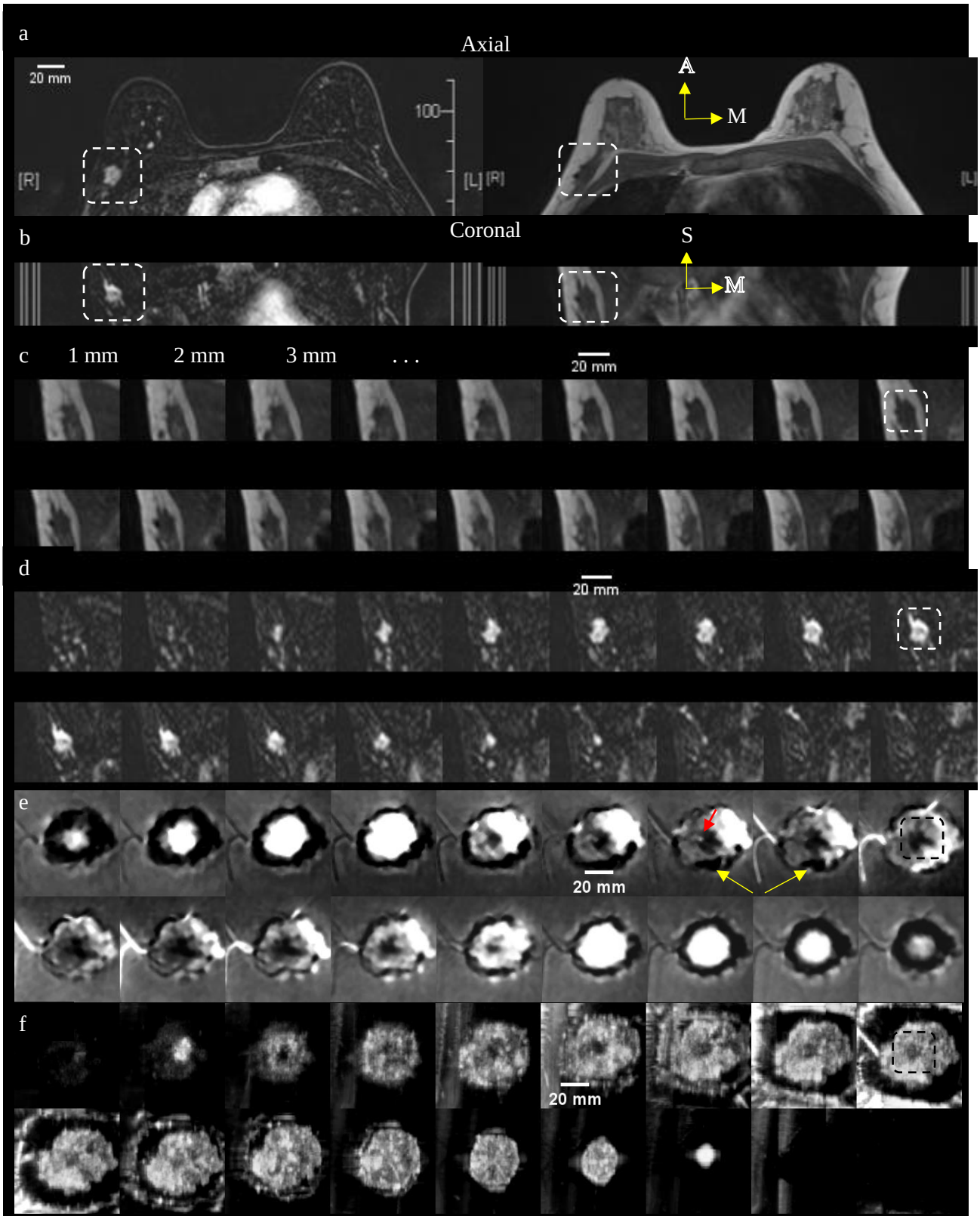
a
Axial
20 mm
100
[R]
[L]
[R]
A
M
[L]
b
Coronal
S
M
c
1 mm
2 mm
3 mm
. . .
20 mm
d
20 mm
e
20 mm
f
20 mm

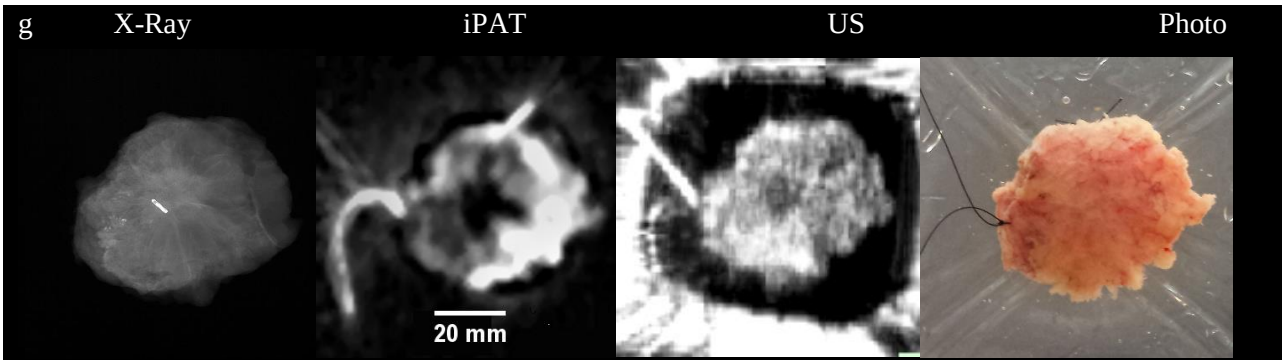

Figure 4.6. (a) Bilateral DCE-MRI (left) and T1w pre-contrast without fat suppression (right) in axial view showing biopsy confirmed 13 mm IDC in the outer right breast (dashed box) as well as yellow orientation arrows indicating the anterior (A) and medial (M) directions. (b) Coronal view showing the same lesion (dashed box) along with orientation arrows indicating the superior (S) and medial (M) directions. The Figure 4.6(b) orientation is then maintained throughout the rest of Figure 4.6. (c) Selected 1 mm-thick slices continuing in coronal view using T1w pre-contrast acquisition without fat subtraction showing tumor region coinciding with fibro-glandular tissue, which makes the tumour margins difficult to delineate (dashed box). (d) Same coronal slices as in (c) but with a DCE-MRI acquisition clearly showing hyper-intense enhancement of tumour making the margins straightforward to identify. (e) 930 nm iPAT slices co-oriented with coronal MRI slices showing hypo-intense tumor (dashed box), along with clearly contrasting margins. The yellow arrows indicate area of "shadowing artefact" (f) 6.6 MHz iPAT-co-registered US slices demonstrating a centrally located hypo-intense mass (dashed box). (g) X-ray, photograph as well as selected zoomed-in iPAT and US slices taken from the stacks in (e) and (f) offering better side-by-side comparison of detected disease extent as well as visualization of the superior (short) and lateral (long) orientation sutures. Note the I-125 localization seed clearly visible in the X-ray transmission image as embedded inside the stellate tumour. The seed is also visible as hyper-intense in the iPAT results of Figure (e) (red arrow) although the limited resolution makes its delineation more challenging. The seed's location within the tumour was confirmed by pathology.

Case 4: Positive margin

Figure 4.7 shows selected slices from an iPAT 3-D image stack, demonstrating the appearance of a specimen representative of a failed surgical excision. A 52-year-old patient was diagnosed by biopsy with left-sided invasive cancer and underwent breast conserving surgery using i-125 radioactive seed localization. The position of the seed can be appreciated on the intraoperative radiograph in Figure 4.7(d). Pathology found a 15 mm grade 1 IDC near the periphery of the specimen, and microscopic examination revealed invasion of the surgical margin. Approximately one month later the patient underwent a second procedure to ensure a clear margin and to minimize recurrence risk. As can be seen in the iPAT slices of Figure 4.7(a), the extension of a hypo-echoic mass (dashed box) can clearly be tracked to the specimen surface and appears to break through near the lateral orientation suture (arrow). This is best visualized in the 9 mm slice on iPAT, and is consistent with the intraoperative X-ray image,

which shows a suspicious lesion at the same location. Corresponding US results show some scattered hypo-intensities (arrows) at the lesion location, however, they fail to demonstrate unambiguously the extent of disease.

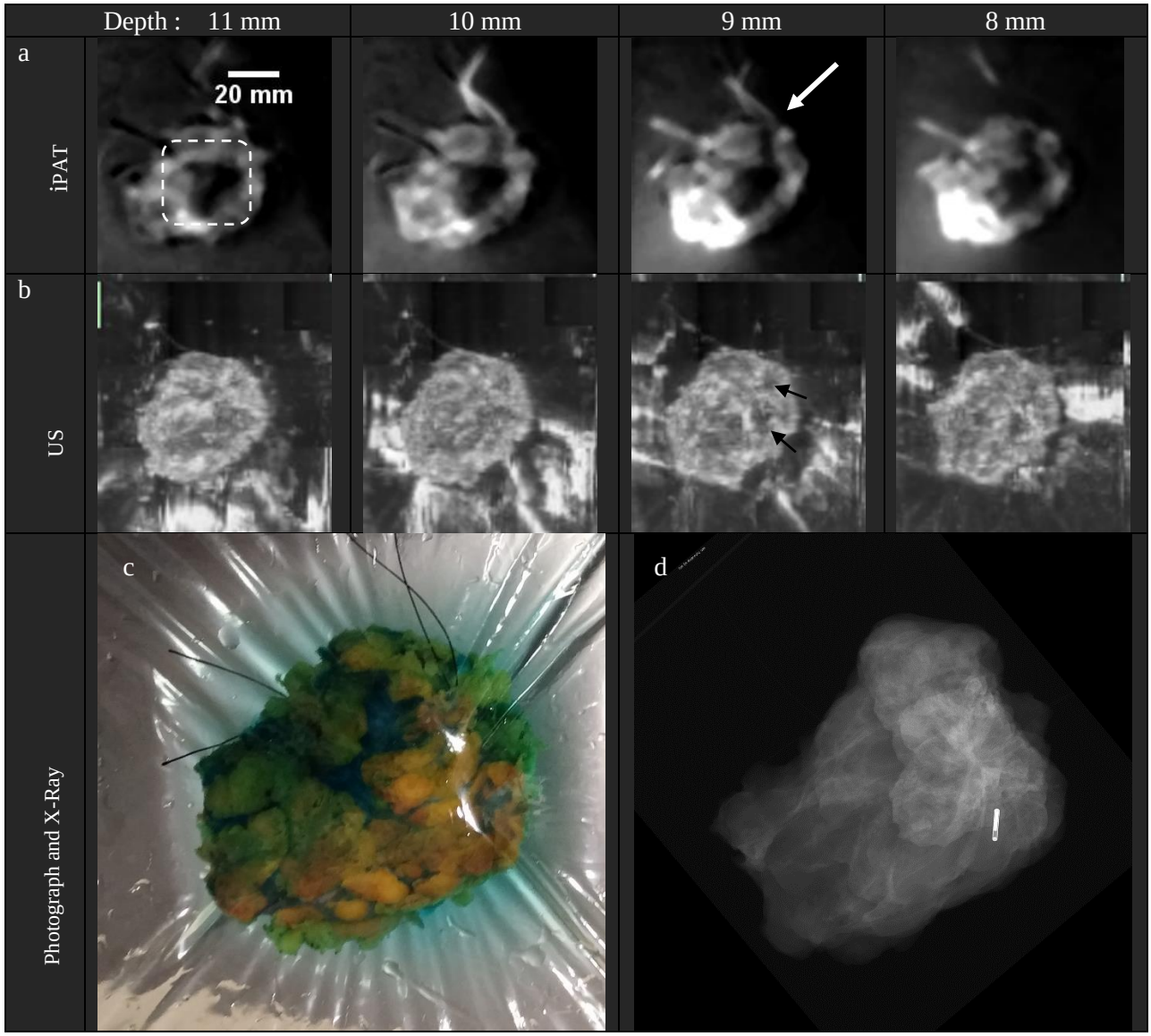

Figure 4.7. The figure shows a lumpectomy specimen belonging to 52-year old patient with 15 mm pathology proven IDC. (a) 930 nm iPAT scan showing apparent infiltration of specimen margin near the lateral orientation suture (arrow) by suspicious hypo-intense mass (dashed box). (b) Co-registered US scan slices demonstrating near occult nature of the lesion on 6.6 MHz ultrasonography. The 9 mm and 10 mm slices show some hypo-intense areas (black arrows) however the image quality makes interpretation of lesion extent difficult. Figure (c) consists of a photograph depicting the black orientation sutures and (d) represents the transmission radiograph clearly showing the I-125 localization seed and suspicious architectural distortion near the periphery of the specimen. The patient subsequently underwent a second operation due to positive margin on pathology.

4.4 Discussion and future directions

4.4.1 Predictive values and potential clinical impact of iPAT

An effective breast conserving therapy will ideally achieve low long-term recurrence rates as well as high patient satisfaction. Therefore the problem is an optimization one. For the patient, this means good cosmetic outcomes combined with minimal repeat surgeries. For the surgeon, this means high quality actionable information at the time of initial excision.

From a practical perspective, having precise pathological information about the width of a specimen margin is less important than the ability to locate malignant tissue left behind in the surgical cavity. Indeed, extra cavity wall shavings are readily undertaken during surgery since the monetary and personal cost is low while the patient is still on the operating table. In contrast, the costs of finding a positive margin on post-operative pathology are higher, since a repeat surgery is indicated. Furthermore, addressing positive margins with separate procedures undertaken weeks or months later comes with additional risk due to the high discordance rates between margin localization by surgery and pathology[19]. Disturbingly, studies show that as much as 37% of surgeries repeated due to positive margins fail to harvest further malignant tissue, implying that the patient did not benefit from the repeated procedure and may in fact still be at high risk of recurrence[48].

Therefore, a surgeon in a busy breast surgical center may be more interested in which margins are closest and simply take a few more shavings. A few mm of extra tissue is unlikely to have significant impact on cosmetic results but can mean a great deal in terms of recurrence risk, especially for high grade aggressive tumours. Our study found that implementing this approach using iPAT would have intervened in 112 of the 318 (35%) margins under investigation, with positive and negative predictive values of approximately 71% and 83%, respectively. In terms of the new "no-ink-on-tumour" definition, this paradigm would have resulted in a surgical failure rate of less than 6%. Compared to the nearly 23% that was experienced in our series, this represents a reduction of about 75%. Conservatively, if taking extra shavings was only

around 50% effective in removing all malignant tissue from an iPAT-detected involved margin, a considerably improved positive rate of 13% would have been achieved.

4.4.2 Lesion maximum diameter comparison to pathology and Statistical Analysis

Since maximum lesion size is limited by lumpectomy specimen size, comparison of tumour sizes in excised specimens is inherently biased toward some level of correlation. For example, it should be expected that relatively large tumours will be contained within relatively large specimens. Not surprisingly, in comparing our gold standard pathology measurements, we found a significant although somewhat weak positive correlation ($r = 0.43$, $p = 0.0004$). In contrast, the stronger positive correlation between diameters determined by iPAT and pathology ($r = 0.61$, $p < 0.0001$) indicated that the influence of whole lumpectomy specimen size on iPAT measured tumour size was limited. This is particularly evident from the large mean overestimate of tumour size based on whole specimen diameters (35.4 ± 13.6 mm) compared to iPAT (10.2 ± 9.9 mm).

On the other hand, in comparing the equivalency of iPAT measurements to pathology, we found a significant difference in maximum diameters determined by iPAT compared to pathology, as indicated by the non-parametric Wilcoxon signed-rank-test ($p < 0.0001$). We believe this to be largely due to specimen compression by the lumpectomy holder, which can be appreciated in the two orthogonal photographs in Figure 4.1(d). The photos show typical stretching and compression of proportions imposed by the holder on the fresh and highly compliant lumpectomy specimen. Nevertheless, artefacts and pathologically undocumented DCIS cannot be ruled out. Future studies should address this confounding factor by implementing an enhanced pathologic examination of the specimens. In particular, detailed pathologic measurements of *in-situ* disease should be included. This would allow a more fair

comparison to iPAT, which, other than on the basis of lesion morphology, may not necessarily differentiate invasive from in-situ components

4.4.3 Influence of scanning geometry: "fast" vs transmission-mode

Intriguingly, Tables 4.2 and 4.3 indicate that specimens scanned using transmission-mode iPAT produce significantly stronger correlations, predictive values, sensitivity and specificity, compared to the whole cohort. Conversely, considering specimens scanned using the "fast"-mode iPAT resulted in weaker values. The differences were largest between the two subgroups with correlation coefficients for transmission-mode versus "fast"-mode being $r = 0.77$ ($p < 0.0001$) and $r = 0.52$ ($p < 0.001$), respectively. Furthermore, the positive and negative predictive values for closest or positive margins based on transmission-mode were 81% and 87%, versus only 63% and 80% for the "fast"-mode, respectively. This indicates that the theoretical basis for superiority of the transmission-mode scanning geometry is sound.

The technical details of the differences between these scan geometries have been discussed in literature, however, the tendency for "shadowing" artefacts to be more pronounced in our transmission-mode images cast doubt on the conclusions. These "shadows" can be appreciated in Figures 4.2 and 4.4 as apparent hypo-intense features typically found near the periphery of lesions. In particular, the 8 mm and 9 mm slices of Figure 4.4 demonstrate the potential confusion that can arise in margin and lesion extent assessment. For example, the hypo-intense area on the bottom right of the 8 mm slice in Figure 4.4 (arrow) could easily be confused with malignant tissue.

Naturally, a potential solution may consist of reflection-mode scans, which suffer from significantly less shadowing, as can be deduced from literature as well as in our earlier work[38]. However, the well documented theoretical inferiority of this approach has prevented its application in our studies[49,50]. Nevertheless, future studies involving iPAT tumour imaging should examine the performance of pure reflection-mode scan geometry. This will enable comparison to transmission-mode in terms of positive

and negative predictive values, sensitivity and specificity. With that information researchers could move towards mitigating the artefacts in iPAT and optimizing the illumination and detection scheme.

4.4.4 Case studies

The four case studies presented in this work visually demonstrate the potential and versatility of iPAT in a clinical setting. In particular, the areolar invasion case exemplified the performance of iPAT when imaging through intact skin. This demonstrated for the first time that *in-vivo* detection of breast tumours may be possible via PAT whose target is healthy breast tissue. Analogous to ultrasonography, the targeting of healthy breast tissue resulted in a contrasting appearance of diseased lesions. The extension to in vivo applications follows since the optical properties of freshly excised specimens at the relevant wavelength are minimally affected by excision. It is expected that the main effect will likely consists of higher blood volume and oxygenation levels for *in-vivo* applications compared to *ex-vivo*. However, since hemoglobin does not dominate absorption at the relevant wavelength of 930 nm, the effects may be negligible. Therefore, this case also served to illustrate the potential role of iPAT in the pre-operative work-up.

The DCIS case validated the ability of iPAT to differentiate *in-situ* disease in a large volume of tissue, suggesting high specificity. Furthermore, it is well known from conventional imaging modalities, such as DCE-MRI, that the presence of segmental morphology correlates with *in-situ* disease. Therefore, iPAT-derived results of the high-grade DCIS specimen further indicate good imaging versatility. In this case, iPAT appeared to outperform conventional ultrasonography, which significantly underestimated the documented extent of disease. Interestingly, while hemoglobin concentration has been named in literature as a biomarker for malignancy, our study found this case to be one of very few featuring agreement with conventional imaging.

As explained above, our findings indicated that tumor tissue may be distinguished from healthy breast tissue using iPAT. This was hypothesized to be due to the relatively low optical absorption coefficient of malignant tissue and subsequent hypo-intense imaging appearance of tumours on scans near a wavelength of 930 nm. However, this wavelength is well-known to be strongly absorbed by bulk-lipid, or, fat-containing tissue.[51] A possible concern with this inference, therefore, is that the hypo-intense regions in iPAT images are volumes of the breast parenchyma with relatively low fat content, and as such they may simply represent dense non-fatty fibro-glandular tissue. Indeed, dense fibro-glandular tissue is also often blamed for sensitivity and specificity deficits in conventional imaging methods, such as ultrasound and mammography, and are often overcome only by use of dynamic contrast enhancement in MRI.[5,52] It was therefore further hypothesized that tumors which are visible on iPAT simply due to surrounding fat tissue should also be seen as surrounded by fat, visualized as hyper-intense on T1 weighted pre-contrast MRI. Surprisingly, the breast density dependence case revealed that this may not be the case. Indeed, a significant portion of the 13 mm IDC discussed in that case was embedded in dense fibro-glandular tissue. Furthermore, close inspection of Figure 4.6 (c, d, and e) indicates that iPAT imaging was able to visualize all tumor edges with good contrast, even when pre-contrast T1w MRI was not. Finally, the photoacoustic mammography, or PAM, study by Manohar et al. also reached the same conclusion, i.e. the optical contrast in PAT is largely independent of tissue density[42].

Lastly, the positive margin case illustrated perhaps the most impactful potential of iPAT. Notably, intraoperative X-ray also demonstrated the presence of a spiculated mass inside the lumpectomy specimen, but the two-dimensional nature of that imaging modality failed to inform the operating surgeon of its true three-dimensional extent. On the other hand, the US examination revealed very little useful indication of lesion position or size. In contrast, iPAT clearly visualized the lesion and its extent. If the iPAT scan results for this case were permitted to be shared with the surgeon, the patient would potentially have been spared a repeat surgery.

4.4.5 iPAT system and intraoperative protocol

While iPAT was able to deliver novel imaging results, the current prototype remains to be optimized to enable smooth operation in a demanding surgical environment. However, straight forward technical improvements should greatly reduce the operator burden. Our experience identified several key shortcomings. For example, the 24-channel photoacoustic transducer array, which was used to detect signals originating from the specimen, spent most of its time scanning the imaging volume to capture the 24,000 projections necessary for high fidelity image reconstruction. Implementing a 240-channel array would in theory reduce scan time from 6 minutes to only 36 seconds. Therefore, the "fast" mode protocol would have taken about 10 minutes instead of 20 minutes. Additionally, a more user-friendly lumpectomy specimen holder and preparation protocol could potentially reduce the entire procedure to just a few minutes.

Another concern involved the laser. We found that energy output stability was sub-optimal, especially for the first few hours of operation. This occasionally resulted in a reduced signal-to-noise ratio and lowered image quality. A better laser system or stabilization method would represent a substantial improvement.

Finally, an increase in the number of wavelengths employed for discrimination of tissue types would represent a well of potential cancer-related information. While tissue lipid and hemoglobin concentration are important biomarkers, collagen, elastin and H_2O may yield further insight into tissue microstructure. Therefore, illumination in the 900 nm to 1300 nm wavelength range, where theses tissue chromophores exhibit unique spectral features, should prove useful in further characterizing breast abnormalities.

4.5 Conclusion

This work established a potential role of photoacoustic tomography in the pre-operative and intra-operative setting during breast conserving surgery. By delivering real-time actionable information within an operational surgical suite, the novel imaging system presented here promises significant clinical impact

through higher surgical success rates. Positive and negative predictive values as high as 81% and 87%, respectively, were found leading to a potential reduction in failed surgeries from 22.6% to as low as 5.7%. In spite of the significant overestimation of lesion size, we found the correlation coefficient, as high as $r = 0.77$ ($p < 0.0001$) between iPAT and pathology, to be encouraging. However, the dependence of PPV, NPV, sensitivity, specificity and correlation on the iPAT scan configuration suggests that optimization of this imaging method is far from complete.

4.6 References

1. Siegel RL, Miller KD, Jemal A. Cancer Statistics , 2015. *CA Cancer J Clin*. 2015;65(1):5-29. doi:10.3322/caac.21254.
2. Yaffe MJ, Bloomquist AK, Hunter DM, Mawdsley GE, Chiarlli AM, Muradali D, Mainprize JG. Comparative performance of modern digital mammography systems in a large breast screening program Comparative performance of modern digital mammography systems in a large breast screening program. *Med Phys*. 2013;40(112):121915. doi:10.1118/1.4829516.
3. Mamounas EP. Continuing evolution in breast cancer surgical management. *J Clin Oncol*. 2005;23(8):1603-1606. doi:10.1200/JCO.2005.01.015.
4. Kornecki A. Current status of breast ultrasound. *Can Assoc Radiol J*. 2011;62(1):31-40. doi:10.1016/j.carj.2010.07.006.
5. Gruber I V, Rueckert M, Kagan KO, Staebler A, Siegmann KC, Hartkopf A, Wallwiener D, Hahn M. Measurement of tumour size with mammography, sonography and magnetic resonance imaging as compared to histological tumour size in primary breast cancer. *BMC Cancer*. 2013;13(June 2005):328. doi:10.1186/1471-2407-13-328.
6. Yang WT, Lam WWM, Cheung H, Suen M, King WWK, Metreweli C. Sonographic, magnetic resonance imaging, and mammographic assessments of preoperative size of breast cancer. *J Ultrasound Med*. 1997;16(12):791-797. http://www.scopus.com/inward/record.url?eid=2-s2.0-0000202613&partnerID=tZOtx3y1.
7. Fisher B. Twenty-Year Follow-Up of a Randomized Trial Comparing Total for the Treatment of Invasive Breast Cancer. *N Engl J Med*. 2002;347(16):1233-1241. doi:10.1056/NEJMoa020128.
8. Brackstone M, Townson JL, Chambers AF. Tumour dormancy in breast cancer: an update. *Breast Cancer Res*. 2007;9(3):208. doi:10.1186/bcr1677.
9. Rusby JE, Smith BL, Gui GPH. Nipple-sparing mastectomy. *Br J Surg*. 2010;97(3):305-316. doi:10.1002/bjs.6970.
10. Ferré R, Paré M, Smith L, Theriault M, Aldis A, Kao E, Mesurolle B. Retroareolar Carcinomas in Breast Ultrasound: Pearls and Pitfalls. *Cancers (Basel)*. 2016;9(1):1. doi:10.3390/cancers9010001.

11. Liberman L, Morris EA, Dershaw DD, Abramson AF, Tan LK. Ductal enhancement on MR imaging of the breast. *Am J Roentgenol*. 2003;181(2):519-525. doi:10.2214/ajr.181.2.1810519.

12. Schiller DE, Le LW, Cho BCJ, Youngson BJ, Mccready DR. Factors Associated with Negative Margins of Lumpectomy Specimen : Potential Use in Selecting Patients for Intraoperative Radiotherapy. *Ann Ourgical Oncol*. 2007;15(3):833-842. doi:10.1245/s10434-007-9711-2.

13. Waljee JF, Hu ES, Newman LA, Alderman AK. Predictors of Re-excision among Women Undergoing Breast-Conserving Surgery for Cancer. *Ann Surg Oncol*. 2008;15(5):1297-1303. doi:10.1245/s10434-007-9777-x.

14. Schulman AM, Mirrielees JA, Leverson G, Landercasper J, Greenberg C, Wilke LG. Reexcision Surgery for Breast Cancer: An Analysis of the American Society of Breast Surgeons (ASBrS) MasterySM Database Following the SSO-ASTRO "No Ink on Tumor" Guidelines. *Ann Surg Oncol*. 2016;(February):52-58. doi:10.1245/s10434-016-5516-5.

15. Houssami N, Macaskill P, Luke Marinovich M, Morrow M. The Association of Surgical Margins and Local Recurrence in Women with Early-Stage Invasive Breast Cancer Treated with Breast-Conserving Therapy: A Meta-Analysis. *Ann Surg Oncol*. 2014;21(3):717-730. doi:10.1245/s10434-014-3480-5.

16. Newman LA, Kuerer HM. Advances in breast conservation therapy. *J Clin Oncol*. 2005;23(8):1685-1697. doi:10.1200/JCO.2005.09.046.

17. Holli K, Saaristo R, Isola J, Joensuu H, Hakama M. Lumpectomy with or without postoperative radiotherapy for breast cancer with favourable prognostic features: results of a randomized study. *Br J Cancer*. 2001;84(2):164-169. doi:10.1054/bjoc.2000.1571.

18. Hainsworth A, Fosh B, Raymond W, Eaton M, Mcleay W. Ductal carcinoma in situ : breast-conserving surgery without radiotherapy. *ANZ J Surg*. 2015;85(4):245-248. doi:10.1111/ans.12655.

19. Ananthakrishnan P, Balci FL, Crowe JP. Optimizing Surgical Margins in Breast Conservation. *Int J Surg Oncol*. 2012;2012. doi:10.1155/2012/585670.

20. Weir L, Worsley D, Bernstein V. The value of FDG positron emission tomography in the management of patients with breast cancer. *Breast J*. 2005;11(3):204-209. doi:TBJ21625 [pii]\r10.1111/j.1075-122X.2005.21625.x.

21. Menezes GL, Knuttel FM, Stehouwer BL, Pijnappel RM, van den Bosch MA. Magnetic resonance imaging in breast cancer: A literature review and future perspectives. *World J Clin Oncol*. 2014;5(2):61-70. doi:10.5306/wjco.v5.i2.61.

22. Groheux D, Cochet A, Humbert O, Alberini J-L, Hindié E, Mankoff D. 18F-FDG PET/CT for Staging and Restaging of Breast Cancer. *J Nucl Med*. 2016;57 Suppl 1:17S-26S. doi:10.2967/jnumed.115.157859.

23. Papa M, Allweis T, Karni T, Sandbanks J, Konichezky M, Diment J, Guterman A, Shapiro M, Peles Z, Maishar R, Gur A, Kolka E, Brem R. An intraoperative MRI system for margin assessment in breast conserving surgery: Initial results from a novel technique. *J Surg Oncol*. 2016;114(1):22-26. doi:10.1002/jso.24246.

24. Britton PD, Sonoda LI, Yamamoto AK, Koo B, Soh E, Goud A. Breast surgical specimen

radiographs : How reliable are they ? *Eur J Radiol*. 2011;79(2):245-249. doi:10.1016/j.ejrad.2010.02.012.

25. Eggemann H, Ignatov T, Dan S. Accuracy of ultrasound-guided breast-conserving surgery in the determination of adequate surgical margins. *Breast Cancer Res Treat*. 2014;145(1):129-136. doi:10.1007/s10549-014-2932-8.

26. Krekel NMA, Haloua MH, Cardozo AMFL, de Wit RH, Bosch AM, de Widt-Levert LM, Muller S, van der Veen H, Bergers E, de Lange de Klerk ESM, Meijer S, Petrousjka van den Tol M. Intraoperative ultrasound guidance for palpable breast cancer excision (COBALT trial): a multicentre , randomised controlled trial. *Lancet Oncol*. 2013;14(1):48-54. doi:10.1016/S1470-2045(12)70527-2.

27. Esbona K, Li Z, Wilke LG. Intraoperative Imprint Cytology and Frozen Section Pathology for Margin Assessment in Breast Conservation Surgery : A Systematic Review. *Ann Surg Oncol*. 2012;19(10):3236-3245. doi:10.1245/s10434-012-2492-2.

28. Thill M, Dittmer C, Baumann K, Friedrichs K, Blohmer J. MarginProbe- Final results of the German post-market study in breast conserving surgery of ductal carcinoma in situ. *The Breast*. 2014;23(1):94-96. doi:10.1016/j.breast.2013.11.002.

29. Koloydenko A, Notingher I. Towards intra-operative diagnosis of tumours during breast conserving surgery by selective-sampling Raman micro-spectroscopy. *Phys Med Biol*. 2014;59(20):6141-6152. doi:10.1088/0031-9155/59/20/6141.

30. Brown JQ, Bydlon TM, Richards LM, Yu B, Kennedy SA, Geradts J, Wilke LG, Junker MK, Gallagher J, Barry WT, Ramanujam N. Optical Assesssment of Tumor Resection Margins in the Breast. *IEEE J Sel Top Quantum Electron*. 2010;16(3):530-544.

31. Lue N, Kang JW, Yu C, Barman I, Dingari NC, Field MS, Dasari RR, Fitzmaurice M. Portable Optical Fiber Probe-Based Spectroscopic Scanner for Rapid Cancer Diagnosis : A New Tool for Intraoperative Margin Assessment. *PLoS One*. 2012;7(1). doi:10.1371/journal.pone.0030887.

32. Breslin TM, Xu F, Palmer GM, Zhu C, Gilchrist KW, Ramanujam N. Autofluorescence and Diffuse Reflectance Properties of Malignant and Benign Breast Tissues. *Ann Surg Oncol*. 2004;11(1):65-70. doi:10.1245/ASO.2004.03.031.

33. Nguyen FT, Zysk AM, Chaney EJ, Kotynek JG, Oliphant UJ, Bellafiore FJ, Rowland KM, Johnson PA, Boppart SA. Intraoperative Evaluation of Breast Tumor Margins with Optical Coherence Tomography. *Cancer Res*. 2009;69(22):8790-8797. doi:10.1158/0008-5472.CAN-08-4340.

34. Wang L V, Hu S. Photoacoustic Tomography : In Vivo Imaging from Organelles to Organs. *Science (80-)*. 2012;335(March):1458-1462.

35. Dogra VS, Chinni BK, Valluru KS, Joseph J V. Multispectral Photoacoustic Imaging of Prostate Cancer : Preliminary Ex - vivo Results. *J Clin Imaging Sci*. 2015;3(3):1-7. doi:10.4103/2156-7514.119139.

36. Kim GR, Kang J, Kwak JY, Chang JH, Kim S Il, Youk JH. Photoacoustic Imaging of Breast Microcalcifications : A Preliminary Study with 8-Gauge Core-Biopsied Breast Specimens. *PLoS One*. 2014;9(8):8-10. doi:10.1371/journal.pone.0105878.

37. Kim C, Erpelding TN, Jankovic L, Pashley MD, Wang L V. Deeply penetrating in vivo photoacoustic

imaging using a clinical ultrasound array system. *Biomed Opt Express*. 2010;1(1):335-340.

38. Kosik I, Carson JJL, Program I, Health L, Joseph S. Combined 3D photoacoustic and 2D fluorescence imaging of indocyanine green contrast agent flow. *Proc SPIE*. 2013;8581:1-8. doi:10.1117/12.2005269.

39. Wong P, Kosik I, Raess A, Carson JJL. Objective Assessment and Design Improvement of a Staring, Sparse Transducer Array by the Spatial Crosstalk Matrix for 3D Photoacoustic Tomography. *PLoS One*. 2015;10(4):e0124759. doi:10.1371/journal.pone.0124759.

40. Roumeliotis MB, Kosik I, Carson JJL. 3D photoacoustic imaging using starting, sparse array with 60 transducers. 2012;8223:82233F-82233F-6. doi:10.1117/12.908841.

41. Roumeliotis M, Ephrat P, Patrick J, Carson JJL. Development and characterization of an omnidirectional photoacoustic point source for calibration of a staring 3D photoacoustic imaging system. *Opt Express*. 2009;17(17):15228-15238. doi:10.1364/OE.17.015228.

42. Heijblom M, Piras D, van den Engh FM, van der Schaaf M, Klasse JM, Steenbergen W, Manohar S. The state of the art in breast imaging using the Twente Photoacoustic Mammoscope: results from 31 measurements on malignancies. *Eur Radiol*. 2016;26(11):3874-3887. doi:10.1007/s00330-016-4240-7.

43. Li R, Wang P, Lan L, Lloyd jr. FP, Goergen CJ, Chen S, Cheng J. Assessing breast tumor margin by multispectral photoacoustic tomography. *Biomed Opt Express*. 2015;6(4):1273. doi:10.1364/BOE.6.001273.

44. Tan KY, Tan SM, Chiang SH, Tan A, Chong CK, Tay KH. Breast specimen ultrasound and mammography in the prediction of tumour-free margins. *ANZ J Surg*. 2006;76(12):1064-1067. doi:10.1111/j.1445-2197.2006.03941.x.

45. Treeby B, Cox B. Iterative Image Improvement Using Time Reversal. http://www.k-wave.org/documentation/example_pr_2D_tr_iterative.php. Published 2016.

46. Chagpar AB. Influence of breast cancer histology on the relationship between ultrasound and pathology tumor size measurements. *Breast Dis*. 2005;16(1):48-49. doi:10.1016/S1043-321X(05)80031-1.

47. Moschetta M, Telegrafo M, Introna T, Coi L, Rella L, Ranieri V. original article Role of specimen US for predicting resection margin status. 2015;36(October):201-204.

48. Scopa CD, Aroukatos P, Tsamandas AC, Aletra C. Evaluation of margin status in lumpectomy specimens and residual breast carcinoma. *Breast J*. 2006;12(2):150-153. doi:10.1111/j.1075-122X.2006.00223.x.

49. Jaeger M, Harris-Birtill D, Gertsch A, O'Flynn E, Bamber J. Deformation-compensated averaging for clutter reduction in epiphotoacoustic imaging in vivo. *J Biomed Opt*. 2012;17(6):66007. doi:10.1117/1.JBO.17.6.066007.

50. Song KH, Wang L V. Deep reflection-mode photoacoustic imaging of biological tissue. *J Biomed Opt*. 2007;12(December):1-3. doi:10.1117/1.2818045.

51. Anderson PG, Kainerstorfer JM, Sassaroli A, Krishnamurthy N, Homer MJ, Graham RA, Fantini S. Broadband optical mammography: Chromophore concentration and hemoglobin saturation

contrast in breast cancer. *PLoS One*. 2015;10(3):1-23. doi:10.1371/journal.pone.0117322.

52. Bosch AM, Kessels AGH, Beets GL, Rupa JD, Koster D, van Engelshoven JMA, von Meyenfeldt MF. Preoperative estimation of the pathological breast tumour size by physical examination, mammography and ultrasound: A prospective study on 105 invasive tumours. *Eur J Radiol*. 2003;48(3):285-292. doi:10.1016/S0720-048X(03)00081-0.

Chapter 5: Discussion and future outlook

The work presented in the preceding chapters covers a considerable breadth of knowledge in various disciplines and topics. It is likely that future developments and applications of this technology and methodology will occur in an equally diverse and multidisciplinary setting, including the physical, biological and medical sciences. With this in mind, an effort has been made to keep the material accessible from a clinical as well as technical perspective. In that spirit, the concluding chapter of this dissertation is organized according to theoretical, clinical and technical considerations and improvements.

5.1 Theoretical considerations and future directions

As a hybrid optical/acoustic imager, the iPAT system that was developed for, and employed in, this work, derived much of its inherently unique capabilities from exploitation of the molecular specificity associated with multispectral optical imaging. In contrast, examination of section 1.4.2 reveals that many groups working on PAT of the breast settled on fixed-wavelength illumination[1–3]. For example, the fundamental Nd-YAG laser emission at 1064 nm was often used, probably due to factors associated with convenience, reliability and expense of employed laser systems. Our group recognized early-on that these wavelengths are rarely optimal for differentiation of various tissue types, as can be appreciated in Figure 2.4 of chapter 2, as well as our earlier work[4,5]. Consequently, multispectral illumination capability was one of the defining features of this investigation. In this section, merits and pitfalls of the employed wavelength-selection are discussed and the theoretical basis behind the proposed wavelength optimization approach are outlined.

5.1.1 Lipids vs Hemoglobin in ex-vivo breast tumour imaging

A survey of photoacoustic imaging literature suggests that the primary contrast of tumours is provided by elevated hemoglobin concentration associated with cancer induced angiogenesis[2,6–9]. Consequently, it was

expected that iPAT scans targeting hemoglobin would exhibit increased signal intensity originating from periphery of tumour regions. However, contrary to this hypothesis, this investigation found that hemoglobin weighted images generally showed little or no correlation with hypoechoic US regions inside *ex vivo* specimens. This was the case for most of the specimens encountered in this study and is exemplified in Figure 2.5 of chapter 2. Therefore, the extendibility of documented *in vivo* results to *ex vivo* applications must be questioned. The extendibility hypothesis rests upon two assumptions.

First, it was assumed that a freshly excised tissue specimen would quickly reach low blood oxygenation levels due to a lack of blood supply. This motivated the 690 nm wavelength selection, where deoxyhemoglobin dominates tissue absorption as shown in Figure 1.4 of the Introduction. The validity of this assumption was corroborated by the increased 690 nm signal intensity associated with bloody regions. For example, note the hyper-intense appearance of the region indicated by the dashed oval in the 690 nm image shown in Figure 2.5(a) of chapter 2. This region corresponds well to the area of high blood content marked by a dashed oval in the photograph of Figure 2.5(h). In comparison, the corresponding 800 nm images in Figure 2.5(b) show reduced intensity. This result suggests a dominance of deoxygenated blood since the 800 nm wavelength is absorbed equally by deoxy- and oxy-hemoglobin while the 690 nm wavelength is dominantly absorbed by only deoxyhemoglobin.

The second assumption is that blood distribution inside the specimen will remain relatively unchanged after excision. However, the blood distribution depends on ability of the vascular network to maintain blood vessel volume, which in turn depends on blood pressure, provided by cardiac output. Because an excised specimen is no longer connected to the cardiovascular system, it is possible that many of its blood vessels collapsed during surgery, leading to a heterogeneous reduction in blood volume. Therefore, hemoglobin distribution inside *excised* tissue specimens may not be a good biomarker of malignancy.

Alternatively, low lipid concentration has been well documented by optical methods as being a significant indicator of breast abnormalities[10]. Furthermore, unlike the mobile nature of blood, the lipid concentration within breast tissue is unaffected by surgical excision. Consequently, it is possible that low

lipid concentration is a good indicator of tumour location and extent, in excised tissue. Moreover, lipid may be a more effective biomarker for *in vivo* tumour mapping as well, and going forward, researchers with access to high-fidelity photoacoustic imaging systems should make an effort to examine this approach. The preliminary results of the study presented here provide motivation for this direction. Finally, recently developed sophisticated lipidomic profiling methods have demonstrated outstanding diagnostic accuracy near 100%[11]. These findings independently indicate that, in differentiating malignant lesions, lipid content may be a promising new alternative to hemoglobin.

5.1.2 Optimizing wavelength selection for tissue discrimination

Beyond the two employed wavelengths, which targeted hemoglobin and lipids, other tissue chromophores should ideally be exploited to maximize the sensitivity and specificity of iPAT. For example, breast density, or the amount of fibro-glandular tissue in the breast, has been correlated to water concentration, and independently, to elevated breast cancer risk[12,13]. Specifically, increases in water concentration were associated with volumes containing increased fibrous and glandular tissue, while still higher concentrations were associated with malignant lesions. Furthermore, NIR optical methods have demonstrated excellent sensitivity to water content, indicating altered concentrations in most malignant breast tumours[10]. Therefore, use of an appropriate water-sensitive illumination wavelength during iPAT imaging of lumpectomy specimens may uncover new, potentially cancer-relevant, indicators of underlying tissue composition.

To that end, there are numerous wavelength selection possibilities in the deeper NIR optical spectrum where hemoglobin plays a reduced role in tissue absorption. For example, the spectral water peaks near 970 nm and 1180 nm seem logical staring points, as can be appreciated in Figure 5.1. On the other hand, the close spectral proximity of those peaks, to the 930 nm and 1210 nm lipid peaks, may cause reduced tissue-differentiation capacity. Consequently, a wavelength near 1140 nm may produce more effective results.

Similarly, the protein collagen and to a lesser degree, elastin, are found throughout the breast, and indeed the entire body. Furthermore, it is well known that malignant neoplasms frequently induce a desmoplastic reaction via elevated secretion of collagen, ultimately leading to an area of increased stiffness, or a palpable lump[14]. Importantly, more recent studies have linked the degree of collagen concentration within a malignant lesion to an increased propensity of tumour metastasis[15,16]. Therefore, in addition to hemoglobin, lipids, and water, collagen may also be a significant indicator of malignancy, and perhaps may even provide insight into the aggressiveness of tumours.

Inspecting Figure 5.1 reveals potential wavelengths that could be used to sway iPAT contrast towards collagen. For example, the absorption peak near 1170 nm may be a good option. However, the high absorption of water and lipids near that spectral region may overshadow collagen contrast. Instead, a wavelength of 1040 nm, where both lipids and water play reduced roles, might yield more effective collagen-biased imaging results. Ultimately, in practice, wavelength optimization will likely require consideration of both theoretical and empirical evidence.

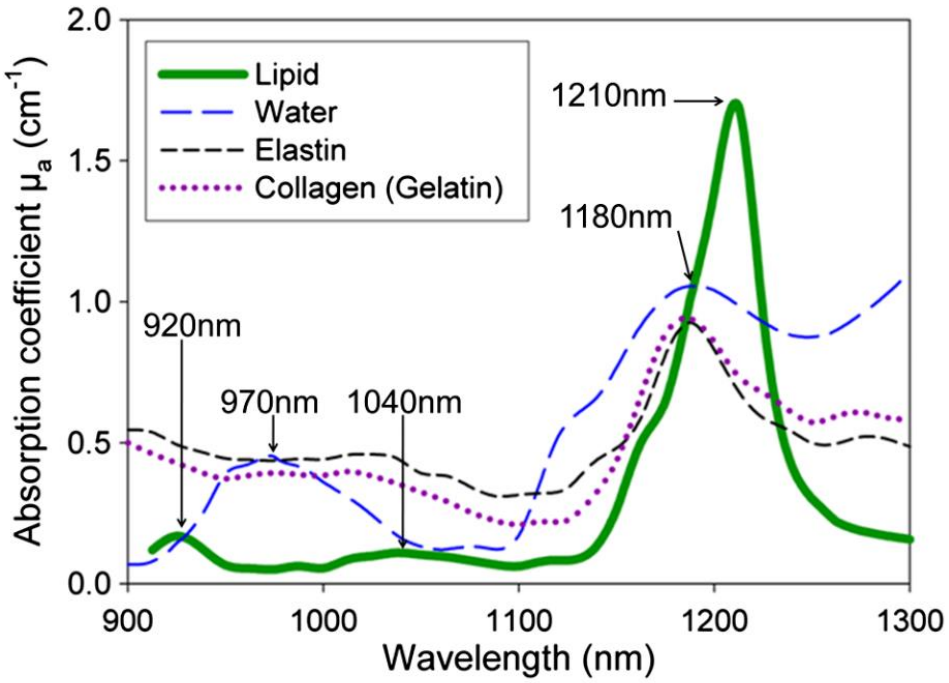

Figure 5.1. Optical absorption spectra of common breast tissue constituents in the 900 nm to 1300 nm range, including collagen, lipid, and water. Adapted from 17.

5.2 Clinical considerations and future outlook

As is often the case, ideal solutions to real-world clinical problems are limited by the technical capabilities that are currently available. Rather than outlining the technical means by which these clinical problems may be solved, here, desirable system features are discussed from an end-user perspective.

5.2.1 iPAT as an intraoperative specimen analyzer

The iPAT system that was used in this work was able to successfully demonstrate some very promising capabilities in a true clinical intraoperative setting. These included high-contrast, non-destructive visualization of lesions belonging to various histologic sub-types such as IDC, DCIS and ILC. Furthermore, unlike the employed conventional sonography imager, the system was also able to

consistently visualize surgical orientation sutures. This feature, in combination with photographs, facilitated specimen orientation with respect to the patient, enabling practical studies comparing iPAT results to diagnostic imaging and pathology. Straight forward implementation of oriented specimen imaging also illustrated what is likely the most impactful use of the iPAT imaging platform, namely intraoperative specimen examination. Therefore, similarly to current intraoperative tissue analyzers and protocols, such as Faxitron, we believe that the system belongs in the operating room where the surgeon can obtain real-time actionable information, with or without radiologist or pathologist input.

On the downside, the system frequently failed to visualize localization wires, tissue clips, as well as I-125 radioactive localization seeds. This is unfortunate because the widespread translation of this technology will likely depend on preservation of the current standard of practice, namely X-ray radiography. As can be appreciated in Figure 1.3 of Chapter 1, X-ray imaging excels at visualization of metallic surgical aides, providing surgeons and radiologists with confidence about surgery outcomes, particularly as it relates to harvesting of radioactive seeds. Therefore to be an effective stand-alone replacement of current intraoperative specimen examination methods, iPAT should be modified to enable visualization of these aides. Fortunately, this is likely possible through iPAT system resolution improvements via modification of the technical specifications, discussed further below, and exemplified in literature[18]. However, it may be possible to overcome this problem by simply employing a metal-optimized illumination wavelength. Alternatively, perhaps selection of iPAT compatible surgical aides, or modification of current aides by coating or otherwise impregnating materials with contrast agents, may enable more efficient PA signal generation, and result in successful surgical aid visualization.

5.2.2 iPAT breast tumour size assessment

The work presented in Chapters 3 and 4 revealed that iPAT produces relatively high correlation values when comparing tumour sizing and extent to pathology and DCE-MRI. Particularly, volumetric assessment by iPAT and DCE-MRI produced highly concordant indications with correlation coefficient

values of up to r=0.78. However, the high dependence of correlation values on the employed iPAT scan geometry indicates that further optimization is needed. Specifically, transmission-mode scans consistently outperformed multi-mode or fast scans. Unfortunately, transmission-mode scans involved scanning two opposing sides of the lumpectomy specimen separately. Consequently, this required double the amount of time to complete, causing delays that threatened to interfere with the clinically established surgical workflow. To remedy this problem, the iPAT system should be modified to enable a faster scan speed, as well as a user-friendly and seamless specimen inversion mechanism or protocol.

It should also be mentioned, that, as described in the methods sections of Chapter 3 and 4, a single observer was responsible for measurements of volumes and diameters, likely introducing some level of bias. This bias stems from that observer's a priori knowledge of results from other imaging studies such as US, X-ray and MRI. However, this situation is similar to realistic clinical conditions where individual lesions will often receive multiple modality imaging scans, producing a pool of information that is used in surgical decisions. Nevertheless, given that inter-observer variability in typical clinical assessment of lesion size can be tens of percent, a more accurately representative comparison of modality measurement performance should ideally average measurements from multiple observers.

5.2.3 iPAT margin evaluation

By employing a preemptive and conservative surgical approach, along with iPAT margin assessment, this investigation promised significant clinical impact by potentially reducing re-excision rates due to positive margins by nearly 75%. However, an ideal margin assessment method should offer similar information as the pathology report, including sub-millimeter measurements of the resection margins. This would enable objective comparison between the gold standard pathology and iPAT. Unfortunately, the relatively low 2.5 mm resolution of the system, combined with shadowing artefacts, typically found near the margins, prevented histologically-comparable measurements. Therefore, future developments of this

technology should include increased imaging resolution, as well as an artefact elimination or mitigation strategy.

5.2.4 Potential for in-vivo applications

Rather than beginning with the considerably more complicated task of performing in-vivo breast cancer imaging, the approach of this work was to focus on tumour detection and assessment technology, ex-vivo. The relative simplicity of this approach facilitated more freedom to experiment and optimize the technology and methodology, resulting in novel results. Nevertheless, these results are directly translatable to in-vivo applications. Accordingly, an in-vivo breast imaging system, based on the technology behind iPAT, should be the next logical step in technology development. For example, the breast angiography system introduced by Kruger et al. demonstrated excellent tissue penetration, clinically-relevant scan times and FOV, as well as volumetric visualization[19]. Therefore, it is likely possible that an imaging system similar in design to the Krueger system, but with illumination and signal detection based on iPAT technology, could perform diagnostic-style patient imaging featuring tumour visualization performance similar to iPAT. Furthermore, literature as well as studies in Appendix 2 have shown that PAT is highly sensitive to conventional optical contrast agents, such as Indocyanine green (ICG) and Methylene blue (MB^{+}). Therefore a fast in-vivo PAT system would permit the development and implementation of dynamic contrast enhanced (DCE) imaging protocols aimed at specific tasks, such as evaluation of tumour perfusion dynamics. Similarly to DCE-MRI, these developments will likely further improve the imaging performance and versatility of this imaging platform.

5.3 iPAT system technical improvements

The current iPAT system prototype embodies many desirable features of an ideal intraoperative specimen analyzer, including 3D volumetric visualization, multispectral capability, large FOV, and sensitivity to multiple lesion sub-types. However, the preceding theoretical and clinical discussion outlined further

unmet needs, including surgical aid visualization, sub-millimeter margin measurements, wavelength selection range encompassing water and collagen spectral peaks, as well as decreased scan time and more user friendly specimen preparation and handling protocol. Here the technical improvements necessary to realize these capabilities are discussed.

5.3.1 Tissue illumination and imaging artefacts

In summary, the current iPAT system illumination employs an Nd-YAG laser coupled to an optical parametric oscillator (OPO) capable of generating output wavelengths in the 670 nm to 950 nm range, with energies up to 40 mJ/pulse and a repetition rate of 20 Hz. To expand the wavelength tuning range and enable efficient excitation of collagen and water, a laser with an OPO that tunes farther into the NIR should be employed, along with fiber optics featuring the appropriate spectral transmission range. For example, one group utilized a laser able to generate output from 670 nm to 2300 nm[20].

In terms of illumination geometry, currently, the laser system directs a 3 cm diameter light beam along a single vertical line of sight, perpendicularly to the largest plane intersecting the compressively flattened specimen. Due to this unidimensional illumination, shadows are cast below highly absorbing features, as well as areas presenting a steep incline to the laser beam, such as near the outer edges of the specimen. While light diffusion in deep tissue typically smoothens out any steep illumination gradients, the surface and sub-surface regions remain vulnerable. To mitigate the shadowing artefact problem, the illumination scheme should be modified to ideally come from multiple directions, similarly to the employed hemispherical signal detection geometry. This would reduce the dependence of the incident laser fluence on one particular angle, hence maintaining a more homogeneous fluence overall.

5.3.2 PA signal detection and scan speed

As previously described, at the heart of the iPAT system is a unique 24-channel acoustic transducer array, featuring highly sensitive wide-band polymer (PVDF) transducer elements with a low sub-MHz peak frequency. This detection scheme is favourable due to its exquisite sensitivity to bulk tissue, enabling visualization of large centimeter-level features, including tumours. However, the use of transducers of a single low-frequency limits the attainable resolution, and in fact, reduces the sensitivity, and ultimately detectability, of signals originating from millimeter and sub-millimeter features, such as surgical aides and vasculature.

Accordingly, redesigning the iPAT transducer array should include use of multiple transducer types to enable the detection of small imaging targets and to increase the attainable imaging resolution. Due to their reasonable compromise between ease of fabrication, sensitivity, and acoustic impedance match to tissue, some groups have begun employing transducer elements with composite piezoelectric materials[7]. Other groups have resorted to using conventional piezoelectric ceramics, such as PZT, due to their excellent sensitivity and widespread availability[19]. These options should be investigated for iPAT array fabrication, however, the resonant properties of these materials may be ill-suited to the detection of transient PA waves in water and tissue. Alternatively, our group has previously reported on use of various PVDF co-polymer materials and PA transducer construction methods, demonstrating excellent acoustic impedance match to tissue, high sensitivity, and sub-millimeter resolution[4,5,21]. Logically, these expertise should be applied to the design and construction of a multi-frequency iPAT transducer array.

To capture a full hemisphere of projection measurements, necessary for high quality PA image reconstruction, the current iPAT scanner spends a majority of time rotating the 24-element arc-shaped transducer array. Therefore, designing a new array with more elements would be a straight-forward way to increase the scan speed. For example, a hemispherical staring transducer array, utilizing 240-elements, would eliminate the need for rotational scan motion, and would potentially reduce scan time from 6

minutes to just 40 seconds. Our group has previously published results demonstrating the capabilities of a staring 128-channel hemispherical PA array, consequently, an array with 240-channels implies a relatively simple extension of existing technology[4].

5.3.3 Sample immobilization

To prepare a fresh lumpectomy for scanning in the iPAT system requires placement of the specimen inside a customized saline-filled Ziploc bag, drainage of excess saline, installation of the sealed and drained bag onto the lumpectomy holder, and insertion of the holder into the iPAT system's water tank. Furthermore, if air bubbles infiltrate the bag or are unintentionally overlooked, the process must be repeated to minimize risk of imaging artefacts. In our experience, this sub-optimal procedure represents one of the best opportunities for improvement, particularly in specimen processing time. There are a number of possible approaches to enable a faster and smoother specimen handling experience. Ideally, a mechanized instrument should be designed that would accept a suture oriented specimen of arbitrary shape. The instrument should be capable of automatically processing, positioning, inverting and finally ejecting the specimen. This could be realized by use of a simple water-proof translation stage, coupled to a modified version of a commercially available vacuum sealer. Alternatively, a simpler design could be implemented by separating the specimen processing task from the specimen-holder insertion task.

5.4 Conclusions

The work presented in this dissertation began with the aim to address high BCS re-excision rates due to positive margins. A dedicated PAT-based lumpectomy specimen scanner, called iPAT, was designed, constructed, and tested in an intraoperative setting on 100 patients undergoing BCS. During the course of the investigation, the novel instrument demonstrated a capability to visualize a variety of breast abnormalities with high concordance compared to established medical imaging modalities, as well as histopathology. These capabilities resulted in a potential reduction in re-excision rates by nearly 75%.

Chapter 2 described the technical details of the iPAT instrument, and presented phantom studies, ex-vivo chicken-tissue studies as well as preliminary results of lumpectomy imaging. At the heart of the iPAT scanner was a novel transducer-array allowing detection of PA signals from bulk-tissue. The array coupled with a tunable laser permitted the differentiation and visualization of various soft tissues including poultry breast, thigh and fat tissues, as well as fresh lumpectomy specimens containing IDC and DCIS lesions. The chapter included a demonstration of the appearance of a positive margin on iPAT images. It also included a report on the discovery of lipids as a potentially alternative source of PA contrast for the visualization of whole breast tumours.

In Chapter 3 the capabilities of iPAT were tested by comparison of breast lesion size to DCE-MRI and pathology. The results were promising with correlation coefficient values for volumetric tumour measurements of up to r=0.78. Furthermore, the dependence iPAT breast tumour contrast on the utilized illumination wavelength was investigated, indicating an optimal range near 930 nm. Finally, the chapter discussed the leading theory behind shadowing artefacts, which were found to appear near the periphery of specimen images and were likely caused by sharp illumination gradients.

Chapter 4 summarized the results of the 100 patient pilot-study by demonstrating potentially significant clinical impact through intraoperative detection of 9 out of 12 positive margins during BCS. Furthermore, margin-status predictive values were calculated yielding scan-type dependent PPV, NPV, sensitivity and specificity of up to 81%, 87%, 80% and 89%, respectively. This chapter also expanded the statistical comparison of lesion diameters to 63 specimens, demonstrating strong, but also scan-type dependent correlations of up to r=0.77. The chapter established that transmission-scan geometry is optimal in visualizing breast tumour extent in lumpectomies. Finally, four case studies concluded the chapter by illustrating the visualization of IDC infiltration of the areolar complex, DCIS, IDC in fibro-glandular tissue, and a positive margin.

The application of the technology developed during this work will likely see a broadening range in the future. The ever-increasing life expectancy of the general population, particularly in the developing

world, means that cancer diagnosis and treatment are going to play an equally increasing role. Excitingly, iPAT-based technology, along with an extension to diagnostic imaging, promises higher BCS success rates, fewer re-excisions, and ultimately a more efficient cancer care administration.

5.5 References

1. Oraevski AA, Andreev VG, Karabutov AA, RD Fleming, Z Gatalica, H Singh, RO Esenaliev. Laser opto-acoustic imaging of the breast: detection of cancer angiogenesis. *Proc SPIE*. 1999;3597:352-363.

2. Manohar S, Vaartjes SE, van Hespen JCG, Klasse JM, van den Engh FM, Steenbergen W, van Leeuwen TG. Initial results of in vivo non-invasive cancer imaging in the human breast using near-infrared photoacoustics. *Opt Express*. 2007;15(19):12277-12285. doi:10.1364/OE.15.012277.

3. Heijblom M, Piras D, van den Engh FM, van der Schaaf M, Klasse JM, Steenbergen W, Manohar S. The state of the art in breast imaging using the Twente Photoacoustic Mammoscope: results from 31 measurements on malignancies. *Eur Radiol*. 2016;26(11):3874-3887. doi:10.1007/s00330-016-4240-7.

4. Kosik I, Carson JJL. Real-time multispectral 3-D photoacoustic imaging of blood phantoms. *Proc SPIE*. 2013;8581:85811V. doi:10.1117/12.2005199.

5. Kosik I, Carson JJL, Program I, Health L, Joseph S. Combined 3D photoacoustic and 2D fluorescence imaging of indocyanine green contrast agent flow. *Proc SPIE*. 2013;8581:1-8. doi:10.1117/12.2005269.

6. Wang L V, Hu S. Photoacoustic Tomography : In Vivo Imaging from Organelles to Organs. *Science (80-)*. 2012;335(March):1458-1462.

7. Ermilov S a., Khamapirad T, Conjusteau A, Leonard MH, Lacewell R, Mehta K, Miller T, Oraevski AA. Laser optoacoustic imaging system for detection of breast cancer. *J Biomed Opt*. 2009;14(2):24007. doi:10.1117/1.3086616.

8. Dogra VS, Chinni BK, Valluru KS, Joseph J V. Multispectral Photoacoustic Imaging of Prostate Cancer : Preliminary Ex - vivo Results. *J Clin Imaging Sci*. 2015;3(3):1-7. doi:10.4103/2156-7514.119139.

9. Xie Z, Hooi FM, Fowlkes JB, Pinsky RW, Wang X, Carson PL. Combined photoacoustic and acoustic imaging of human breast specimens in the mammographic geometry. *Ultrasound Med Biol*. 2013;39(11):2176-2184. doi:10.1016/j.ultrasmedbio.2013.05.018.

10. Anderson PG, Kainerstorfer JM, Sassaroli A, Krishnamurthy N, Homer MJ, Graham RA, Fantini S. Broadband optical mammography: Chromophore concentration and hemoglobin saturation contrast in breast cancer. *PLoS One*. 2015;10(3):1-23. doi:10.1371/journal.pone.0117322.

11. Balog J, Sasi-szabó L, Kinross J, Lewis MR, Muirhead LJ, Vesekov K, Mirnezami R, Dezso B, Damjanovich L, Darzi A, Nicholson JK, Takats Z. Intraoperative Tissue Identification Using Rapid Evaporative Ionization Mass Spectrometry. 2013;5(194).

12. Green VL. Mammographic Breast Density and Breast Cancer Risk : Implications of the Breast Density Legislation for Health Care Practitioners. 2016;59(2):419-438.

13. Graham, S. J, Bronskill, M. J, Byng, J. W, Yaffe MJ, Boyd, N. F. Quantitative correlation of breast tissue parameters using magnetic resonance and X-ray mammography. *Br J Cancer*. 1996;168:162-168.

14. Walker RA. The complexities of breast cancer desmoplasia. *Braest Cancer Res*. 2001.

15. Zhang K, Corsa CA, Ponik SM, Prior JL, Piwnica-Worms D, Eliceiri KW, Keely PJ Longmore GD. The Collagen Receptor Discoidin Domain Receptor 2 Stabilizes Snail1 Protein to Facilitate Breast Cancer Metastasis. *Nat Cell Biol*. 2013;15(6):677-687. doi:10.1038/ncb2743.The.

16. Fenner J, Stacer AC, Winterroth F, Johnson TD, Luker KE, Luker GD. Macroscopic Stiffness of Breast Tumors Predicts Metastasis. *Sci Rep*. 2014:1-8. doi:10.1038/srep05512.

17. C. Tsai, J. Chen and WW. Near-infrared absorption property of biological soft tissue constituents. *J Med Biol Eng*. 2001;21(1):7-13.

18. Su J. Photoacoustic imaging of clinical metal needles in tissue. *J Biomed Opt*. 2010;15(April):1-6. doi:10.1117/1.3368686.

19. Kruger RA, Kuzmiak CM, Lam RB, Reinecke DR, SP Del Rio, Steed D. Dedicated 3D photoacoustic breast imaging. *Med Phys*. 2013;40(11):113301. doi:10.1118/1.4824317.

20. Li R, Wang P, Lan L, Lloyd jr. FP, Goergen CJ, Chen S, Cheng J. Assessing breast tumor margin by multispectral photoacoustic tomography. *Biomed Opt Express*. 2015;6(4):1273. doi:10.1364/BOE.6.001273.

21. Roumeliotis MB, Kosik I, Carson JJL. 3D photoacoustic imaging using starting, sparse array with 60 transducers. 2012;8223:82233F-82233F-6. doi:10.1117/12.908841.

Appendix 1: Real-Time Multispectral 3-D Photoacoustic Imaging of Blood Phantoms

Citation:

Kosik I, Carson JJL. Real-time multispectral 3-D photoacoustic imaging of blood phantoms. *Proc SPIE*. 2013;8581:85811V. doi:10.1117/12.2005199.

This work focused on development of acoustic transducer technology with high sensitivity. While the frequency was found to be too high for bulk tissue sensing, the integrated pre-amplifiers demonstrated excellent sensitivity by detecting signals from blood phantoms at various oxygenation levels. The work was focused on real time imaging, as a result, the individual image quality is low, however the temporal resolution was high. This was accomplished by use of two separate lasers tuned to different wavelengths. Ultimately, the findings of this investigation indicated that highly specialized transducers with ultra-wideband frequency response and sensitivity were needed if tumour-sized objects were to be visualized using PAT. This led to the development of the sensors that made the work of this dissertation possible.

A1.1 Introduction

A1.1.1 Background

Our group has previously reported 3D PAI with a 60 element staring, sparse hemispherical transducer array with single wavelength laser excitation, where we were able to demonstrate 3D reconstruction of a variety of targets [1]. Here, we present early results of an improved 128 element multispectral 3D PAI system featuring a staring, sparse hemispherical transducer array with better angular coverage, more sensitive detectors and dual wavelength excitation. The system was tested using blood phantoms with different oxygenation states.

A1.1.2 Motivation and Approach

One routinely studied contrast mechanism in PAI is the strong absorption of near infrared (NIR) light by blood. Hence, a 3D PAI system holds the potential to provide visualization of tissue vasculature without the need for ionizing radiation or contrast agents. Furthermore, the optical contrast sensitivity and laser tunability of PAI provides the means to perform multispectral imaging of blood based on the wavelength-dependent absorption of hemoglobin, which is the dominant chromophore in blood. Specifically, multispectral PAI provides images with inherent blood oxygenation contrast and as such might aid in the detection of tissues affected by diseases, such as cancer [2].

The PAI scheme typically employs a transducer array whose shape determines many characteristics of the system. Linear ultrasound arrays hold the advantage of being commercially available and hence are often used. However the downside is a high level of difficulty in obtaining sufficient angular coverage for meaningful 3D image reconstruction without the use of mechanical translation or rotation stages. Furthermore, current commercial arrays intended for ultrasound imaging feature transducers that tend to be highly resonant with a narrow bandwidth response, thereby greatly affecting resolution and frequency coverage. Hence, custom built, low resonance and wide bandwidth transducers are highly desirable when designing an ultrasound detection array for PAI.

Multispectral illumination schemes often employ one laser to scan through wavelengths and collect images widely spaced in time. The downside is inability to temporally synchronize the multispectral contrast, consequently functional information related to fast oxygenation dynamics is compromised.

To overcome this issue, near simultaneous illumination at multiple wavelengths must be used to capture independent images each with specific wavelength contrast. This can be accomplished by using a rapid series of synchronized pulses from multiple lasers, while measuring ultrasound output. To test this concept, we adapted our 3D PAI approach to dual wavelength imaging.

Our approach was to synchronize two independent laser systems one at 690 nm and another at 1064 nm with inter pulse duration of 200 µs and a repetition rate of 10 Hz. This approach facilitated two independent 3D photoacoustic images to be captured in less than 300 µs at close to video frame rate. We then used the system to demonstrate two color imaging of an oxygenated blood-containing spherical gel phantom with a tube filled with deoxygenated blood passing through.

A1.2. Methods

A1.2.1 Multispectral photoacoustic imaging system

The broadband nature of photoacoustic signals, which can range from kHz to hundreds of MHz, motivates the design of broadband transducers. To that end we have redesigned the transducer elements for our new array using a copolymer of PVDF, which is known to have an enhanced bandwidth response compared to uniaxialy stretched PVDF. Figure A1.1 shows the response of our custom built transducers as a function of frequency, ranging from 100 kHz to 10 MHz.

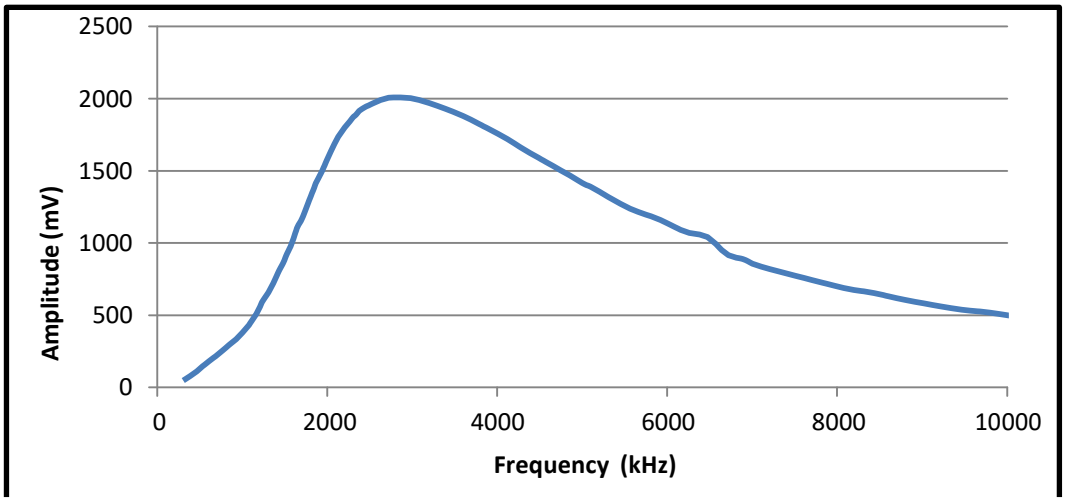

Figure A1.1. Plot of amplitude vs. frequency for an active 4.5 mm diameter PVDF copolymer transducer.

The copolymer transducers exhibited a 2.7 MHz peak frequency and a 124% fractional bandwidth at – 6 dB, which represented a 23% increase over our previous PVDF detector design. To aid in detector sensitivity, high input impedance amplifiers were built into the transducer housing, providing line driving current and minimizing signal loss.

The transducers populated a 128 channel hemispherical array manufactured using 3D printing technology. The result, shown in Figure A1.2(a), was a watertight, staring and sparse transducer array. The individual transducers were connected to a 128 channel, 40 MHz, parallel data acquisition system (DAQ) (SonixDAQ, Ultrasonix, Vancouver, BC), which was connected to a workstation using an USB 2.0 interface.

Illumination of the imaging volume was facilitated by two custom built, high power, fused, 4-to-1 optical fiber bundles. As a result, eight individual light injection points could be used to deliver single wavelength, synchronized laser pulses. Alternatively, in multispectral mode, the system could illuminate the imaging volume from four directions per wavelength.

The input sides of the fiber bundles were optically coupled to two Nd:YAG laser systems. The output of a 10 Hz near infrared (NIR) laser system (Phocus™, Opotek Inc., Carlsbad, CA), tunable in the 680-950 nm wavelength range, was tuned to 690 nm and injected light directly into one bundle. The other illumination source was provided by a 20 Hz laser system (Surelite™ SLI, Continuum Inc). The 1064 nm output of this laser was directed into the fused input of the second bundle. The eight output arms of the fiber bundles were inserted into openings in the transducer array, as seen in Figure A1.2(b). This was done such that outputs of different wavelengths were spaced as close together as possible.

(a) 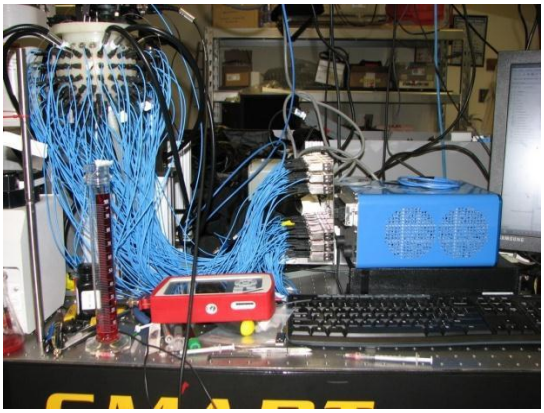 b) 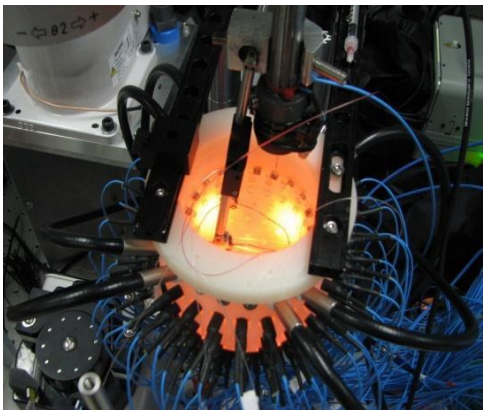

Figure A1.2. (a) A side view of a PAI system showing transducer array connected to the parallel DAQ. (b) A top view showing illumination scheme employing eight light injection points fused into two fiber bundles.

A1.2.2 System set-up and operation

For single wavelength, structural imaging, the system can be used with one laser. Alternatively when more light input is desired, synchronization of both lasers can be achieved using a 250 ps temporal resolution pulse delay generator (TCU -1, Continuum Inc.). In either case, the DAQ can be triggered by the Q-switch of either laser and this will ensure the recording of all photoacoustic signals associated with that trigger.

Real-time multispectral imaging, however, requires a more sophisticated timing method. For proper operation, a Q- switched, Nd:YAG laser system requires precision nanosecond timing between the firing of the flash lamp, and Q- switch. Because the delay between these events controls both pulse energy and time of pulse delivery, synchronization is critical. To complicate matters, thermal lensing in the Nd:YAG rod dictates the repetition rate of the laser flash lamp, and prevents arbitrary on-demand pulse delivery. Hence, if multispectral information in a single continuous US measurement is desired, both lasers must be synchronized to a single clock.

To realize this goal we designated the Surelite™ as the "Master" laser and the Phocus™ as a "Slave" laser. The "Master" flash lamp was run at a frequency of 20 Hz, as required by thermal lensing,

while the pulse divisor was chosen such that the "Master" Q-switch was allowed to free run at a pulse repetition frequency of 10 Hz. Next, the "Master" Q- switch BNC-output was connected to the flash lamp BNC-input on the "Slave" laser. This provided synchronization of the "Slave" laser to the "Master" clock. Finally, the "Slave" Q-switch delay was set to 190 µs relative to the "Master" Q- switch for optimal pulse energy. The result was capability to complete a multispectral US measurement in less than 300µs. Figure A1.3 illustrates a typical multispectral US mesasurement.

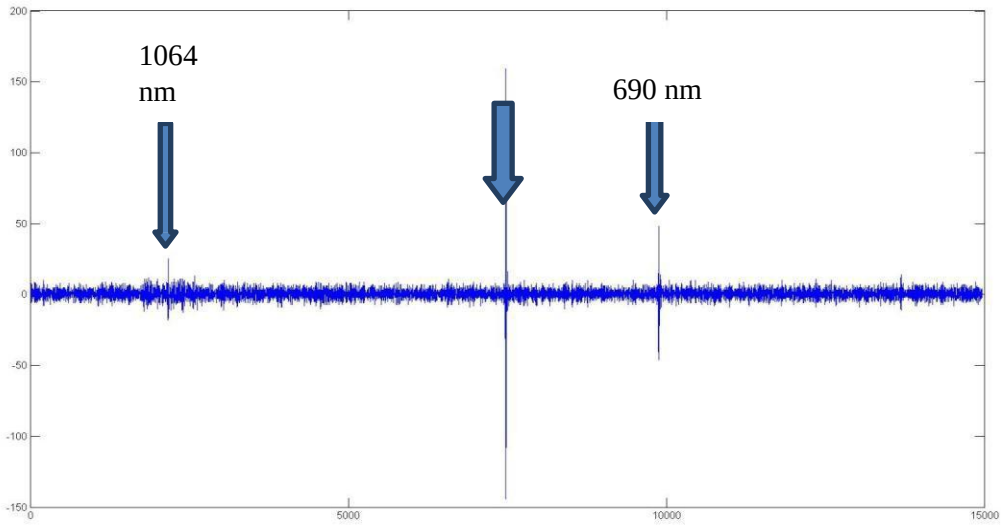

Figure A1.3. Multispectral photoacoustic signal showing the relative timing of "Master" Q-switch, which occurs prior to time index 0 and "Slave" Q-switch. Vertical axis is in digitization units with ±2048 representing full scale.

The "Slave" Q-switch trigger is visible in the raw data capture, depicted in Figure A1.3, because stray laser light was absorbed by the detector surface causing a photoacoustic signal to be generated and recorded. The "Master" Q-switch is not seen because the DAQ used it to trigger its measurement cycle, and hence it occurred prior to the time of data capture.

A relatively straight forward extension of single wavelength image reconstruction was implemented by mathematically separating the multispectral signal into two independent photoacoustic measurements.

The separated data was then used to reconstruct images using the single wavelength image reconstruction method as outlined in the next section.

A1.2.3 Image Reconstruction

Our model based 3D photoacoustic image reconstruction method has been described in previous publications and hence only a general overview will be given here [3]. It should be noted that model based techniques usually employ a combination of experimental and analytical elements, while our system model is experimentally determined.

The reconstruction method operates on the principle of modeling imaging targets as ensembles of individual omnidirectional photoacoustic point sources. The "quality" of our imaging operator, which contains the complete system response to a point source in every voxel, is therefore highly dependent on the uniformity of our point source signal. In the past we have used cleaved optical fiber, either coated or submerged in optically absorbent material, to generate photoacoustic signals. While this produced signals that were point-like, the zenith angle uniformity suffered. To improve the signal consistency as a function of zenith angle, previous flat cleaved fiber, which produced signals of higher amplitude in the forward direction, was replaced by a fiber whose tip has been machined to a hemisphere shape.

To produce an imaging operator for our system we experimentally captured the response of each transducer channel to a robotically positioned photoacoustic point source. A LabVIEW (National Instruments™) controlled, SCARA robot (Model E2C351S-UL, Epson, Nagano, Japan) with fiber optic point source attached to the effector, raster scanned the object space. At each voxel location the laser fired a ~10 ns pulse into the fiber, and consequently, the point source generated an approximately omnidirectional ultrasonic signal via the photoacoustic effect. The signal was measured by the transducer array, captured and digitized by the DAQ and finally transferred to a workstation for analysis. Matlab®

was used to process the data and reshape it into an imaging operator, which represented our system model, shown in Equation 1

$$\mathbf{g} = \mathbf{Hf} \qquad (1)$$

where **g** represents an experimental measurement captured by the transducer array and **f** is the associated image vector. This model fully described our system and singular value decomposition (SVD) was employed as a method to estimate the inverse of **H.** Equation 2 shows how knowledge of $\mathbf{H}^{\dagger}$, defined as the pseudoinverse of **H,** allows 3D image reconstruction to be carried out by solving for image vector **f** via matrix multiplication.

$$\mathbf{f} = \mathbf{H}\dagger\, \mathbf{g} \qquad \mathbf{(2)}$$

Because matrix multiplication is computationally inexpensive and generally a fast operation, this image reconstruction method allows for very fast frame rates, limited only by the repetition rate of the laser and the data transfer rate of the DAQ hardware.

A1.2.4 Multispectral photoacoustic imaging

To test the multispectral aspect of the imaging system, blood oxygenation level dependent image contrast was investigated. A 9 mm diameter agarose sphere, impregnated with 25% porcine blood concentration, was used to represent oxygenated tissue. In addition, polyethylene tubing, with a 0.28 mm inner diameter (Intramedic, Sparks, MD) was used as a deoxygenated blood vessel mimicking phantom. The sphere was mounted onto the tubing to simulate close contact between tissues of different oxygenation states, as seen in Figure A1.4. Yeast was added to porcine blood in order to reduce its oxygenation level, and then the deoxygenated blood was pumped by a peristaltic pump (Gilson® MINIPULS 3, Middleton, WI) into the tube. A stainless-steel rod fixture (6.0 mm diameter, Thorlabs, Newton, NJ) combined with a wire jig, was used to position the phantom. The fixture was mounted such that the tube and sphere were suspended inside the imaging volume.

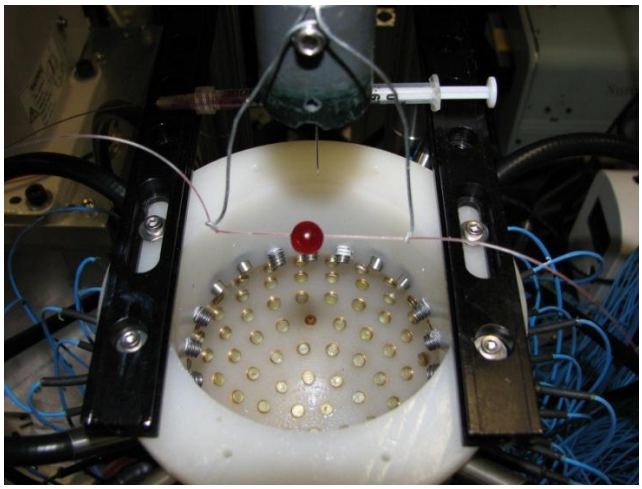

Figure A1.4. A phantom composed of polyethylene tubing and a 9 mm diameter, 25% blood-agarose sphere and a 0.28 mm (ID) blood filled tube.

Two imaging experiments were performed. First, the sphere phantom along with the blood filled tubing was translated along the *z*-axis. Image acquisition was performed at 10 Hz. Then, deoxygenated blood was pumped through the tube within the blood-agarose sphere while multispectral images were captured at 10 frames per second.

Based on the absorption spectrum of dominant tissue chromophores, imaging was performed in the so-called "NIR optical window" due to optimal light penetration. Furthermore, illumination wavelengths were chosen to maximize the difference in absorption between oxyhemoglobin and deoxyhemoglobin. The "Master" laser was tuned to 1064 nm, for oxyhemoglobin contrast, while the "Slave" laser was tuned to 690 nm for maximal deoxyhemoglobin absorption. The lasers were turned on and the DAQ collected the multispectral data. The data was transferred to a workstation and images of the *z*-planes, where the phantom was located were reconstructed.

A1.3 Results and Discussion

Figure A1.5 shows results of the first imaging experiment. The perimeter of the sphere is not well defined in all images, however, the sphere visualization is sufficient for the purpose of estimating its size,

approximate shape and location. Moreover, in Figure A1.5(f) the polyethylene tube comes into view, indicating the system's ability to resolve internal structures in spite of several mm of simulated intervening tissue with 25% blood concentration.

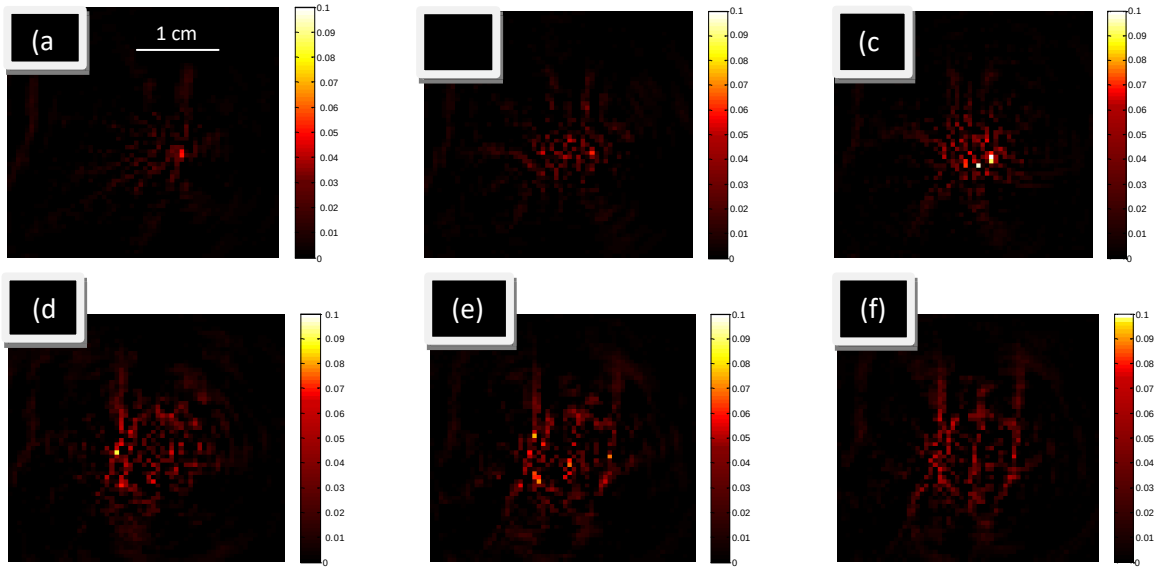

Figure A1.5. Images (a) to (f) represent consecutive captures of a *z*-slice through a 9 mm blood-agarose sphere as it is translated along the *z*-axis.

Figure A1.6 depicts results of the multispectral experiment. The 5 second duration imaging experiment generated a total of 50-690 nm images as well as 50-1064 nm images. Column (a) shows results for 690 nm where primarily the flow of deoxygenated blood is seen. Imaging performed at 1064 nm is shown in column (b). All images contain streaking artifacts caused by limited projection counts, but the phantom is clearly depicted. Of interest is the multispectral contrast between oxygenated and deoxygenated constituents, seen to appear as the flow front passes through the tube. This feature holds the potential to aid in disease diagnosis as well as functional tissue monitoring.

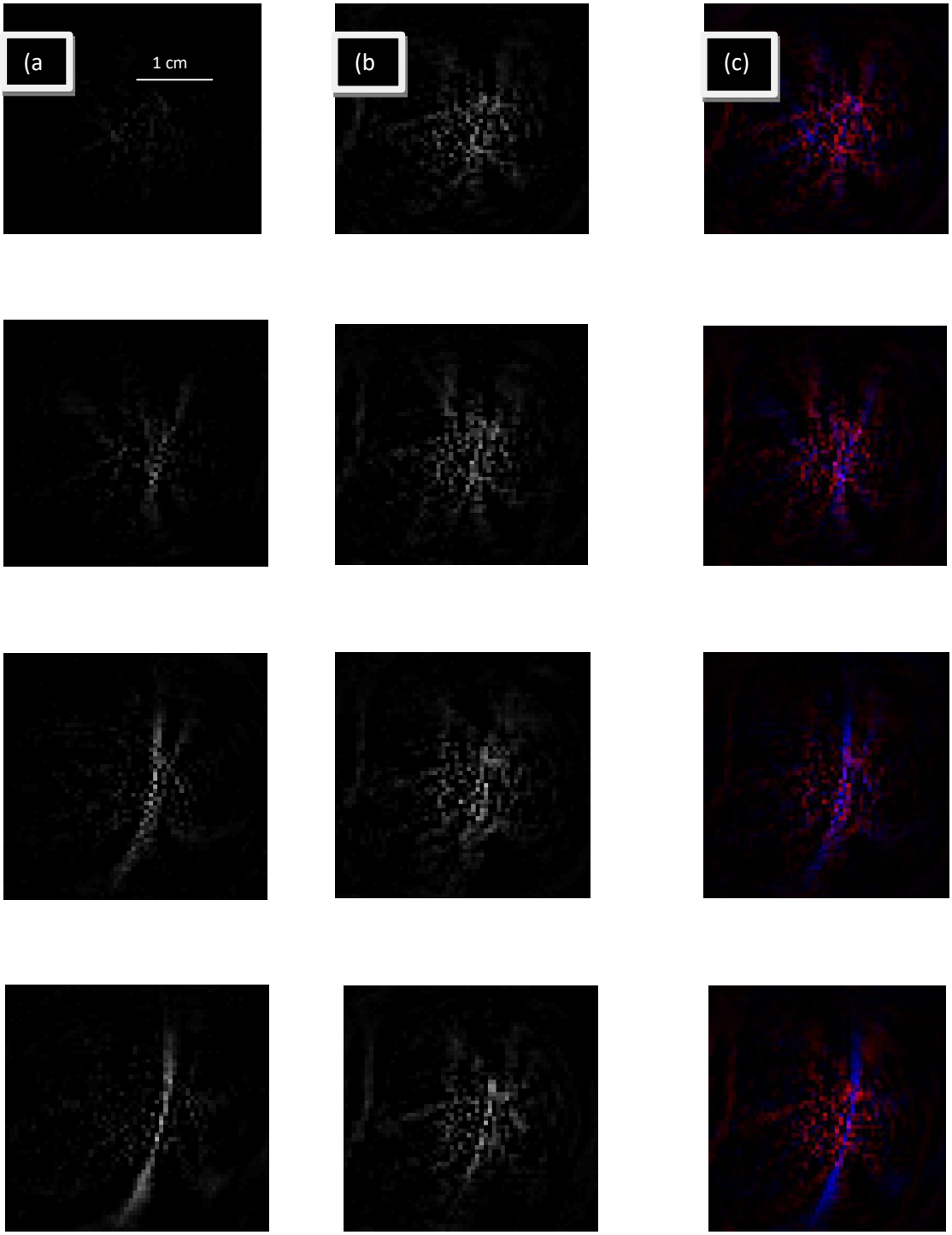

Figure A1.6. Multispectral images of a 9 mm diameter agarose sphere impregnated with 25% blood concentration and mounted on a 0.28mm I.D. polyethylene tube. The image frame dimensions are 30 mm x 30 mm, and the entire experiment lasted less than 5 seconds. Column (a) shows result of real-time 10 FPS imaging at 690 nm while deoxygenated blood is pumped through the tube. Column (b) represents imaging at 1064 nm and is separated in time from column (a) by less than 300µs. Column (c) contains overlaid images for enhanced multispectral contrast visualization.

A1.4 Conclusion

A 3D multispectral photoacoustic imaging system was built and tested. Real-time dual wavelength imaging was performed on blood phantoms with different oxygenation states. Polyethylene tubing, containing deoxygenated blood, was clearly visualized passing through a 9 mm gel sphere with 25% blood concentration. Our images exhibit clear blood oxygen contrast. At 690 nm only the deoxygenated blood was seen, while at 1064 nm primarily oxygenated blood was observed. The results demonstrate that our system is capable of providing maps of blood at different oxygenation states non-invasively at high speed and with mm-level resolution.

A1.5 Acknowledgements

Ivan Kosik was supported by the Translational Breast Cancer Research Unit (TBCRU) as well as The University of Western Ontario (WGRS). Research funding was provided by the Canadian Foundation for Innovation (CFI), the Natural Sciences and Engineering Research Council (NSERC), the Canadian Institute for Health Research (CIHR), and the Lawson Health Research Institute (LHRI). MultiMagnetics Inc. provided support with respect to the development of the data acquisition hardware.

A1.6 References

[1] Roumeliotis, M., Kosik I., and Carson, J. J. L.,"3D photoacoustic imaging using a staring-sparse array with 60 transducers", Proc. SPIE 8223, 82233F (2012).

[2] Xu, M. and Wang, L.V. “Photoacoustic imaging in biomedicine,” Rev. Sci. Instrum. 77, 041101 (2006). [3] Roumeliotis, M.B., Stodilka, R.Z., Anastasio, M.A., Ng, E. and Carson, J.J.L., "Singular value decomposition analysis of a photoacoustic imaging system and 3D imaging at 0.7 FPS," Opt. Express 19(14), 13405-13417 (2011).

Appendix 2: Combined 3D photoacoustic and 2D fluorescence imaging of indocyanine green contrast agent flow

Citation:

Kosik I, Carson JJL, Program I, Health L, Joseph S. Combined 3D photoacoustic and 2D fluorescence imaging of indocyanine green contrast agent flow. *Proc SPIE*. 2013;8581:1-8. doi:10.1117/12.2005269.

In Appendix 2, we used a custom built photoacoustic imaging system consisting of a 60-channel transducer array, a 50 MHz data acquisition system, and an Nd:YAG pumped OPO laser, to perform simultaneous photoacoustic and fluorescence imaging. A single 780 nm laser pulse generated both ultrasound and fluorescence, enabling reconstruction of images for both modalities with near perfect temporal co-registration. The result highlighted the ability of photoacoustic imaging to supplement fluorescence data when optical scatter reduces fluorescence resolution beyond its useful range. This work motivated the inclusion of fluorescence imaging during the lumpectomy evaluation procedure, which was the main target of this doctoral study. Since it was found that a single laser pulse could deliver excitation for both modalities, it seemed that fluorescence could be a convenient supplemental source of information, particularly sensitive to the surface of the specimen. Unfortunately, the complexity of implementing the iPAT system alone was found to be too great to add any further complication.

A2.1 Introduction

A2.1.1 Background

When short, pulsed laser light is absorbed by optically dense media, ultrasonic transients in the MHz frequency range are created via the photoacoustic effect [1]. Provided that the stress and thermal confinement conditions are met, sub- millimetre resolution is possible in images reconstructed from the acoustic transients detected with transducers of sufficient bandwidth [2,3]. Photoacoustic images can be created using a number of different reconstruction approaches such as back-projection algorithms, which require explicit knowledge of the transducer location and orientation; and model-based algorithms that can

recover images utilizing the system response to a photoacoustic point source, in some cases without prior knowledge of transducer location or orientation [4-8].

We have previously reported on a photoacoustic imaging (PAI) system that used a custom built hemispherical ultrasound transducer array with 60 detectors and a staring and sparse geometry, combined with an Nd:YAG pumped Optical Parametric Oscillator (OPO) laser system [9]. We were able to show an improvement in real time 3D reconstruction capability compared to previous attempts [4]. We now report on combining our 3D PAI system with a 2D fluorescence imaging system into a single co-registered optical imaging modality. Single shot, dual modality functional imaging was performed on ICG impregnated phantoms demonstrating the ability of the system to accurately reconstruct co-registered fluorescence and photoacoustic images.

A2.1.2 Motivation

Resulting from the relatively low scatter and absorption of acoustic waves in tissue, PAI is effective at much greater depths than any other optical imaging method. As a result, PAI complements other optical imaging techniques, such as fluorescence imaging (FI), which may provide superior resolution and contrast, but suffer from low depth penetration in turbid media. A number of attempts to marry the two techniques have been demonstrated; however a common problem has been long image acquisition times for PAI [10-12]. The difference between excitation and emission during FI allows a simple optical filter system to separate the two signals, resulting in fluorescence images which exhibit extremely high contrast against background. This can be very useful when visualization of contrast-enhanced vasculature, such as near a tumour, is desired. However, when imaging behind other fluorescence sources, behind highly absorbing or scattering tissue, or beyond a few millimetres deep, the resolution of FI rapidly degrades. On the other hand PAI is much less affected by the optical properties of intervening tissue, and can accurately reconstruct structural images of absorbers down to several centimetres. Real-time 3D PAI combined with

FI therefore holds the potential to provide superior visualization of tissue vasculature, as well as of functional processes such as bolus tracking and perfusion.

A2.1.3 Objective and approach

We aimed to take advantage of the superior penetration depth of PAI and the high contrast capability of FI, by combining the two modalities into a co-registered imaging system. To accomplish this aim we used a 3D staring and sparse photoacoustic system capable of real-time 3D image reconstruction. For FI we mounted a CCD camera above the photoacoustic system in such a way that real-time image co-registration was possible by using a single laser pulse to generate images for both modalities.

A2.2 Methods

A2.2.1 Imaging System

The PAI system consisted of a custom built 60-channel transducer array connected to a 14 bit, 50 MHz custom data acquisition system (DAQ128, MultiMagnetics Inc). The array featured a staring and sparse hemispherical geometry, with cylindrical transducers arranged along 4 rungs. The hemispherical bowl had an inside diameter of 86 mm. The front face of the each transducer was flush with the internal surface of the bowl. The 4.5 mm diameter transducer elements had a center frequency of 2.6 MHz and a bandwidth of 101% at -6 dB. The individual transducers were connected to the DAQ128, with custom built anti-aliasing filters and amplifiers using coaxial cables and SMA connectors.

The principle component of the fluorescence imaging system was a Photometrics Cascade 12 bit CCD camera. The camera featured a thermoelectrically cooled 0.5 Megapixel detector array. To prevent the 780 nm excitation light from damaging the CCD detector, as well as to enable image contrast, light entering the camera was first filtered using an 830 nm narrow band optical filter (customized by Comar

Optics) and mounted directly in front of the camera lens (Xenon 0.95/17, Schneider Kreuznach). The camera was mounted in a vertical orientation 40 cm directly above the focus of the hemispherical ultrasound detector array as shown in Figure A2.1. Laser light was delivered from the OPO (Surelite PLUS pumped by a SLIII at 532 nm, Continuum Inc.) using a series of mirrors such that the beam entered the bowl from the top at a slight angle to allow observation of the sample by the camera.

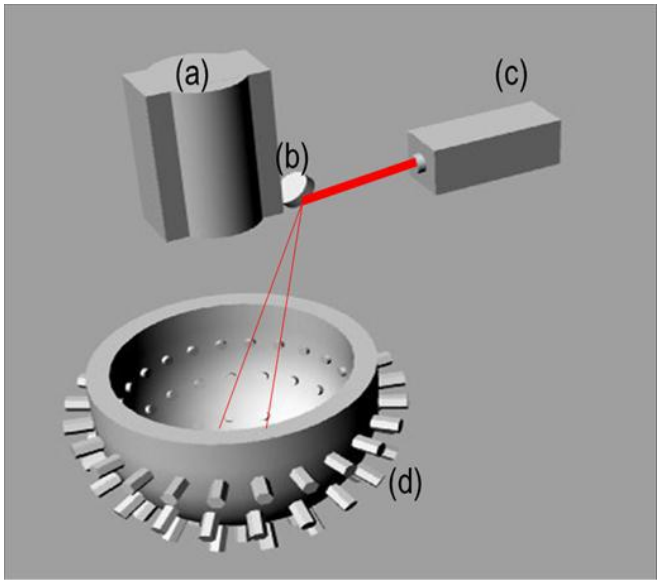

Figure A2.1. A 3D rendering (not to scale) of the dual modality imaging system composed of (a) CCD camera, (b) mirror, (c) Nd:YAG pumped OPO, and (d) 60-element, 86 mm diameter transducer array.

A2.2.2 Image Reconstruction

Our model based 3D photoacoustic image reconstruction method has been described in previous publications and hence only a general overview will be given here. To produce the imaging operator for our system, we experimentally captured the response of each transducer channel to a robotically placed photoacoustic point source, as described in [13]. A SCARA robot (Model E2C351S-UL, Epson, Nagano, Japan), with a fiber optic point source attached to the robot effector was raster scanned within the bowl to cover a grid representative of 60 x 60 x 5 voxels. At each grid location, the fiber-based point source was illuminated by the pulsed laser and the DAQ128 was triggered to record the conditioned signal from each

transducer simultaneously. The data was then transferred from the DAQ128 to the workstation and stored for processing in Matlab®. Figure A2.2 shows a subset of the imaging operator with panels showing additional detail to visualize typical transducer responses.

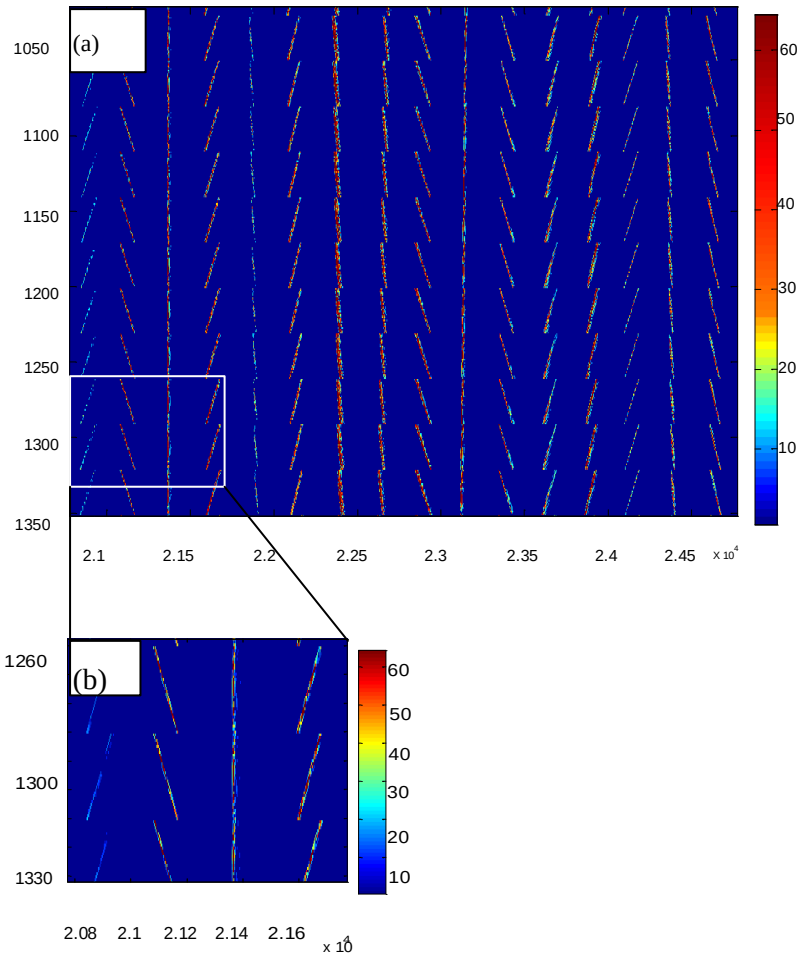

Figure A2.2. (a) Calibration map showing the temporal response of a subset of 16 transducers (horizontal axis) at 380 voxel positions (vertical axis). Color scale indicates the signal amplitude in digitization counts. (b) Enlarged view of the temporal response of 4 transducers at 80 voxels indicated by the highlighted rectangle in (a).

The imaging volume measured 30x30x2.5 mm^3 with a voxel size of 0.5 mm on edge, for a total of 18,000 voxels. The 60 transducer signals were down sampled to 350 points per position measurement per transducer, which was then assembled into an imaging operator **H**, consisting of 18,000 rows by 21,000 columns. This formed the basis of a linear system model, shown in Equation 1, which described our system

$$\mathbf{g} = \mathbf{Hf} \qquad (1)$$

where **g** represents an experimental measurement captured by the transducer array and **f** is the associated image vector. Singular Value Decomposition (SVD) was used to decompose the linear system model and

calculate an estimate of the inverse of **H**. Image reconstruction was then reduced to solving for the image vector **f** by simple matrix multiplication as seen in Equation 2.

$$\mathbf{f} = \mathbf{H}\dagger\, \mathbf{g} \qquad (2)$$

where the matrix $\mathbf{H}^{\dagger}$ is defined as the pseudoinverse of **H**. Regularization was performed to improve image quality. Software used to control the calibration scan robot was implemented using Labview (National Instruments™), while reconstruction and signal processing tasks were completed using Matlab®.

Fluorescence images were captured using RSImage and PVCam (Photometrics).

A2.2.3 Imaging Tasks

Imaging was performed on ICG phantoms under two different conditions. First, dual modality imaging was carried out using clear deionised water as an acoustic coupling agent. A syringe pump (Harvard 22, South Natick, MS) was used to inject 30 μM ICG in water (Hamilton Gastight 1002 syringe, Reno, NV) into 0.27 mm I.D. S-shaped polyethylene tubing (Intramedic, Sparks, MD). A flow rate was selected to ensure capture of the flow front over a 30 s period of time. The tube was suspended in the hemispherical bowl using a stainless-steel rod-based fixture (6.0 mm diameter, Thorlabs, Newton, NJ) and a wire jig as shown in Figure A2.3.

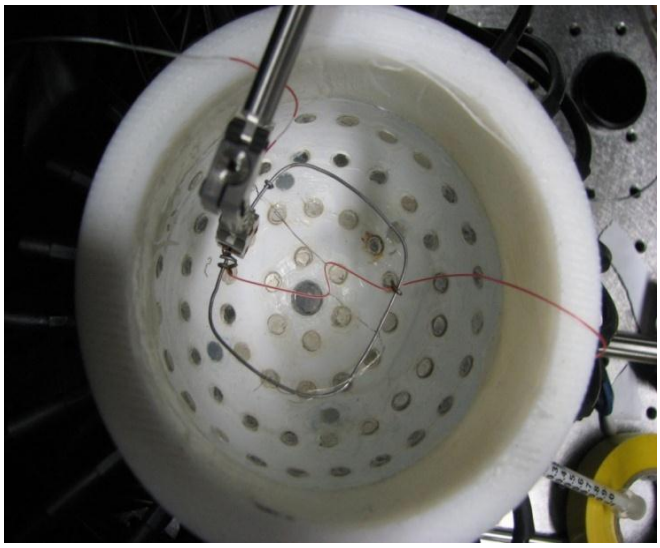

Figure A2.3. Photograph of the hemispherical bowl holding the transducer array and showing the S-shaped tube suspended by a wire jig. Here, the tube is filled with blood instead of ICG to aide in visualization of the tube in the photograph.

The OPO, pumped by a Nd:YAG pulsed laser system, was used to illuminate the phantom at a wavelength of 780 nm. Each laser pulse generated both fluorescence and photoacoustic signals, which were captured simultaneously by the CCD camera and transducer array, respectively. Photoacoustic images were reconstructed of the *z*-plane representative of the phantom location. For the second phantom, light scattering conditions similar to biological tissue were used. The bowl was filled with a 1% Intralipid^{TM} in water solution. An agarose sphere, impregnated with 30 μM ICG and measuring 9 mm in diameter, was mounted on a thin steel wire, approximately 0.2 mm in diameter, and suspended near the center of the hemispherical bowl. The transducer array was filled such that the top of the ICG sphere was 10 mm below the surface of the Intralipid^{TM} solution. Photoacoustic imaging was performed as described above and images were reconstructed for five *z*-planes, each separated by 0.5 mm.

A2.3. Results

Figure A2.4(a) is a summary of PAI results for four representative time points during the ICG flow through the S-shaped tube. Figure A2.4(b) shows the FI results corresponding to the images in Figure

A2.4(a). Each image in Figure A2.4(a) was acquired using a single 780 nm laser pulse and took less than 50 ms to reconstruct via matrix multiplication.

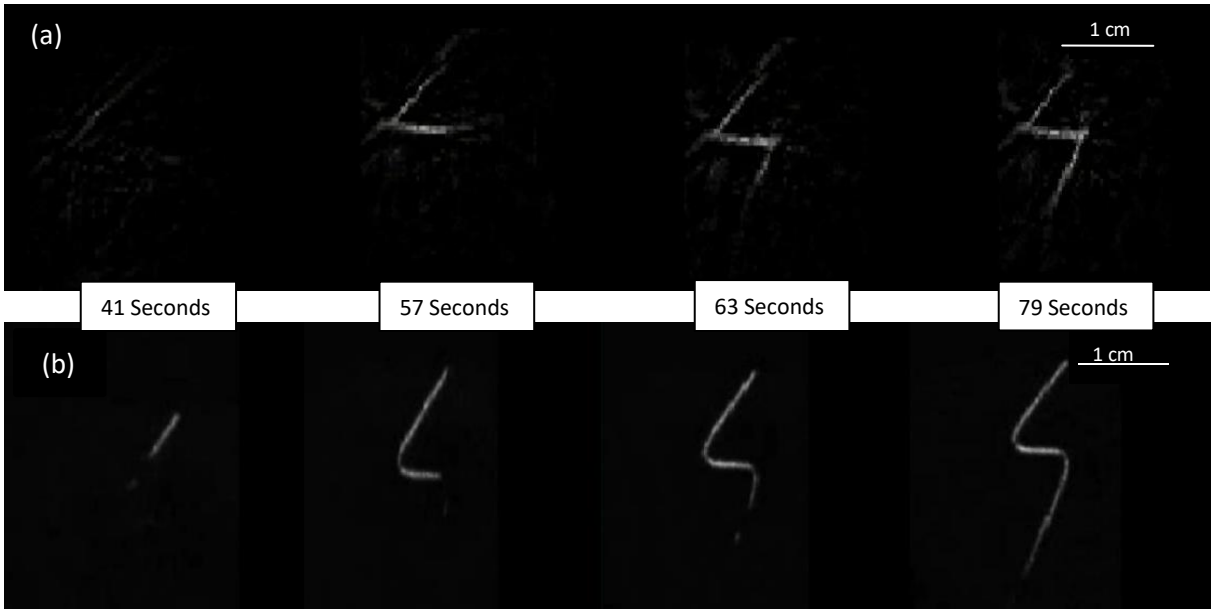

Figure A2.4. (a) Photoacoustic images of ICG flowing through a 0.27 mm ID tube. (b) Co-registered fluorescence images of the same tube shown in panel (a).

In the second experiment, presence of over 10 mm of 1% Intralipid™ solution between the 9 mm ICG sphere and the surface prevented the detection of fluorescence by FI; however, the sphere was visible in images reconstructed during PAI. Figure A2.5(a-e) shows the reconstructed images of five *z*-planes intersecting the ICG sphere phantom as well as the thin steel mounting wire (indicated by the arrow in Figure A2.5(b)).

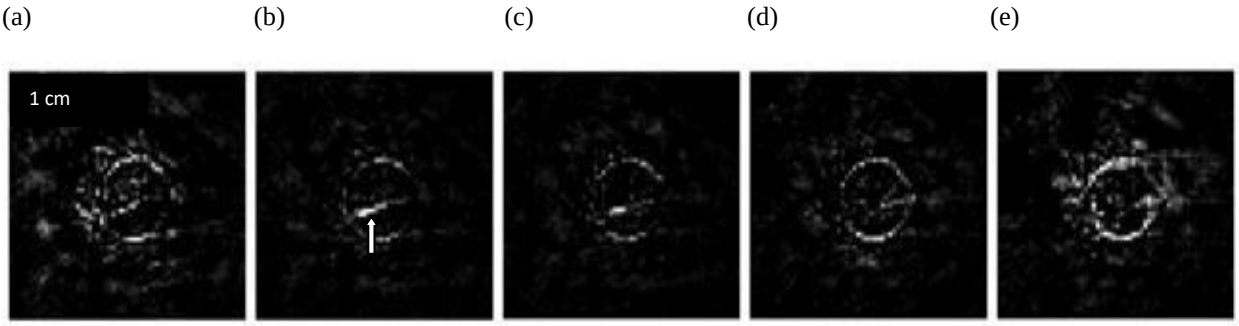

Figure A2.5. Reconstructed PAI images of five *z*-plane slices intersecting a 9-mm diameter agarose-ICG sphere. The bottom-most plane is shown in panel (a) and is located at z = -1.0 mm relative to the center of the bowl. The top-most plane is shown in panel (e) and is located z = +1.0 mm relative to the center of the bowl. Note the thin steel mounting wire indicated by the arrow in (b). The wire entered the sphere on the bottom left side of the sphere as shown in (a) and was observed to cross the five planes and exit at the top right side of the sphere as shown in panel (e).

A2.4. Discussion

While the complexity of the objects we imaged was not sufficient to demonstrate applicability to imaging biological systems, we were able to show that 3D photoacoustic reconstruction of relatively complex objects is possible with only 60 projections. Hence, if the volume of interest contains one, or a few, sparsely located targets our approach may provide 3D visualization capability.

Figure A2.4 illustrates that the system effectively tracked the flow of ICG; however, significant artefacts were present in the photoacoustic images due to the low number of projections used for reconstruction. For example, in Figure A2.4(a) the image of the tube contained streak artefacts, near corners as well as the ends, which ran parallel or tangential to the direction of the tube. Nevertheless, the flow front of the ICG bolus was clearly observed, which indicated that the method could potentially be used to estimate flow velocity. Using a linear transducer array to perform 2D photoacoustic imaging, Ma et al. [14] demonstrated the capability to perform similar measurements. Although our images contained artefacts, a significant improvement to image quality could be achieved through relatively straight forward technical improvements such as increasing the transducer array channel count and the sensitivity of each transducer. The practical limit in terms of transducer channel count for the hemispherical bowl used in these experiments is about 256 transducer channels. This would likely provide a dramatic improvement in

image quality compared to the 60 channel transducer array. Gamelin et al. have shown excellent results with a 2D PAI system incorporating 512 channels [15].

The 3D nature of our PAI imaging system is clearly observed in Figure A2.5. The figure shows the outer perimeter of an ICG agarose sphere mounted on a thin steel wire. As one inspects the consecutive *z*-slice images, the wire is seen to enter the sphere on the bottom and can be tracked as it makes its way up through the vertical planes on an oblique angle. Finally, the wire is seen to exit the sphere on the top. Due to the limited bandwidth of our transducers, photoacoustic signals due to thermoelastic expansion of the entire sphere was not detected. Instead, higher frequency signals from the light absorption near the surface of the sphere were detected and visualized in the reconstructed images. The perimeter of the sphere was accurately reconstructed at a depth of 1 cm inside the turbid medium, where fluorescence was not detected.

A2.5. Conclusion

A combined 3D photoacoustic and 2D fluorescence imaging system was constructed and calibrated. Single shot co- registered PAI and FI was performed on ICG phantoms. Functional imaging was demonstrated on a polyethylene tube phantom where the ICG bolus injection, including the flow front, was clearly visualized. Three dimensional PAI of a 9 mm agarose-ICG sphere phantom mounted on a thin steel wire and immersed in 1% Intralipid^{TM} was successful at a depth where fluorescence was not detected. Photoacoustic images were successfully captured with excellent temporal co-registration to fluorescence images, demonstrating the benefits of supplementing fluorescence data with photoacoustic information, when deep imaging is desired. Although artefacts were present in PAI images due to few available projections and electronic noise, these limitations can be overcome with relatively straight forward technological improvements.

A2.6. Acknowledgements

Ivan Kosik was supported by the Translational Breast Cancer Research Unit (TBCRU) as well as The University of Western Ontario (WGRS). Research funding was provided by the Canadian Foundation for Innovation (CFI), the Natural Sciences and Engineering Research Council (NSERC), the Canadian Institute for Health Research (CIHR), and the Lawson Health Research Institute (LHRI). MultiMagnetics Inc. provided support with respect to the development of the data acquisition hardware.

A2.7. References

[1] Sigrist, M.W. “Laser generation of acoustic waves in liquids and gases,” J. Appl. Phys. 60, R83 (1986).

[2] Xu, M. and Wang, L.V. “Photoacoustic imaging in biomedicine,” Rev. Sci. Instrum. 77, 041101 (2006).

[3] Ku, G., Wang, X. Stoica, G. and Wang, L.V. “Multiple-bandwidth photoacoustic tomography,” Phys. Med. Biol. 49(7), 1329-1338 (2004).

[4] Roumeliotis, M.B., Stodilka, R.Z., Anastasio, M.A., Ng, E. and Carson, J.J.L., "Singular value decomposition analysis of a photoacoustic imaging system and 3D imaging at 0.7 FPS," Opt. Express 19(14), 13405-13417 (2011).

[5] Carson, J.J.L., Roumeliotis, M., Chaudhary, G., Stodilka, R.Z., and Anastasio, M.A., “3D photoacoustic imaging,” Proc. SPIE 7750, 775009-1 (2010).

[6] Ephrat, P., Keenliside, L., Seabrook, A., Prato, F.S., & Carson, J.J.L., Three-dimensional photoacoustic imaging by sparse-array detection and iterative image reconstruction. J. Biomed. Opt. 13(5): 054052(2008).

[7] Ephrat, P., Roumeliotis, M., Prato F.S., and Carson, J.J.L., “Four-dimensional photoacoustic imaging of moving targets,” Opt. Express 16(26), 21570–21581 (2008).

[8] Roumeliotis, M., Stodilka, R.Z., Anastasio, M.A., Chaudhary, G., Al-Aabed, H., Ng, E., Immucci, A., and Carson, J.J.L., "Analysis of a photoacoustic imaging system by the crosstalk matrix and singular value decomposition," Opt. Express 18(11), 11406-11417 (2010).

[9] Roumeliotis, M., Kosik I., and Carson, J. J. L.,"3D photoacoustic imaging using a staring-sparse array with 60 transducers", Proc. SPIE 8223, 82233F (2012).

[10] Wang, B., Zhao, Q., Barkey, N.M., Morse, D.L., and Jiang, H.,“Photoacoustic tomography and fluorescence molecular tomography: A comparative study based on indocyanine green,” Med. Phys. 39(5), 2512-2517 (2012).

[11] Wang, L., Xie X., Oh, J.T., Li, M.L., Ku, G., Similache, S., Li C., and Stoica, G., "Combined Photoacoustic and Molecular Fluorescence Imaging In Vivo," Conf. Proc. IEEE Eng. Med. Biol. Soc. 1, 190-192 (2005).

[12] Wang, Y., Maslov, K.; Kim, C., Hu, S., Wang, L.V.; , "Integrated Photoacoustic and Fluorescence Confocal Microscopy," IEEE Trans. Biomed. Eng. 57(10), 2576-2578 (2010).

[13] Roumeliotis, M., Ephrat, P., Patrick, J. and Carson, J. J. L. , "Development and characterization of an omnidirectional photoacoustic point source for calibration of a staring 3D photoacoustic imaging system,"

Opt. Express 17(17), 15228-15238 (2009).

[14] Ma, S., Yang, S.,and Xing, D., “Photoacoustic imaging velocimetry for flow-field measurement,” Opt. Express 18(10), 9991-10000 (2010).

[15] Gamelin, J., Maurudis, A., Aguirre, A., Huang, F., Guo, P., Lihong V. Wang, and Zhu, Q., "A real-time photoacoustic tomography system for small animals," Opt. Express 17(13), 10489-10498 (2009)

Curriculum Vitae

IVAN KOSIK

EDUCATION

2011- 2017	Ph.D. Medical Biophysics, University of Western Ontario
2011	B.Sc. Honours Specialization in Medical Physics, University of Western Ontario
2006	B.Sc. Physics, University of Western Ontario

HONOURS & AWARDS

2016-2017	London Health Research Day (platform presentation winner)
2015-2016	Ontario Graduate Scholarship
	Translational Breast Cancer Research Unit Traineeship
	Western Graduate Research Scholarship
2014-2015	Translational Breast Cancer Research Unit Traineeship
	CIHR STP CaRTT Scholarship
	Western Graduate Research Scholarship

2013-2014	Translational Breast Cancer Research Unit Traineeship
	Western Graduate Research Scholarship
2012-2013	Translational Breast Cancer Research Unit Traineeship
	Western Graduate Research Scholarship
2011-2012	Translational Breast Cancer Research Unit Traineeship
	Western Graduate Research Scholarship
2010-2011	Faculty of Science Dean's Honour List
2004-2005	Faculty of Science Dean's Honour List

PUBLICATIONS

1. Wong, P., **Kosik, I**., Raess, A., & J.J.L. Carson. Objective Assessment and Design Improvement of a Staring, Sparse Transducer Array by the Spatial Crosstalk Matrix for 3D Photoacoustic Tomography. *PLOS ONE 10(4): e0124759 (2015)* [Published]

2. **Kosik, I**., & J.J.L. Carson. Real-time multispectral 3-D photoacoustic imaging of blood phantoms. *Proc. SPIE* 8581: 85811V-1-85811V-8 (2013) - [Published]

3. **Kosik, I**., & J.J.L. Carson. Combined 3D photoacoustic and 2D fluorescence imaging of indocyanine green contrast agent flow. *Proc. SPIE* 8581: 858143-1-858143-8 (2013) - [Published]

4. Wong, P., **Kosik, I**., & J.J.L. Carson. Dynamic contrast enhanced 3D photoacoustic imaging. *Proc. SPIE* 8581: 858152-1-858152-6 (2013) - [Published]

5. Tavakolian, P., **Kosik, I**., Chamson-Reig, A., St. Lawrence, K., & J.J.L. Carson. Potential for photoacoustic imaging of the neonatal brain. *Proc. SPIE* 8581: 858147-1-858147-6 (2013) - [Published]

6. Tavakolian, P., Todd, R., **Kosik, I**., Chamson-Reig, A., Vasefi, F., St. Lawrence, K., & J.J.L. Carson. Development of a neonatal skull phantom for photoacoustic imaging. *Proc. SPIE* 8581: 858146-1-858146-6 (2013) - [Published]

7. Roumeliotis, M., **Kosik, I**., & J.J.L. Carson. 3D photoacoustic imaging using a staring-sparse array with 60 transducers. *Proc. SPIE* 8223: 82233F-1-82233F-6 (2012) - [Published]

PRESENTATIONS

1. Comparison of breast tumour assessment by photoacoustic tomography, magnetic resonance imaging and pathology. *CSHRF*, Winnipeg, June 2017.

2. Comparison of breast tumour size by photoacoustic tomography, magnetic resonance imaging and pathology. *London Health Research Day*, London, March, 2017 (Platform presentation)

3. Intraoperative photoacoustic imaging of breast cancer. *Oncology Research and Education Day,* London, June, 2016. (Platform presentation)

4. Intraoperative breast lumpectomy imaging with dedicated photoacoustic tomography system. *London Health Research Day*, London, March, 2016

5. Photoacoustic imaging system for breast lumpectomy characterization. *Imaging Network of Ontario,* London, March, 2015.

6. Photoacoustic imaging system for breast lumpectomy characterization. *London Health Research Day,* London, March, 2015 (Platform presentation)

7. Hand-held real-time multispectral photoacoustic imaging of blood oxygen saturation *Oncology Research and Education Day,* London, June, 2014.

8. Hand-held real-time multispectral photoacoustic imaging of blood oxygen saturation. *London Health Research Day,* London, March, 2014.

9. Real-time 3D photoacoustic imaging. *Artimino Ultrasound Conference*, Muskoka, June, 2013. (Platform presentation)

10. Combined 3D photoacoustic and 2D fluorescence imaging of indocyanine green contrast agent flow. *London Health Research Day*, London, March, 2012.

11. 3D photoacoustic imaging using a staring-sparse array with 60 transducers. *London Health Research Day,* London, March, 2013.

12. Real-time multispectral 3-D photoacoustic imaging of blood phantoms. *SPIE Photonics West,* San Francisco, February 2013. (Platform presentation)

WORK EXPERIENCE

2002 –present ***Director***

Superior Assembly Inc.

- Founder of company with recent expansion into small production run, biomedical device manufacturing with contract to major University
- long standing (10 years) contracts to major retailers for their bicycle assembly and warranty service
- Managed all aspects of business including recruitment, training, customer service, accounting, research and development
- Developed and expanded the business, through recruitment and training, resulting in an autonomous operation

May 2011 – ***Summer Student***

September 2011 **Lawson Health Research Institute**

- Performing biomedical research in imaging department
- Troubleshooting complicated computer interface devices
- Working independently and as part of a team

February - ***Supervisor***

September 2001 **Statistics Canada: Federal Government of Canada**

- Supervisor at a call centre working for the 2001 Canada Census project
- Responsible for standardized testing, interviewing, and hiring of call centre phone operators
- Gained valuable experience by training a group of 35 operators in classroom setting
- Responsible for day-to-day scheduling and supervision of operators, handling of difficult callers and situations
- Collected and organized statistical data and maintained efficient communication of new developments in a dynamic environment
- Explained the importance of statistical research to concerned citizens